TECHNISCHE UNIVERSITÄT WIEN
Vienna | Austria

Diploma Thesis

Characterization of equilibrium phases in 8xxx alloys for the optimization of the thermodynamic database for MatCalc

carried out for the purpose of obtaining the degree of Master of Science (MSc or Dipl.-Ing. or DI), submitted at TU Wien, Faculty of Mechanical and Industrial Engineering, by

Laura Witzmann, BSc

Mat.Nr.: 01527188

[redacted]

under the supervision of

Univ.Prof. Dipl.-Ing. Dr.techn. Ernst Kozeschnik

Projektass. Robert Kahlenberg, MSc.

Institute of Materials Science and Technology, E308

Vienna, December 2021

I confirm, that going to press of this thesis needs the confirmation of the examination committee.

Affidavit

I declare in lieu of oath, that I wrote this thesis and performed the associated research myself, using only literature cited in this volume. If text passages from sources are used literally, they are marked as such.

I confirm that this work is original and has not been submitted elsewhere for any examination, nor is it currently under consideration for a thesis elsewhere.

I acknowledge that the submitted work will be checked electronically-technically using suitable and state-of-the-art means (plagiarism detection software). On the one hand, this ensures that the submitted work was prepared according to the high-quality standards within the applicable rules to ensure good scientific practice "Code of Conduct" at the TU Wien. On the other hand, a comparison with other student theses avoids violations of my personal copyright

City and Date *Signature*

Abstract

Experimental investigations on equilibrium phases in 8xxx alloys were undertaken in the present thesis.

In the characterisation of the 8xxx alloys, particular emphasis was placed on the quaternary system Al-Fe-Mn-Si. Hence, the industrial alloys AA8011, AA8014, AA8021 and AA8079 were investigated. The alloys were subjected to long-term annealing at temperatures of 400°C, 500°C and 600°C in order to reach the equilibrium states, which were subsequently characterized.

Scanning electron microscopy (SEM), energy dispersive X-ray spectroscopy (EDX) and X-ray diffraction (XRD) were used to characterize the equilibrium phases. Two different sample types were used for the X-ray diffraction: Bulk samples and powder samples. The powders were produced by chemically dissolving the aluminium matrix with phenol and therefore only the intermetallic phases remain. The measurement of the powders was necessary, because the bulk samples only had very small proportions of the phases and therefore it was difficult to make qualitative as well as quantitative statements with the bulk samples alone. The main reason for this were the large Al-peaks of the matrix in the diffractogram, which covered the smaller peaks of the intermetallic phases.

Since the phase fractions in the alloys are comparably low - at 2 to a maximum of 6 wt.%, the quantification via the measurement of bulk samples with X-ray diffraction is not quite as reliable, as already mentioned, and therefore the measurement of the powders must be used for this purpose. This procedure allows an improved quantification of the intermetallic phases present in the samples. Furthermore, this method has the advantage, that even phases with comparably small fractions can be identified. The total phase fraction was calculated with an optical evaluation of unetched light microscope images, for which the software ImageJ was used.

In summary, all three different characterisation methods are mostly congruent. The stable phases in the alloys corresponds to the stable phases characteristic for the system: $Al_{13}(Fe,Mn)_4$, $Al_6(Fe,Mn)$, α-AlFeMnSi, β-AlFeSi, and pure Si. The results were compared with the current MatCalc equilibrium calculations and the available literature data of the alloys and a clear discrepancy was observed between the simulations and the experimental/literature data. However, the assembled results of this thesis in combination with the literature data should pave the way for an improved MatCalc database to describe 8xxx series alloys.

Occasionally dispersoids were found in unetched light microscopy images of the heat-treated samples. In order to get a better insight, these samples were etched with 0.5% hydrofluoric acid. A chemical analysis was not performed as this would exceed the scope of this thesis. Furthermore, Cu- and Ni-rich regions were detected inside some of the phases of the samples annealed at 600°C, for which further investigations would also be necessary.

Deutsche Kurzfassung

In der vorliegenden Thesis wurden experimentelle Untersuchungen zu Gleichgewichtsphasen in 8xxx-Legierungen unternommen.

Bei der Charakterisierung der 8xxx Legierungen wurde vor allem Wert auf das quartäre System Al-Fe-Mn-Si gelegt, weshalb die vier technischen Legierungen AA8011, AA8014, AA8021 und AA8079 untersucht wurden. Hierfür wurden die Materialien bei den Temperaturen 400°C, 500°C, sowie 600°C langzeitgeglüht, um die Gleichgewichtszustände zu erreichen, welche im Anschluss charakterisiert wurden.

Als Charakterisierungsmethoden der Gleichgewichtsphasen wurden das Rasterelektronenmikroskop (SEM), die energiedispersive Röntgenspektroskopie (EDX) und die Röntgendiffraktometrie (XRD) verwendet. Für die Röntgendiffraktometrie wurden zwei verschiedene Probentypen verwendet: Festkörperproben und pulverförmige Proben. Die Pulver wurden durch eine chemische Auflösung der Aluminiummatrix mithilfe von Phenol hergestellt und wiesen demnach nur die übriggebliebenen intermetallischen Phasen auf. Die Messung des Pulvers war notwendig, da die Festkörperproben nur sehr geringe Anteile an den Phasen aufwiesen und es dementsprechend schwierig war, qualitative und auch quantitative Aussagen allein mit diesen Proben zu machen. Den Hauptgrund hierfür stellten die großen Al-Peaks der Matrix dar, welche die kleineren Peaks der intermetallischen Phasen im Diffraktogramm überdeckten.

Da die Phasenanteile in den Legierungen mit 2 bis maximal 6 wt.% vergleichsweise gering sind, ist die Quantifizierung der Festkörperproben mittels Röntgendiffraktometrie nicht sehr zuverlässig, wie bereits erwähnt, und für diesen Zweck wurde die Analyse mit dem Pulvern durchgeführt. Durch diese Vorgehensweise kann eine verbesserte Quantifizierung der Phasen erreicht werden. Des Weiteren hat diese Methode den Vorteil, dass auch Phasen mit vergleichsweisen geringen Anteilen identifiziert werden können. Der Gesamtphasenanteil wurde mittels einer optischen Auswertung von ungeätzten Lichtmikroskopaufnahmen berechnet, wofür die Software ImageJ verwendet wurde.

Zusammenfassend lässt sich sagen, dass alle drei unterschiedlichen Charakterisierungsmethoden weitgehend kongruent sind. Die stabilen Phasen in den Legierungen entsprechen den für das System charakteristischen stabilen Phasen: $Al_{13}(Fe,Mn)_4$, $Al_6(Fe,Mn)$, α-AlFeMnSi, β-AlFeSi und reinem Si. Die Ergebnisse wurden mit den aktuellen MatCalc-Simulationen und den verfügbaren Literaturdaten zu den untersuchten Legierungen verglichen, wobei eine deutliche Diskrepanz zwischen den Simulationen und den verfügbaren Daten festgestellt wurde. Die in dieser Arbeit zusammengestellten Ergebnisse sollten jedoch in Kombination mit den Literaturdaten den Weg für eine verbesserte MatCalc-Datenbank zur Beschreibung von Legierungen der 8xxx-Serie ebnen.

Gelegentlich wurden in ungeätzten lichtmikroskopischen Aufnahmen der wärmebehandelten Proben Dispersoide gefunden. Um einen besseren Einblick zu erhalten, wurden diese Proben mit 0.5%iger Flusssäure geätzt. Eine chemische Analyse wurde nicht durchgeführt, da dies den Rahmen dieser Arbeit sprengen würde. Außerdem wurden in einigen Phasen der bei 600°C geglühten Proben Cu- und Ni-reiche Bereiche festgestellt, welche ebenfalls weiter untersucht werden müssten.

Acknowledgement

At this point I would first like to thank all those people who have made the success of this work possible through their support.

I would like to thank Prof. Dr. Dipl.-Ing. Ernst Kozeschnik for making this interesting topic available and for the helpful suggestions that enabled me to benefit from his scientific experience.

A big thank also goes to my thesis supervisor Projektass. Robert Kahlenberg MSc., who always supported me with his comprehensive professional knowledge and encouraged me to continue, even if my motivation was sometimes not so great due to failed attempts. Without Robert's support, this thesis would not be possible in this form.

I would also like to thank the company AMAG (Austria Metall AG) for providing the materials used in this thesis.

Furthermore, I would like to thank Edith Asiemo and Christian Zaruba for their help and support in the metallographic laboratory.

For any constructive criticism, I would like to thank Dipl.-Ing. Tomasz Wojcik for answering various questions regarding material characterisation, as well as Dipl.-Ing. Werner Artner for measuring the samples with X-ray powder diffraction and for helpful tips regarding the evaluation.

Furthermore, I would like to thank Dr. Aurelie Jacob for implementing my research results in the MatCalc thermodynamic database. I would also like to thank Dipl.-Ing. Ella Staufer for providing her optimised experimental procedure for the dissolution of the aluminium matrix using phenol.

Last but not least, I would like to thank my parents, my grandparents, my sister and my friends for all their support during my entire time at school and university. Thank you for supporting me in all situations and always giving me advice and support.

“Wer nichts weiß, muss alles glauben.”

- Marie von Ebner-Eschenbach

Table of Contents

1. Introduction

As the consumption of each household increases every year, it becomes more and more important to recycle the products used. In relation to the aluminium production one of the main challenges of the future will be the increasing usage of recycled material for the production of Al-based wrought alloys. Various aspects must be taken into account when recycling Al-based alloys [1]. One important aspect is e.g. the iron content: since Fe has a very low solubility in Al, Fe leads to the formation of large intermetallic phases [2]. These have a significant influence on the ductility and formability of the alloys, as they become more brittle with increasing Fe content [1].

Therefore, it is very important to know what the microstructure in these alloying systems looks like in order to optimise the production and processing route depending on the chemical composition. Kinetic simulations can be of assistance here. However, to describe the microstructural evolution in any alloying system, a thermodynamic database is required first, which contains the information on the experimentally determined stability range of the occurring phases and their composition. In the case of the present thesis the relevant phases are primarily Fe-rich intermetallics.

Although the equilibrium phases have been sufficiently investigated for many aluminium series (e.g. 6xxx series), comparably few papers exist for lean 8xxx series alloys. The seminal work in this area is that of Phillips and Varley [3,4] for temperatures above 550°C as well as the work of Mondolfo and Barlock [5–7]. A summary was provided in 2005 by Belov et al. [8].

Furthermore, several aluminium alloys of the Al-Fe-Mn-Si system were investigated by Davignon et al. [9], but with the difference to this thesis, that the chemical composition of the alloys had higher Si contents with 4 wt.%. An optimisation of the description of the Al-Fe-Mn-Si system was carried out by Balitchev et al. [10], but also for high Si contents based on Zakharov et al. [11–13]. Their results at lower concentrations agreed to that of Phillips and Varley only for the liquidus line. The stability ranges of intermetallic phases predicted for lean alloys deviated significantly from the experimental data. Lacaze et al. [14] performed a similar assessment of the Al-Fe-Mn-Si system - primarily based on the work of Phillips and Varley and with more emphasis on low concentrations of alloying elements. The experimental data used limits the verified temperature range to 550°C and above.

Regarding technical alloys, Lentz et al. [2] investigated AA8011 and AA8079 for temperatures between 500°C and 600°C. Furthermore, simulations with the software FactSage were carried out. Santora et al. [15] investigated the precipitates and their influence on mechanical properties for the same two alloys at 500°C and 620°C. Another important reference for the phases in industrial 8xxx series alloys is Engler et al. [16]. The authors investigated the homogenization treatment for the alloy AA8006 for 480°C and 600°C and simulated the phase diagram with FactSage.

Since there is only limited access to commercial databases and the experimental data on equilibrium phases of lean industrial 8xxx alloys below 550°C is scarce, the present thesis aims at experimentally determining the stability ranges of the intermetallic phases between 400°C and 600°C and compare them to the current predictions of the existing database in MatCalc as well as to the literature.

2. Objectives

The main objective of the present thesis is to analyse the different equilibrium phases for technical AA8xxx alloys. An important point is the diversification of different alloys with respect to the elements Si, Mn and Fe.

For the present thesis the technical alloys AA8011, AA8014, AA8021 and AA8079 with different chemical compositions are chosen and long-term annealing is carried out at three different temperatures (400°C, 500°C and 600°C). The characterization of the phases is carried out depending on the crystal structure with X-ray powder diffraction and based on the chemical composition of the different precipitates, which are measured with energy dispersive X-ray spectroscopy. Furthermore, the total quantity of the individual phases is important for the analysis of the equilibrium phases, which is carried out with images from the light microscope and further analysis with the ImageJ software.

The objective is to provide an overview of the stability ranges of the different phases.

3. State of the art

3.1 The extraction of aluminium

Aluminium is the most common metal found in the earth's crust with 7.5 wt.%. It is called a light metal because of its low density of 2.7 g/cm³ [17]. In nature, aluminium is predominantly present as a chemical compound and must be separated in multi-stage processes to obtain pure aluminium [18].

The starting material for the extraction of primary aluminium is bauxite. Bauxite is a weathering product of limestone and silicate rock and owes its name to the first place of discovery in southern France, the town of Le Baux, where it was discovered in 1821 [18]. The average composition of bauxite is about 50-70% alumina, hydrate water, and various percentages of Fe-, Si-, Ti-, and other oxides depending on the deposit [19]. About 90% of the bauxite deposits are located in countries of the tropical belt and predominantly mined by opencast methods [18].

The production of aluminium from bauxite takes place in 2 process stages: (1) the extraction of aluminium oxide in the Bayer process and (2) the reduction of the oxide to metallic primary aluminium by the Hall-Hérault process [18].

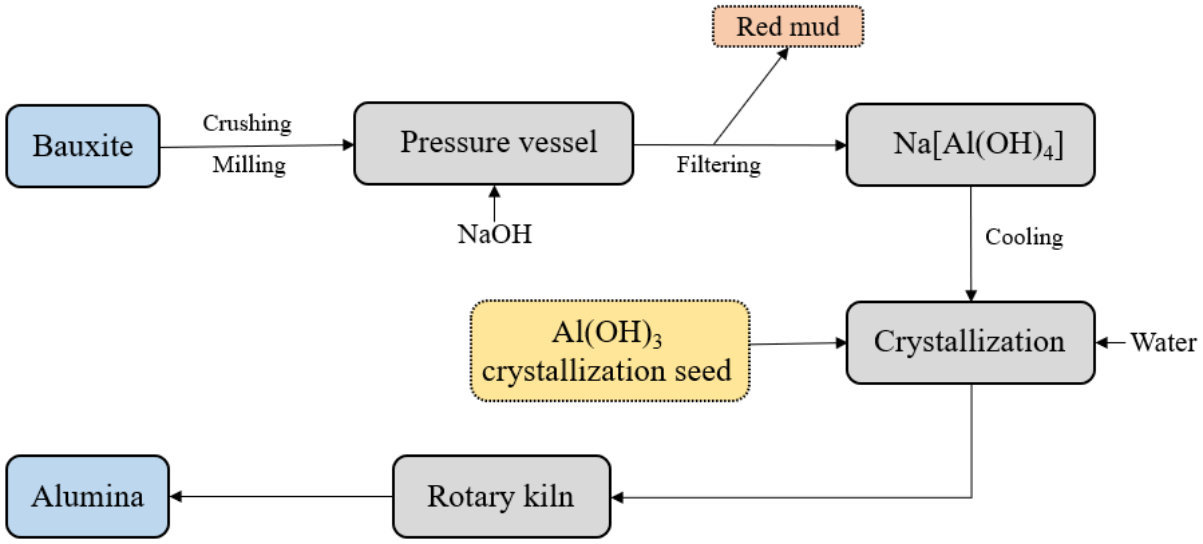

Figure 1: Schematic illustration of the Bayer-process [20]

The extraction of alumina is based on the patents of K.J. Bayer from 1887-1892, as shown in Figure 1. In this process, finely grained bauxite is added into a pressure vessel together with a sodium hydroxide NaOH solution at 160-270°C. Here the aluminium oxide is dissolved and sodium aluminate forms. The remaining components of the bauxite, above all iron oxide, remain undissolved in the residue and form the so-called red mud, which is a waste product [18]:

$$Bauxite + NaOH \xrightarrow[pressure]{\Delta} Na[Al(OH)_4] + Fe_2O_3 \quad (1)$$

The sodium aluminate liquor is then diluted to a lower alkali concentration and cooled to 60°C with a heat exchanger. After cooling, the liquid is seeded with fine-grained aluminium hydroxide in the stirrer, causing the majority to precipitate as aluminium hydroxide [18]:

$$Na[Al(OH)_4] \xrightarrow{\nabla} Al(OH)_3 + NaOH \quad (2)$$

The aluminium hydroxide is then washed and calcined to aluminium oxide in rotary kilns or fluidized bed furnaces at 1200-1300 ° C [18]:

$$2Al(OH)_3 \xrightarrow{\Delta} Al_2O_3 + 3H_2O \quad (3)$$

The oxide has a relatively high degree of purity and is used in the subsequent Hall-Hérault process [18,21].

The Hall-Hérault process is named after its inventors C.M. Hall and P. L. T. Hérault, who at the same time and independently of each other, applied for the patents for the process of the electrolysis in 1886. The schematic structure of the electrolytic reduction is shown in Figure 2 [18].

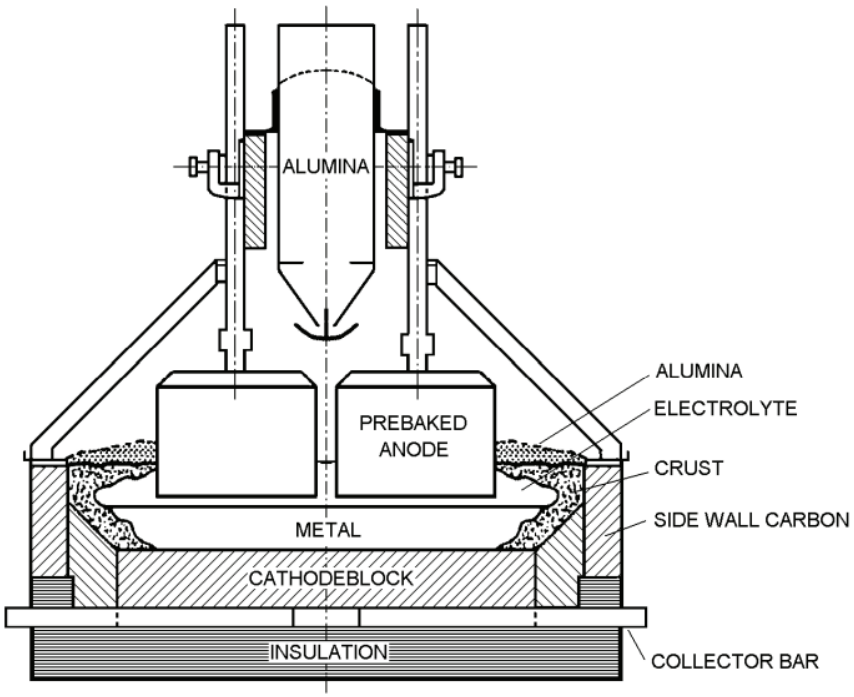

Figure 2: Schematic illustration of the Hall-Hérault-process [22]

In the process, the aluminium oxide obtained from the Bayer process is dissolved in molten cryolite (Na_3AlF_6) in order to reduce the melting point of the mixture. The melting point of pure aluminium oxide would be comparably high (2050 °C). The reduction of Al_2O_3 takes place at temperatures between 950-970°C by electrolysis, for which steel tubs with embedded cathode leads and carbon bricks are used. The anode consists of petroleum coke and pitch, while the liquid aluminium forms the cathode. As a result of the reduction, the anodes are decomposed and oxygen is released, which forms carbon monoxide (CO) and carbon dioxide (CO_2). The obtained aluminium is extracted for further processing [18].

3.2 Basics of phase diagrams and their numerical calculation using the CALPHAD-method

3.2.1 Phases

A phase is a sharply defined volume with the same crystal structure and largely uniform physical properties. The chemical composition does not necessarily have to be uniform. In the case that only one element is present, the different states of aggregation describe the possible phases. In multi-component systems several phases with the same state of aggregation may be present [23].

3.2.2 Phase diagrams

With infinite time, every thermodynamic system will react in such a way as to minimize its energy. This is thermodynamically defined by the minimum of the Gibbs free energy, which is also called the state of equilibrium [24].

In equilibrium, the different interacting phases are stable/unstable or in balance with each other depending on the specific conditions under which the system was equilibrated. The primary influencing factors that define the domains of stability are the temperature, the composition and the pressure [24].

The stability ranges of equilibrium phases are represented in so-called phase diagrams, which are also referred to as equilibrium or state diagrams. In the case of binary alloys, the phase diagram can be shown in a two-dimensional coordinate system, with the temperature plotted on the ordinate and the concentration plotted on the abscissa, as shown in an exemplary representation in Figure 3 [24].

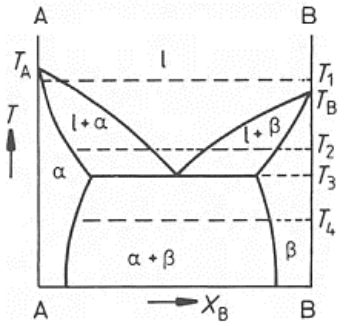

Figure 3: Eutectic phase diagram with 3 different phases [25]

Alloy systems with 3 or more components require additional dimensions for representation. Ternary systems can be represented in triangular diagrams. Isothermal sections of such a diagram are schematically drawn in Figure 4. The composition of a phase is defined by a point in the concentration triangle. Perpendicular to the drawing plane is the temperature axis. For an alloy with 4 components, a three-dimensional tetrahedron is required for the chemical composition alone [24].

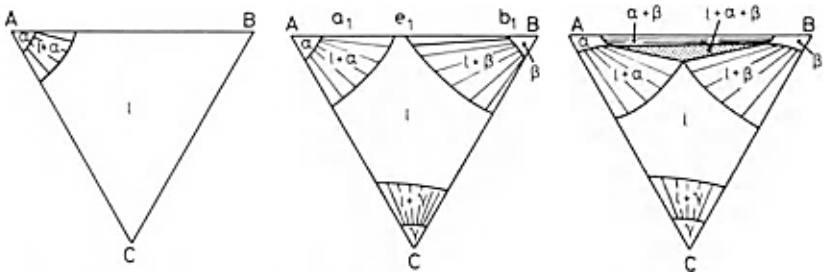

Figure 4: Isothermal sections for 4 different phases [25]

3.2.3 Thermodynamic background of the phase diagrams

In thermodynamics, the relative stability of a system is defined by its Gibbs free energy [25,26]:

$$G = U + PV - TS \tag{4}$$

In this formula *U* represents the internal energy of a system, *P* defines the pressure, *V* the volume, *T* the temperature and *S* the entropy. The entropy describes the degree of disorder and depends on the probability of finding a system in a given configuration [25,26]. Another important quantity is the enthalpy *H*, which is a measure for the heat content of a system and may be calculated as follows:

$$H = U + PV \tag{5}$$

Hence, the Gibbs energy *G* can be represented as

$$G = H - TS \tag{6}$$

As can be seen from equations 4, 5 and 6, the *PV* term is cancelled by subtraction, meaning that *G* excludes energy contributions from purely mechanical work. Another important point is, that the Gibbs energy *G* is thus a state function of systems with a constant pressure. This is particularly important because solid-state phase transformations usually take place under isobaric conditions [26]. A given system is in equilibrium when it has reached the most stable state. This is defined as the point where the lowest value of the Gibbs energy is reached, or in mathematical terms [25]:

$$dG = 0 \tag{7}$$

To calculate the change and ultimately the minimum in Gibbs energy upon mixing two elements A and B, enthalpy and entropy contributions are required.

$$\Delta G_{mix} = \Delta H_{mix} - T * \Delta S_{mix} \tag{8}$$

The mixing entropy is solely dependent on the composition and weighted by temperature. The enthalpy is frequently described by applying the so called quasi-chemical approach. This evolves around the assumption, that the heat of mixing ΔH_{mix} only depends on the bond energies between adjacent atoms. For an *ideal* mixture $\Delta H_{mix} = 0$ meaning that the atoms are essentially randomly arranged. For a *regular* mixture either $\Delta H_{mix} > 0$ or $\Delta H_{mix} < 0$, so that the atoms in the system will either prefer atoms of the opposite type ($\Delta H_{mix} < 0$) or atoms of the same type ($\Delta H_{mix} > 0$) [25].

Consequently, the shape of the Gibbs curve is largely determined by the enthalpy and the temperature, as shown in Figure 5 and Figure 6.

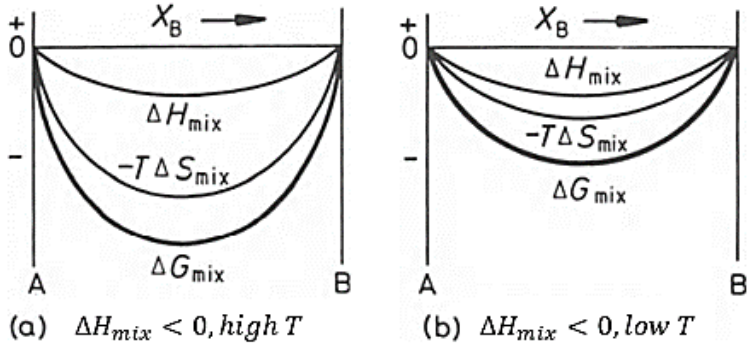

Figure 5: The effect of a negative ΔH_{mix} and different T on ΔG_{mix} [10]

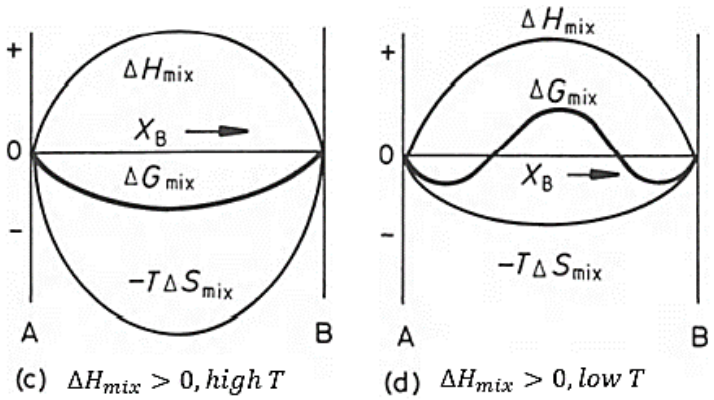

Figure 6: The effect of a positive ΔH_{mix} and different T on ΔG_{mix} [10]

From the Gibbs energy curves the phase diagrams can be constructed. In Figure 7 the Gibbs-curves of 3 phases (α, β and liquid) are depicted in different isothermal diagrams. Outside the single-phase regions i.e., in the miscibility gaps, the total energy of the system can be reduced if the system separates into a mixture of the respective 2 phases. Using the double tangent construction, the compositions of the separated phases are found, for which the elements A and B experience the same chemical potential μ in every phase. These are the equilibrium concentrations of the phases at the given total composition and temperature. For instance, the tangent construction for Figure 7 (T1 top left) essentially finds the phase compositions for α and β, where [25,26]:

$$\mu_A^\alpha = \mu_A^\beta, \quad \mu_B^\alpha = \mu_B^\beta \tag{9}$$

with

$$\mu_i = \frac{\partial G}{\partial N_i} = g + \frac{\partial g}{\partial N_i} \tag{10}$$

whereby N_i represents the number of moles of the component i [26].

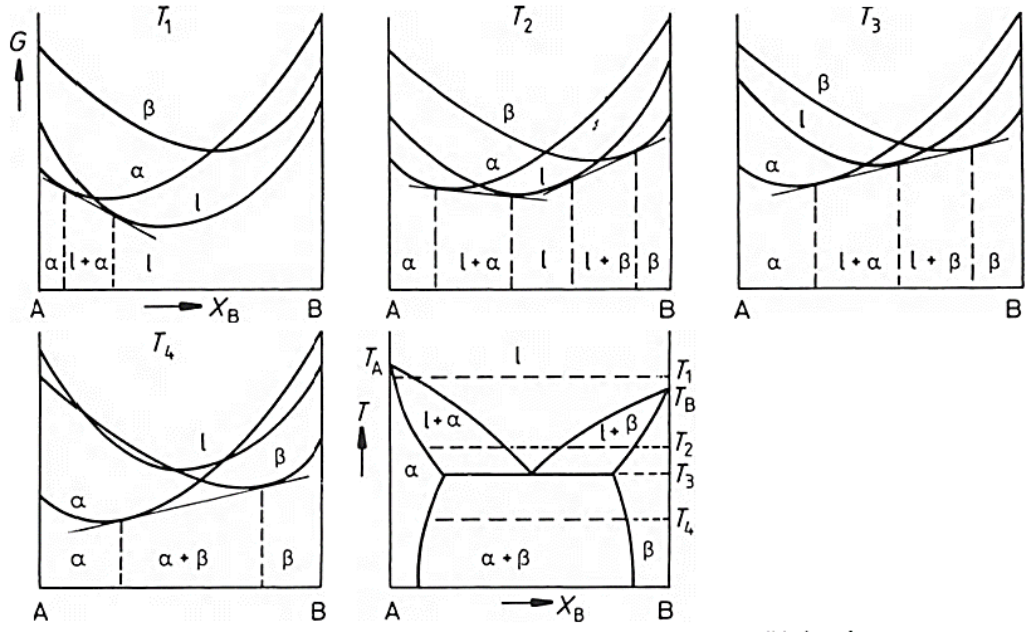

Figure 7: The derivation of a eutectic phase diagram with different crystal structures of the solid phases [25]

3.2.4 Calculation of phase diagrams – The CALPHAD approach

The CALPHAD approach is used for describing the Gibbs energy of "real" alloys. Hereby all chemical interactions between atoms in multicomponent systems will be included. The name CALPHAD stands for CALculation of PHAse Diagrams and was developed in the late 1960s and early 1970s by Kaufmann and Bernstein. By applying the CALPHAD method, thermodynamic databases can be developed using extrapolation methods in conjunction with well-studied binary and ternary systems, to ultimately allow the description of systems with higher orders. To that end, a large amount of experimental data must be given as input to fit the Gibbs energy [26,27].

Real thermodynamic systems are usually characterized by complex chemical interactions. The ideal solution is hereby taken as a basis for a more general solution, which is the sum of the Gibbs energy of an ideal solution g_{IS} and and the excess Gibbs energy g_{EX}. This excess Gibbs energy is composed of complex chemical interactions, magnetism or short-ranged ordering [26]:

$$g = g_{IS} + g_{EX} \tag{11}$$

Inserting the expressions for both contributions lead to the following:

$$g = \sum_i X_i g_i^0 + RT \sum_i X_i \ln X_i + g_{EX}^{RK} + g_{EX}^{magn} + g_{EX}^{SRO} + \cdots \tag{12}$$

The first two terms of the Gibbs energy represent the equation of an ideal solution, where X_i denotes the mole fraction of a given component, g_i^0 denotes the molar Gibbs energy of a component, R denotes the universal gas constant and T denotes the temperature. The terms g_{EX}^{RK}, g_{EX}^{magn}, and g_{EX}^{SRO} are energy contributions required by the CALPHAD method and describe the proportion of the nonideal chemical interaction, magnetism, and short-range ordering, respectively. These contributions represent the main challenge of the CALPHAD method [26].

The contribution of the non-ideal chemical interactions g_{EX}^{RK} is accounted for by using specific polynomials to model the excess Gibbs energy curves [26]:

$$g_{EX}^{RK} = \sum_{i,j} X_i X_j (X_i - X_j)^n \cdot L_{ij}^n \tag{13}$$

These expressions are called Redlich-Kister polynomials. The parameter L_{ij}^n describes the weighting, which must be determined for each system individually and is a function of temperature and pressure. The exponent n is usually a number between 0 and 3, its effect is shown graphically in Figure 8. It can be seen that the Redlich-Kister polynomials have a symmetric form for even exponents and an asymmetric form for odd exponents [26].

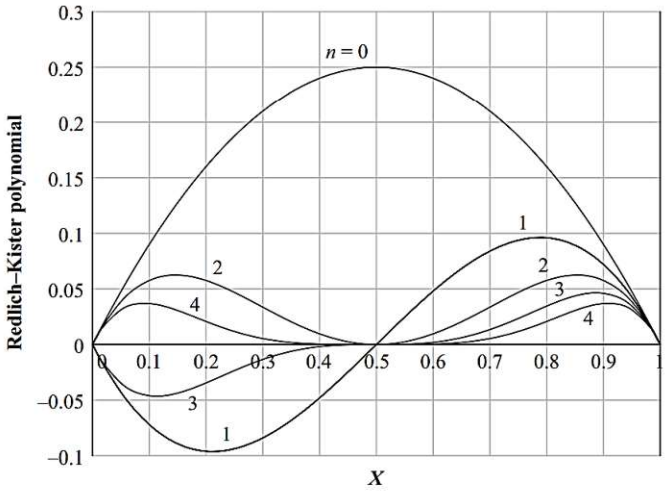

Figure 8: Redlich-Kister polynomials for different values of the exponent n and X_j=1-X_i [26]

The two terms g_{EX}^{magn} and g_{EX}^{SRO} can be modelled in several different approaches, which would be too extensive for this thesis. Therefore, the reader is referred to further literature [28,29] [26].

3.3 Systems of the type Al-Fe-Mn-Si

3.3.1 8xxx – aluminium alloys

In engineering, apart from pure aluminium Al99.99, mainly aluminium alloys are used, which contain other elements to change the properties of the material. The main alloying elements include copper, silicon, magnesium, zinc and manganese. In smaller quantities, iron, chromium or titanium are also added [30].

Depending on the main alloying elements, the various alloys are subdivided into groups to ensure a uniform and quick classification. These groups are shown in Table 1.

Group	Type of alloy
1xxx	Pure aluminium
2xxx	Al Cu
3xxx	Al Mn
4xxx	Al Si
5xxx	Al Mg
6xxx	Al Mg Si
7xxx	Al Zn Mg
8xxx	**others**
9xxx	not in use

Table 1: Designation system for wrought Al alloys [18]

Aluminium alloys are further subdivided into wrought and cast alloys. Since the present work deals with wrought alloys of the 8xxx series, other alloying systems will not be discussed in detail.

8xxx aluminium alloys are characterized by an excellent combination of strength and ductility at room temperature, as well as a high formability and good corrosion resistance [2,31]. These characteristics result from solutes and/or precipitates as well a small grain size which is stabilized by finely dispersed second-phase particles [16]. Fe, Si and Mn are usually the main alloying elements in 8xxx Al alloys, with typical contents of 0.4-1.7 wt.% for Fe, 0.05-1.1 wt.% for Si and 0.01-1.0 wt.% for Mn [31,32]. The areas of application for 8xxx Al alloys include, for example, the field of packaging materials, as the oxide layer on the surface forms an effective barrier against gases and liquids. In addition, they are used in the automotive industry, in cooling systems, for construction and in many other areas [16,31,33].

3.3.2 Relevant phase diagrams in the system Al-Fe-Si-Mn

This chapter focuses on those systems, in which the phases relevant for the present thesis have their origin. For the remaining binary and ternary phase diagrams that are part of the Al-Fe-Mn-Si system, the reader is referred to further literature [3–8,34].

3.3.2.1 Binary phase diagrams

Al-Fe

Fe has a very low solubility in Al, which is why commercial aluminium alloys frequently contain large Fe-rich phases [2]. In the Al-rich corner of the binary Al-Fe diagram, the eutectic point is located at 928 K (655 °C) and approximately 1.8 wt.% Fe. The monoclinic binary equilibrium phase, typically denoted as Al_3Fe or $Al_{13}Fe_4$, is formed directly from the melt. Furthermore, metastable phases exist in the Al-Fe-system, like e.g. the Al_6Fe phase, which is based on the binary Al_6Mn and will be discussed in more detail below [35].

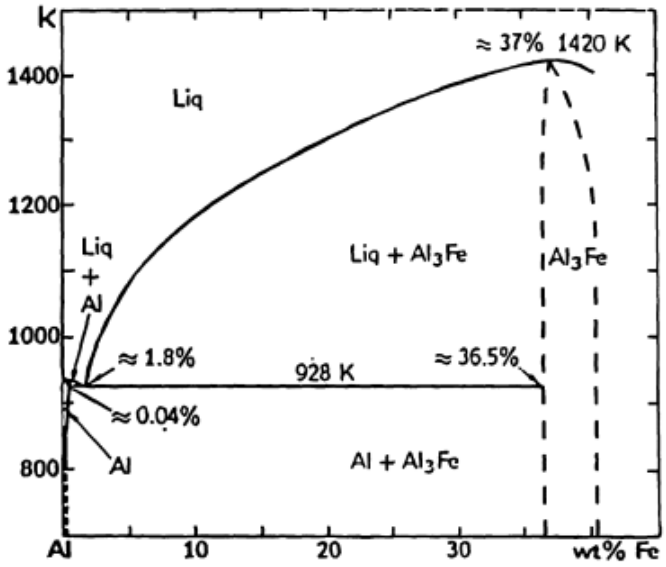

Figure 9: Al-rich corner of the binary Al-Fe phase diagram [34]

Al-Mn

As seen in Figure 10 Al and Mn form a eutectic at high Al contents, with a eutectic temperature of 931K (658 °C) at 1.95 wt.% Mn. With high cooling rates (> 10 K/s) up to around 1.9 wt.% Mn can be forcibly dissolved in the Al matrix. The comparatively high solubility decreases sharply with decreasing temperature and the orthorhombic binary phase Al_6Mn forms next to the solid solution at lower temperatures [6,35].

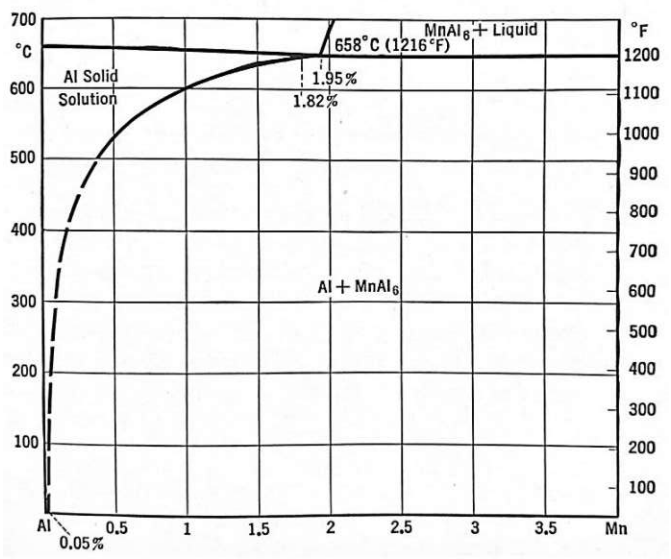

Figure 10: Al-rich corner of the binary Al-Mn phase diagram [6]

Al-Si

Silicon is a very important alloying element in Al-alloys, because it significantly improves the casting properties. This includes the reduction of the melting temperature (which suggests lower energy consumption), the increase of the flowability and the improved mold filling capacity. Al and Si form a simple eutectic system with very limited solubility at both edges at room temperature. The eutectic point is located at 11.7 wt.% Si and 850 K (577 °C). Excess silicon precipitates as pure Si from the matrix, with a diamond-like crystal structure [6,35].

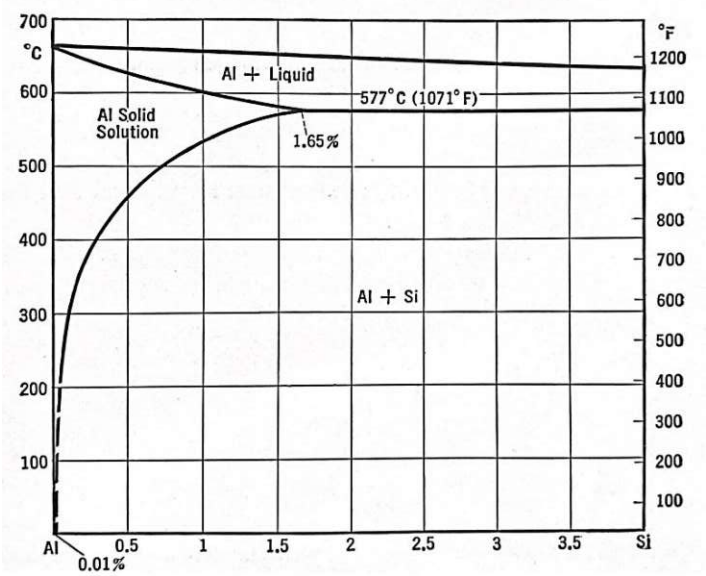

Figure 11: Al-rich corner of the binary Al-Si phase diagram [6]

3.3.2.2 Ternary phase diagrams

Al-Fe-Si

In the Al-Fe-Si ternary system only a small part of the silicon and iron contents are in solid solution. The main part of Fe and Si are located in binary and/or ternary intermetallic phases [36]. In the system 10 ternary phases (stable as well as metastable) and 19 invariant reactions were listed in [37,38]. A detailed investigation was performed in the Al-rich corner of the Al-Fe-Si diagram [39].

In the Al-rich corner of the Al-Fe-Si system pure Si, Al_3Fe (from the binary Al-Fe system), the hexagonal ternary Al_8Fe_2Si (also denoted as α_h) and the monoclinic Al_5FeSi (also indicated as β) are the most important equilibrium phases. Besides these phases in Si- and Fe-rich aluminium alloys two more ternary compounds Al_3FeSi and Al_4FeSi_2 can occur under nonequilibrium conditions, which are neglected for this thesis, however [8]. An overview of the whole ternary Al-Fe-Si system is given in [40,41].

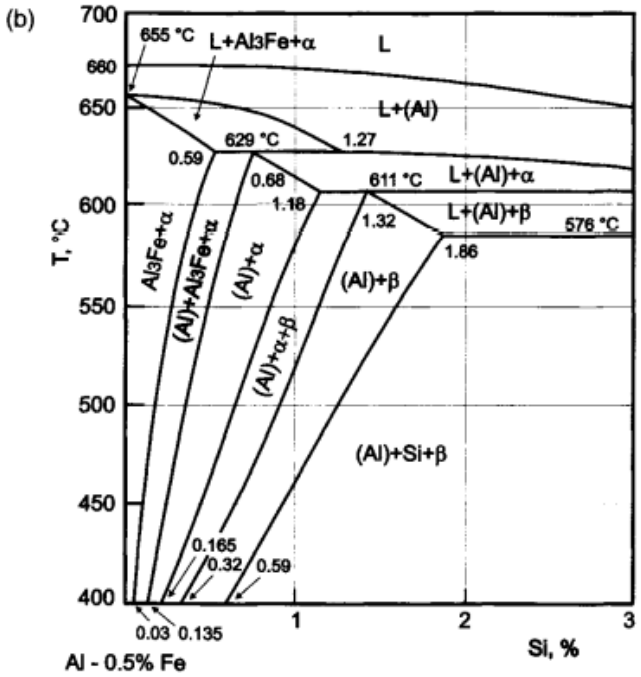

Figure 12: Polythermal Section of the system Al-Fe-Si with 0.5 wt.% Fe [8]

Lentz et al. [2] investigated the 2 alloys AA8011 and AA8079. Since these two phases contain almost no Mn (<0.02 wt.% Mn), the Al-Fe-Si ternary phase diagram with an Fe content of 0.8 wt.% was simulated with FactSage, as shown in Figure 13. It has to be mentioned, that the authors used the cubic alpha phase α_c-AlFeMnSi as opposed to the hexagonal one, since the impurities present in technical alloys tend to fully destabilize the hexagonal variation in favour of the cubic one [2].

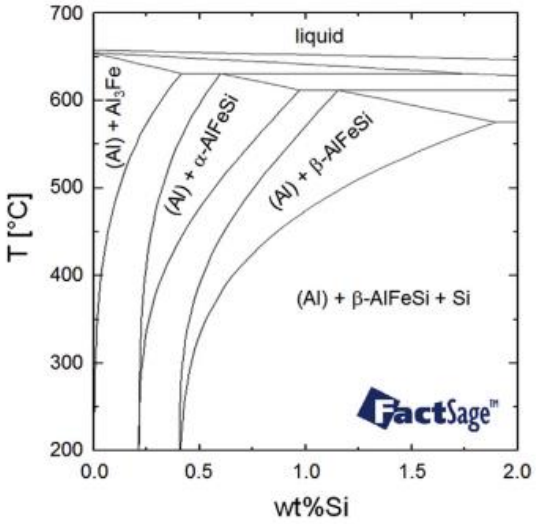

Figure 13: FactSage Simulation of the ternary Al-Fe-Si system with 0.8 wt.% Fe [2]

Al-Fe-Mn

The equilibrium phases in the aluminium corner are those originating from the binary systems, namely Al_3Fe, Al_6Mn and Al_4Mn. In the case of Al_6Mn it should be noted that manganese can be replaced by iron up to the composition $Al_{12}FeMn$ [7]. The solubility of Fe in the Al_6Mn crystals after quenching depends on the temperature, as can be seen in Table 2, which can be taken from Reference [42].

Temperature	Composition		
	Fe	Mn	Al
300°C	12.80	12.63	balance
460°C	12.55	12.87	balance
600°C	11.45	14.09	balance

Table 2: Compositions of extracted crystals of $Al_6Mn_{1-x}Fe_x$ at various temperatures (in wt.%) [42,43]

Furthermore, Mn can also replace iron up to 4-5 wt.% in the Al_3Fe phase [7].

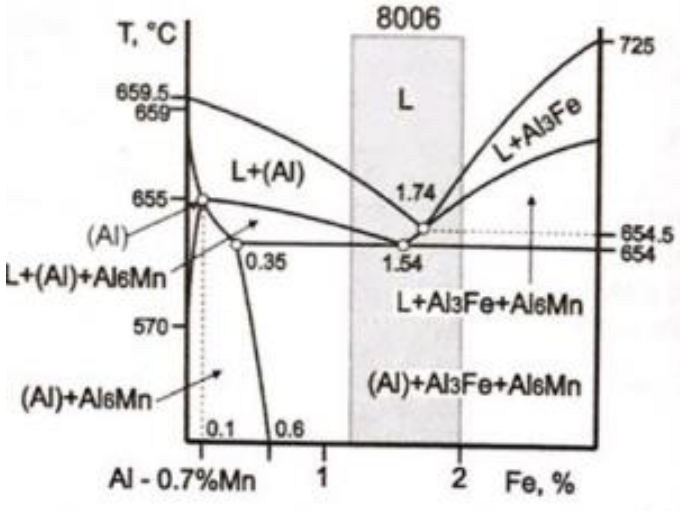

Figure 14: Phase diagram of the system Al-Fe-Mn with 0.7 wt.% Mn [8]

Al-Mn-Si

Two phases from the binary systems, Al_6Mn and Si as well as one ternary phase $Al_{15}Mn_3Si_2$ - with a homogeneity range of 25-29 wt.% Mn and 8-13 wt.% Si – can occur in the equilibrium state, depending on the exact chemical composition and the temperature. It should be noted that the ternary phase $Al_{15}Mn_3Si_2$ is the original variant of the cubic alpha phase $Al_{15}(Fe,Mn)_3Si_2$ [8].

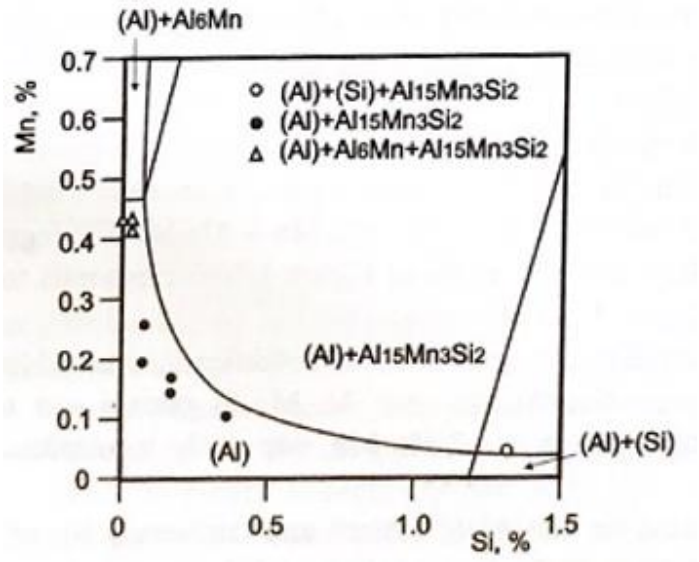

Figure 15: Isothermal section at 550°C [8] with experimental data (points) after [44]

3.3.2.3 Quaternary phase diagrams

Al-Fe-Mn-Si

Iron can replace most of the manganese in the ternary phase $Al_{15}Mn_3Si_2$, up to a composition 31% Fe, 1.5% Mn, 8% Si. Consequently $Al_{15}(Fe,Mn)_3Si_2$ is found over a large range of alloy compositions, as can be seen in Figure 16. Furthermore, Fe can also replace Mn in the (originally) binary phase $Al_6(Fe,Mn)$, as already mentioned [7]. In [14] the presence of a separate quaternary phase was evaluated and the authors concluded that there is no stable quaternary phase in the aluminium corner of the Al-Fe-Mn-Si system.

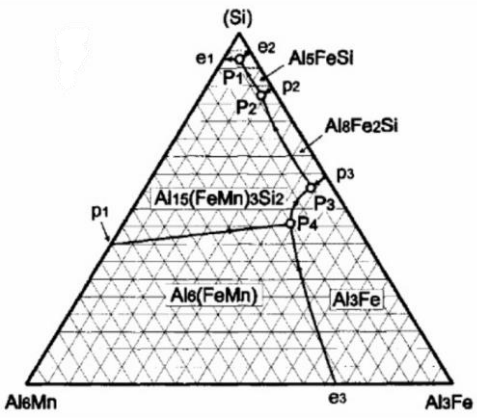

Figure 16: Polythermal projection of the solidification surface of an Al-Fe-Mn-Si system [8,33]

There are already some phase diagrams of the system Al-Fe-Mn-Si in the literature. The relevant ones for this thesis are those with lower contents of the alloying elements (up to 2 wt.%). The seminal research by Phillips and Varley [3,4] is frequently referenced and the key results for the present thesis are shown in Figure 17. It should be noted that Phillips and Varley did not perform equilibrium annealing. Instead, the alloys were cooled down at a rate of 8-10°C per minute [3,4].

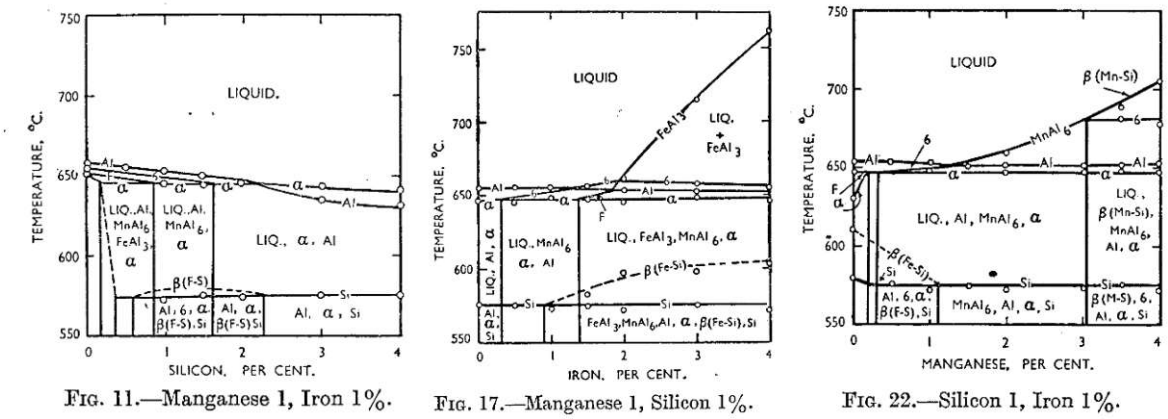

FIG. 11.—Manganese 1, Iron 1%. FIG. 17.—Manganese 1, Silicon 1%. FIG. 22.—Silicon 1, Iron 1%.

Figure 17: Different phase diagrams of Al-Fe-Mn-Si [3]

In Lacaze et al. [14], the Al-Fe-Mn-Si system was investigated and an experimental microstructure map with 1 wt.% Mn and 3 wt.% Si was compiled, which can be seen in Figure 18. In this paper α describes the cubic α-AlFeMnSi $Al_9(Fe,Mn)_2Si$ and τ_6 corresponds to the monoclinic β-phase Al_5FeSi [14].

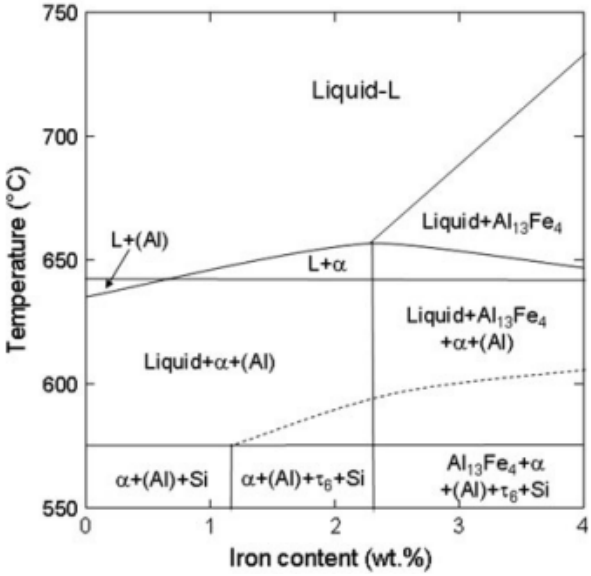

Figure 18: Experimental microstructure map of Al-Fe-Mn-Si; 1 wt.% Mn and 3 wt.% Si [14]

The paper of Engler et al. [16] investigated the alloy AA8006 with 1.5 wt.% Fe and 0.5 wt.% Mn. For this purpose, a FactSage phase diagram was simulated, which is shown in Figure 19. Here, α represents the chemical $Al_{15}(Fe,Mn)_3Si_2$ or $Al_{12}(Fe,Mn)_3Si$. For the CALPHAD simulation of the α-phase an average composition of 17 wt.% Fe, 14 wt.% Mn and 7 wt.% Si is used [16].

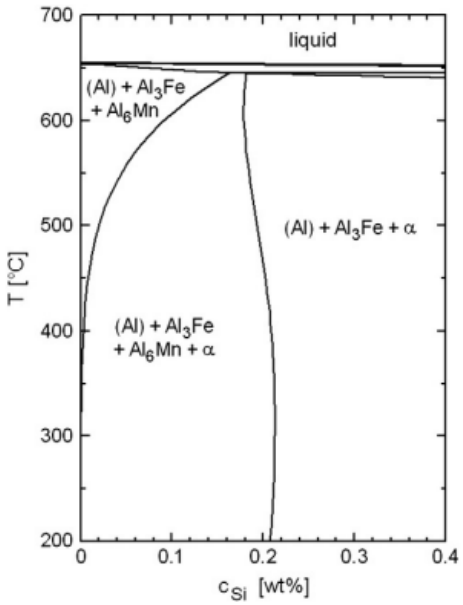

Figure 19: FactSage simulation of the Al-corner of a Al-Fe-Mn-Si diagram with 1.5 wt.% Fe and 0.5 wt.% Mn [16]

3.3.3 Present intermetallic phases

An intermetallic phase is a homogeneous chemical compound of two or more metals. In contrast to alloys, intermetallic phases have lattice structures that differ from the original elements that they consist of. Furthermore, the chemical bonds also show covalent or ionic characteristics to some extent, as opposed to the predominantly metallic bonds in metals and alloys [45].

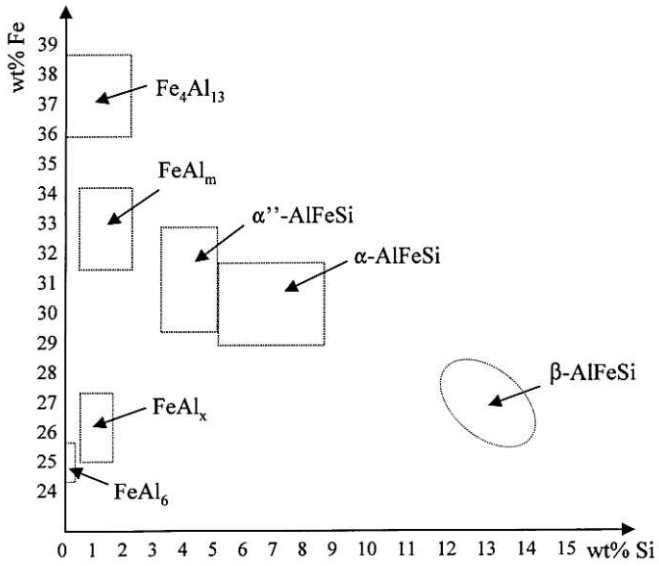

Figure 20: Chemical composition of binary and ternary phases in Al-Fe-Si alloys [46]

An overview of the most important intermetallic phases in the 8xxx system is shown in Figure 20. In this thesis, the most important phases are $Al_{13}(Fe,Mn)_4$, $Al_6(Fe,Mn)$, α-AlFeMnSi and β-AlFeSi. A detailed listing of the chemical composition can be found in the appendix 13.2.

3.3.3.1 $Al_{13}(Fe,Mn)_4$

$Al_{13}(Fe,Mn)_4$ is often referred to as $Al_3(Fe,Mn)$ in the literature. This phase originated from the binary Al-Fe system. In the ternary System Al-Fe-Mn manganese can substitute iron in Al_3Fe up to a limit solubility of 4-5 wt.% Mn, which corresponds to the formula $Al_3Fe_{0.88}Mn_{0.12}$. It has a c-centred monoclinic structure and forms needle-shaped precipitates which are detrimental to the formability of the material. 8xxx alloys with a low Si content usually contain a large number of $Al_{13}(Fe,Mn)_4$ -precipitates [2,8,34]. One ratio that can help to distinguish $Al_{13}(Fe,Mn)_4$ from similar phases such as $Al_6(Fe,Mn)$ is Fe:Mn. If this ratio exceeds 10, it can be assumed that $Al_{13}(Fe,Mn)_4$ is present [16]. Another important point is that this phase can dissolve up to 2.5 wt.% Si [34].

3.3.3.2 $Al_6(Fe,Mn)$

The stable phase Al_6Mn, which originates from the binary phase diagram Al-Mn, is c-centred orthorhombic. For alloys with a higher Fe content, the isomorphous phase Al_6Fe can be formed from the melt. In alloys with low Mn contents this phase is metastable and only occurs if the cooling rates exceed a certain limit. If the alloy contains sufficient Mn, the thermodynamic stability of the Al_6Fe phase increases since manganese and iron can substitute each other and arrange in an $Al_6(Fe,Mn)$ lattice [34]. Similar to the $Al_{13}(Fe,Mn)_4$ phase, there is also a characteristic Fe:Mn ratio for $Al_6(Fe,Mn)$, with ratios significantly below 6. Furthermore, this phase is practically free of Si [16].

3.3.3.3 α-AlFeMnSi

In alloys with a higher Si content, ternary AlFeSi or quaternary AlFeMnSi phases are formed. The α-Al(Fe,Mn)Si phase can exist in two different crystal systems: in the cubic (α_c) as well as in the hexagonal (α_h) form. In general, the hexagonal α_h form is assumed to exist in alloys with a Mn content of <0.01 wt.%. If only minimal amounts of manganese are added, the cubic α-phase is present [1,5,47]. The α-phase has an atomic ratio (Fe+Mn):Si of approximately 2 to 3 or a weight percent ratio of 4 to 6 [1,2,47]. The chemical composition of α-Al(Fe,Mn)Si can vary, hence different stoichiometries are reported in the literature. Usually, the cubic α phase is denoted as $Al_{19}Fe_4MnSi_2$, $Al_{15}(Fe,Mn)_3Si_2$ or $Al_{12}(Fe,Mn)_3Si$ whereas the hexagonal α-phase is given as Al_8Fe_2Si [1]. The morphology of the α-phase can be chinese-script style, star-shaped or polygonal [35].

3.3.3.4 β-AlFeSi

β-AlFeSi has a monoclinic crystal structure and is an important phase in the AlFeSi ternary phase diagram of wrought aluminium alloys [34]. The chemical formula for this phase is Al_5FeSi or $Al_9Fe_2Si_2$ [8]. The phase tends to stabilize at higher Si contents and lower temperatures. The β-phase has an atomic ratio of (Fe+Mn):Si of about 1 or a weight percent ratio of about 2 , which distinguishes it from the α-phase in addition to the crystal structure [1,2,47]. Furthermore the phase has a plate-shaped morphology, and therefore appears as needles in polished samples [35].

3.4 Methods of material characterization

Various examination methods were used to characterize the alloys in the present thesis. In microscopic examinations, the resolution represents a major difference between the various examination methods. A light microscope is required for smaller objects that can no longer be recognized macroscopically. In this case structures up to 500nm can be visualized - using darkfield or video microscopy, resolutions down to 50nm are possible. For objects with a resolution below 500nm, an electron microscope is required. Here the lower limit of the resolution is 0.5nm [48]

3.4.1 Light microscopy

Light microscopy is the most important method for characterizing the microstructure, despite the ongoing development of electron microscopes. A distinction can be made between reflected light and transmitted light microscopy, depending on the beam path of the microscope. In the present work reflected light microscopy was used. The choice of method depends on the imaging requirements in terms of resolution, magnification and depth of field. In reflected light microscopy, special optical techniques can be used to identify details of the microstructure. These include bright field lighting, dark field lighting, polar light microscopy, phase contrast microscopy and differential interference contrast [49].

The schematic principle of a reflected-light microscope is shown in Figure 21 . The specimen is uniformly illuminated using the Köhler illumination principle. The light travels through the collector and two condenser lenses. It is then redirected by a reflector and imaged through an objective on the surface of the specimen [50].

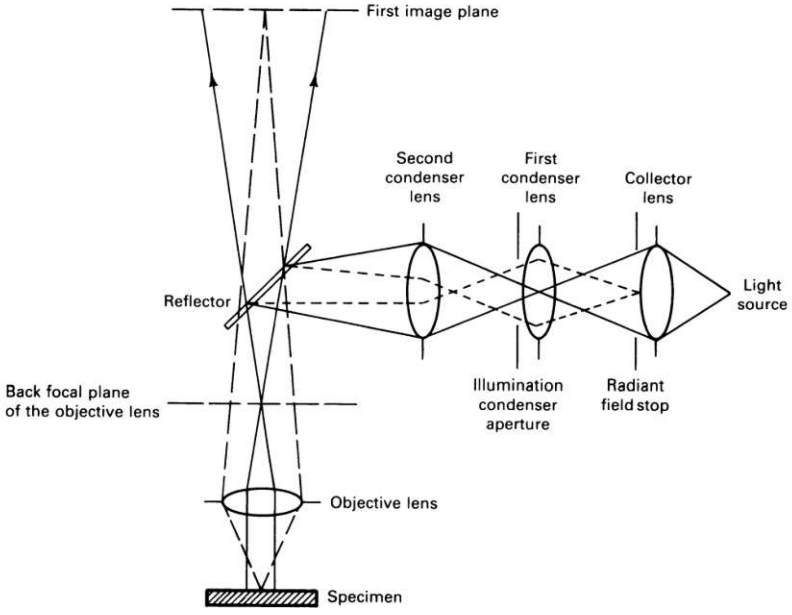

Figure 21: Beam path of a reflected light microscope [50]

The resolving power *d* of the light microscope to separate two adjacent points is [48,49]:

$$d = \frac{\lambda}{A} = \frac{\lambda}{n * \sin(\alpha)} \tag{14}$$

Hereby λ represents the wavelength of the light used for illumination, *d* the resolving power, *n* describes the optical refractive index of the medium located between the sample to be examined and the objective (air), and α describes the aperature angle (half opening angle) of the objective [49].

3.4.2 Scanning electron microscopy

Scanning electron microscopy (SEM) can be used to examine conductive material surfaces of components, material fractures or also of polished surfaces of samples on the microscale.

The physical principle of a scanning electron microscope is based on a raster scan of the sample with a finely focused electron beam with an excitation energy E_0, which interacts with the sample surface. Secondary and backscattered electrons are generated within the interaction volume, which can be detected and enable the graphical representation of the scanned area [49].

Figure 22 shows the schematic structure of a scanning electron microscope. Electron emission occurs in the filament (the hot cathode) under vacuum by thermal emission. In special cases, electron egress occurs by field emission [51]. The emerging electrons are accelerated by the high voltage applied between the cathode and anode. The cathode is located in a Wehnelt cylinder, which has a negative potential as opposed to the cathode, so that the electron beam can be bundled [52]. Afterwards the electron beam is directed through several magnetic electron lenses onto the sample. Two detectors pick up the secondary and backscattered electrons, respectively. To scan the sample surface with a grid pattern, the beam is deflected by transverse magnetic fields. The imaging of the sample surface based on the secondary or backscattered electrons is based on the intensity of the signal at each point of the scanning pattern and displayed on an external screen [51].

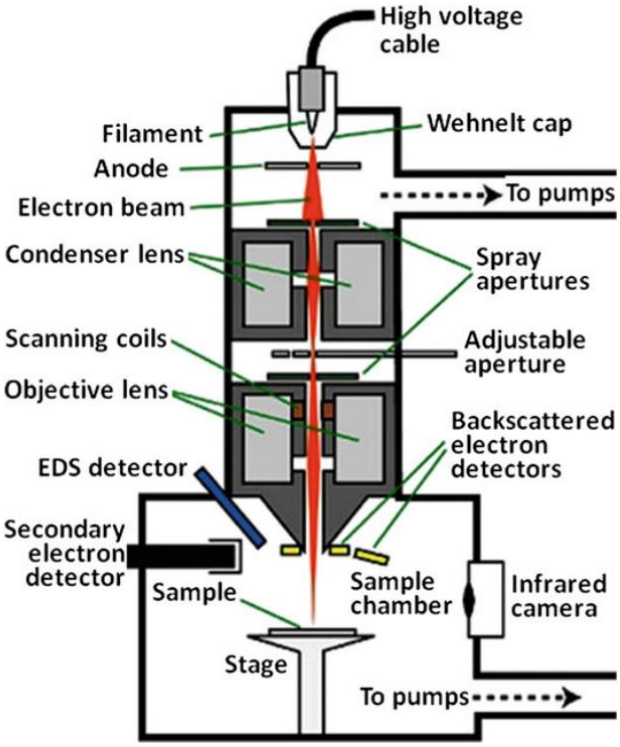

Figure 22: Schematic structure of a SEM [31]

Because of the interactions of the high-energy primary electrons with the object, Auger electrons, secondary electrons (SE), backscattered electrons (BSE), absorbed electrons, X-rays, electric charge shifts and visible light due to cathodoluminescence at the point of impact are created, as summarized in Figure 23. Secondary electrons are low energy electrons that emerge from the sample surface and have an energy ≤ 50eV. Electrons that emerge from the sample surface and have an energy > 50 eV are

referred to as backscattered electrons. In Figure 23 the interaction bulb with SEs and BSEs is shown. The size of the bulb depends on the excitation energy and the atomic number of the sample material [53].

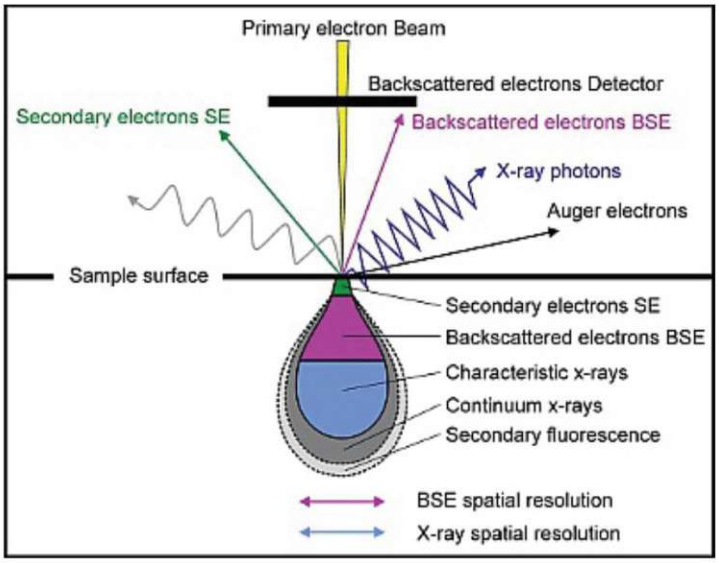

Figure 23: Representation of the secondary and backscattered electrons [54]

For the investigation of surface topographies, secondary electron images are mostly used, since the contrasts here result mainly from the angle of inclination between the sample surface and the direction of the primary electrons. Backscattered electron images can reveal contrasts due to both topography and different atomic numbers. This is used to visualize different chemical compositions [51].

The advantage of an SEM is, that any surface can be imaged with great depth of field, provided that the surface of the sample is electrically conductive and the sample is vacuum stable [51].

3.4.3 Energy dispersive X-ray spectroscopy

For Energy dispersive X-ray spectroscopy (EDX) analysis, as with the scanning electron microscope, a focused electron beam is required. Corresponding detectors are therefore standard in electron microscopes. The method is based on characteristic X-rays, which are emitted by the sample when a beam of electrons is focused on the surface, and which can be used to determine elements both qualitatively and quantitatively.

When a primary electron strikes the sample and kicks out an electron from an energy level close to the nucleus, this is immediately replaced by an electron from a higher level, as shown in Figure 24 [49].

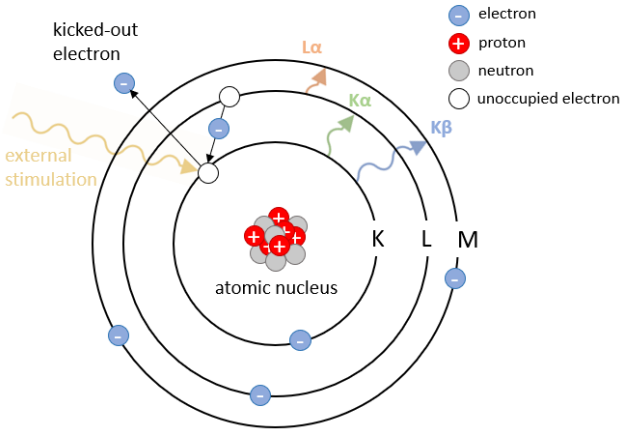

Figure 24: Physical principle of the EDX

This results in X-ray quanta, which are marked with K_α, K_β, L_α et cetera. After the electron exchange, the emitted X-rays enter a semiconductor detector where they generate charges proportional to their energy, which are registered and counted as voltage-impulses in a multichannel analyser [49]. The resulting spectrum consist of characteristic peak that can be assigned to the different elements. The energy of an X-ray peak gives information about which element is present while the intensity gives information about the concentration in which the element is present within the interaction volume [55]. The deceleration of electrons in the Coulomb field of the atomic nuclei further produces a continuous X-ray signal, which represents the background of the EDX spectrum as seen in Figure 25 [55]. The peaks in Figure 25 depict the element-specific peaks.

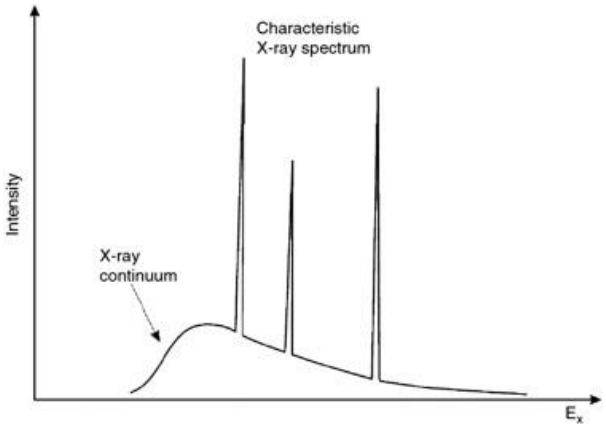

Figure 25: Representation of an EDX-Diagram [56]

If the EDX detector is combined with a transmission electron microscope (TEM) rather than a scanning electron microscope, higher spatial resolutions can be realized because TEM analysis requires a very thin sample (<100 nm) and thus the incident electron beam cannot spread as far in the volume [55].

3.4.4 X-ray powder diffraction

3.4.4.1 Basics of the X-ray powder diffraction

X-rays can be diffracted by crystal lattices because the wavelengths of the X-rays and the lattice parameters of the crystals are of the same order of magnitude.

In X-ray diffraction (XRD), the cathode emits electrons, which are accelerated towards the anode in the electric field of the applied high voltage. There, they strike the anode material and generate the radiation during their deceleration. This X-ray beam is directed onto the sample, for example, to analyse the crystal structures of the phases present or to determine lattice constants. Theoretically, the diffraction of X-rays by crystals can also be mapped as the reflection of X-rays by parallel lattice plane arrays. This relation is described by Bragg's law [49,57]:

$$2 \cdot d \cdot \sin(\theta) = n \cdot \lambda \tag{15}$$

Hereby, *d* represents the distance between the lattice planes, θ represents the diffraction angle, *n* the order of the interference and λ describes the wavelength. The geometric relationship is illustrated in Figure 26. The radiation diffracted at those lattice planes that fulfil Bragg's law is registered by the detector. Thus, for a known wavelength λ, the angle θ (or 2θ) at which constructive interference occurs can be measured. The diffraction patterns depend on the crystal structures of the phases present in the sample and thus enable crystallographic phase analysis. Finally, the quantitative composition of the samples can be determined via the intensity of the reflections [49,57].

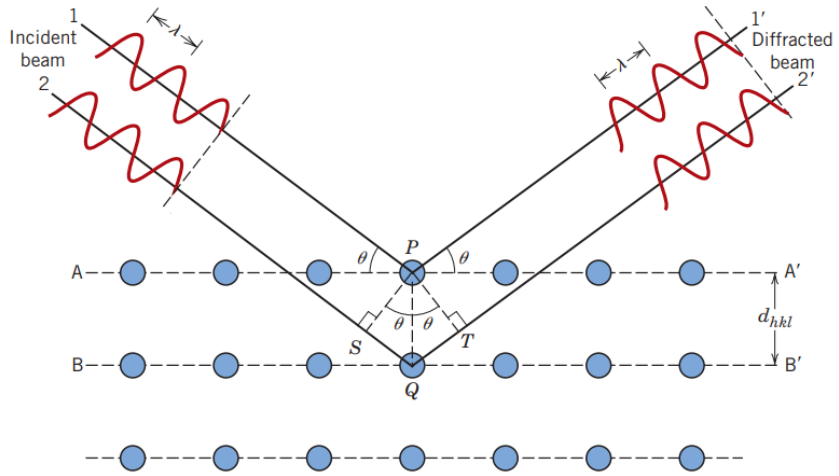

Figure 26: Diffraction of X-rays from atomic planes [58]

3.4.4.2 Measurement geometry

Most measurement setups have a reflection geometry, such as the Bragg-Brentano geometry or the parallel beam geometry [49]. For the measurements in the present work, the Bragg-Brentano geometry was used.

The Bragg-Brentano geometry is shown in Figure 27. Hereby the X-ray source, the sample, and the detector are on a focusing circle. The radius of the focusing circle becomes smaller with increasing diffraction angle [59]. The focusing can be done as θ-θ- or θ-2θ-focusing. In θ-θ focusing, the sample is fixed, while in θ-2θ focusing, the X-ray source is fixed [49].

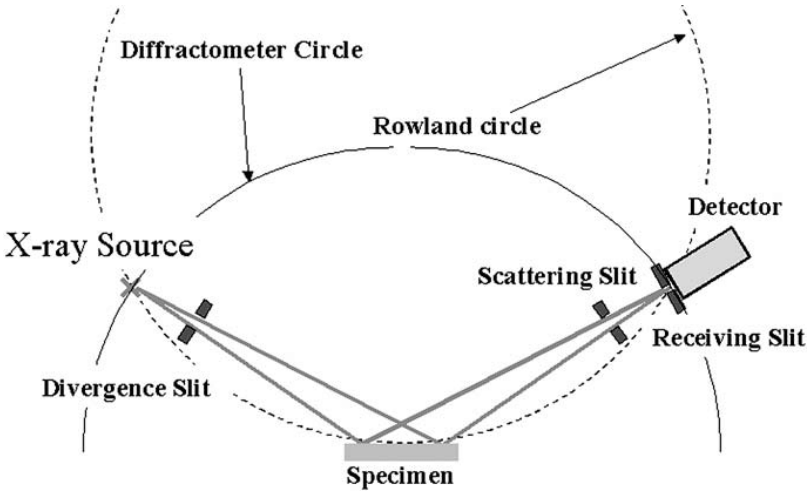

Figure 27: Bragg-Brentano geometry for XRD [60]

The X-ray beam leaving the X-ray tube is divergent. The divergence is reduced, using a divergence slit for the X-ray beam before it is directed onto the sample. After the diffraction, the X-ray beam passes a scattering slit, which have the same function as the divergence slit. The detector divergence is determined by the receiving slit, which ensures that the detector record only the sample area illuminated with X-rays [59].

The focus of the X-ray source and the focus of the detector are at a constant, equal distance from the sample. The detector and the X-ray source move on a circular arc, named diffractometer circle. The X-ray source, the tangent of the sample surface and the focus of the detector are always on this arc. This arc radius becomes smaller with increasing diffraction angle, which is represented by the Rowland circle [59].

The diffraction condition in the Bragg-Brentano geometry is satisfied by those crystallites whose lattice plane is parallel to the surface, as shown in Figure 28 [59].

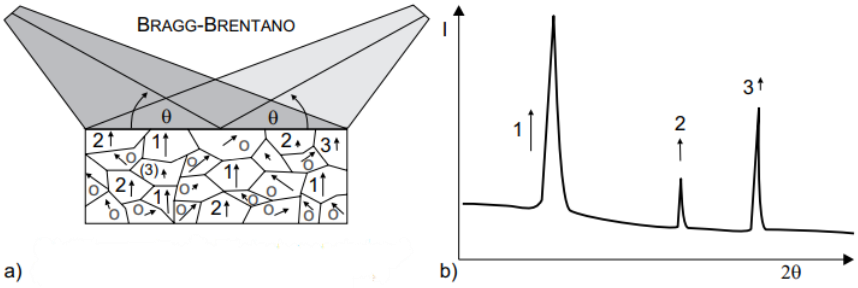

Figure 28: a) Schematic representation of the crystal structure b) received diffractogram [59]

4. Experimental part

In this thesis, the investigated aluminium alloys are AA8011, AA8014, AA8021 and AA8079, which were provided by the company AMAG (Austria Metall AG). The chemical composition of the samples is given in Table 3.

Alloy	Si	Fe	Cu	Mn	Ti	Other	Al
AA8011	0.816	0.884	0.012	0.07	0.019	-	balance
AA8014	0.11	1.54	0.01	0.42	-	0.048	balance
AA8021	0.105	1.422	0.002	0.019	0.017	-	balance
AA8079	0.124	1.011	0.001	0.022	0.035	-	balance

Table 3: The chemical composition of the samples (in wt.%)

4.1 Preparation of the samples

For the characterisation of the phases, all alloys were long time annealed to reach the equilibrium state. Subsequently, the samples were either polished, etched or the aluminium matrix was dissolved to perform the different characterisation methods.

4.1.1 Long-term annealing for the equilibrium state

To obtain sufficient experimental data for the optimisation of the thermodynamic database, three different temperatures were chosen, at which the materials were held in order to equilibrate the microstructures. Since diffusion occurs at different rates, depending on the temperature, different holding times were used. To determine whether equilibrium states were reached or not, the specimen were divided into two groups – the full-time and the half-time samples.

For the full-time samples the times were selected conservatively to yield an equilibrated microstructure. To cross check this, one sample of each specimen was taken out of the oven halfway through the annealing time and compared with the full-time sample. Ideally, the two samples should not show any differences with respect to the phases present and their respective quantities. The holding times for the different temperatures are given in Table 4 and were applied for each material. The respective abbreviation of the holding times, which is often used in this thesis, is given in brackets in the table.

Temperature	Half-time	Full-time
400 °C	1 week (H4)	2 weeks (F4)
500 °C	3 days (H5)	1 week (F5)
600 °C	3 days (H6)	1 week (F6)

Table 4: Different holding times for the alloys and their abbreviation

Furthermore, the heat treatment was carried out in the absence of oxygen to avoid oxidation. This was achieved by first cutting the samples into small pieces and then placing them in glass tubes. These were heated and then pressed together with pliers, until they were hermetically sealed. When the sample was removed from the oven, the test tubes were smashed, and the samples were quenched in a water bath to preserve the equilibrium state.

4.1.2 Preparation of the polished samples

The heat-treated samples were embedded in the 2-component cold embedding mixture CEM3070 of the company Cloeren Technology to obtain electrically conductive samples that are examinable with the SEM. After embedding, the specimens were polished on a Struers TegraPol-31. The parameters used are shown in Table 5.

Step	Grinding material	Liquid	Time [min]	Force [N]	Velocity [rpm]
1	SiC-Paper #320	Water	2	25	300
2	SiC-Paper #500	Water	2	20	150
3	SiC-Paper #1000	Water	2	15	150
4	SiC-Paper #2000	Water	4	10	150
5	SiC-Paper #4000	Water	4	15	150
6	DP suspension 3µm	Lubricant	6	10	150
7	OPS	-	10	10	150

Table 5: Parameters used for grinding and polishing the samples

The polished samples were first analysed with the light microscope and the images were used to evaluate the total phase fraction with the program ImageJ. Furthermore, the polished specimen were used to make investigations with the SEM and to measure chemical compositions with EDX analysis.

4.1.3 Dissolution of the aluminium matrix with phenol

To determine the intermetallic phases based on the crystal structure, the aluminium matrix was dissolved using boiling phenol. The basic procedure for the extraction of the secondary phases is described in [61]. The modified procedure can be seen in Table 5 and was carried out similar to the diploma thesis [62].

Figure 29: Dissolution of the aluminium matrix - boiling phenol with added Al sample

Figure 29 shows the process of dissolving the aluminium matrix in boiling phenol. The aluminium sample has already been added been dissolved in this figure.

Step	Description
1	2-3 g of the aluminium sample to be examined are needed for the procedure. The sample must be cut into small pieces and thoroughly cleaned using ethanol and an ultrasonic cleaner.
2	80 g of phenol are weighed out and must be heated up to the boiling point under constant stirring **in a fume hood**. The melting point of phenol is 40°C and the boiling point is 182°C. During boiling, the glass vessel should also be covered with a watch glass to further minimize the exposure to phenol vapor, as phenol is classified as toxic.
3	When the boiling point is reached, the mixture has to be held at that temperature for 5-10 minutes, to ensure that all of the residual water within the phenol can evaporate. Otherwise, the water could disrupt the process.
4	Addition of the sample fragments with tweezers.
5	The reaction starts as soon as the mixture changes the colour (from a clear solution to a yellowish and then to a dark grey solution). In total the mixture should be boiled for 15-20 minutes, after which the solution is almost black. It is important not to boil the solution for too long, otherwise the intermetallic precipitates will dissolve as well.
6	To the mixture - which contains the dissolved aluminium, the phenol and the intermetallic phases - 70 ml of benzyl alcohol is added and then stirred for 10 minutes. The benzyl alcohol is added to purify the intermetallic phases from the phenol, as the phenol would otherwise interfere with the further measurements.
7	The sample must be left overnight for the powder (extracted intermetallic phases) to settle at the bottom, so that the liquid can be carefully decanted (without swirling the powder!). The residual consists of powder and a certain amount of remaining phenol/benzyl alcohol.
8	30 - 50 ml of fresh benzyl alcohol is added to the residual. The mixture is put into a special container for centrifuging, quickly swayed to properly mix everything and then placed in the centrifuge to separate the liquid from the powder. The centrifuge was set to 3000 RPM for 3 minutes. In case not all intermetallic phases had settled to the bottom, the respective samples were centrifuged a second time at these settings. The supernatant liquid can be decanted again.
9	Repeat step 8 two to three times until the supernatant liquid is clear and transparent. This indicates that all the phenol and reaction by-products have been washed out and only benzyl alcohol is left.
10	The second washing cycle is carried out with methanol. This procedure is analogous to the previous one, using methanol instead of benzyl alcohol. Repeat the methanol step 2-3 times.
11	Transfer the washed powder into a petri dish using a little methanol, cover the sample with perforated aluminium foil and heat gently to evaporate the excess methanol.
12	In the last step, dry the powder in the desiccator.

Table 6: The necessary steps for the dissolution of the aluminium matrix with phenol

The dissolved intermetallic phases were subsequently examined by X-ray powder diffraction.

4.1.4 Etching of the samples with hydrofluoric acid

To make any dispersoids visible, the samples were etched with 0.5% hydrofluoric acid for 5 to 30 seconds to subsequently take images with the light microscope. The method chosen for etching, is normally used for the 6xxx series alloys to highlight Fe-rich dispersoids. Most of the samples were etched for 5s except the samples AA8011 F4, AA8011 F5, AA8079 F4 and AA8079 F5, which were etched for 30s, as the dispersoids were otherwise only partially highlighted by the hydrofluoric acid.

4.2 Characterization

The characterization of the stability ranges as well as the phase fractions was done by the combined use of light microscopy, scanning electron microscopy, energy dispersive X-ray spectroscopy and X-ray powder diffraction. These methods are discussed in more detail in the following chapters.

4.2.1 Light microscopy

Both the unetched and the etched samples were used for the analysis with the light microscope Zeiss AxioImager.M2m. The purpose was to gain insight into the morphology of the phases, but also to evaluate the total phase fraction of the constituents. For this purpose, images with 200x and 500x magnification were taken in the bright field. For inclined samples, a height adjustment was carried out with "*Z-Stapel*" function.

The examination of the etched samples was used for the qualitative evaluation of the presence of dispersoids, the results can be found in chapter 6.3.

Prerequisite for the evaluation of the phase fraction for each alloy-temperature combination was a minimum of 30 different pictures and an empirical standard deviation around 10% of the mean value. For the evaluation of the total phase fraction, based on the light microscopy images, the image processing program ImageJ, more specifically the extended version Fiji was used. In the following paragraphs, the procedure for the evaluation of the total phase fraction is explained. The complete macro can be found in appendix 13.1.

In the macro, a loop was implemented in order to evaluate all pictures in the target folder. Possible contaminations, which were visible in the images, were removed manually in advance. Afterwards, the individual images were converted into greyscales and through different thresholds (depending on the brightness of the images) darker pixels (constituents) were converted into black and lighter pixels (matrix) into white areas. Thereby, the percentage of black pixels (which represents the phase fraction) could be determined.

Subsequently, the processed images were re-examined to check whether the phases detected with ImageJ correspond to the original images.

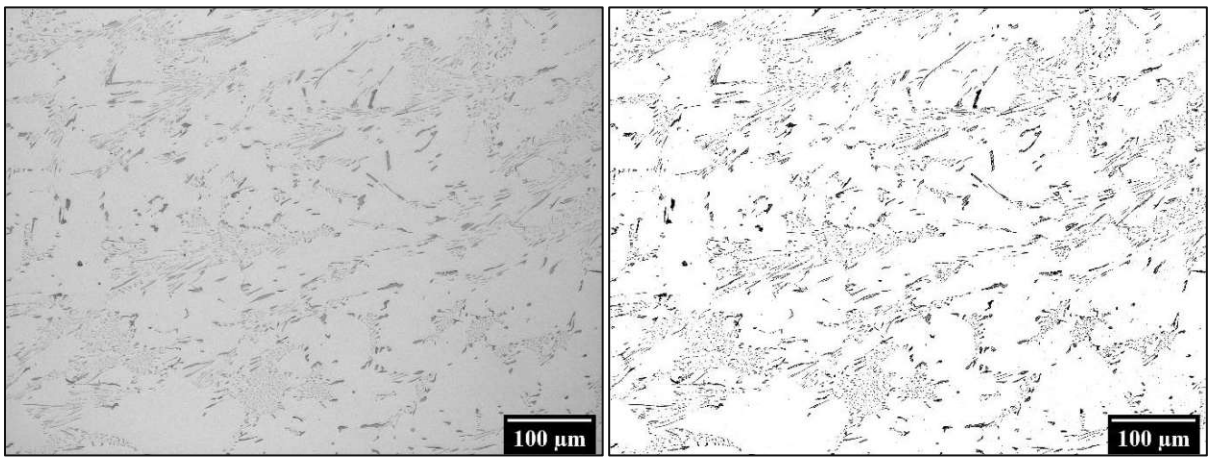

Figure 30: Comparison of the image of the light microscope (left) with the evaluation of ImageJ (right), AA8014 AC

Figure 30 shows the comparison of a sample picture taken with the light microscope and the evaluation by ImageJ.

4.2.2 Scanning electron microscopy

The embedded (electrically conductive), polished samples were examined in the unetched state under a scanning electron microscope. A FEI Philips XL30 was used for this purpose. The aluminium samples were investigated using an acceleration voltage of the primary electron beam of 20 kV and spot sizes in the range of 4.5 - 5.0 , which corresponds to an electron beam diameter of 90-120 nm [63]. A tungsten wire was used as the glow cathode. The samples were positioned at a working distance of 10 mm.

4.2.3 Energy dispersive X-ray spectroscopy

For the investigation of the chemical composition of intermetallic phases, the EDAX Sapphire Energy Dispersive X-ray detector was used, which is controlled with the software EDAX Genesis.

The investigation by EDX was carried out with the same settings as the SEM imaging. The co-measurement of some Al matrix could not be avoided in most cases, because the excitation bulb in aluminium is comparably large, with a diameter around 3µm. This can be seen in the exemplary measurement in Figure 31.

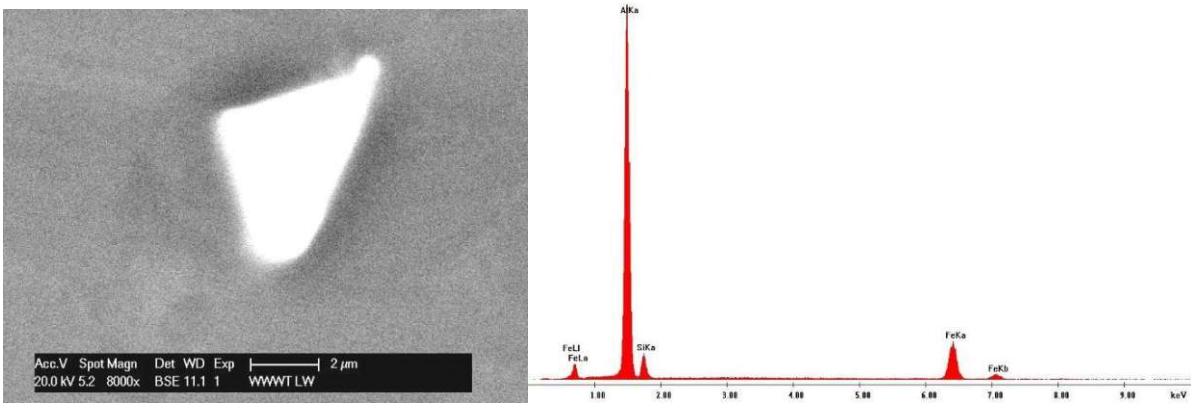

Figure 31: EDX measurement of a precipitate in AA8011 F4 - left: SEM image, right: EDX measurement

After the measurement and the assignment of the elements, the EDAX Genesis programme gives the calculated weight percentages and atomic percentages, as shown in Table 7.

Element	wt.%	at.%
Al	63.71	75.18
Si	7.32	8.3
Fe	28.97	16.52

Table 7: Output of the software EDAX Genesis

From these chemical compositions, the precipitates can be assigned to different phases. Different ratios and homogeneity ranges were used for the classification of the phases. The latter can be found in appendix 13.2. The basic assumption for the classification is, that the aluminium matrix contains only negligible amounts of silicon, iron and manganese so that any signal associated with these elements originates from the intermetallic precipitates.

The distinction between α-AlFeMnSi and β-AlFeSi is mainly based on the ratio (Fe+Mn):Si. For the differentiation between $Al_{13}(Fe,Mn)_4$ and $Al_6(Fe,Mn)$, the silicon contents of the particles were analysed first. Depending on the source, $Al_6(Fe,Mn)$ either dissolves virtually no Si [16] or up to 0.5 wt.% [34]. For the differentiation with EDX in this work the homogeneity range up to 0.5 wt.% Si for $Al_6(Fe,Mn)$ was

used – the choice is discussed in the evaluation. There are also sources [16] which used the ratio Fe:Mn to differentiate between $Al_{13}(Fe,Mn)_4$ and $Al_6(Fe,Mn)$. This did not prove feasible in the present thesis, however.

4.2.4 X-ray powder diffraction

The X-ray powder diffraction measurements were carried out on an Empyrean from PANalytical. A Bragg-Brentano HD mirror, a ½° divergence slit and 0.04 rad Soller were used on the primary side. On the secondary side, a GalliPix detector was used. With a copper K_α radiation, °2θ was measured from 5 to 120° with a step size of 0.026°.

The evaluation was carried out with the program HighScore Plus [64] and the databases [65] and [66]. This allowed the phases to be assigned to the peaks of the diffractogram. Furthermore, the peaks of the phases were evaluated quantitatively by fitting with a Pseudo-Voigt profile. A Rietveld refinement was performed to obtain the phase fractions. It should be noted that Rietveld refinement does not deliver exact results for minor components (<10 %). The error that can be expected with a Rietveld refinement is in the range of 1-2% for main constituents [59,62].

Both bulk samples and powders, whose extraction was described in chapter 4.1.3, were examined with XRD.

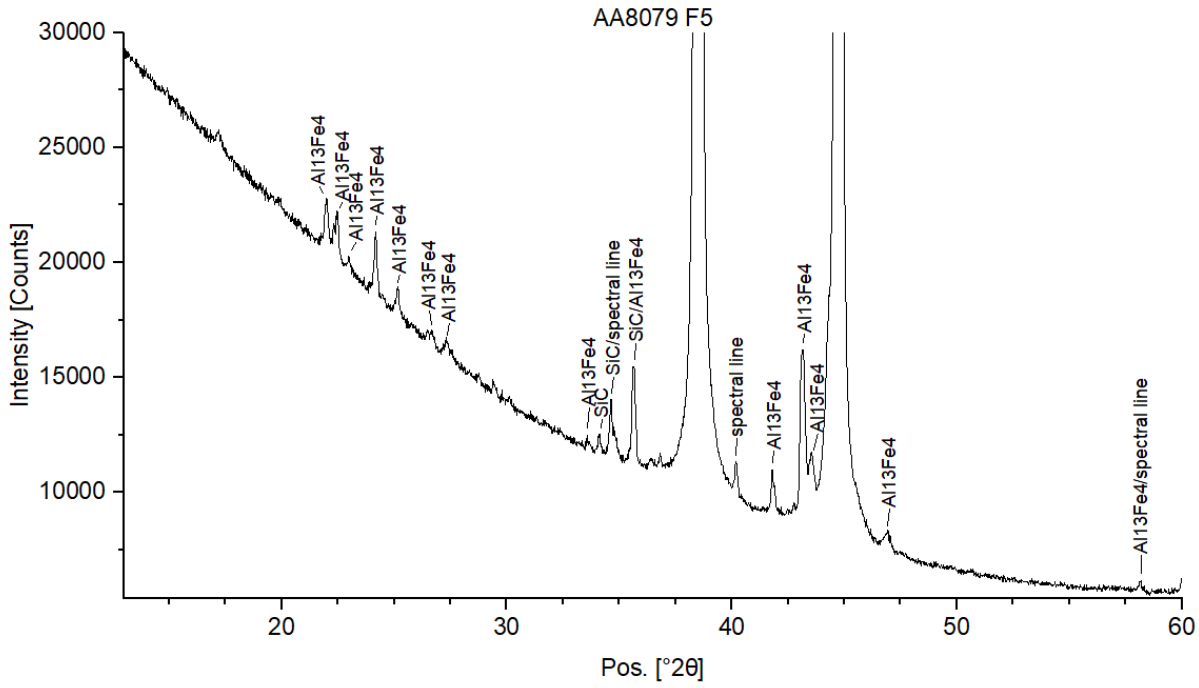

Figure 32: Evaluated diffractogram of a bulk sample

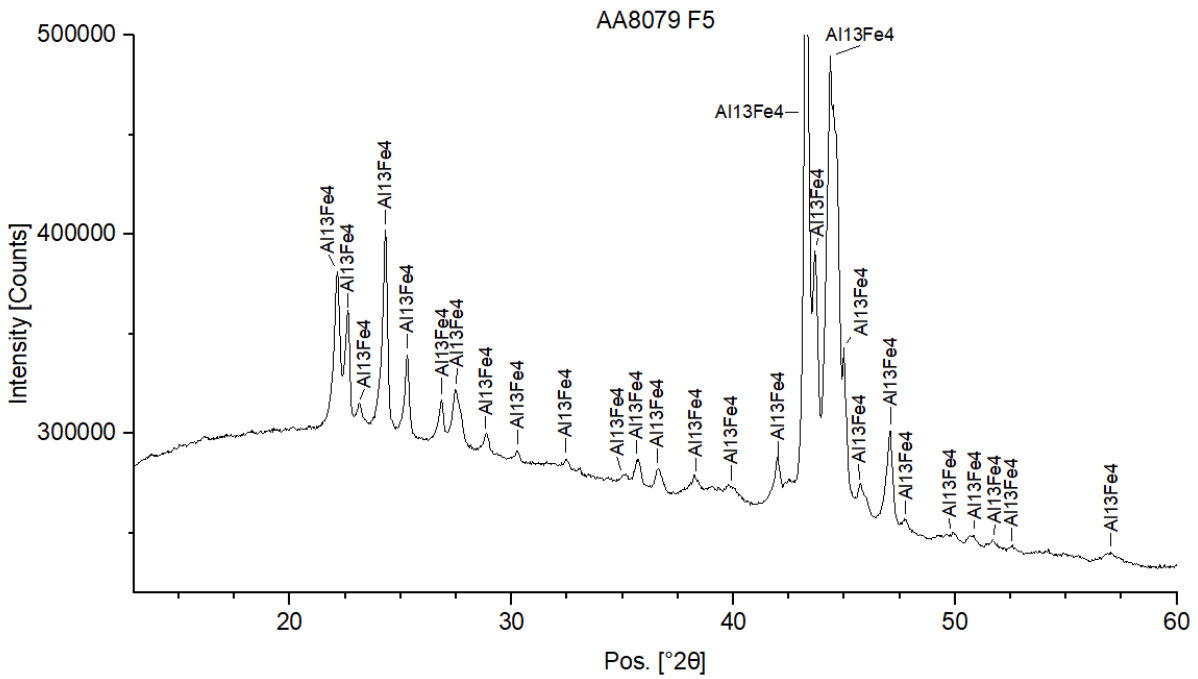

Figure 33: Evaluated diffractogram of a powder sample

As can be seen in the comparison of the exemplary diffractograms of a bulk sample (Figure 32) and a powder sample (Figure 33), more precise results are possible with the powders. One reason is, that in the bulk samples the Al peak is dominant in the diffractogram and obscures possible smaller peaks. Furthermore, the large peaks lead to the formation of spectral peaks. Another disadvantage of the bulk samples is, that the phase fraction is of the same order of magnitude as the measurement error. Furthermore, residual silicon carbide (SiC) is located on the samples, as a consequence of previous grinding steps. Hence, for the bulk samples the SiC signal had to be subsequently subtracted for the quantitative calculations.

Differences in the background signals can be related to a) variations in the chemical composition, b) the type of sample (bulk or powder) or c) the sample preparation (e.g. the amount of powder that was extracted). These differences are not expected to affect the qualitative or the quantitative evaluation of the diffractograms significantly.

The half-time samples were omitted for the powder analysis, as the bulk XRD measurements already provided sufficient information with respect to the similarities of full-time and half-time samples. The only exception being the sample of alloy AA8011 at a temperature 600°, for which both AA8011 H6 and AA8011 F6 were measured. This is due to the fact that for the sample AA8011 F6 the Al matrix dissolved only with difficulty (also after different attempts). To make sure that there was enough powder and that no phases had dissolved in the phenol method due to the long boiling time of the mixture, sample AA8011 H6 was also analysed.

The phases used for the evaluation, including the chemical compositions and crystallographic parameters, are given in the appendix 13.3. An important point is, that the Al_6Fe phase was replaced with the $Al_6Fe_{0.5}Mn_{0.5}$ phase for the evaluation of the AA8014. The manganese-rich phase has slightly different peaks, which describe the measured peaks in AA8014 better than the pure Al_6Fe phase. The former is subsequently referred to as Al_6(Fe,Mn) in AA8014, to avoid ambiguity.

The results of the XRD analysis are summarized in chapter 6.1.3. The diffractograms of the bulk samples and the powders are located in the appendix 13.10.1 and 13.10.2, respectively.

5. Stepped equilibrium calculations

The following equilibrium calculations were done using the software MatCalc [67] and the referenced aluminium database [68].

Phase alias	Designation in the database
Matrix	FCC_A1
α-AlFeMnSi	ALCRFEMNSI_A
β-AlFeSi	ALFESI_T6
$Al_{13}(Fe,Mn)_4$	AL13FE4
$Al_6(Fe,Mn)$	AL6MN
Si	SI_DIAMOND_A4

Table 8: Phases from the database used for the MatCalc equilibrium calculation

Table 8 lists the phases used for the MatCalc equilibrium calculation.

5.1 Equilibrium states of the alloys

The following figures show the current, non-optimised, simulations of the 4 alloys by MatCalc.

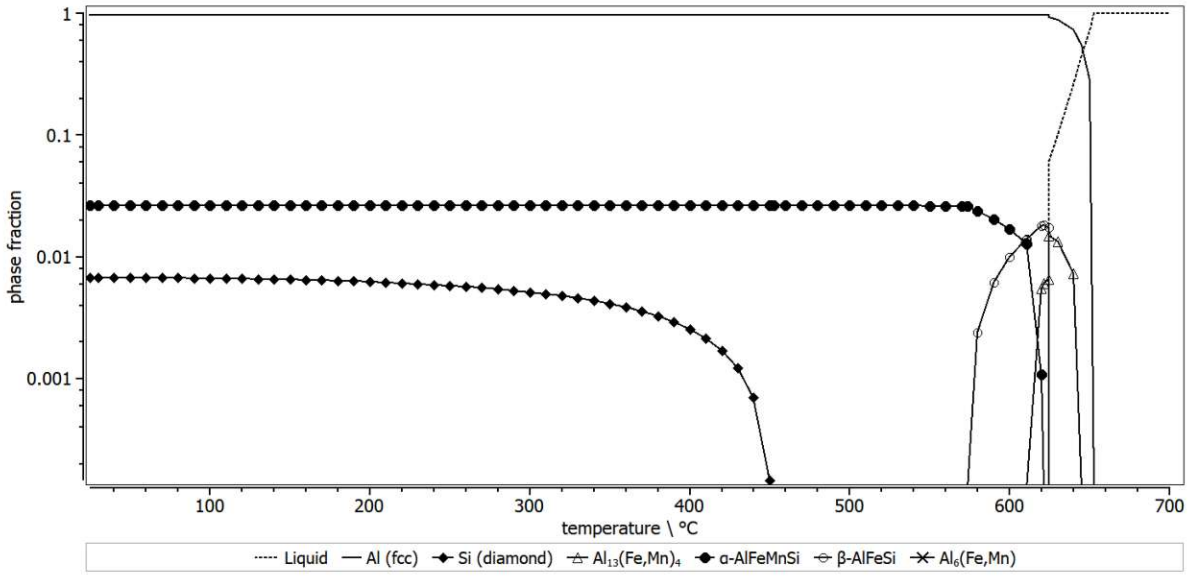

Figure 34: Stepped equilibrium calculation in MatCalc of AA8011

For the given chemical composition of the alloy AA8011, MatCalc calculates the equilibrium phases as shown in Figure 34. The Si phase is stable beginning at room temperature up to about 450°C, while the α-AlFeMnSi phase is stable from room temperature up to about 620°C and disappears in favour of the β-AlFeSi and $Al_{13}(Fe,Mn)_4$ phase. The latter two phases first appear in the equilibrium calculation at

570°C and 610°C, respectively. β-AlFeSi disappears almost simultaneously with α-AlFeMnSi whereas $Al_{13}(Fe,Mn)_4$ dissolves shortly before the matrix phase melts completely.

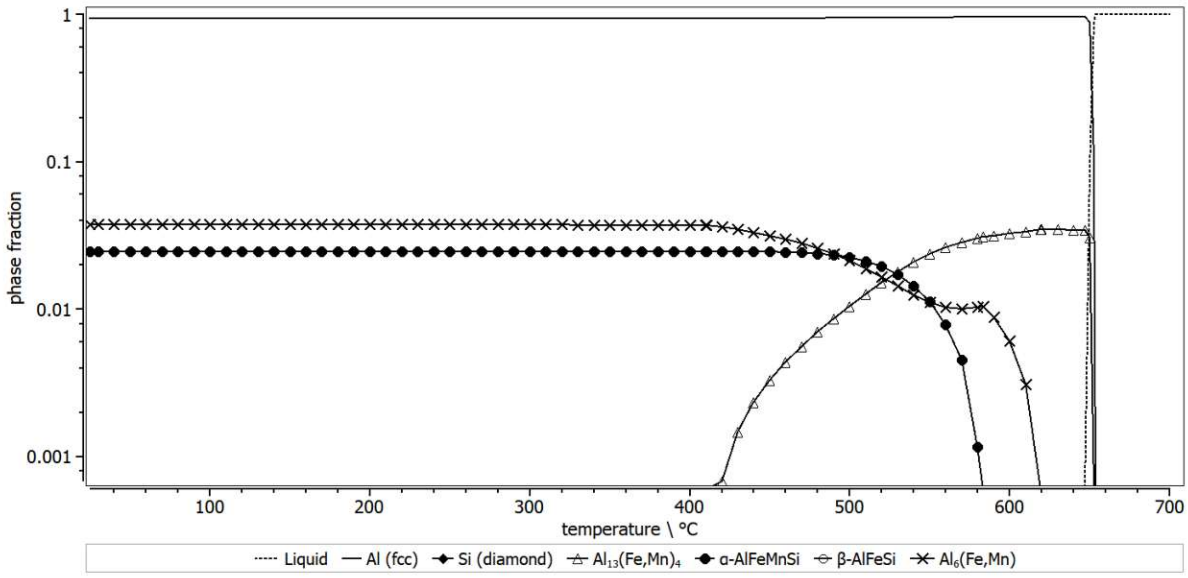

Figure 35: Stepped equilibrium calculation in MatCalc of AA8014

In the alloy AA8014, the two phases α-AlFeMnSi and $Al_6(Fe,Mn)$ are stable beginning at room temperature and disappear at 580°C and 620°C, respectively. The $Al_{13}Fe_4$ phase is stable from 420° up to the liquidus line.

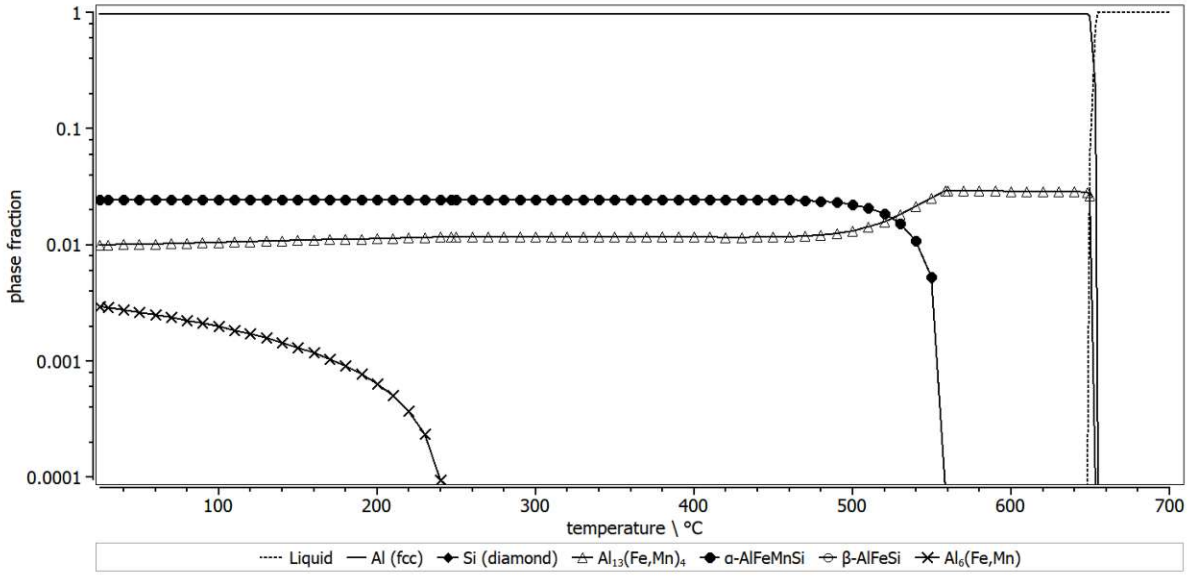

Figure 36: Stepped equilibrium calculation in MatCalc of AA8021

Figure 36 shows the MatCalc calculation for AA8021. At room temperature, the 3 phases $Al_6(Fe,Mn)$, $Al_{13}(Fe,Mn)_4$ and α-AlFeMnSi are stable, whereas $Al_6(Fe,Mn)$ is only stable up to 240°C. The phase α-AlFeMnSi is stable up to 560°C and $Al_{13}(Fe,Mn)_4$ up to the liquidus line.

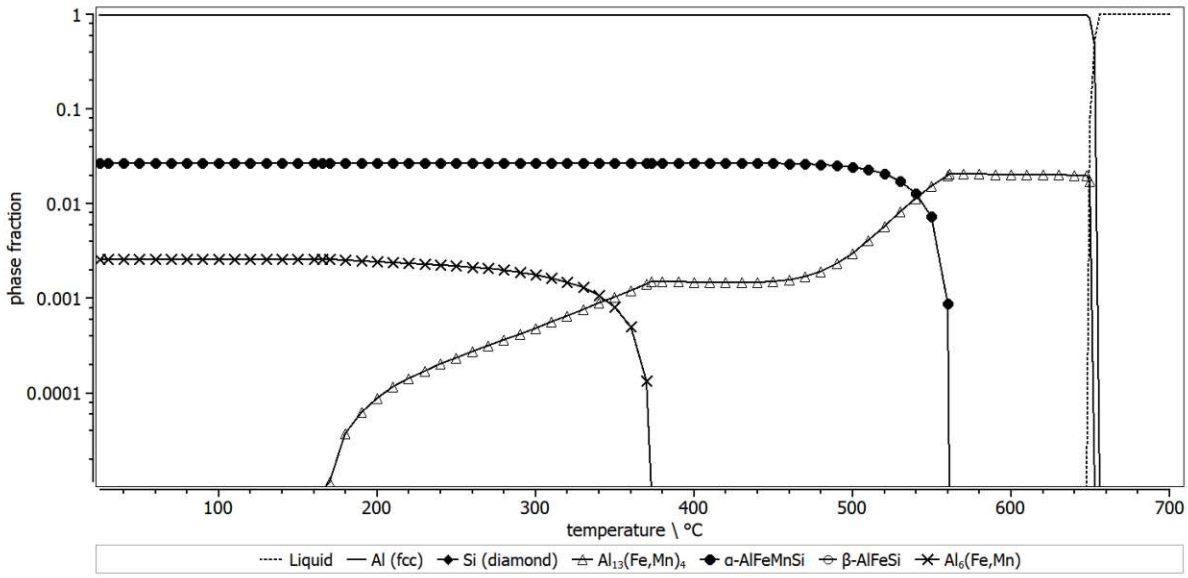

Figure 37: Stepped equilibrium calculation in MatCalc of AA8079

In the fourth alloy AA8079, the phases $Al_6(Fe,Mn)$ and α-AlFeMnSi are stable at room temperature, but only up to 370°C and 560°C, respectively. The phase $Al_{13}(Fe,Mn)_4$ is stable from approx. 170°C up to the liquidus line.

5.2 Comparison to simulations in the literature

Three papers that reflect the state of the art in the context of this work, which were previously mentioned in chapter 3.3.2, have been calculated with MatCalc. The comparison of the literature with the simulations is covered in the discussion.

Reference [16] dealt with the alloy AA8006 and a FactSage calculation with the composition in Table 9 was presented. For comparison with the MatCalc database, the equilibrium phases for this chemical composition were calculated.

	Al	Fe	Mn	Si
Composition	balance	1.5	0.5	0.1

Table 9: Composition for the simulation acc. to [16] (in wt.%)

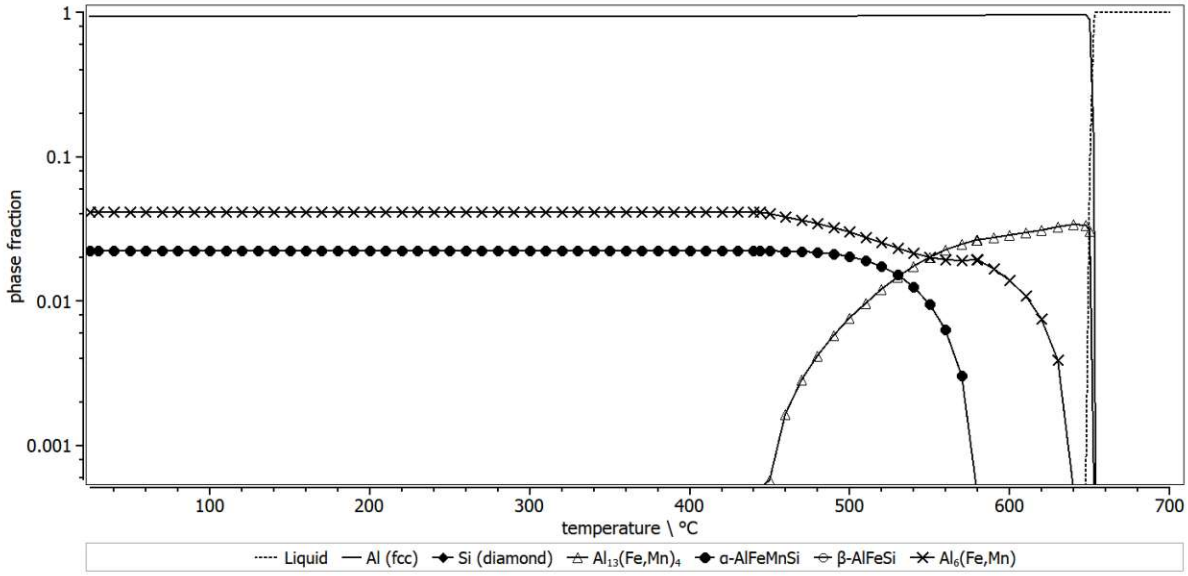

Figure 38: Stepped equilibrium calculation in MatCalc of AA8006; composition according to Table 9

As can be seen in Figure 38, the two phases α-AlFeMnSi and $Al_6(Fe,Mn)$ are in stable from room temperature up to 580°C and 620°C, respectively. The $Al_{13}(Fe,Mn)_4$ phase has its stability range from 450°C up to the liquidus line. This composition is almost identical to AA8014, which is why reference [16] is discussed in connection with AA8014 in chapter 7.1.2.

In reference [2], the ternary phase diagram Al-Fe-Si was simulated with FactSage. For this purpose, the chemical composition in Table 10 was used. It should be noted that minimal amounts of Mn were added for the simulation with MatCalc, as the paper assumed the cubic α-AlFeMnSi variant, which is only stable above a manganese content of 0.01 wt.%.

	Al	Fe	Mn	Si
Composition	balance	0.8	0.01	0.8

Table 10: Composition for the simulation acc. to [2] (in wt.%)

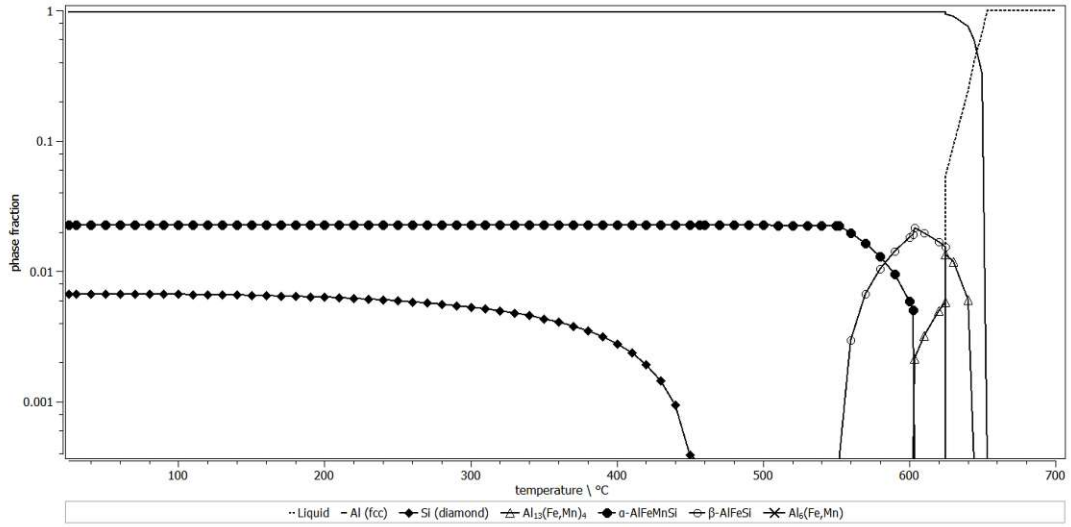

Figure 39: Stepped equilibrium calculation in MatCalc of AA8011; composition according to Table 10

Figure 39 shows 4 different phases. The pure Si phase, which is stable at room temperature up to approx. 450°C, the α-AlFeMnSi phase, whose stability range extends from room temperature up to 600°C, as well as β-AlFeSi and $Al_{13}(Fe,Mn)_4$. β-AlFeSi becomes stable at 550°C and $Al_{13}(Fe,Mn)_4$ at 600°C. The stability ranges extend up to about 620°C for β-AlFeSi and up to about 640°C for $Al_{13}(Fe,Mn)_4$. Again, the simulation of Figure 39 is almost identical to the simulation of the alloy AA8011, as almost the same chemical composition was also used. Therefore, in chapter 7.1.1, reference [2] is discussed in connection with AA8011.

For comparison with Lacaze et al. [14], three simulations were carried out with MatCalc, as the authors provide a large set of experimental data where easy comparisons with the MatCalc simulations are possible. The difference in the chemical composition in the simulations is the Fe content, which varies between 0.5 and 1.5 wt.%.

	Al	Fe	Mn	Si
Composition	balance	0.5	1.0	3.0

Table 11: Composition of the 1. simulation of [14] with MatCalc (in wt.%)

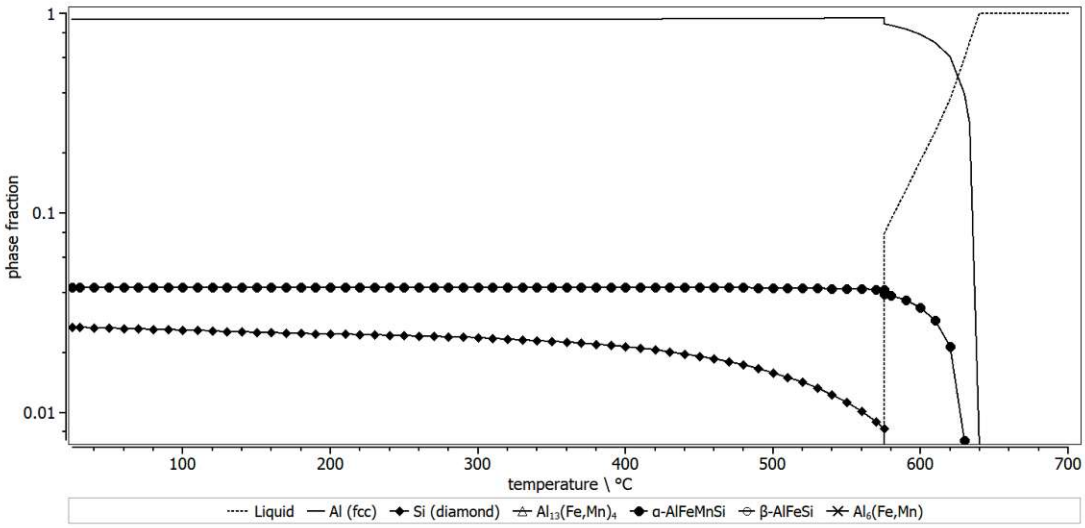

Figure 40: Stepped equilibrium calculation in MatCalc; composition according to Table 11

As can be seen in the equilibrium simulation in Figure 40, the two phases Si and α-AlFeMnSi are stable until approx. 580°C and 630°C, respectively.

	Al	Fe	Mn	Si
Composition	balance	1.0	1.0	3.0

Table 12: Composition of the 2. simulation of [14] with MatCalc (in wt.%)

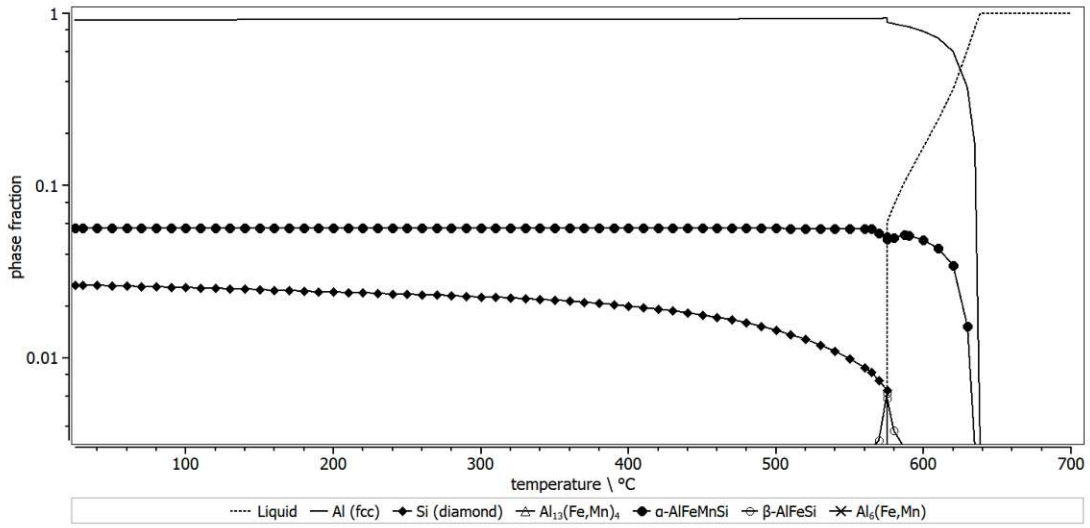

Figure 41: Stepped equilibrium calculation in MatCalc; composition according to Table 12

For the second simulation of [14], a higher Fe content was used, as shown in Table 12. The simulation is similar to the one with an Fe content of 0.5 wt.% with the difference that in the range 560-590°C β-AlFeSi is formed.

	Al	Fe	Mn	Si
Composition	balance	1.5	1.0	3.0

Table 13: Composition of the 3. simulation of [14] with MatCalc (in wt.%)

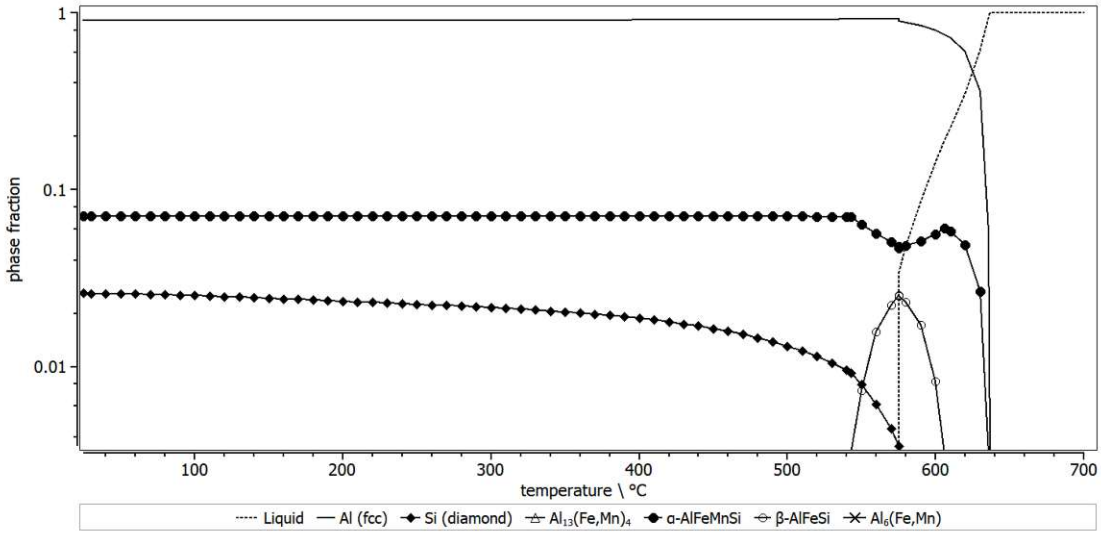

Figure 42: Stepped equilibrium calculation in MatCalc; composition according to Table 13

The last simulation of paper [14] show the highest Fe content with 1.5 wt.%. The simulation is almost analogous to the previous simulation with the difference that β-AlFeSi forms earlier, in the range of 540-610°C, and reaches a higher phase fraction.

6. Results

The results of the experimental observations can be divided into:

- the **qualitative** identification of the equilibrium phases
- the phase quantification i.e. **phase fraction**
- the investigation of **dispersoids**
- miscellaneous microstructural features and remaining questions

6.1 Equilibrium phases

In the following chapter, the results from the investigation of the equilibrium phases by EDX and XRD are presented. XRD was used to examine both bulk samples and the extracted powders of the intermetallic phases after the dissolution of the aluminium matrix.

6.1.1 EDX Analysis

For the phase-identification via EDX analysis, 3 different diagrams were used in which the chemical compositions of the analysed precipitates are plotted. Depending on the main phases expected in the samples, different characteristic element ratios were chosen for the identification – according to the descriptions in chapter 3.3.3. The exact values of the EDX analysis can be found in the appendix 13.6.

Furthermore, it should be noted that the slope of 3:1 (in wt.%) in the figures for the identification of α-AlFeMnSi is analogous to the figures of Lentz et al. [2]. The ratio (Fe+Mn):Si should technically be in the range 4:1 - 6:1 for α-AlFeMnSi, but Lentz et al. frequently measured a ratio of 3.5:1, which was also observed in this work. It is possible, that this deviation is due to the co-measurement of an aluminium matrix that actually contains non-negligible amounts of Si, which would distort this ratio. Since Lentz et al. used EPMA measurements, which are more accurate than the EDX measurements presented here and the adapted ratio describes the EDX measurements reasonably well, the slope 3:1 is also used in the evaluations below.

6.1.1.1 AA8011

Figure 43 shows the EDX results of sample AA8011 for each state.

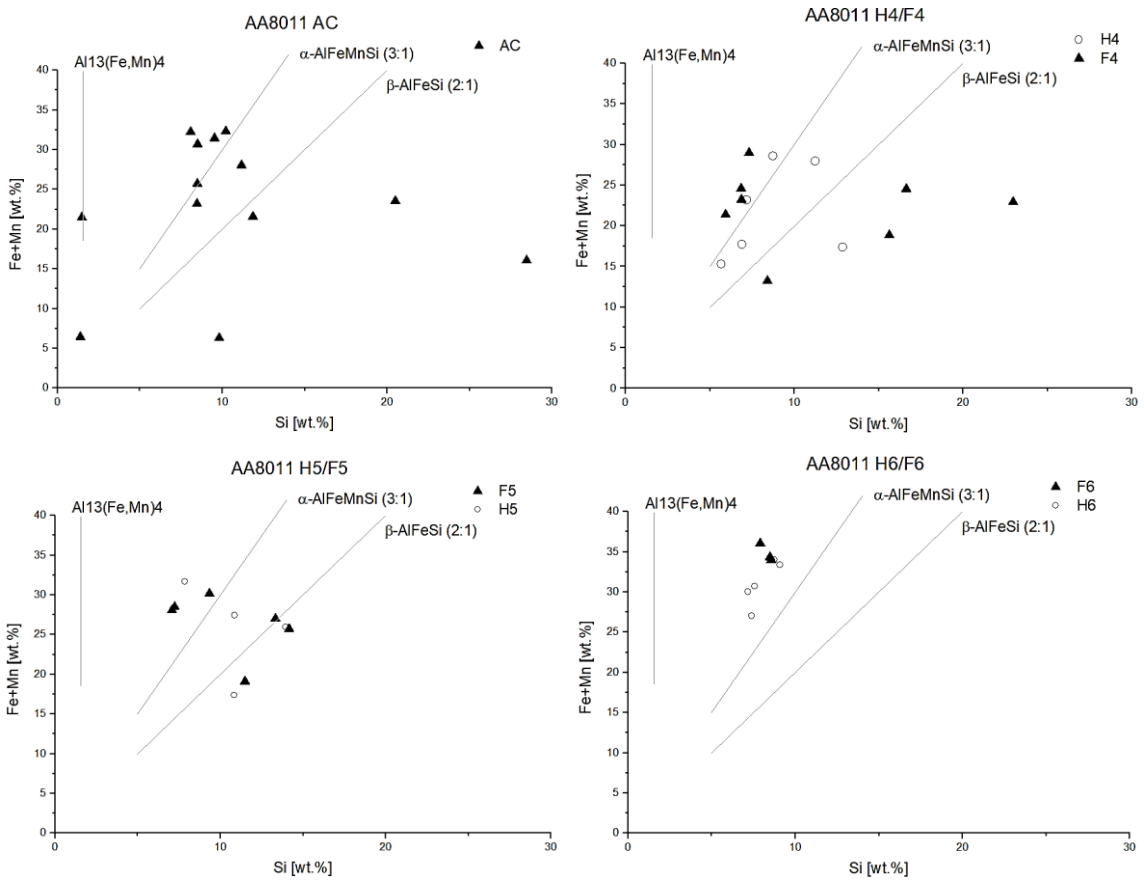

Figure 43: EDX analysis of AA8011 AC, 400°C, 500°C, 600°C, half and fulltime respectively

As shown in Figure 43, the as-cast state of AA8011 contains the phases α-AlFeMnSi and β-AlFeSi. The Si rich precipitates may either be metastable phases with increased Si content or the co-measurement of a pure Si precipitate in the excitation bulb. One composition close to $Al_{13}Fe_4$ was also found in AA8011 AC, but is considered an outlier, as relatively little of this phase was found and it is also generally not expected that this phase is present in the alloy. In AA8011 H4/F4, both α-AlFeMnSi and β-AlFeSi were found. Also, Si-richer phases occur in some measurements. For the AA8011 H5/F5 states, the presence of α-AlFeMnSi and β-AlFeSi are quite clear. β-AlFeSi disappears above 500°C, which is reported in the literature as well [69]. For AA8011 H6/F6, only α-AlFeMnSi phases are found for both states, with all measurements showing a higher slope than 3:1. This can be attributed to the fact that at 600°C a different morphology (spherical and coarse) is present, which makes the EDX measurements more accurate, as not much of the matrix is measured in contrast to the thinner and branched Chinese Script morphology. It could also indicate a change in the chemical composition.

The Si-rich precipitates found in the samples AA8011 AC, AA8011 H4, AA8011 F4 (not represented in Figure 43) were identified as pure Si. These Si phases only became apparent in the SEM, when comparing selected areas on the sample surface under the SEM with images taken using the light microscope. The reason being that there is almost no contrast between the Al matrix and pure Si phases in the SEM (BSE detector), as can be seen in Figure 44.

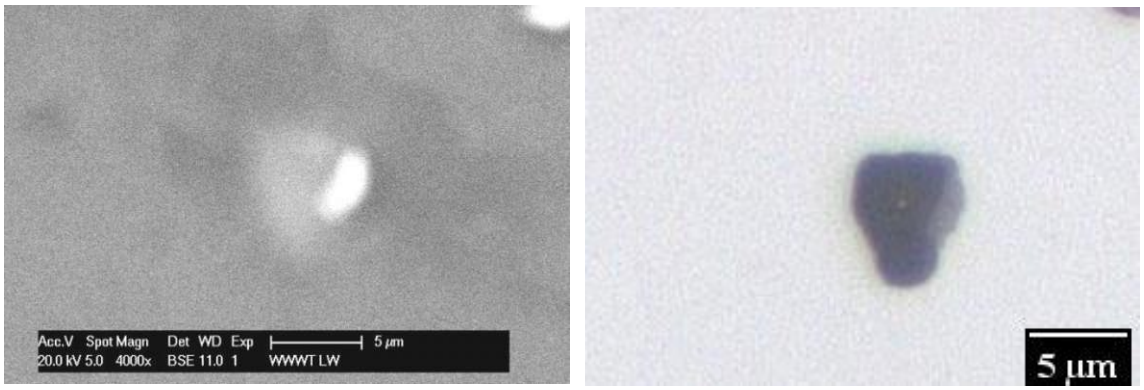

Figure 44: AA8011 F4 – left: SEM image; right: light microscopy image

The bright spot in the SEM (BSE) image represents an Fe-rich phase, which is directly next to the Si precipitate (dark grey in the light microscope image). The reason why there is almost no difference between pure Si and pure Al in the SEM image is, that the BSE detector makes the elements appear darker or brighter according to their atomic number. Since Si is next to Al in the periodic table of elements, there is only a small difference in contrast in the BSE detector.

The Si-precipitate in the central area was measured with EDX. The result of the analysis is shown in Table 14. It can be seen that only Si and Al matrix were measured, as would be expected for a pure Si phase.

Element	wt.%	at.%
Al	44.64	45.64
Si	55.36	54.36

Table 14: AA8011 F4 - EDX measurement of the Si precipitate

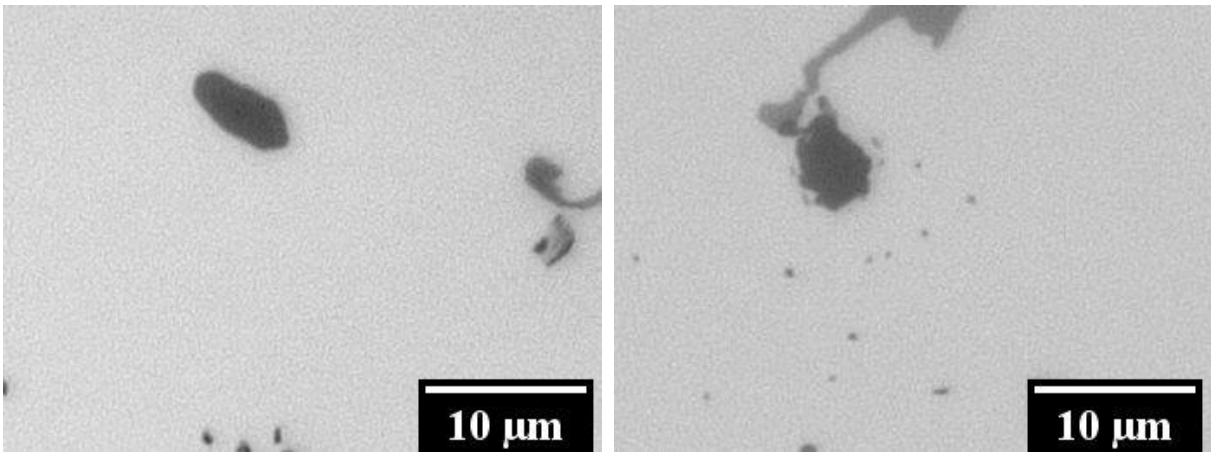

Figure 45: Si precipitates in the light microscope - left: AA8011 AC, right: AA8011 H4

In the light microscope images of AA8011 AC and AA8011 H4 shown in Figure 45, the Si precipitates are also visible as dark grey areas. Analogous to AA8011 F4, they were examined in the SEM and identified as pure Si phases.

6.1.1.2 AA8014

The following figures show the results of the EDX analysis of AA8014 for each state.

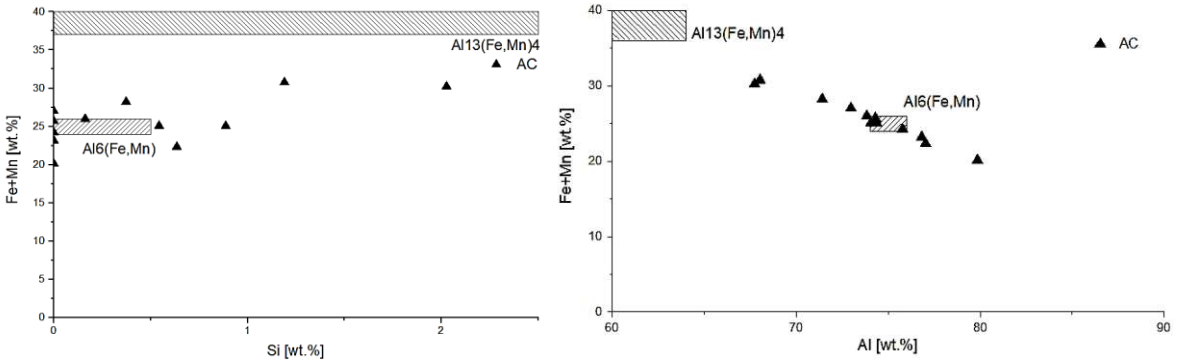

Figure 46: EDX analysis of AA8014 AC

As can be seen in Figure 46, both $Al_{13}(Fe,Mn)_4$ and $Al_6(Fe,Mn)$ are present in the as-cast state of AA8014 according to the defined homogeneity ranges drawn in the diagrams. The Si content was used as a starting point for the differentiation between $Al_{13}(Fe,Mn)_4$ and $Al_6(Fe,Mn)$, since $Al_6(Fe,Mn)$ is assumed to dissolve only limited amounts of Si up to a maximum of 0.5 wt.%. Everything above this value or above the reference range of Fe+Mn is assigned to $Al_{13}(Fe,Mn)_4$.

It is important to note that based on the morphology of the precipitates and their size a lot of Al matrix was measured during the EDX analysis. Therefore, the actual composition of $Al_{13}(Fe,Mn)_4$ (according to the stoichiometry) would only be measured for a sufficiently large phase. This is hardly possible based on the needle-like morphology of the phases in AA8014 AC. The results are distorted accordingly, which can be seen in the figure on the right. Hence, the interpretation of absolute element concentrations has to be done carefully, since an $Al_{13}(Fe,Mn)_4$ precipitate may be interpreted as $Al_6(Fe,Mn)$ if a large volume of aluminium matrix lies within the excitation bulb. Essentially, high contents of Fe+Mn or Si are good indicators for $Al_{13}(Fe,Mn)_4$, but vice versa low amounts of Fe+Mn and Si are not necessarily a reliable indicator for $Al_6(Fe,Mn)$.

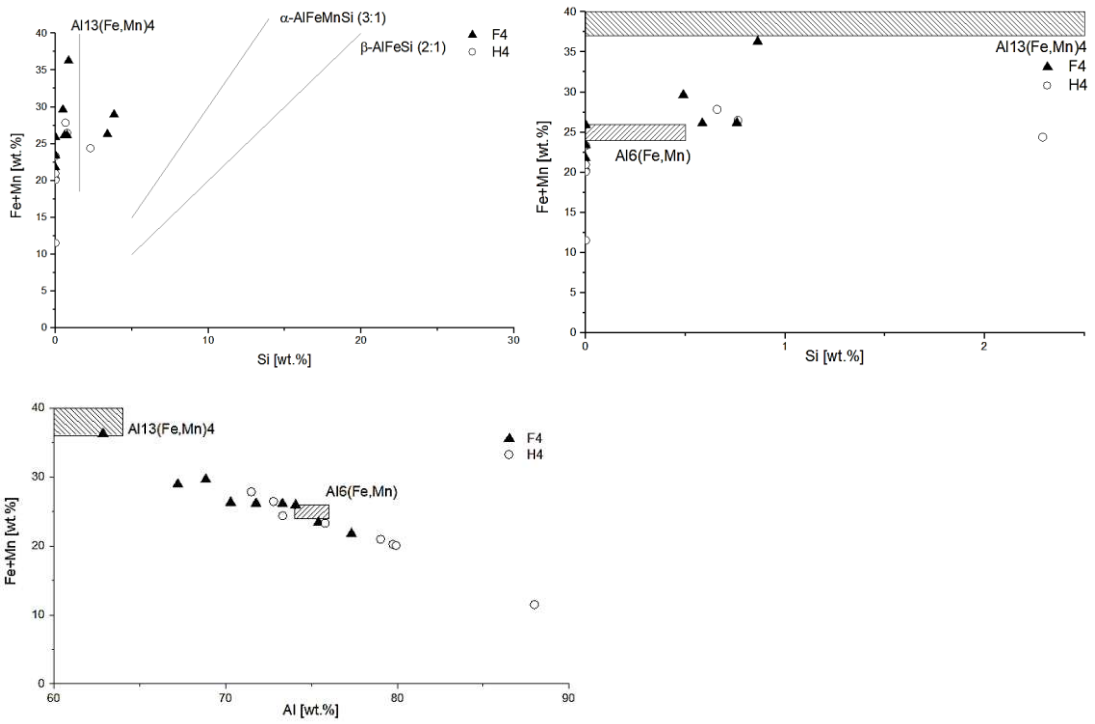

Figure 47: EDX analysis of AA8014 H4/F4

The results of the EDX measurements of AA8014 H4/F4 are shown in Figure 47. In the half-time samples as well as in the full-time samples, the phases $Al_{13}(Fe,Mn)_4$ and $Al_6(Fe,Mn)$ are present, according to the defined criteria. The 3 points with higher Si content cannot be classified as $Al_{13}(Fe,Mn)_4$. Furthermore, the measurements also show high ratios of (Fe+Mn):Si, which exceeds the reference ratio for α-AlFeMnSi, that is 3:1. Since the theoretical ratio of α-AlFeMnSi may reach up to 6:1 and the points have a ratio around 7 to 10, it could be assumed that an α-variant is present in AA8014.

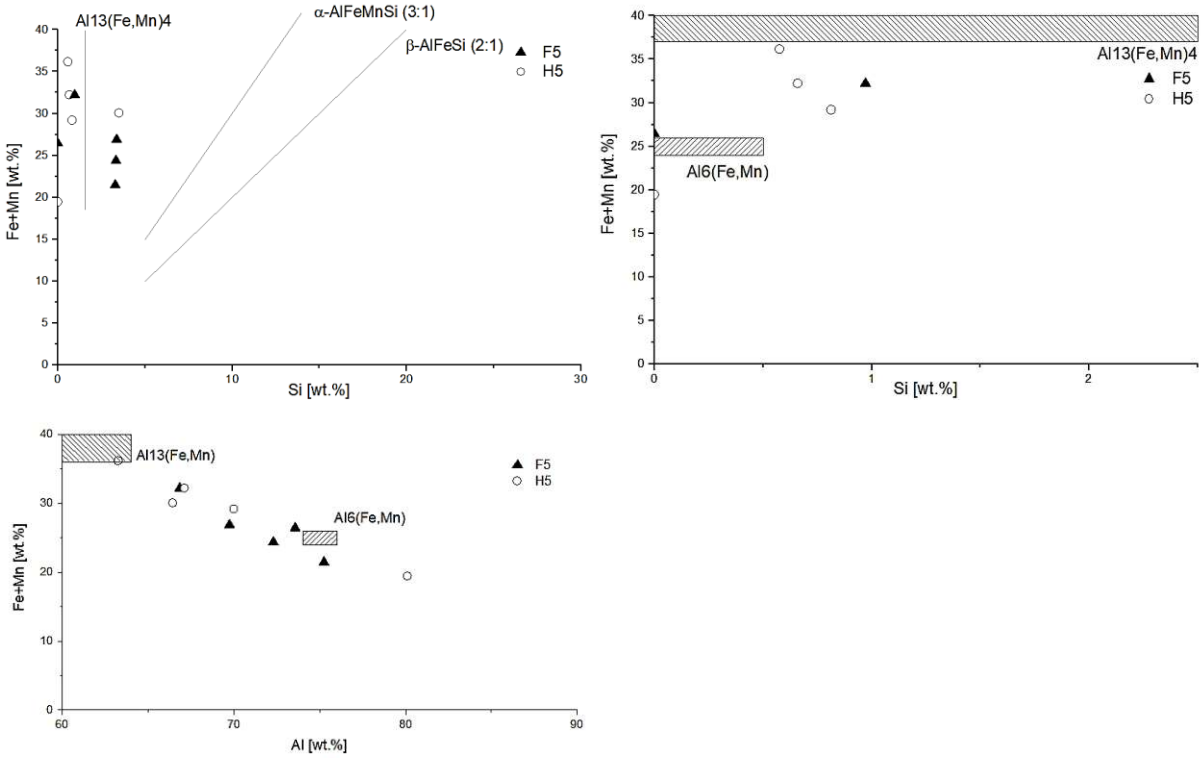

Figure 48: EDX analysis of AA8014 H5/F5

As seen in Figure 48, the phases $Al_{13}(Fe,Mn)_4$ and $Al_6(Fe,Mn)$ are both present in AA8014 H5/F5. Furthermore, both the half-time samples and the full-time samples show measurements that exceed the (Fe+Mn):Si ratio of α-AlFeMnSi as well as the Si content of $Al_{13}(Fe,Mn)_4$. Analogous to the 400°C samples α-AlFeMnSi is also assumed here.

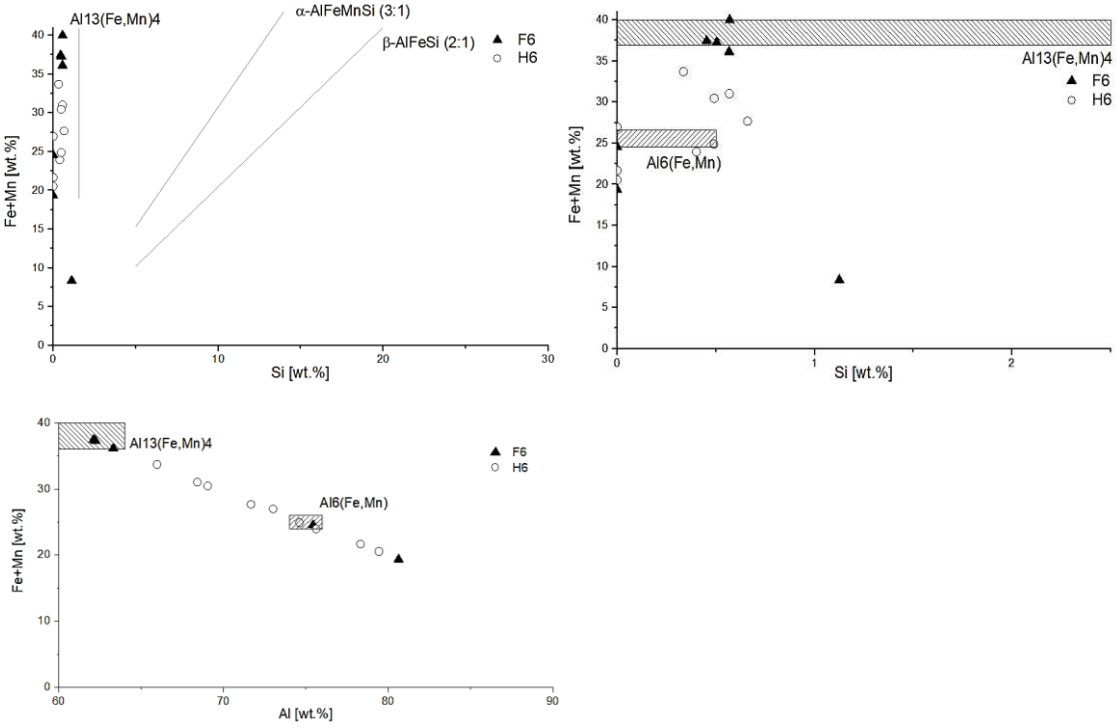

Figure 49: EDX analysis of AA8014 H6/F6

In the case of AA8014 H6/F6, shown in Figure 49, $Al_{13}(Fe,Mn)_4$ and $Al_6(Fe,Mn)$ are stable in the half-time and full-time samples. In AA8014 F6, there is an outlier, which can be assigned to α-AlFeMnSi based on the ratio, or $Al_{13}(Fe,Mn)_4$ if solely based on the Si content.

6.1.1.3 AA8021

The following figures show the results of the EDX analysis of AA8021 for each state.

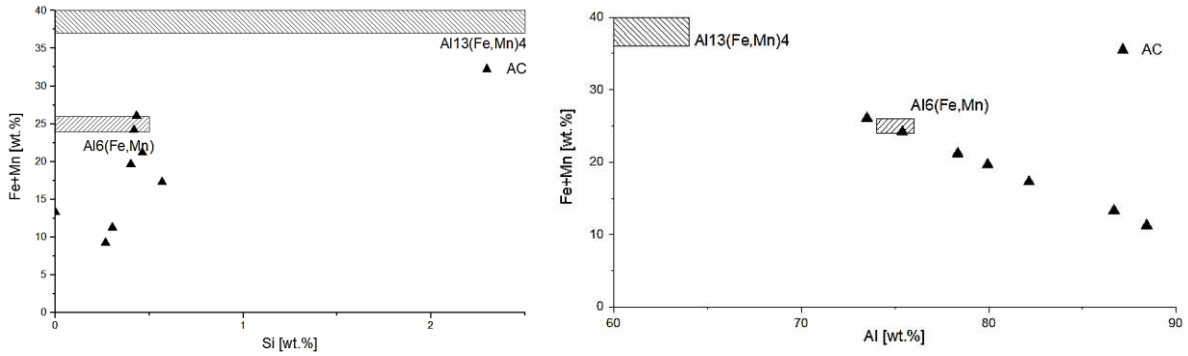

Figure 50: EDX analysis of AA8021 AC

For the as-cast state of AA8021, the chemical compositions from the EDX measurements are shown in Figure 50. Almost all of the measured points would have to be assigned to $Al_6(Fe,Mn)$ according to the chemical composition range defined. Again, it should be noted that these points could also be $Al_{13}(Fe,Mn)_4$ phases with high fractions of co-measured Al matrix. This is also supported by the fact that multiple points show comparably high Si contents and the maximum solubility of 0.5 wt% for $Al_6(Fe,Mn)$ is not undisputed.

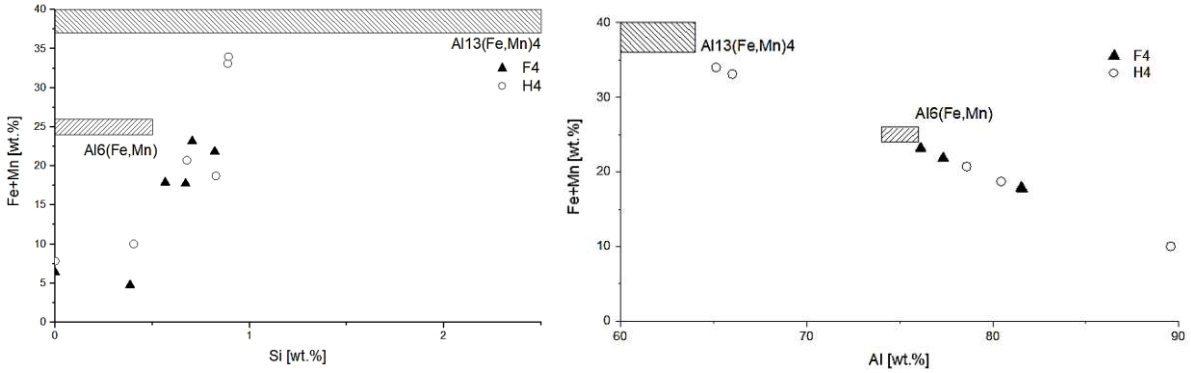

Figure 51: EDX analysis of AA8021 H4/F4

In Figure 51, which shows the EDX measurements of AA8021 H4/F4, both $Al_{13}(Fe,Mn)_4$ and $Al_6(Fe,Mn)$ were assigned to the measured phases.

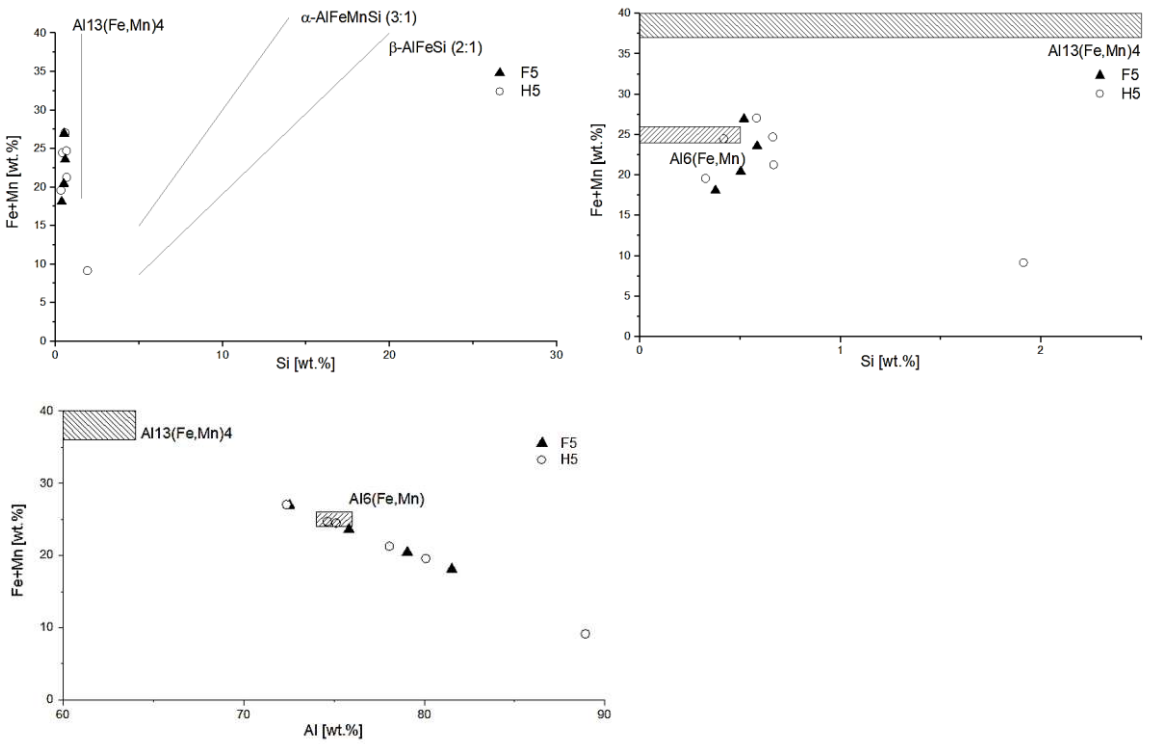

Figure 52: EDX analysis of AA8021 H5/F5

In the sample AA8021 H5/F5 only $Al_{13}(Fe,Mn)_4$ was assigned to the measured precipitates, even though the points lie very close to the area of $Al_6(Fe,Mn)$. The reason being that $Al_6(Fe,Mn)$ should be unstable in this temperature range and the distortion favours $Al_6(Fe,Mn)$, as mentioned earlier. This sample especially highlights the possible ambiguities of the EDX measurements. A Si-rich outlier is contained in AA8021 H5, which could be assigned to α-AlFeMnSi based on the ratio.

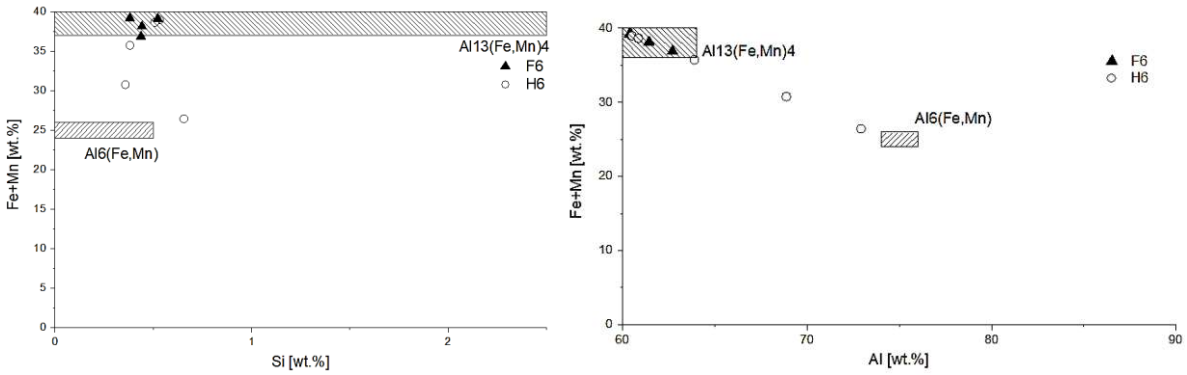

Figure 53: EDX analysis of AA8021 H6/F6

The EDX measurements of the samples AA8021 H6/F6 can be seen in Figure 53. In both half-time and full-time samples, the only phase is $Al_{13}(Fe,Mn)_4$. For the full-time samples the precipitates have spheroidized and coarsened sufficiently in order to yield the undistorted chemical composition with EDX. This supports the assumption that most of the $Al_{13}(Fe,Mn)_4$ will actually result in datapoints close to the range of $Al_6(Fe,Mn)$ – as was seen in samples AA8021 H5/F5 before. Another point to consider would be the possibility that the solubility of Si in $Al_6(Fe,Mn)$ is actually closer to 0 that it is to 0.5 wt% and that EDX-measurements of $Al_6(Fe,Mn)$ result in virtually no Si content.

6.1.1.4 AA8079

The following figures show the results of the EDX analysis of AA8079 for each state.

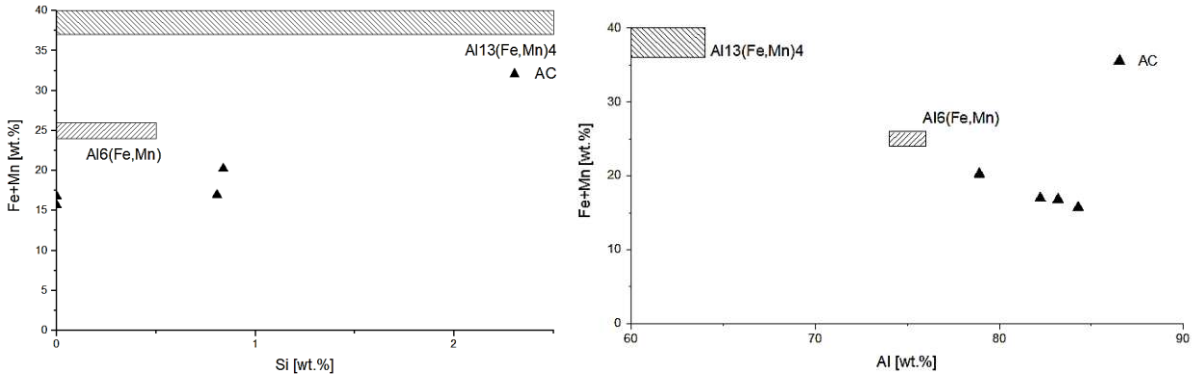

Figure 54: EDX analysis of AA8079 AC

According to Figure 54, the two phases $Al_{13}(Fe,Mn)_4$ and $Al_6(Fe,Mn)$ can be expected in the as-cast state of alloy AA8079. The former assignment is primarily based on the limits of the Si content of the respective phases.

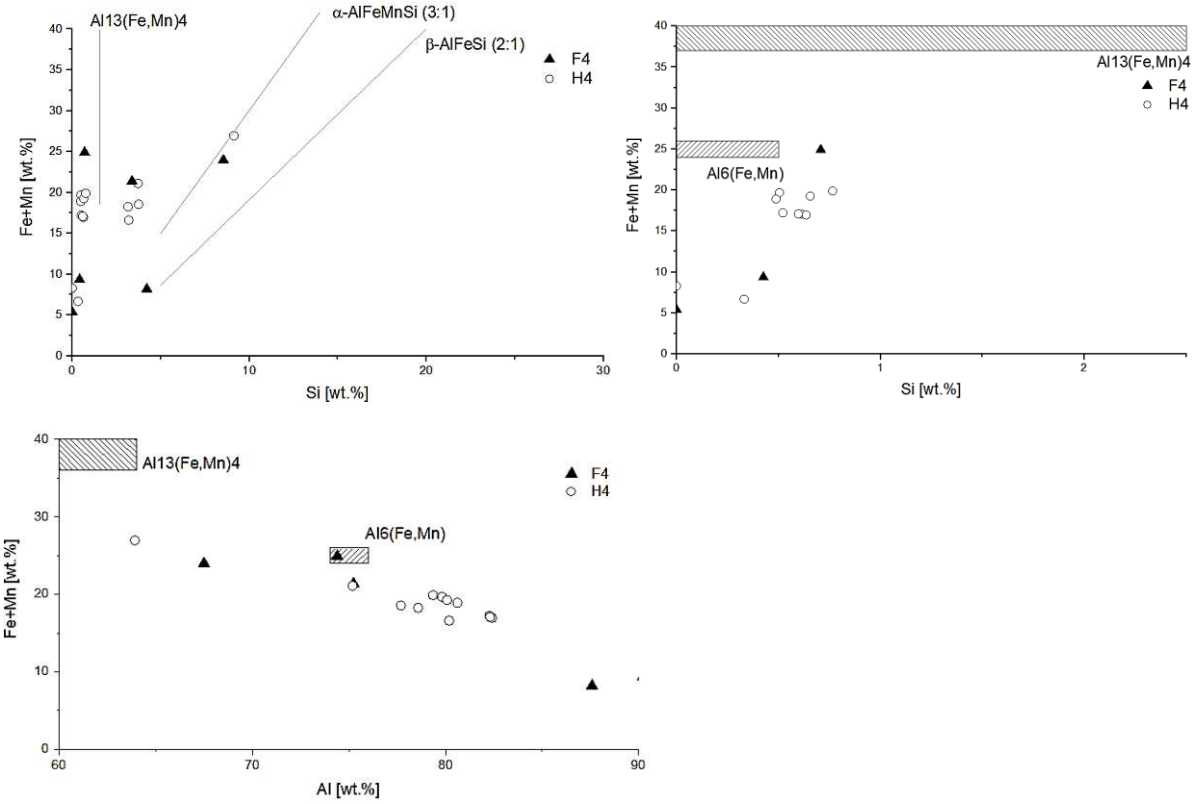

Figure 55: EDX analysis of AA8079 H4/F4

Figure 55 shows the EDX measurements of AA8079 H4/F4. For both the half-time and full-time samples, the equilibrium phases $Al_{13}(Fe,Mn)_4$, $Al_6(Fe,Mn)$ and α-AlFeMnSi were found. The phase β-AlFeSi was only measured in the full-time sample. This can either be due to the fact, that a complete equilibrium has not yet been reached in the half-time sample, or that by chance no β-AlFeSi precipitate was measured in the half-time sample.

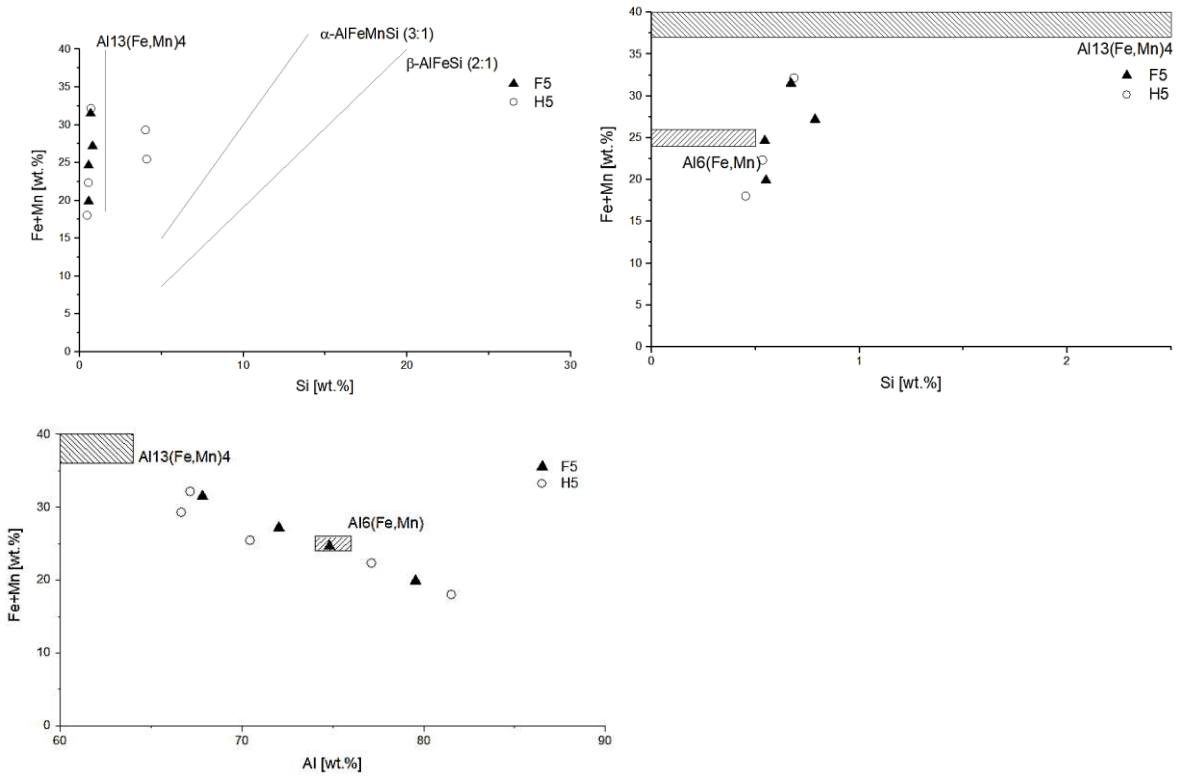

Figure 56: EDX analysis of AA8079 H5/F5

The results of the EDX analysis of AA8079 H5/F5 are shown in Figure 56. For the half-time samples, $Al_{13}(Fe,Mn)_4$ was found. Furthermore, two data points of the half-time samples have a higher Si content, outside the homogeneity ranges of $Al_{13}(Fe,Mn)_4$ and $Al_6(Fe,Mn)$. It is possible, that the α-phase corresponds to these points. The existence of the α-AlFeMnSi phase in the half-time sample is explainable, if we consider the possibility that the equilibrium state is not fully reached in this sample yet. Furthermore, it should be noted that the points close to the area of $Al_6(Fe,Mn)$ have been interpreted as a measurement inaccuracy i.e. co-measurement of the aluminium matrix, since $Al_6(Fe,Mn)$ should be unstable in this alloy. For the full-time samples only the phase $Al_{13}(Fe,Mn)_4$ is present.

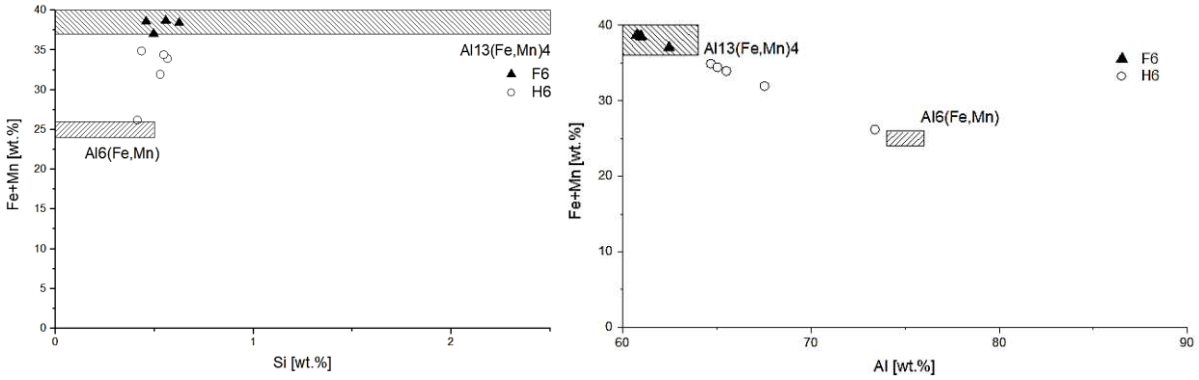

Figure 57: EDX analysis of AA8079 H6/F6

Figure 57 shows the measurement results of AA8079 H6/F6. For both, the half-time and the full-time samples, only the phase $Al_{13}(Fe,Mn)_4$ was found. The measured values are very close to the theoretical composition of $Al_{13}(Fe,Mn)_4$ compared to the measurements of the same phase at lower temperatures.

As with AA8011, this is due to the change in morphology and size, which result in an improved accuracy of the EDX evaluation.

6.1.2 XRD Analysis

The diffractograms with the peaks assigned to the corresponding phases can be found in the appendix. The diffractograms of the bulk samples are in chapter 13.10.1, those of the powders in chapter 13.10.2.

In the XRD evaluation almost all measured peaks could be explained. The only exceptions were samples AA8011 AC and AA8079 AC. For the alloy AA8011 AC in the bulk samples the peak at 27.6 °2θ is unexplained, but this peak is virtually absent in the diffractogram of the powders and might have been caused by residual impurities on the sample surface. The situation is different for alloy AA8079 AC, where an unknown peak appears at 19.2 °2θ in both the bulk samples and the powder. The signal could possibly arise from other metastable phases that have not been considered in the evaluation. Since the aim of this thesis is the characterization of the equilibrium phases after long-term annealing, the identification of these peaks has not been pursued any further.

6.1.3 Summary of the equilibrium phases

The following tables show the qualitative results of the EDX analysis, the XRD analysis of the bulk samples and the powders for all 4 alloys.

Sample	EDX - analysis	XRD - analysis of the bulk sample	XRD - powder analysis
AA8011 AC	α-AlFeMnSi + β-AlFeSi + Si	α-AlFeMnSi + β-AlFeSi + Si	α-AlFeMnSi + β-AlFeSi + Si
AA8011 H4	α-AlFeMnSi + β-AlFeSi + Si	α-AlFeMnSi + β-AlFeSi + Si	-
AA8011 F4	α-AlFeMnSi + β-AlFeSi + Si	α-AlFeMnSi + β-AlFeSi + Si	α-AlFeMnSi + β-AlFeSi + Si
AA8011 H5	α-AlFeMnSi + β-AlFeSi	α-AlFeMnSi + β-AlFeSi	-
AA8011 F5	α-AlFeMnSi + β-AlFeSi	α-AlFeMnSi + β-AlFeSi	α-AlFeMnSi + β-AlFeSi
AA8011 H6	α-AlFeMnSi	α-AlFeMnSi	α-AlFeMnSi
AA8011 F6	α-AlFeMnSi	α-AlFeMnSi	α-AlFeMnSi

Table 15: Summary of the detected equilibrium phases in AA8011

As can be seen in Table 15, all results of the different analysis methods for AA8011 are identical. It can also be assumed that equilibrium has been reached everywhere, as both the half-time and the full-time samples contain the same phases.

Sample	EDX - analysis	XRD - analysis of the bulk sample	XRD - powder analysis
AA8014 AC	$Al_{13}(Fe,Mn)_4$ + $Al_6(Fe,Mn)$	$Al_{13}(Fe,Mn)_4$ + $Al_6(Fe,Mn)$	$Al_{13}(Fe,Mn)_4$ + $Al_6(Fe,Mn)$
AA8014 H4	$Al_{13}(Fe,Mn)_4$ + $Al_6(Fe,Mn)$ + α-AlFeMnSi	$Al_{13}(Fe,Mn)_4$ + $Al_6(Fe,Mn)$ + α-AlFeMnSi	-
AA8014 F4	$Al_{13}(Fe,Mn)_4$ + $Al_6(Fe,Mn)$ + α-AlFeMnSi	$Al_{13}(Fe,Mn)_4$ + $Al_6(Fe,Mn)$ + α-AlFeMnSi	$Al_{13}(Fe,Mn)_4$ + $Al_6(Fe,Mn)$ + α-AlFeMnSi
AA8014 H5	$Al_{13}(Fe,Mn)_4$ + $Al_6(Fe,Mn)$ + α-AlFeMnSi	$Al_{13}(Fe,Mn)_4$ + $Al_6(Fe,Mn)$ + α-AlFeMnSi	-
AA8014 F5	$Al_{13}(Fe,Mn)_4$ + $Al_6(Fe,Mn)$ + α-AlFeMnSi	$Al_{13}(Fe,Mn)_4$ + $Al_6(Fe,Mn)$ + α-AlFeMnSi	$Al_{13}(Fe,Mn)_4$ + $Al_6(Fe,Mn)$ + α-AlFeMnSi
AA8014 H6	$Al_{13}(Fe,Mn)_4$ + $Al_6(Fe,Mn)$	$Al_{13}(Fe,Mn)_4$ + $Al_6(Fe,Mn)$	-
AA8014 F6	$Al_{13}(Fe,Mn)_4$ + $Al_6(Fe,Mn)$	$Al_{13}(Fe,Mn)_4$ + $Al_6(Fe,Mn)$	$Al_{13}(Fe,Mn)_4$ + $Al_6(Fe,Mn)$

Table 16: Summary of the detected equilibrium phases in AA8014

The summary of the equilibrium phases in AA8014 is shown in Table 16. It should be noted that α-AlFeMnSi was underlined wavy in the EDX analysis, because the phase could not be clearly identified due to the high ratio of (Fe+Mn):Si. However, the α-AlFeMnSi phase is congruent with both XRD analyses, which is why the assignment of the phase via EDX is likely correct. Apart from this aspect, all three different analysis methods are identical, and it is also evident that equilibrium has been reached in all different states, as both the half-time and the full-time samples show the same phases.

Sample	EDX - analysis	XRD - analysis of the bulk sample	XRD - powder analysis
AA8021 AC	$Al_{13}(Fe,Mn)_4$ + $Al_6(Fe,Mn)$	$Al_{13}(Fe,Mn)_4$ + $Al_6(Fe,Mn)$	$Al_{13}(Fe,Mn)_4$ + $Al_6(Fe,Mn)$
AA8021 H4	$Al_{13}(Fe,Mn)_4$ + $Al_6(Fe,Mn)$	$Al_{13}(Fe,Mn)_4$ + $Al_6(Fe,Mn)$	-
AA8021 F4	$Al_{13}(Fe,Mn)_4$ + $Al_6(Fe,Mn)$	$Al_{13}(Fe,Mn)_4$ + $Al_6(Fe,Mn)$	$Al_{13}(Fe,Mn)_4$ + $Al_6(Fe,Mn)$
AA8021 H5	$Al_{13}(Fe,Mn)_4$	$Al_{13}(Fe,Mn)_4$	-

AA8021 F5	$Al_{13}(Fe,Mn)_4$	$Al_{13}(Fe,Mn)_4$	$Al_{13}(Fe,Mn)_4$
AA8021 H6	$Al_{13}(Fe,Mn)_4$	$Al_{13}(Fe,Mn)_4$	-
AA8021 F6	$Al_{13}(Fe,Mn)_4$	$Al_{13}(Fe,Mn)_4$	$Al_{13}(Fe,Mn)_4$

Table 17: Summary of the detected equilibrium phases in AA8021

The equilibrium phases found in AA8021 by the individual methods are shown in Table 17. The phase $Al_{13}(Fe,Mn)_4$ is found in all states and with all methods. In the XRD bulk sample AA8021 H4 the phase $Al_6(Fe,Mn)$ is still present next to the phase $Al_{13}(Fe,Mn)_4$. In the sample AA8021 F4 only $Al_{13}(Fe,Mn)_4$ is present according to the quantification of the bulk sample AA8021 F4 with HighScore Plus - the phase $Al_6(Fe,Mn)$ could not be calculated. Generally, the peak at 18.27 °2θ is an indicator for $Al_6(Fe,Mn)$. Based on the small peak at this specific value (as can be seen in the diffractogram AA8021 F4 in the appendix 13.10.1.3) it can be assumed that the phase is actually present in very small quantities in the bulk sample of AA8021 F4, but HighScore Plus does not recognize the peak in its evaluation. It can be assumed, that this phase probably occurs in the bulk sample of AA8021 F4, so it has been included in the table, underlined wavy. Furthermore, the presence of this phase is also supported by the fact, that that a small residual fraction of $Al_6(Fe,Mn)$ is found in the powders of AA8021 F4.

Sample	EDX - analysis	XRD - analysis of the bulk sample	XRD - powder analysis
AA8079 AC	$Al_{13}(Fe,Mn)_4$ + $Al_6(Fe,Mn)$	$Al_{13}(Fe,Mn)_4$ + $Al_6(Fe,Mn)$	$Al_{13}(Fe,Mn)_4$ + $Al_6(Fe,Mn)$
AA8079 H4	$Al_{13}(Fe,Mn)_4$ + $Al_6(Fe,Mn)$ + α-AlFeMnSi	$Al_{13}(Fe,Mn)_4$ + $Al_6(Fe,Mn)$ + α-AlFeMnSi + β-AlFeSi	-
AA8079 F4	$Al_{13}(Fe,Mn)_4$ + $Al_6(Fe,Mn)$ + α-AlFeMnSi + β-AlFeSi	$Al_{13}(Fe,Mn)_4$ + $Al_6(Fe,Mn)$ + α-AlFeMnSi + β-AlFeSi	$Al_{13}(Fe,Mn)_4$ + $Al_6(Fe,Mn)$ + α-AlFeMnSi + β-AlFeSi
AA8079 H5	$Al_{13}(Fe,Mn)_4$ + α-AlFeMnSi	$Al_{13}(Fe,Mn)_4$	-
AA8079 F5	$Al_{13}(Fe,Mn)_4$	$Al_{13}(Fe,Mn)_4$	$Al_{13}(Fe,Mn)_4$
AA8079 H6	$Al_{13}(Fe,Mn)_4$	$Al_{13}(Fe,Mn)_4$	-
AA8079 F6	$Al_{13}(Fe,Mn)_4$	$Al_{13}(Fe,Mn)_4$	$Al_{13}(Fe,Mn)_4$

Table 18: : Summary of the detected equilibrium phases in AA8079

The equilibrium states of the AA8079 are described in Table 18. The phases of the as-cast states, as well as the full-time samples are congruent for all three methods. According to the XRD analysis of the bulk samples, equilibrium was reached everywhere. The EDX analysis did not find any β-AlFeSi at 400°C, however. This discrepancy is neglected since the XRD method measures a comparably large volume as opposed to a few selected precipitates and is most likely more reliable. Another uncertainty in the EDX analysis occurs in AA8079 H5, where the phase α-AlFeMnSi was again underlined wavy, because the ratio of (Fe+Mn):Si is above the reference value for 2 measurements. It is possible that the equilibrium state has not yet been reached. Ultimately - however, attention should be paid to the more precise powder XRD analysis, in which this phase was not found.

6.2 Phase quantification

To determine the total phase fractions, light microscopy was used on the one hand and X-ray powder diffraction on the other. It should be noted, that any dispersoids were not considered in the phase quantification with the light microscopy. This is different for the XRD measurement, where dispersoids can be part of the extracted powder.

6.2.1 Total phase fraction

Figure 58 shows the comparison of the total phase fraction from the XRD bulk sample measurements, as well as from the ImageJ Analysis. The legend entry “total share LIMI” corresponds to the empirical mean value of the ImageJ Analysis of the light microscope images - the values of which are shown in the appendix 13.4.

It should be noted here that the values of the XRD measurement were converted from weight fractions w_i to volume fractions φ_i using the following formulae:

$$\varphi_i = \frac{\frac{w_i}{\rho_{th,i}}}{\sum_{n=1}^{N}\left(\frac{w_n}{\rho_{th,n}}\right)} \tag{16}$$

with the theoretical density ρ_{th}:

$$\rho_{th} = \frac{Z * M}{V_{cell} * N_A} \tag{17}$$

Here Z describes the formula units, M the molar mass, V_{cell} the volume of the cell and N_A the Avogadro constant.

Although the volume fractions (from the XRD) are actually compared to area fractions (from the light microscope), they should yield similar values for the total phase fraction.

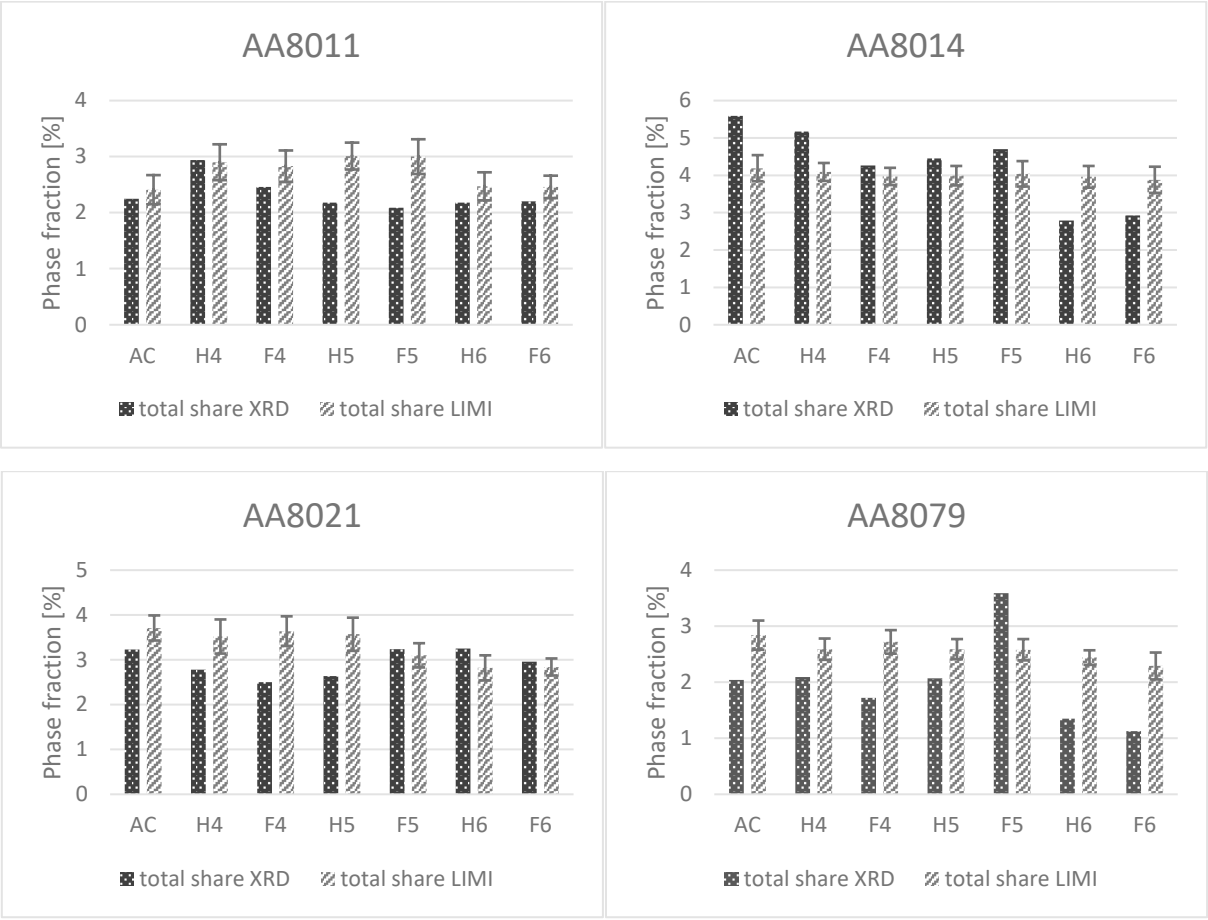

Figure 58: Comparison of the total phase fraction determined by XRD (bulk samples) and the ImageJ Analysis

When comparing the total area fractions of the ImageJ Analysis and the bulk sample measurements by XRD, a certain deviation has to be expected. The first obvious point to mention is that the XRD evaluation only has limited precision for phases that are present in very small quantities (<10 %), as mentioned in chapter 4.2.4. Any quantitative result obtained from the XRD analysis in the range of the phase fractions given above has to be interpreted with utmost care.

Furthermore, the XRD result depends on the evaluation with HighScore Plus i.e. the quality of the fitting procedure, which is increasingly difficult for small peaks such as those in the bulk samples.

With respect to the evaluation with ImageJ, a high number of pictures on the one hand and a comparably small standard deviation on the other hand is observed. Hence, it can be concluded that this value is at least more trustworthy that the XRD evaluation of the bulk samples.

6.2.2 The bulk samples

For the bulk samples, the as-cast states were examined, as well as the half times and the full times of each temperature. Figure 59 shows the relative amounts of all intermetallic phases in the bulk samples (all phases except the aluminium matrix) as determined by XRD to allow the comparison of the bulk samples with the powder samples.

Figure 59: Results of the XRD analysis of the bulk samples (based on wt.%)

It should be noted here, that $Al_6(Fe,Mn)$ is also present in AA8021 F4, but due to the fact, that the peak is too small to be evaluated with HighScore Plus, the phase is not shown in Figure 59.

The absolute values of the XRD measurement of the bulk samples can be found in the appendix 13.5.1.

6.2.3 The powders

In the XRD analysis of the powders, the as-cast states and the fulltime samples were analysed. An exception is the alloy AA8011 – in this case the AA8011 H6 sample was also analysed because a possible error had occurred in the extraction method of AA8011 F6, as already mentioned in chapter 4.2.4.

The exact values of the phase quantities can be found in the appendix 13.5.2. A graphical representation of these quantities is given in Figure 60 below.

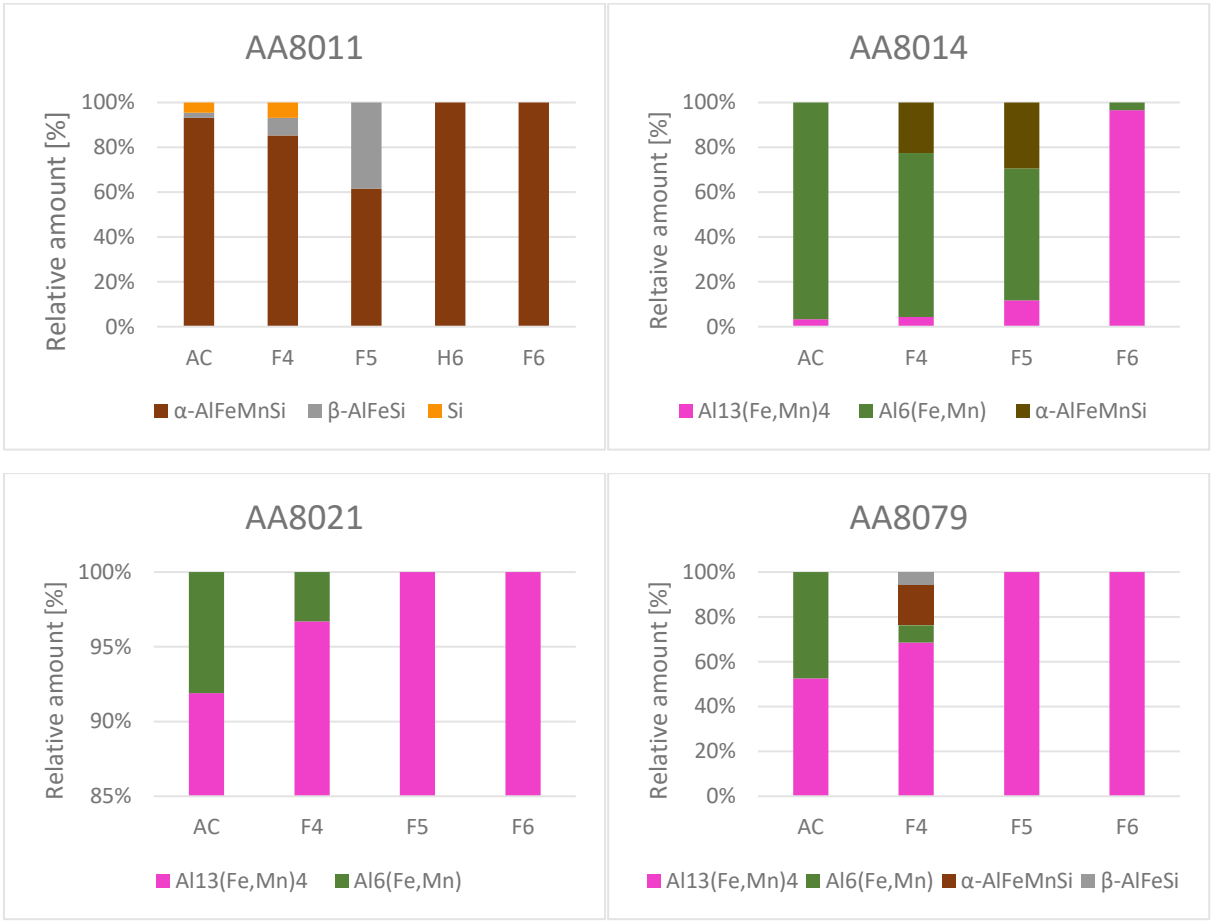

Figure 60: Results of the powders (based on wt.%)

The quantity of the single phases of the two different XRD analysis (bulk sample and powders) mostly agrees. The only exceptions are AA8014 F4 and AA8079 AC. Here the phases occur in other ratios depending on the bulk samples and the powders. However, since the powder analysis is more accurate, this measurement is used as a reference for the phase quantity.

6.3 Dispersoids

The dispersoids were partially visible in some unetched light microscope images, as exemplified for AA8011 H5 in Figure 61. Therefore, it was decided to etch the surfaces with hydrofluoric acid for all full-time samples to get an overview for which states dispersoids are present.

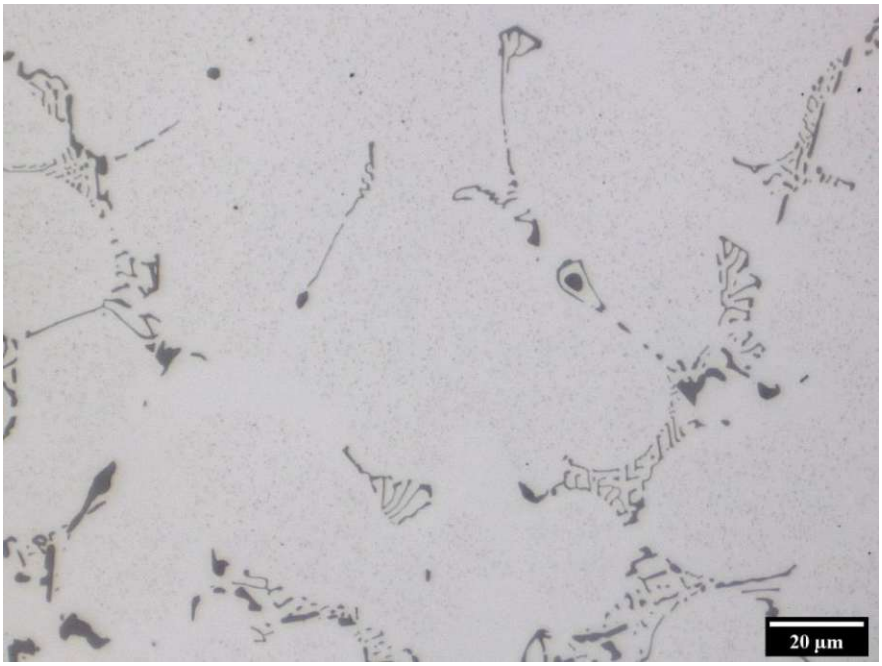

Figure 61: Dispersoids in unetched light microscope image (AA8011 H5)

The light microscope images of the samples, etched with HF, can be found in the appendix 13.9. According to etchings with HF, dispersoids are present in the following fulltime samples:

Sample	Dispersoids present	Sample	Dispersoids present
AA8011 F4	Yes	AA8021 F4	Uncertainty
AA8011 F5	Yes	AA8021 F5	Few dispersoids
AA8011 F6	Sporadically	AA8021 F6	No
AA8014 F4	Yes	AA8079 F4	Yes
AA8014 F5	Yes	AA8079 F5	Yes
AA8014 F6	No	AA8079 F6	Sporadically

Table 19: Present dispersoids in the full-time samples

Furthermore, SEM recordings were also taken with the BSE Detector, which can be seen for AA8011 H5 in Figure 62.

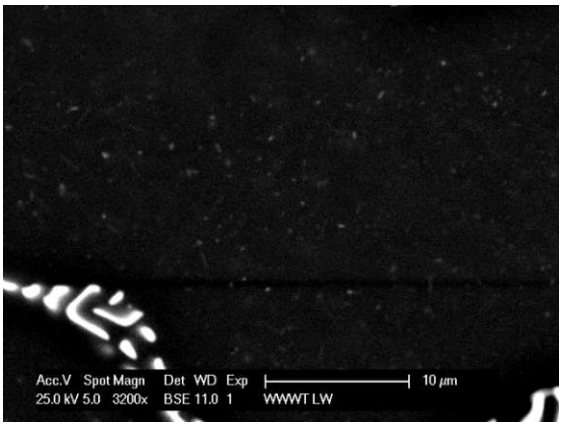

Figure 62: Dispersoids in an unetched SEM image (AA8011 H5)

6.4 Unexpected features

In the light microscope images of some unetched samples the core regions of the constituents appear darker.

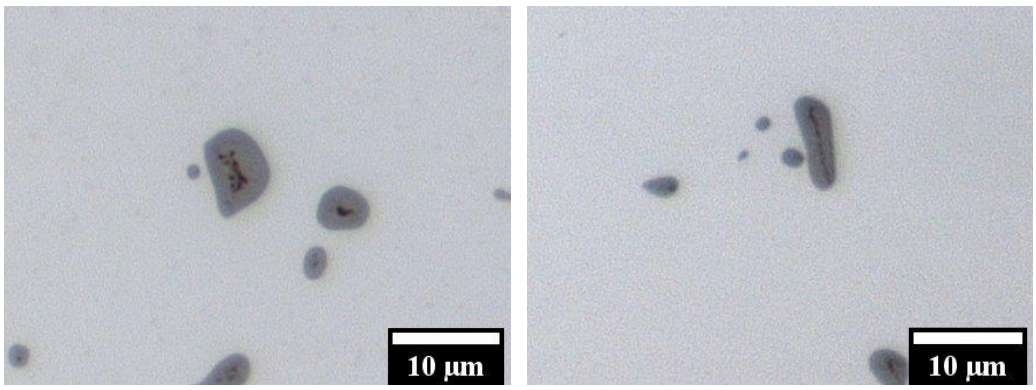

Figure 63: Dark regions in the middle of the phases, left: AA8011 H6, right: AA8011 F6

Figure 63 shows the core regions of the phases in AA8011. In this alloy, they occur both: at half time and full time at 600°C.

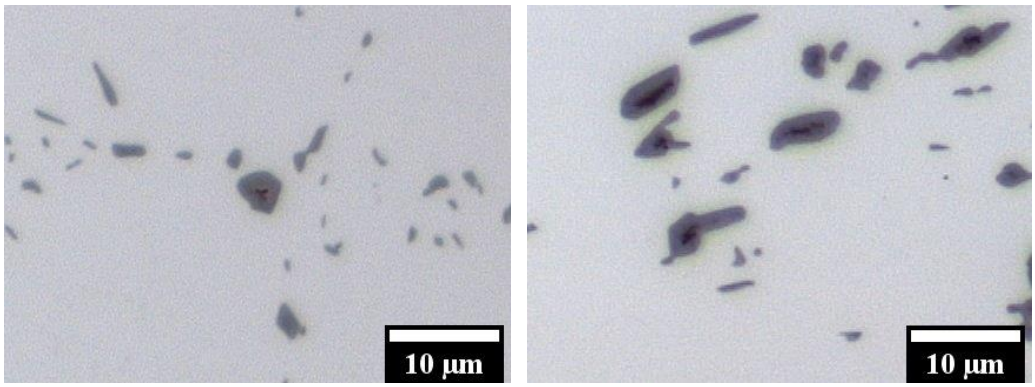

Figure 64: Dark regions in the middle of the phases, left: AA8079 F6, right: AA8021 F6

In AA8079 F6 and AA8021 F6 the dark core regions also appear, as shown in Figure 64. In summary, these dark regions are found in the samples AA8011 H6, AA8011 F6, AA8021 F6 and AA8079 F6.

To examine these areas, SEM images were taken with the SE detector. The alloy AA8011 H6 is shown in Figure 65. In the left picture spheroidized α-AlFeMnSi precipitates can be seen, which contain lighter areas in the centre. The close up image is on the right. The different regions of a selected precipitate were examined using EDX.

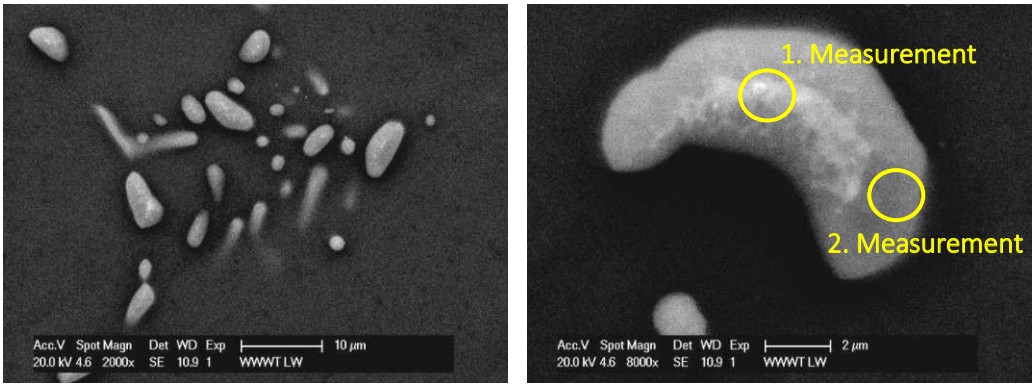

Figure 65: SEM images of AA8011 H6

The EDX measurement of the core region (1. Measurement) is given in Table 20. The result for the slightly darker area (2. Measurement) is given in Table 21.

Element	wt.%	at.%
Al	59.69	72.22
Si	7.57	8.8
Mn	1.71	1.02
Fe	27.89	16.3
Ni	0.92	0.51
Cu	2.22	1.14

Table 20: EDX result of the 1. measurement of AA8011 H6

Element	wt.%	at.%
Al	66.4	77.18
Si	7.11	7.94
Mn	1.44	0.82
Fe	25.06	14.07

Table 21: EDX result of the 2. measurement of AA8011 H6

The analysis by SEM and EDX was also carried out for the alloy AA8011 F6. The following images were taken, using the SE-detector.

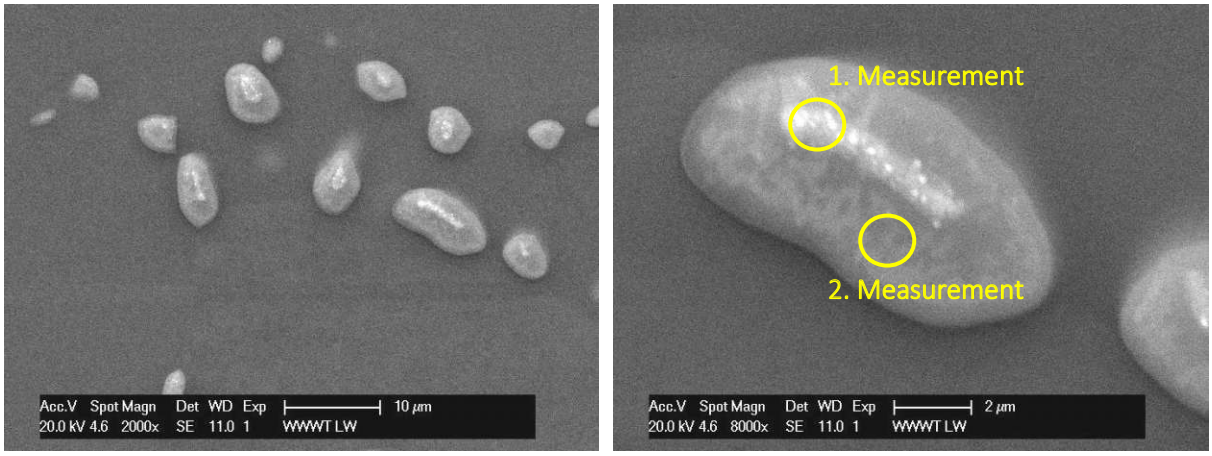

Figure 66: SEM images of AA8011 F6

Element	wt.%	at.%
Al	58.89	72.54
Si	6.32	7.48
Mn	1.73	1.05
Fe	22.73	13.53
Cu	10.34	5.41

Table 22: EDX result of the 1. measurement of AA8011 F6

The 2. measurement of the sample AA8011 F6 again showed the same values as for the α-AlFeMnSi phase, but no Cu or Ni traces were found here. Unfortunately, the values of this measurement were not saved, because directly after the measurement the cathode of the SEM broke, leading to a malfunction that did not allow to store the measured data. This is also the reason why the difference between the core region and the outer region was not measured in the other two samples AA8021 F6 and AA8079 F6.

7. Discussion

7.1 Comparison of the MatCalc equilibrium calculation with experimental and literature data

In this chapter the experimental results of the 4 alloys, as well as already literature data from various experimental studies and simulations with other software tools are compared to the current MatCalc equilibrium calculations.

The bar charts are designed as follows: for experimental studies, the temperature range in which a given phase was confirmed to be stable is coloured and opaque. Conversely, if the phase is known to be unstable, the respective temperature range is left blank. Regions of uncertainty are coloured and transparent. This includes e.g. the region of the experiments in this work between the last temperature at which a phase was found and the first temperature at which it could not be detected. It should be noted here that the melting point of pure aluminium (660°C) was assumed as the upper limit of the uncertainty ranges for all 4 different alloys. For simulations the same concept applies, whereas transparent regions occur only if the respective calculations did not cover the given temperature range. Furthermore, a uniform colour code was used for the following figures, where dark blue was used for the experimental results from this work, green for the MatCalc equilibrium calculations, yellow for any experimental data from the literature and grey for simulations with other software tools from the literature.

7.1.1 AA8011

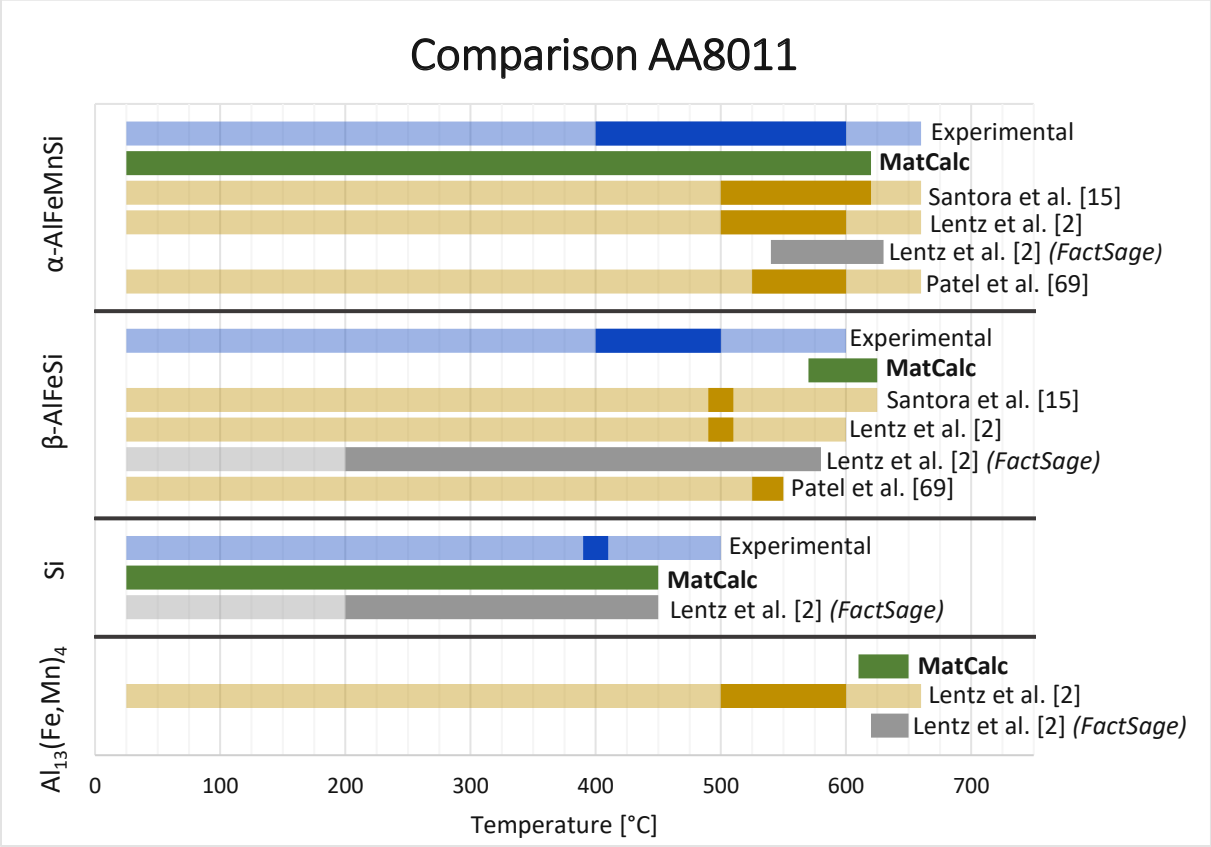

Figure 67: Comparison of the MatCalc equilibrium calculation with experimental and literature data (AA8011)

As shown in Figure 67, 4 different phases are found in AA8011, according to the simulations & experimental data. Comparing the data for α-AlFeMnSi, it can be seen that the MatCalc equilibrium calculation is consistent with the experimental investigation in this thesis, as well as with the literature of Santora et al. [15], Lentz et al. [2] and Patel et al. [69]. The only difference here is the stability range for α-AlFeMnSi in the FactSage simulation of Lentz et al. [2], which starts at appr. 530°C. This was calculated with 0.8 wt.% Fe and in the present alloy 0.88 wt.% Fe was measured, while the remaining composition is identical. Possibly, the discrepancy is due to this fact.

The stability range for β-AlFeSi is quite clear when comparing the experimental data with investigations by Santora et al. [15] and Lentz et al. [2]. It should be noted here that the transparent part of the bar chart of Santora et al. is drawn up to 620°C and the bar chart of the experimental data of Lentz et al. is drawn till 600°C, since they performed the next annealing step at these temperatures, whereby the β-AlFeSi was not found in both cases. According to Patel et al. [69], at a temperature of 575°C the phase transformation from β-AlFeSi to α-AlFeMnSi takes place, which is in accordance with the experimental data of this thesis. The MatCalc equilibrium calculation for β-AlFeSi has a shorter stability range, which is located at higher temperatures compared to other sources. Here, the experimental data is given more credence, as various literature sources support the existence of the β-AlFeSi phase its range.

According to the FactSage simulation of Lentz et al. [2] Si has a stability range that extends from room temperature to about 450°C, which is equivalent to the MatCalc equilibrium calculation. For temperatures below 450°C, no experimental data on 8xxx series was found in the literature. This is congruent with the experimental data, where Si is still stable at 400°C, but no longer stable at 500°C.

The phase $Al_{13}(Fe,Mn)_4$ was experimentally verified at 500°C and 600°C by Lentz et al. [2], but this may be due to the short holding times at the homogenisation temperatures in this paper, meaning that a complete equilibrium state has not been reached yet. The discussion in this paper also mentions, that $Al_{13}(Fe,Mn)_4$ is usually not thermodynamically stable in this range according to thermodynamic simulations. No homogenisation treatments were carried out in the range above 600°C within the framework of this thesis, so no comparison can be made for temperatures above 600°C with the MatCalc equilibrium calculation based on experimental data. The only point of reference here is the FactSage simulation by Lentz et al. [2], in which $Al_{13}(Fe,Mn)_4$ becomes stable again at high temperatures (around 610°C-650°C), which supports the equilibrium calculation of MatCalc.

7.1.2 AA8014

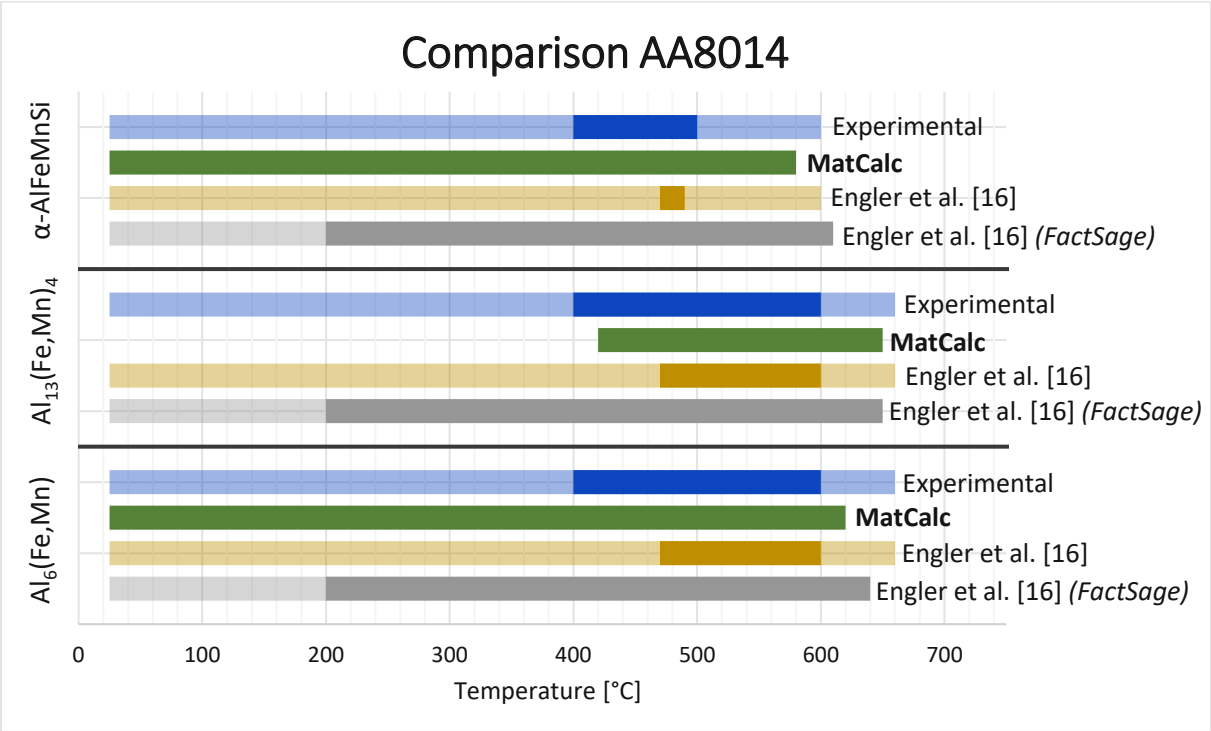

Figure 68: Comparison of the MatCalc equilibrium calculation with experimental and literature data (AA8014)

In Figure 68 it should be noted that the experimental data of Engler et al. [16], as well as their simulation with FactSage were investigated with the material AA8006. However, the chemical composition of AA8006 (Si=0.12 wt.%, Fe=1.54 wt.%, Mn=0.5 wt.%) differs only slightly from the composition of the investigated sample AA8014. The main difference is the manganese content, which is 0.42 wt.% for AA8014 and 0.5 wt.% for AA8006.

If the MatCalc equilibrium calculation of the α-AlFeMnSi phase is compared with the experimental data and the work of Engler et al. [16], the stability ranges are approximately the same. One deviation is the FactSage simulation, where the α-AlFeMnSi phase is still stable at 600°C but was not found in the experimental investigations of AA8014. This may be due to the higher manganese content in AA8006. Furthermore, it should be noted that Engler et al. [16] only performed homogenisation annealing at 480°C and at 600°C, so no further conclusions can be made in the range in between. However, the α-AlFeMnSi phases found at these temperatures matches the MatCalc equilibrium calculation.

For $Al_{13}(Fe,Mn)_4$, the experimental data have largely the same stability range as the data from the literature. Also, the stability range for $Al_{13}(Fe,Mn)_4$ at 420°C-650°C from MatCalc is congruent with the data. However, according to the MatCalc equilibrium calculation, $Al_{13}(Fe,Mn)_4$ is only stable above 420°C, which cannot be confirmed by the experiments, as $Al_{13}(Fe,Mn)_4$ could also be detected in equilibrium annealing at 400°C.

The stability range of $Al_6(Fe,Mn)$ extends from room temperature to over 600°C, both in the experimental data and in the literature data of Engler et al. [16]. This is congruent with the MatCalc equilibrium calculation.

7.1.3 AA8021

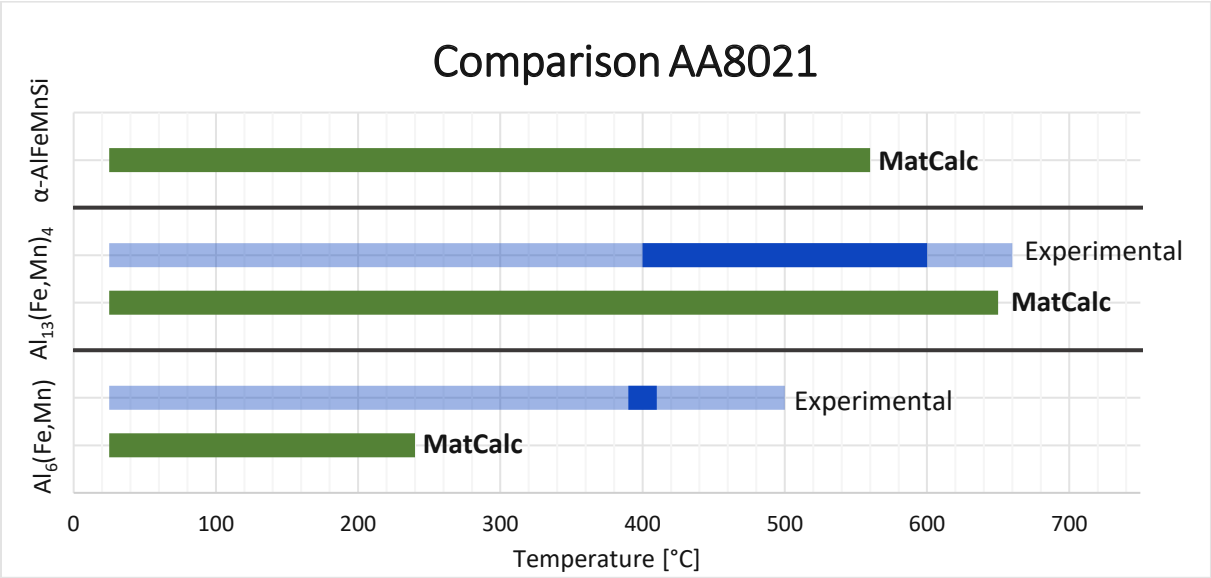

Figure 69: Comparison of the MatCalc equilibrium calculation with experimental and literature data (AA8021)

For the alloy AA8021, the MatCalc equilibrium calculation and the experimental data are shown in Figure 69. According to MatCalc, the α-AlFeMnSi phase should be stable beginning at room temperature up to 560°C. This is contradicted upon comparison with the experimental characterisation methods, as this phase was not detected at any temperature. As the experimental data is expected to be more trustworthy, it can be assumed that the α-AlFeMnSi phase is not stable in this temperature range.

The $Al_{13}(Fe,Mn)_4$ phase has nearly the same stability range for MatCalc and the experimental data. Furthermore, the MatCalc equilibrium calculation describes a stability range of 0-240°C for $Al_6(Fe,Mn)$. According to the experimental data, $Al_6(Fe,Mn)$ should still be present at 400°C. Due to the fact, that $Al_6(Fe,Mn)$ is present in larger amounts in the as-cast state and the quantitative amount of this phase decreases at 400°C, the possibility that $Al_6(Fe,Mn)$ is eventually not stable at 400°C should not be ignored. This may be due to very slow kinetics, so that $Al_6(Fe,Mn)$ is actually unstable at 400°C and 2 weeks are not enough to establish a state of equilibrium. This could be clarified either by increasing the holding time or by using a sample that has been first annealed at a higher temperature (with no residual $Al_6(Fe,Mn)$), which is then annealed at 400°C afterwards.

According to e.g. Shakiba et al. [70] and Santora et al. [15] the transformation from $Al_6(Fe,Mn)$ to $Al_{13}(Fe,Mn)_4$ must take place in the temperature range between 500-560°C via a dissolution-reprecipitation mechanism, which supports the results of the present thesis. Another reference regarding the dissolution of the metastable phase is the work of Kim et al. [71]. The authors investigated rapidly solidified Al-Fe alloys with 5 at.% and 10 at.% Fe, in which microquasicrystalline phases decompose into $Al_6(Fe,Mn)$ over the temperature ranges from 340-420°C and 390-450°C, respectively. Furthermore, the $Al_6(Fe,Mn)$ decomposes into the stable phase $Al_{13}(Fe,Mn)_4$ over the temperature range of 480-590°C and 480-560°C for the alloys with 5 at.% Fe and 10 at.% Fe, respectively. It should be noted that there is less Fe in AA8021, but nevertheless the temperature ranges support the experimental data found in this thesis.

7.1.4 AA8079

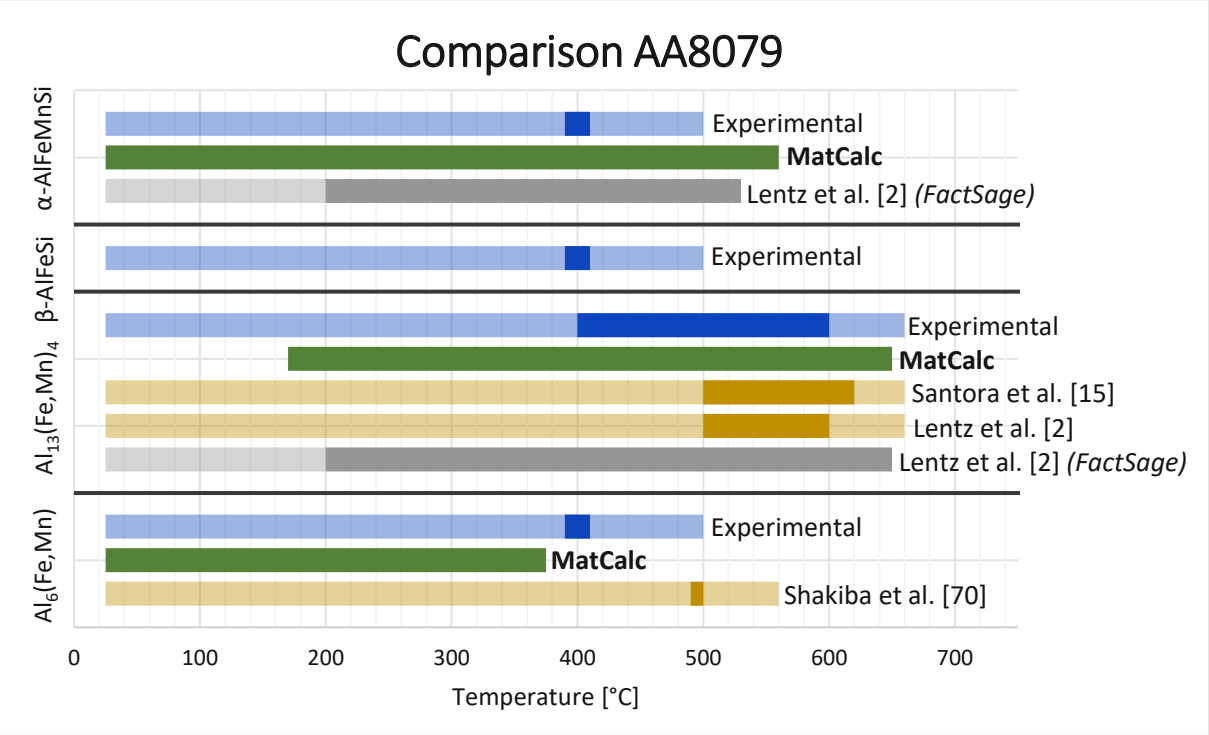

Figure 70: Comparison of the MatCalc equilibrium calculation with experimental and literature data (AA8079)

For the alloy AA8079, four different stable phases were found experimentally for the respective equilibrium temperatures, as shown in Figure 70.

The α-AlFeMnSi phase is still stable at 400°C according to the characterisation methods in this work, while it is no longer present at 500°C. According to the MatCalc equilibrium calculation, it has a stability range starting at room temperature up to 560°C. Here, the two stability ranges contradict each other. Furthermore, experiments at 400°C confirmed that the β-AlFeSi phase should be stable, which does not appear in the MatCalc equilibrium calculation. It should be noted, that Santora et al. [15] have not done equilibrium annealing at 400°C, therefore there is no experimental literature data available for this temperature. Lentz et al. [2] carried out a FactSage simulation with a content of 0.8 wt.% Fe, which is slightly lower than in AA8079 (Fe=1.01 wt.%). This resulted in a stability range of α-AlFeMnSi from 200° to about 530°C. In the experiments, no more α-AlFeMnSi was found at 500°C, which may be attributed to the deviating chemical composition.

The $Al_{13}(Fe,Mn)_4$ phase of the MatCalc equilibrium calculation agrees with the experimental data at all three temperatures. Furthermore, the stability range of Santora et al. [15] is also congruent with the experimental data and the MatCalc equilibrium calculation. Also Lentz et al. [2] described a stability range of $Al_{13}(Fe,Mn)_4$ up to 600°C.

Since the phase content of $Al_6(Fe,Mn)$ of the as-cast sample is quite high compared to the equilibrium annealing at 400°C, there is again the possibility that $Al_6(Fe,Mn)$ is unstable at 400°C, but the slow kinetics lead to a residual amount even after two weeks - as already mentioned for the alloy AA8021. In principle, the transformation from $Al_6(Fe,Mn)$ to $Al_{13}(Fe,Mn)_4$ takes place in a temperature range that is in accordance with the results of Shakiba et al. [70] and Kim et al. [71].

7.1.5 Experimental data from the literature

The paper of Lacaze et al. [14] is one of the references for the α-AlFeMnSi phase of the thermodynamic database used in this thesis, so the following simulations provide a good comparison, whether MatCalc describes the range of the equilibrium phases as intended. The data of Lacaze et al. [14] allows many different combinations with the Fe content, but it should also be noted that the experimental microstructure map (Figure 18 in this thesis) only start at 550°C and no statements can be made below this temperature. Three different equilibrium calculations were carried out with MatCalc. The chemical compositions of these equilibrium calculations are always 1 wt.% Mn, 3 wt.% Si and different iron contents.

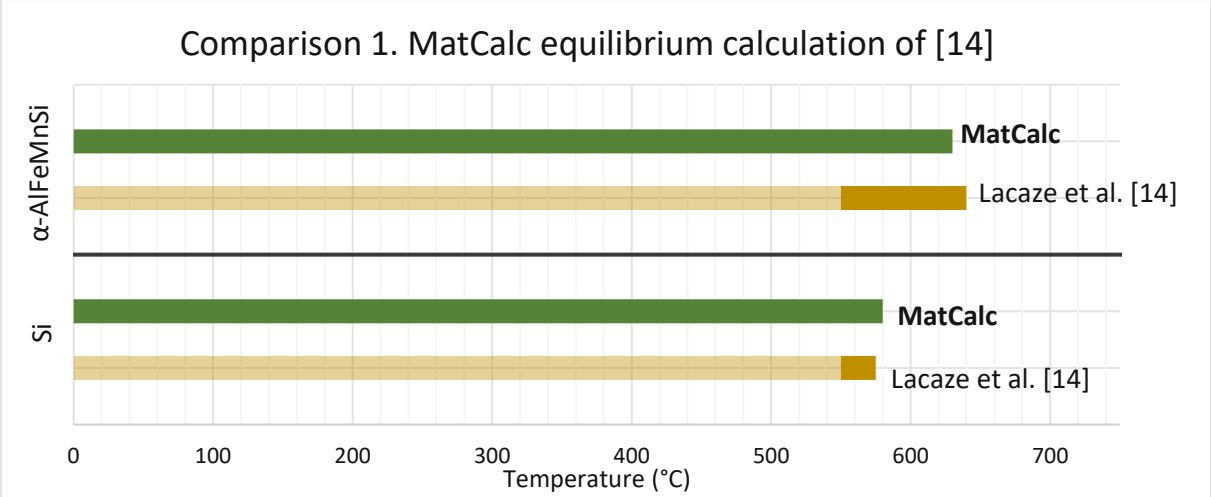

Figure 71: Comparison of the MatCalc equilibrium calculation with the literature data of [14]

In the first MatCalc equilibrium calculation with the lowest Fe content of 0.5 wt.%, the stability ranges of α-AlFeMnSi and Si agrees completely with the literature (above 550°C), as it can be seen in Figure 71.

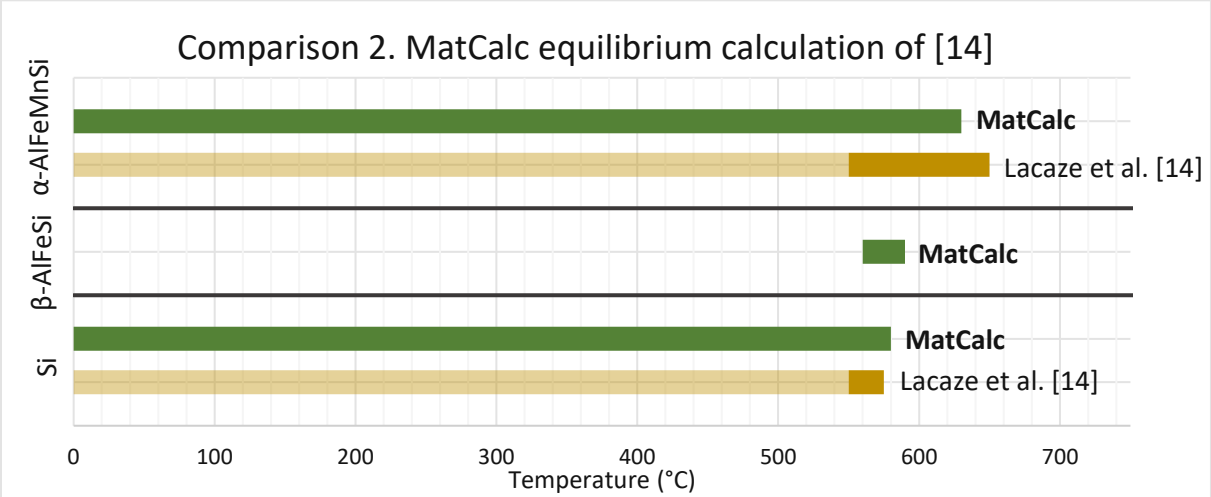

Figure 72: Comparison of the MatCalc equilibrium calculation with the literature data of [14]

In the second MatCalc equilibrium calculation (Figure 72) with 1.0 wt.% Fe, the stability ranges of α-AlFeMnSi and Si are analogous to the previous figure. The only change is that β-AlFeSi is stable in the range of 560-590°C in small amounts. Compared to the experimental map, it is not congruent as no β-AlFeSi occurs here.

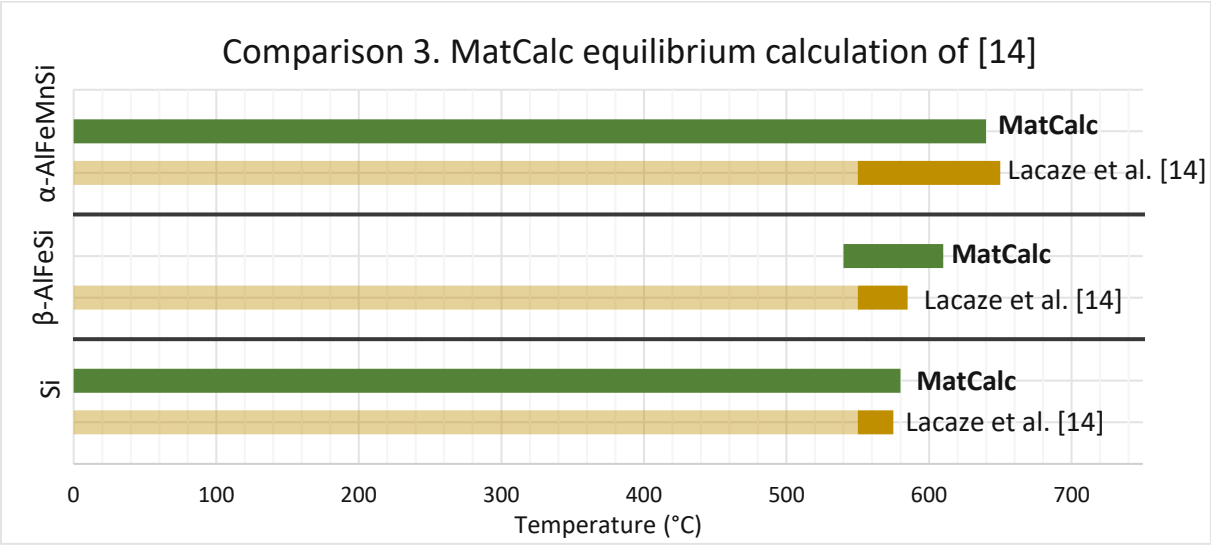

Figure 73: Comparison of the MatCalc equilibrium calculation with the literature data of [14]

In Figure 73 the third equilibrium calculation by MatCalc (1.5 wt.% Fe) can be seen, which is again almost identical to the previous figures. The only difference is a larger part of β-AlFeSi in the range of 540-610°C. According to Lacaze et al. [14] the β-AlFeSi phase is stable above 550°C, but not up to such a high temperature.

Basically, the MatCalc equilibrium calculations are very similar to the experimental data of Lacaze et al. [14], so the equilibrium calculation with MatCalc describes the range of nearly all equilibrium phases as intended.

7.2 Dispersoids

Dispersoids typically form from the supersaturated matrix during homogenisation treatments [15]. They were found in some unetched images taken with the light microscopy. It was therefore decided to etch the samples with hydrofluoric acid. Initially, all samples were etched with 0.5% HF for 5s. However, as the etching sometimes did not affect the whole surface of the sample to be examined, some samples were etched longer. It is possible, that small areas of the samples still not show any dispersoids after the etching. This could be due to an orientation dependency of the reaction between the surface and the etchant.

The chemical compositions of the dispersoids were not investigated in detail, as this would go beyond the scope of the thesis and require more precise measurements using e.g. TEM or EPMA. Therefore, the existing literature must be taken as a basis regarding the chemical composition [2,15,16]:

- Engler et al. [16] assigned the dispersoids in AA8006 to α-AlFeMnSi. Since the chemical composition of AA8006 is very similar to those of AA8014, these two alloys can be compared to each other. This reference also describes a strong precipitation of α-AlFeMnSi dispersoids at low homogenisation temperatures. For temperatures above 500°C, the α-AlFeMnSi dispersoids re-dissolve, leading to a re-increase of Fe, Mn and Si in solid solution and consequently a growth of the pre-existing constituent phases [16]. This can also be observed in the experimental results of the AA8014 alloy, where many dispersoids are visible at 400°C and 500°C, but at 600°C the dispersoids are no longer present. The α-AlFeMnSi phase is also congruent with the equilibrium phases found at 400°C and 500°C.
- According to Lentz et al. [2], dispersoids were found in AA8011 as well as in AA8079. In AA8011, the dispersoids were identified as α-AlFeMnSi dispersoids at both 500°C and 550°C. This is in accordance with the experiments in this work, because α-AlFeMnSi is found at these temperatures, and at 500°C dispersoids were visible in the etched light micrographs. At 600°C, only few dispersoids were visible, which could be due to the fact, that the dispersoids dissolve in favour of the primary phases.
- In the alloy AA8079, α-AlFeMnSi and also $Al_{13}(Fe,Mn)_4$ dispersoids were found at 500°C, while at 550°C only $Al_{13}(Fe,Mn)_4$ dispersoids were identified [2]. The experimental data of this thesis is congruent with this literature in relation to the existence of dispersoids at 500°C. Furthermore, at 600°C there are only few to no dispersoids left, which could be due to dissolution in favour of the primary phases.
  However, in the XRD analysis (which also measures the dispersoids) only $Al_{13}(Fe,Mn)_4$ was found at 500°C, whereas α-AlFeMnSi is no longer stable here according to the experiments. This could either be, because the dispersoids are present in such small amounts that the XRD does not measure them, or because of the difference in the chemical composition of the two different AA8011.
- Furthermore, according to Santora et al. [15], the highest volume fraction of dispersoids in AA8011 and AA8079 is found at the heat treatment with 500°C [15]. Since the authors performed homogenisation annealing at 500°C and 620°C, no statement can be made about the volume fraction of the dispersoids at 400°C. If the different heat-treated samples of AA8011 and AA8079 are compared, a few more dispersoids were found in the full-time samples of 400°C than in the samples of 500°C, whereas at 600°C only sporadic dispersoids were visible. Accordingly, the literature agrees with the experiments in this work.

7.3 Unexpected features

In the light microscope images of the unetched samples, darker regions were found in the inside of some phases. These regions appear in alloys with high temperatures (600°C) and long holding times (1 week – exception AA8011 H6 after 3 days). This was observed in the alloys AA8011 F6, AA8011 H6, AA8021 F6 and AA8079 F6. According to the EDX measurements on precipitates in AA8011 H6 and AA8011 F6, traces of Cu and Ni are present in the core regions and also minimal deviations of the chemical homogeneity compared to the outer areas. The Cu-bearing regions in AA8011 might be due to the increased Cu content of 0.012 wt.% of the alloy, which is higher than that of the other alloys. For a more accurate measurement of the chemical composition, measurements with TEM would have to be carried out.

In the thesis of Liu [72], similar inhomogeneous distributions of the chemical composition were observed in individual dispersoids. The main difference to the present thesis is the scale (dispersoids vs. constituents) as well as the alloying system (6xxx series vs. 8xxx series). A higher Mn concentration was measured in the central area of the dispersoid, while the change in Fe concentrations across the dispersoid showed no obvious trend [72].

Another reference is provided by Muggerud et al. [73], who also measured chemical inhomogeneities in dispersoids in 3xxx alloys. The edges of the dispersoids contained more Fe than the central part. The authors argued that the α-Al(Fe,Mn)Si dispersoids have precipitated as α-AlMnSi without Fe and as they grow, Fe diffuses into the precipitates. The significant gradient of Fe across the diameter was due to the slow diffusion of Fe and Mn into the phases [73].

In order to make more precise statements corresponding to these core regions in the 8xxx aluminium alloys, further investigations with e.g. TEM or EPMA would have to be carried out.

8. Summary and Conclusions

The initial reason for this thesis was a certain ambiguity with respect to the stability ranges and quantities of different phases in the literature data on 8xxx series alloys. The investigations aimed at clarifying the equilibrium conditions at three different temperatures (400°C, 500°C and 600°C) for four different aluminium alloys, to provide a sufficiently large matrix for the optimization of the thermodynamic database in MatCalc for 8xxx series alloys.

The investigations of the individual samples with the different characterisation methods were congruent and the equilibrium states were reached in nearly every sample. In most samples any minor differences between the phases in the half-time samples and the full-time rehearsals are most likely due to measurement inaccuracies so that (at least at 500°C and 600°C) it can safely be assumed that equilibrium has been reached in every sample. The only specimen for which there are still uncertainties regarding the equilibrium are AA8021 F4 and AA8079 F4. It is possible that the kinetics at 400°C are just slow enough so that unstable phases from the as-cast state are still present. To clarify this would require further investigation with either a longer holding time or another upstream equilibrium annealing at higher temperatures to get the potentially metastable phases out of the initial condition.

An important point is the successful use of the phenol method to dissolve the aluminium matrix for 8xxx series alloys, which was previously used for 6xxx alloys [61,62]. By using this method, the equilibrium phases could be reliably identified based on the crystal structure using XRD. The comparison with existing literature on 8xxx Al alloys is widely in accordance with the experimental results. The present thesis has shown the existing discrepancies between the MatCalc equilibrium calculations and the experimental from this work as well as the literature data. It has been confirmed that the thermodynamic database needs to be revised for the 8xxx series alloys.

Some questions regarding the influence of dispersoids and the chemically altered core regions remain, which occur inside the phases at high temperatures for certain alloys. These questions arose during the course of this work and give way to additional investigations.

In conclusion it can be said that the investigations of the four materials with different characterization methods provide reasonable, congruent results regarding the constituent equilibrium phases and the phase quantities. They offer complementary data on stability ranges which, in combination with the existing literature, should allow for an improvement of the CALPHAD description of the Al-Fe-Mn-Si system in MatCalc.

9. References

[1] L. Sweet, S.M. Zhu, S.X. Gao, J.A. Taylor, M.A. Easton, The Effect of Iron Content on the Iron-Containing Intermetallic Phases in a Cast 6060 Aluminum Alloy, Metall and Mat Trans A 42 (2011) 1737–1749.

[2] M. Lentz, G. Laptyeva, O. Engler, Characterization of second-phase particles in two aluminium foil alloys, Journal of Alloys and Compounds 660 (2016) 276–288.

[3] H.W.L. Phillips, The constitution of alloys of aluminium with manganese, silicon, and iron. I. - The binary system: aluminium-manganese. II. - The ternary systems: aluminium-manganese-silicon and aluminium-manganese-iron, Journal of the Institute of Metals 69 (1943) 275–316.

[4] H.W.L. Phillips, P.C. Varley, The constitution of alloys of aluminium with manganese, silicon and iron. III. - The ternary system: aluminium-silicon-iron. IV. - The quarternary system: aluminium-manganese-silicon-iron., Journal of the Institute of Metals 69 (1943) 317–350.

[5] J.G. Barlock, L.F. Mondolfo, Structure of Some Aluminium-Iron-Magnesium-Manganese- Silicon Alloys, International Journal of Materials Research 66 (1975) 605–611.

[6] L.F. Mondolfo, Metallography of Aluminium Alloys, John Wiley & Sons, Inc., New York, 1943.

[7] L.F. Mondolfo, Aluminium Alloys: Structrure and Properties, Butterworth-Heinemann, 1976.

[8] N.A. Belov, Eskin D.G., A.A. Aksenov, Multicomponent Phase Diagrams: Applications for Commercial Aluminium Alloys, 1st Edition, Elsevier Science, 2005.

[9] G. Davignon, B. Verlinden, L. Delaey, A. Serneels, An isothermal section at 550 °C in the Al-Rich corner of the Al-Fe-Mn-Si system, Metall and Mat Trans A 27 (1996) 3357–3361.

[10] E. Balitchev, T. Jantzen, I. Hurtado, D. Neuschütz, Thermodynamic assessment of the quaternary system Al–Fe–Mn–Si in the Al-rich corner, Calphad 27 (2003) 275–278.

[11] A. Zakharov, I. Gul'din, A. Arnol'd, Y. Matsenko, Izvestiya Akademii Nauk SSSR, Seriya Metally (4) (1989) 214–218.

[12] A. Zakharov, I. Gul'din, A. Arnol'd, Y. Matsenko, Izvestiya Vysshikh Uchebnykh Zavedenii, Tsvetnye Metally (4) (1988) 89–94.

[13] A. Zakharov, I. Gul'din, A. Arnol'd, Y. Matsenko, Izvestiya Vysshikh Uchebnykh Zavedenii, Tsvetnye Metally (4) (1989) 78–81.

[14] J. Lacaze, L. Eleno, B. Sundman, Thermodynamic Assessment of the Aluminum Corner of the Al-Fe-Mn-Si System, Metall and Mat Trans A 41 (2010) 2208–2215.

[15] E. Santora, R. Morak, Microchemistry Evolution for 8xxx Alloys by Homogenization, in: L. Perander (Ed.), Light Metals 2021, Springer International Publishing, Cham, 2021, pp. 263–269.

[16] O. Engler, G. Laptyeva, N. Wang, Impact of homogenization on microchemistry and recrystallization of the Al–Fe–Mn alloy AA 8006, Materials Characterization 79 (2013) 60–75.

[17] H. Schumann, Metallographie, 12. Auflage, VEB Deutscher Verlag für Grundstoffindustrie, Leipzig, 1989.

[18] F. Ostermann (Ed.), Anwendungstechnologie Aluminium, Springer Berlin Heidelberg, Berlin, Heidelberg, 2014.

[19] F.A. Brockhaus Mannheim (Ed.), Brockhaus Enzyklopädie, 19., 1987.

[20] Y. Zhang, Y. Qi, J. Li, Aluminum Mineral Processing and Metallurgy: Iron-Rich Bauxite and Bayer Red Muds, in: K. Omar Cooke (Ed.), Aluminium Alloys and Composites, IntechOpen, 2020.

[21] https://www.chemie-schule.de/KnowHow/Bayer-Verfahren (accessed: December 2021).

[22] A. Hoda, J. Donizak, J. Nonell, Z. Kolenda, On the entropy generation in aluminium electrolysis cell, TMS Light Metals (2006).

[23] G. Gottstein, Physikalische Grundlagen der Materialkunde, Springer Berlin Heidelberg, Berlin, Heidelberg, 2007.
[24] E. Hornbogen, H. Warlimont, Metalle: Struktur und Eigenschaften der Metalle und Legierungen, 6., aktualisierte Auflage, Springer Vieweg, 2016.
[25] D.A. Porter, K.E. Easterling, Phase Transformations in Metals and Alloys, Springer US, Boston, MA, 1992.
[26] E. Kozeschnik, Modeling Solid-State Precipitation, Momentum Press, 2012.
[27] U.R. Kattner, The Calphad method and its role in material and process development, Tecnologia em metalurgia, materiais e mineracao 13 (2016) 3–15.
[28] N. Saunders, A.P. Miodownik, CALPHAD (Calculation of Phase Diagrams): A Comprehensive Guide, Pergamon Press, 1998.
[29] H.L. Lukas, S.G. Fries, B. Sundman, Computational Thermodynamics: The CALPHAD Method, Cambridge University Press, 2007.
[30] W. Hufnagel, Aluminium-Taschenbuch, 14. Auflage, 1983.
[31] E. Santora, J. Berneder, F. Simetsberger, M. Doberer, Mechanical Properties Evolution for 8xxx Foil Stock Materials by Alloy Optimization—Literature Review and Experimental Research, in: C. Chesonis (Ed.), Light Metals 2019, Springer International Publishing, Cham, 2019, pp. 365–372.
[32] W. Schneider, G. Laptyeva, M. Lentz, K.F. Karhausen, Through Process Microchemistry Effects on the Properties of 8xxx Sheet, MSF 706-709 (2012) 323–328.
[33] M. Vončina, K. Kresnik, D. Volšak, J. Medved, Effects of Homogenization Conditions on the Microstructure Evolution of Aluminium Alloy EN AW 8006, Metals 10 (2020) 419.
[34] C.M. Allen, K. O'Reilly, B. Cantor, P.V. Evans, Intermetallic phase selection in 1XXX Al alloys, Progress in Materials Science 43 (1998) 89–170.
[35] T.K. Stürzel, Maßnahmen zur Verbesserung der mechanischen Eigenschaften von Recycling Al-Druckgusslegierungen für Powertrain-Anwendungen, 2015.
[36] Á. Griger, V. Stefániay, Equilibrium and non-equilibrium intermetallic phases in Al-Fe and Al-Fe-Si Alloys, JOURNAL OF MATERIALS SCIENCE 31 (1996) 6645–6652.
[37] G. Gosh, Aluminium-Iron-Silicon, Light Metal systems: Phase diagrams, crystallographic and thermodynamic data (2005) 359–409.
[38] G. Gosh, G. Petzow, G. Effenberg, Ternary alloys, VCH Publisher (1992) 394–437.
[39] M. Marker, Phase-equilibria, structural and physical characterization in the ternary system Al-Fe-Si and the quarternary system Al-Fe-Si-Ti, 2013.
[40] Al-Fe-Si (Aluminium - Iron - Silicon), in: W. Martienssen, G. Effenberg, S. Ilyenko (Eds.), Light Metal Systems. Part 2, Springer Berlin Heidelberg, Berlin, Heidelberg, 2005, pp. 1–51.
[41] V. Raghavan, Al-Fe-Si (Aluminum-Iron-Silicon), J. Phase Equilib. Diffus. 33 (2012) 322–326.
[42] V.G. Rivlin, 12: Critical review of constitution of aluminium–iron–manganese and iron–manganese–silicon systems, International Metals Reviews 28 (1983) 309–337.
[43] G.V. Raynor, Journal of the Institute of metals 70, 1944, pp. 531-542.
[44] Y. Du, Z. Jin, B. Huang, W. Gong, H. Xu, Z. Yuan et al., A thermodynamic description of the Al-Mn-Si system over the entire composition and temperature ranges, Metall and Mat Trans A 35 (2004) 1613–1628.
[45] https://www.chemie.de/lexikon/Intermetallische_Verbindung.html (accessed: December 2021).
[46] Y. Langsrud, Silicon in Commercial Aluminium Alloys - What Becomes of it during DC-Casting?, KEM 44-45 (1991) 95–116.

[47] N. Kuijpers, W.H. Kool, P. Koenis, K.E. Nilsen, I. Todd, S. van der Zwaag, Assessment of different techniques for quantification of α-Al(FeMn)Si and β-AlFeSi intermetallics in AA 6xxx alloys, Materials Characterization 49 (2002) 409–420.
[48] Volgger M., Lichtmikroskopie - Theorie und Anwendung, Wien, 2008.
[49] J. Bauch, R. Rosenkranz, Physikalische Werkstoffdiagnostik, Springer Berlin Heidelberg, Berlin, Heidelberg, 2017.
[50] Light Microscopy Subject Guide, Metallogr. Microstruct. Anal. 2 (2013) 48–52.
[51] L. Reimer, G. Pfefferkorn, Raster-Elektronenmikroskopie, 2., neubearbeitete und erweiterte Auflage, Springer-Verlag, Berlin Heidelberg New York, 1977.
[52] https://oberflaeche.de/wissen/lexikon/begriffe/elektronenmikroskop (accessed: December 2021).
[53] E. Macherauch, H.-W. Zoch, Praktikum in Werkstoffkunde: 91 ausführliche Versuche aus wichtigen Gebieten der Werkstofftechnik, 11. Auflage, Vieweg+Teubner, 2011.
[54] R. Kelsall, I.W. Hamley, M. Geoghegan, Nanoscale Science and Technology, John Wiley & Sons, Inc., 2005.
[55] https://www.wikiwand.com/de/Energiedispersive_R%C3%B6ntgenspektroskopie (accessed: December 2021).
[56] P.W. Hawkes, J.C.H. Spence (Eds.), Science of Microscopy, Springer New York, New York, NY, 2007.
[57] W. Borchardt-Ott, H. Sowa, Kristallographie, Springer Berlin Heidelberg, Berlin, Heidelberg, 2013.
[58] Callister, W.D., Jr., D.G. Rethwisch, Material Science and Engineering: An Introduction, John Wiley & Sons, Inc., 2007.
[59] L. Spieß, G. Teichert, R. Schwarzer, H. Behnken, C. Genzel, Moderne Röntgenbeugung, Vieweg+Teubner, Wiesbaden, 2009.
[60] T. Taguchi, R. Matsuo, T. Mitsunaga, C. Broennimann, E.F. Eikenberry, Novel pixel detector for in-house XRD applications, Acta Crystallogr A Found Crystallogr 64 (2008) C192-C192.
[61] A.K. Gupta, P.H. Marois, D.J. Lloyd, Review of the techniques for the extraction of second-phase particles from aluminum alloys, Materials Characterization 37 (1996) 61–80.
[62] E. Staufer, Physics-based investigation of relative beta-alpha AlFeSi phase stabilities in AA6082 Al-alloy, Wien, 2021.
[63] https://docplayer.org/45382359-Einfuehrung-bedienung-rem-xl30-tu-ilmenau-imn-prof-dr-l-spiess.html (accessed: December 2021).
[64] T. Degen, M. Sadki, E. Bron, U. König, G. Nénert, The HighScore suite, Powder Diffr. 29 (2014) S13-S18.
[65] J. Faber, T. Fawcett, The Powder Diffraction File: present and future, Acta Crystallogr B Struct Sci 58 (2002) 325–332.
[66] S.N. Kabekkodu, J. Faber, T. Fawcett, New Powder Diffraction File (PDF-4) in relational database format: advantages and data-mining capabilities, Acta Crystallogr B Struct Sci 58 (2002) 333–337.
[67] MatCalc, The Materials Calculator, http://matcalc.at/ (accessed: December 2021).
[68] E. Povoden-Karadeniz, ME-Al.tdb (rel 1.0), Institute of Materials Science and Technology TU, Wien, 2020.
[69] S. Patel, J. Mukhopadhyay, Effect of Homogenization on Al-Fe-Si Centerline Segregation of Twin-Roll Cast Aluminum Alloy AA 8011, in: C. Chesonis (Ed.), Light Metals 2019, Springer International Publishing, Cham, 2019, pp. 351–355.

[70] M. Shakiba, N. Parson, X.-G. Chen, Effect of homogenization treatment and silicon content on the microstructure and hot workability of dilute Al–Fe–Si alloys, Materials Science and Engineering: A 619 (2014) 180–189.

[71] D.H. Kim, B. Cantor, Structure and decomposition behaviour of rapidly solidified Al-Fe alloys, JOURNAL OF MATERIALS SCIENCE 29 (1994) 2884–2892.

[72] C. Liu, Microstructure evolution during homogenization and its effect on the high temperature deformation behaviour in AA6082 based alloys, University of British Columbia, 2017.

[73] A.M.F. Muggerud, Y. Li, R. Holmestad, Composition and orientation relationships of constituent particles in 3xxx aluminum alloys, Philosophical Magazine 94 (2014) 556–568.

[74] H.M. Otte, W.G. Montague, D.O. Welch, X-Ray Diffractometer Determination of the Thermal Expansion Coefficient of Aluminum near Room Temperature, Journal of Applied Physics 34 (1963) 3149–3150.

[75] P.J. Black, The structure of FeAl 3 I, Acta Cryst 8 (1955) 43–48.

[76] E.H. Hollingsworth, G.R. Frank Jr., R.E. Willett, Transactions of the Metallurgical Society of AIME (1962) 188.

[77] M. Cooper, The crystal structure of the ternary alloy α(AlFeSi), Acta Cryst 23 (1967) 1106–1107.

[78] L. Zeng, ICDD Grant-in-Aid, Guangxi University, Institute of Materials Science, P.R. China, 2002.

[79] C. Rømming, V. Hansen, J. Gjønnes, Crystal structure of β-Al 4.5 FeSi, Acta Crystallogr B Struct Sci 50 (1994) 307–312.

[80] Y. Okada, Y. Tokumaru, Precise determination of lattice parameter and thermal expansion coefficient of silicon between 300 and 1500 K, Journal of Applied Physics 56 (1984) 314–320.

[81] P. Krishna, A.R. Verma, An x-ray diffraction study of silicon carbide structure types [(33) n 34] 3R, Zeitschrift für Kristallographie 117 (1962) 1–15.

10. List of Abbreviations and Symbols

Symbol	Description	Symbol	Description
Al_2O_3	Aluminium oxide	N_i	Number of moles of the component i
AA	Aluminium alloy	NaOH	Sodium hydroxide
AC	as-cast	P	Pressure
at.%	Atomic percentage	R	Universal gas constant
bal.	Balance	RPM	Rounds per minute
BSE	Backscattered electrons	s	Empirical standard deviation
CALPHAD	CALculation of PHAse Diagrams	S	Entropy
d	Resolving power	ΔS_{mix}	Mixing Entropy
DC	Direct chill	SE	Secondary electrons
E_0	Excitation energy	SEM	Scanning electron microscope
EDX	Energy-dispersive X-ray spectroscopy	SiC	Silicon Carbide
eV	Electron volt	T	Temperature
F4, F5, F6	Full-time of the respective temperature annealing	TEM	Transmission electron microscopy
g	Gibbs Energy	U	Internal energy of a system
g_{EX}	Excess molar Gibbs energy	V	Volume
g_{EX}^{RK}	Energy contribution of the Gibbs energy of nonideal chemical interaction	V_{cell}	Volume of the cell
g_{EX}^{SRO}	Energy contribution of the Gibbs energy of short-range ordering	vol.%	Volume percentage
g_{EX}^{magn}	Energy contribution of the Gibbs energy of magnetism	w_i	mass fraction of a component i
g_{IS}	Molar Gibbs energy of ideal solution	wt.%	Weight percentage
g_i^0	Molar Gibbs energy of pure component i	$\bar{x}$	Empirical mean value
ΔG_{mix}	Mixing Gibbs energy	X_i	Mole fraction of component
H	Enthalpy	XRD	X-ray (powder) diffraction
ΔH_{mix}	Mixing Enthalpy	Z	Formula Units
H4, H5, H6	Half-time of the respective temperature annealing	α	Aperature angel of the objective
HF	Hydrofluoric acid	θ	Diffraction angle
L_{ij}^n	Weighting of the Redlich-Kister polynomials	λ	Wavelength of the light
M	Molar mass	μ_i	Chemical potential of a component i
N_A	Avogadro constant	$\rho_{th,i}$	Theoretical density of a component i
n	Number of images (Phase quantity), exponent of the Redlich-Kister polynomials, Order of interference (XRD), optical refractive index (light microscopy)	φ_i	Volume fraction of a component i

11. List of Figures

12. List of Tables

13. Appendix

13.1 Code in ImageJ

```
requires("1.33s");                                  //version control

  dir = getDirectory("C:\Users\... ");              //insert the path of the directory
  setBatchMode(true);
  count = 0;
  countFiles(dir);
  n = 0;
  processFiles(dir);

  function countFiles(dir) {
     list = getFileList(dir);
     for (i=0; i<list.length; i++) {
        if (endsWith(list[i], "/"))
           countFiles(""+dir+list[i]);
        else
           count++;
     }
  }
  function processFiles(dir) {
     list = getFileList(dir);
     for (i=0; i<list.length; i++) {
        if (endsWith(list[i], "/"))
           processFiles(""+dir+list[i]);
        else {
          showProgress(n++, count);
          path = dir+list[i];
          print(path);
          processFile(path);
        }
     }
  }
  function processFile(path) {
      if (endsWith(path, ".jpg")) {                 //depending on the file type change the extension
         open(path);
run("8-bit");
run("Sharpen");
run("Subtract Background...", "rolling=200 light disable");
run("Close");
setAutoThreshold("Default");
run("Threshold...");
setThreshold(0,176);                                //change the threshold manually
//setOption("BlackBackground", false);
run("Convert to Mask");
run("Set Measurements...", "shape area_fraction limit redirect=None decimal=3");
run("Set Scale...", "distance=363 known=100 unit=µm global");// here the respective scale must be set manually
run("Analyze Particles...", "  show=Nothing summarize");
save(path + "_edited");
close();
      }
  }
```

13.2 Chemical composition and homogeneity range of the phases

Name	Chemical composition	Homogeneity range				Unit	References
		Al	Fe	Si	Mn		
$Al_{13}(Fe,Mn)_4$	$Al_{13}Fe_4$	bal.	36-38.5	0-2.5		wt.%	[34]
	$Al_3(Fe,Mn)$	bal.	31-38.5	0-2.5	up to 4-5 wt.%	wt.%	[7]
$Al_6(Fe,Mn)$	Al_6Fe	bal.	24.5-26	0-0.5		wt.%	[34]
	$Al_{12}FeMn$	bal.	< 13		14-26	wt.%	[7]
α_c-AlFeSi	$Al_{15}(Fe,Mn)_3Si_2$	bal.	< 31	< 8	0.01-1.5	wt.%	[7]
α_h-AlFeSi	Al_8Fe_2Si, $Al_{12}Fe_3Si_2$	bal.	30-33	6-12		wt.%	[7]
β-AlFeSi	Al_5FeSi, $Al_9Fe_2Si_2$	bal.	25-30	12-15		wt.%	[7]
Si	Si			99.5+		wt.%	[5]

13.3 Crystallographic parameters of the databases for the XRD evaluation

Phase	Chemical composition	Crystallographic parameters	Space group	Space group number	a (Å)	b (Å)	c (Å)	α (°)	β (°)	γ (°)	References
Al	Al	Cubic	Fm-3m	225	4.0493	4.0493	4.0493	90.00	90.00	90.00	[74]
$Al_{13}(Fe,Mn)_4$	$Al_{13}Fe_4$	Monoclinic	C2/m	12	15.489	8.0831	12.476	90.00	107.72	90.00	[75]
$Al_6(Fe,Mn)$	Al_6Fe	Orthorhombic	Cmc21	36	7.437	6.492	8.788	90.00	90.00	90.00	[76]
	$Al_6Fe_{0.5}Mn_{0.5}$	Orthorhombic	Cmcm	63	7.498	6.495	8.837	90.00	90.00	90.00	[5]
α-AlFeMnSi	$(Al_{19}Fe_4MnSi_2)_{5.31}$	Cubic	Pm-3	200	12.560	12.560	12.560	90.00	90.00	90.00	[77]
β-AlFeSi	$Al_9Fe_2Si_2$	Monoclinic	C2/c	15	20.80	6.1639	6.1556	90.00	90.72	90.00	[78,79]
Si	Si	Cubic	Fd-3m	227	5.431	5.431	5.431	90.00	90.00	90.00	[80]
SiC	SiC	Rhombohedral	R3m	160	3.078	3.078	53.056	90.00	90.00	120.00	[81]

13.4 ImageJ Analysis

(Everything in vol.%)

Sample	Empirical mean value of the total area fraction	Empirical standard deviation of the total area fraction	Number of images
AA8011 AC	$\bar{x}$ = 2.4	s = 0.3	n = 30
AA8011 H4	$\bar{x}$ = 2.9	s = 0.3	n = 34
AA8011 F4	$\bar{x}$ = 2.8	s = 0.3	n = 36
AA8011 H5	$\bar{x}$ = 3.0	s = 0.2	n = 37
AA8011 F5	$\bar{x}$ = 3.0	s = 0.3	n = 30
AA8011 H6	$\bar{x}$ = 2.5	s = 0.3	n = 34
AA8011 F6	$\bar{x}$ = 2.5	s = 0.2	n = 36
AA8014 AC	$\bar{x}$ = 4.2	s = 0.4	n = 36
AA8014 H4	$\bar{x}$ = 4.1	s = 0.2	n = 30
AA8014 F4	$\bar{x}$ = 4.0	s = 0.2	n = 30
AA8014 H5	$\bar{x}$ = 4.0	s = 0.3	n = 46
AA8014 F5	$\bar{x}$ = 4.0	s = 0.3	n = 46
AA8014 H6	$\bar{x}$ = 4.0	s = 0.3	n = 36
AA8014 F6	$\bar{x}$ = 3.9	s = 0.4	n = 38
AA8021 AC	$\bar{x}$ = 3.7	s = 0.3	n = 30
AA8021 H4	$\bar{x}$ = 3.5	s = 0.4	n = 34
AA8021 F4	$\bar{x}$ = 3.6	s = 0.3	n = 43
AA8021 H5	$\bar{x}$ = 3.6	s = 0.4	n = 36
AA8021 F5	$\bar{x}$ = 3.1	s = 0.3	n = 42
AA8021 H6	$\bar{x}$ = 2.8	s = 0.3	n = 33
AA8021 F6	$\bar{x}$ = 2.8	s = 0.2	n = 35
AA8079 AC	$\bar{x}$ = 2.8	s = 0.3	n = 36
AA8079 H4	$\bar{x}$ = 2.6	s = 0.2	n = 37
AA8079 F4	$\bar{x}$ = 2.7	s = 0.2	n = 36
AA8079 H5	$\bar{x}$ = 2.6	s = 0.2	n = 33
AA8079 F5	$\bar{x}$ = 2.6	s = 0.2	n = 35
AA8079 H6	$\bar{x}$ = 2.4	s = 0.1	n = 30
AA8079 F6	$\bar{x}$ = 2.3	s = 0.2	n = 40

13.5 The quantification in the XRD-Analysis

13.5.1 The quantification of the bulk samples

(Everything in wt.%)

Sample	Al	α-AlFeMnSi	β-AlFeSi	$Al_{13}(Fe,Mn)_4$	$Al_6(Fe,Mn)$		Si
		$(Al_{19}Fe_4MnSi_2)_{5.31}$	$Al_9Fe_2Si_2$	$Al_{13}Fe_4$	Al_6Fe	$Al_6Fe_{0.5}Mn_{0.5}$	
AA8011 AC	97.19	2.74	0.20				0.1
AA8011 H4	96.37	3.63	0.10				0.2
AA8011 F4	97.00	2.53	0.51				0.2
AA8011 H5	97.28	1.81	1.11				
AA8011 F5	97.37	1.81	1.01				
AA8011 H6	97.21	3.03					
AA8011 F6	97.19	3.05					
AA8014 AC	93.35			0.40		6.52	
AA8014 H4	93.53	4.83		0.60		1.51	
AA8014 F4	94.66	4.03		0.50		1.21	
AA8014 H5	94.58	1.71		0.50		3.51	
AA8014 F5	94.23	2.01		1.00		3.11	
AA8014 H6	96.47			2.91		0.90	
AA8014 F6	96.29			3.11		0.90	
AA8021 AC	95.91			3.32	1.11		
AA8021 H4	96.46			3.03	0.81		
AA8021 F4	96.77			3.54			
AA8021 H5	96.59			3.73			
AA8021 F5	95.83			4.56			
AA8021 H6	95.82			4.58			
AA8021 F6	96.18			4.18			
AA8079 AC	97.51			0.40	2.21		
AA8079 H4	97.57	0.20	0.40	1.41	0.60		
AA8079 F4	98.03	0.20	0.20	1.32	0.40		
AA8079 H5	97.33			2.93			
AA8079 F5	95.38			5.06			
AA8079 H6	98.25			1.91			
AA8079 F6	98.53			1.61			

13.5.2 The quantification of the powders

(Everything in wt.%)

Sample	α-AlFeMnSi	β-AlFeSi	$Al_{13}(Fe,Mn)_4$	$Al_6(Fe,Mn)$		Si
	$(Al_{19}Fe_4MnSi_2)_{5.31}$	$Al_9Fe_2Si_2$	$Al_{13}Fe_4$	Al_6Fe	$Al_6Fe_{0.5}Mn_{0.5}$	
AA8011 AC	93.1	2.4				4.5
AA8011 F4	85.3	7.9				6.8
AA8011 F5	61.6	38.4				
AA8011 H6	100.0					
AA8011 F6	100.0					
AA8014 AC			3.3		96.7	
AA8014 F4	22.6		4.4		73.0	
AA8014 F5	29.4		11.7		58.9	
AA8014 F6			96.6		3.4	
AA8021 AC			91.9	8.1		
AA8021 F4			96.7	3.3		
AA8021 F5			100.0			
AA8021 F6			100.0			
AA8079 AC			52.5	47.5		
AA8079 F4	18.2	5.5	68.6	7.7		
AA8079 F5			100.0			
AA8079 F6			100.0			

13.6 Results of the EDX-Analysis

Note: the following ratios and compositions are in weight ratios/percentage

13.6.1 AA8011

Sample	Phase	Al	Si	Fe	Mn	Cu	(Fe+Mn):Si	Fe:Mn	Al:(Fe+Mn)
AA8011 AC	α-AlFeMnSi	60.80	8.50	30.02	0.68		3.61	43.99	1.98
AA8011 AC	α-AlFeMnSi	59.69	8.07	31.19	1.05		3.99	29.76	1.85
AA8011 AC	α-AlFeMnSi	59.04	9.52	31.44			3.30		1.88
AA8011 AC	α-AlFeMnSi	92.18	1.38	6.44			4.67		14.32
AA8011 AC	α-AlFeMnSi	56.72	10.21	31.58	0.74	0.76	3.17	42.74	1.76
AA8011 AC	β-AlFeSi	55.97	20.49	23.54			1.15		2.38
AA8011 AC	β-AlFeSi	68.35	8.46	23.19			2.74		2.95
AA8011 AC	α-AlFeMnSi	65.79	8.48	25.73			3.03		2.56
AA8011 AC	Si-rich phase	83.87	9.81	6.32			0.64		13.27
AA8011 AC	$Al_{13}(Fe,Mn)_4$	77.04	1.47	21.49			14.62		3.58
AA8011 AC	Si-rich phase	55.47	28.46	16.07			0.56		3.45
AA8011 AC	β-AlFeSi	66.56	11.86	21.59			1.82		3.08
AA8011 AC	β-AlFeSi	60.80	11.16	28.05			2.51		2.17
AA8011 H4	α-AlFeMnSi	69.63	7.17	23.21			3.24		3.00
AA8011 H4	α-AlFeMnSi	62.66	8.73	28.61			3.28		2.19
AA8011 H4	β-AlFeSi	60.80	11.23	27.97			2.49		2.17
AA8011 H4	Si-rich phase	69.74	12.86	17.40			1.35		4.01
AA8011 H4	β-AlFeSi	75.38	6.89	17.73			2.57		4.25
AA8011 H4	β-AlFeSi	79.03	5.66	15.31			2.70		5.16
AA8011 F4	α-AlFeMnSi	68.57	6.85	24.59			3.59		2.79
AA8011 F4	α-AlFeMnSi	63.70	7.32	28.97			3.96		2.20
AA8011 F4	α-AlFeMnSi	72.70	5.93	21.37			3.61		3.40
AA8011 F4	Si-rich phase	58.82	16.64	24.54			1.48		2.40
AA8011 F4	α-AlFeMnSi	69.91	6.87	23.22			3.38		3.01
AA8011 F4	Si-rich phase	65.52	15.63	18.85			1.21		3.48
AA8011 F4	Si-rich phase	54.10	22.97	22.36	0.57		1.00	39.33	2.36
AA8011 F4	β-AlFeSi	78.38	8.41	12.82	0.40		1.57	32.29	5.93
AA8011 H5	α-AlFeMnSi	60.45	7.83	30.92	0.80		4.05	38.78	1.91
AA8011 H5	β-AlFeSi	71.41	10.82	17.39		0.38	1.61		4.11
AA8011 H5	β-AlFeSi	61.70	10.84	26.65	0.80		2.53	33.32	2.25
AA8011 H5	β-AlFeSi	60.10	13.92	25.98			1.87		2.31
AA8011 F5	β-AlFeSi	59.66	13.32	26.27	0.75		2.03	35.08	2.21
AA8011 F5	α-AlFeMnSi	64.29	7.23	28.48			3.94		2.26
AA8011 F5	α-AlFeMnSi	60.49	9.33	30.18			3.23		2.00
AA8011 F5	β-AlFeSi	60.11	14.16	25.73			1.82		2.34
AA8011 F5	β-AlFeSi	69.40	11.48	19.12			1.67		3.63
AA8011 F5	α-AlFeMnSi	64.85	7.07	27.05	1.02		3.97	26.43	2.31
AA8011 H6	α-AlFeMnSi	56.31	8.73	33.03	1.00	0.94	3.90	33.16	1.65
AA8011 H6	α-AlFeMnSi	60.20	7.56	28.78	1.96	1.50	4.07	14.69	1.96
AA8011 H6	α-AlFeMnSi	64.86	7.37	25.19	1.88	0.70	3.67	13.42	2.40
AA8011 H6	α-AlFeMnSi	57.25	9.06	32.56	0.84	0.29	3.68	38.89	1.71

AA8011 H6	α-AlFeMnSi	61.01	7.14	28.25	1.81	1.78	4.21	15.59	2.03
AA8011 F6	α-AlFeMnSi	57.19	8.48	34.34			4.05		1.67
AA8011 F6	α-AlFeMnSi	56.06	7.90	35.00	1.04		4.56	33.66	1.56
AA8011 F6	α-AlFeMnSi	57.47	8.56	33.08	0.90		3.97	36.63	1.69

13.6.2 AA8014

Sample	Phase	Al	Si	Fe	Mn	Cu	(Fe+Mn):Si	Fe:Mn	Al:(Fe +Mn)
AA8014 AC	$Al_6(Fe,Mn)$	74.30		24.13	1.57			15.35	2.89
AA8014 AC	$Al_{13}(Fe,Mn)_4$	77.03	0.64	21.13	1.21		35.16	17.51	3.45
AA8014 AC	$Al_6(Fe,Mn)$	73.83	0.16	24.12	1.89		160.32	12.79	2.84
AA8014 AC	$Al_{13}(Fe,Mn)_4$	74.37	0.54	23.28	1.81		46.14	12.88	2.97
AA8014 AC	$Al_6(Fe,Mn)$	72.97		25.64	1.38			18.53	2.70
AA8014 AC	$Al_{13}(Fe,Mn)_4$	74.05	0.89	23.40	1.67		28.23	14.05	2.95
AA8014 AC	$Al_{13}(Fe,Mn)_4$	68.03	1.19	28.21	2.57		25.86	10.99	2.21
AA8014 AC	$Al_6(Fe,Mn)$	79.85		18.38	1.77			10.39	3.96
AA8014 AC	$Al_6(Fe,Mn)$	76.82		21.28	1.90			11.20	3.31
AA8014 AC	$Al_6(Fe,Mn)$	75.78		22.76	1.46			15.58	3.13
AA8014 AC	$Al_{13}(Fe,Mn)_4$	67.73	2.03	29.35	0.89		14.92	32.88	2.24
AA8014 AC	$Al_{13}(Fe,Mn)_4$	71.41	0.37	27.24	0.97		75.57	27.97	2.53
AA8014 H4	$Al_6(Fe,Mn)$	75.79		21.47	1.85	0.89		11.59	3.25
AA8014 H4	$Al_6(Fe,Mn)$	79.75		17.70	2.55			6.93	3.94
AA8014 H4	$Al_6(Fe,Mn)$	87.99		9.98	1.53	0.51		6.53	7.65
AA8014 H4	$Al_6(Fe,Mn)$	79.93		18.50	1.57			11.78	3.98
AA8014 H4	α-AlFeMnSi?	73.32	2.29	21.53	2.86		10.65	7.52	3.01
AA8014 H4	$Al_{13}(Fe,Mn)_4$	72.78	0.76	24.33	2.13		34.65	11.44	2.75
AA8014 H4	$Al_{13}(Fe,Mn)_4$	71.49	0.66	25.86	1.99		42.25	13.02	2.57
AA8014 H4	$Al_6(Fe,Mn)$	79.03		19.14	1.83			10.44	3.77
AA8014 F4	$Al_6(Fe,Mn)$	74.08		24.76	1.16			21.27	2.86
AA8014 F4	$Al_{13}(Fe,Mn)_4$	71.76	0.76	23.97	2.20	1.31	34.50	10.90	2.74
AA8014 F4	$Al_6(Fe,Mn)$	77.33		20.29	1.49	0.89		13.61	3.55
AA8014 F4	$Al_6(Fe,Mn)$	75.41		21.22	2.20	1.17		9.63	3.22
AA8014 F4	$Al_{13}(Fe,Mn)_4$	62.85	0.86	33.78	2.51		42.08	13.44	1.73
AA8014 F4	$Al_{13}(Fe,Mn)_4$	73.30	0.59	24.38	1.73		44.62	14.13	2.81
AA8014 F4	$Al_{13}(Fe,Mn)_4$	68.84	0.49	27.47	2.17	1.03	60.47	12.63	2.32
AA8014 F4	α-AlFeMnSi?	67.21	3.84	26.85	2.11		7.55	12.73	2.32
AA8014 F4	α-AlFeMnSi?	70.29	3.40	24.36	1.95		7.73	12.49	2.67
AA8014 H5	Al_6 (Fe,Mn)	80.10		16.88	2.58	0.44		6.55	4.12
AA8014 H5	$Al_{13}(Fe,Mn)_4$	63.24	0.58	33.40	2.78		62.88	12.01	1.75
AA8014 H5	$Al_{13}(Fe,Mn)_4$	69.98	0.81	27.23	1.97		35.93	13.82	2.40
AA8014 H5	α-AlFeMnSi	66.42	3.50	27.81	2.27		8.59	12.27	2.21
AA8014 H5	$Al_{13}(Fe,Mn)_4$	67.11	0.66	30.13	2.10		48.90	14.32	2.08
AA8014 F5	α-AlFeMnSi	75.25	3.29	17.81	3.65		6.52	4.88	3.51
AA8014 F5	α-AlFeMnSi	72.30	3.33	22.17	2.20		7.31	10.06	2.97
AA8014 F5	$Al_{13}(Fe,Mn)_4$	66.83	0.97	30.63	1.56		33.14	19.62	2.08
AA8014 F5	$Al_6(Fe,Mn)$	73.57		22.90	3.53			6.48	2.78
AA8014 F5	α-AlFeMnSi	69.74	3.37	23.28	3.61		7.97	6.45	2.59
AA8014 H6	$Al_{13}(Fe,Mn)_4$	68.40	0.57	28.50	2.53		54.62	11.26	2.20

AA8014 H6	$Al_6(Fe,Mn)$	75.63	0.40	22.14	1.82		59.71	12.17	3.16
AA8014 H6	$Al_{13}(Fe,Mn)_4$	65.96	0.34	31.40	2.30		100.53	13.63	1.96
AA8014 H6	$Al_6(Fe,Mn)$	74.62	0.49	23.06	1.83		50.83	12.62	3.00
AA8014 H6	$Al_{13}(Fe,Mn)_4$	69.04	0.49	28.58	1.89		62.04	15.15	2.27
AA8014 H6	$Al_{13}(Fe,Mn)_4$	71.67	0.66	25.89	1.78		41.93	14.55	2.59
AA8014 H6	$Al_6(Fe,Mn)$	78.32		15.69	5.99			2.62	3.61
AA8014 H6	$Al_6(Fe,Mn)$	79.45		14.23	6.32			2.25	3.87
AA8014 H6	$Al_6(Fe,Mn)$	73.02		19.18	7.80			2.46	2.71
AA8014 F6	$Al_{13}(Fe,Mn)_4$	63.30	0.57	33.95	2.19		63.72	15.53	1.75
AA8014 F6	$Al_{13}(Fe,Mn)_4$	59.43	0.57	37.42	2.58		70.21	14.48	1.49
AA8014 F6	$Al_{13}(Fe,Mn)_4$	62.10	0.45	35.03	2.41		82.62	14.52	1.66
AA8014 F6	$Al_{13}(Fe,Mn)_4$	62.21	0.50	34.94	2.35		73.96	14.86	1.67
AA8014 F6	α-AlFeMnSi/ $Al_{13}(Fe,Mn)_4$	90.52	1.13	5.70	2.65		7.42	2.15	10.84
AA8014 F6	$Al_6(Fe,Mn)$	80.64		18.24	1.12			16.31	4.17
AA8014 F6	$Al_6(Fe,Mn)$	75.44		23.17	1.39			16.71	3.07

13.6.3 AA8021

Sample	Phase	Al	Si	Fe	Mn	Cu	(Fe+Mn):Si	Fe:Mn	Al:(Fe+ Mn)
AA8021 AC	$Al_6(Fe,Mn)$	79.95	0.40	19.65			48.88		4.07
AA8021 AC	$Al_6(Fe,Mn)$	75.39	0.42	24.19			57.75		3.12
AA8021 AC	$Al_6(Fe,Mn)$	73.50	0.43	26.07			60.32		2.82
AA8021 AC	$Al_6(Fe,Mn)$	78.35	0.46	21.19			45.73		3.70
AA8021 AC	$Al_6(Fe,Mn)$	90.49	0.27	9.24			34.54		9.79
AA8021 AC	$Al_{13}(Fe,Mn)_4$	82.15	0.57	17.28			30.39		4.75
AA8021 AC	$Al_6(Fe,Mn)$	86.68		13.32					6.51
AA8021 AC	$Al_6(Fe,Mn)$	88.43	0.30	11.27			37.08		7.85
AA8021 H4	$Al_{13}(Fe,Mn)_4$	66.00	0.89	33.11			37.28		1.99
AA8021 H4	$Al_{13}(Fe,Mn)_4$	80.45	0.83	18.72			22.64		4.30
AA8021 H4	$Al_{13}(Fe,Mn)_4$	78.59	0.68	20.73			30.56		3.79
AA8021 H4	$Al_{13}(Fe,Mn)_4$	65.12	0.89	33.99			38.11		1.92
AA8021 H4	$Al_6(Fe,Mn)$	89.57	0.40	10.03			24.78		8.93
AA8021 H4	$Al_6(Fe,Mn)$	92.17		7.83					11.78
AA8021 F4	$Al_{13}(Fe,Mn)_4$	81.54	0.57	17.90			31.58		4.56
AA8021 F4	$Al_{13}(Fe,Mn)_4$	81.59	0.67	17.74			26.44		4.60
AA8021 F4	$Al_{13}(Fe,Mn)_4$	77.34	0.82	21.84			26.59		3.54
AA8021 F4	$Al_{13}(Fe,Mn)_4$	76.13	0.71	23.17			32.85		3.29
AA8021 F4	$Al_6(Fe,Mn)$	94.85	0.39	4.76			12.35		19.91
AA8021 F4	$Al_6(Fe,Mn)$	93.60		6.40					14.61
AA8021 H5	$Al_{13}(Fe,Mn)_4$	78.06	0.67	21.27			31.90		3.67
AA8021 H5	$Al_{13}(Fe,Mn)_4$	72.36	0.58	27.05			46.50		2.67
AA8021 H5	α-AlFeMnSi	88.93	1.91	9.16			4.79		9.71
AA8021 H5	$Al_{13}(Fe,Mn)_4$	75.11	0.42	24.48			58.53		3.07
AA8021 H5	$Al_6(Fe,Mn)$	80.09	0.33	19.59			59.82		4.09
AA8021 H5	$Al_{13}(Fe,Mn)_4$	74.63	0.66	24.71			37.29		3.02
AA8021 F5	$Al_6(Fe,Mn)$	81.52	0.38	18.10			47.97		4.50
AA8021 F5	$Al_{13}(Fe,Mn)_4$	75.83	0.58	23.59			40.33		3.22

AA8021 F5	$Al_{13}(Fe,Mn)_4$	79.06	0.50	20.43			40.65		3.87
AA8021 F5	$Al_{13}(Fe,Mn)_4$	72.53	0.52	26.95			51.87		2.69
AA8021 H6	$Al_{13}(Fe,Mn)_4$	60.50	0.53	38.97			73.26		1.55
AA8021 H6	$Al_{13}(Fe,Mn)_4$	63.88	0.38	35.74			93.59		1.79
AA8021 H6	$Al_{13}(Fe,Mn)_4$	60.84	0.51	38.65			76.08		1.57
AA8021 H6	$Al_{13}(Fe,Mn)_4$	72.92	0.66	26.43			40.29		2.76
AA8021 H6	$Al_{13}(Fe,Mn)_4$	68.87	0.36	30.77			85.75		2.24
AA8021 F6	$Al_{13}(Fe,Mn)_4$	62.69	0.44	36.87			84.17		1.70
AA8021 F6	$Al_{13}(Fe,Mn)_4$	60.44	0.38	39.18			102.62		1.54
AA8021 F6	$Al_{13}(Fe,Mn)_4$	61.43	0.44	38.13			86.10		1.61
AA8021 F6	$Al_{13}(Fe,Mn)_4$	60.35	0.52	39.12			74.80		1.54

13.6.4 AA8079

Sample	Phase	Al	Si	Fe	Mn	Cu	(Fe+Mn):Si	Fe:Mn	Al:(Fe+Mn)
AA8079 AC	$Al_{13}(Fe,Mn)_4$	82.22	0.81	16.97			21.03		4.85
AA8079 AC	$Al_{13}(Fe,Mn)_4$	78.92	0.84	20.25			24.15		3.90
AA8079 AC	$Al_6(Fe,Mn)$	83.20		16.80					4.95
AA8079 AC	$Al_6(Fe,Mn)$	84.29		15.71					5.37
AA8079 H4	α-AlFeMnSi	77.69	3.76	18.55			4.94		4.19
AA8079 H4	α-AlFeMnSi	80.19	3.20	16.61			5.19		4.83
AA8079 H4	$Al_{13}(Fe,Mn)_4$	79.81	0.50	19.68			39.00		4.05
AA8079 H4	$Al_{13}(Fe,Mn)_4$	80.61	0.49	18.90			38.70		4.27
AA8079 H4	$Al_{13}(Fe,Mn)_4$	82.33	0.62	17.06			27.65		4.83
AA8079 H4	$Al_{13}(Fe,Mn)_4$	82.41	0.64	16.95			26.65		4.86
AA8079 H4	$Al_{13}(Fe,Mn)_4$	82.27	0.52	17.21			33.01		4.78
AA8079 H4	$Al_{13}(Fe,Mn)_4$	80.08	0.66	19.27			29.37		4.16
AA8079 H4	$Al_{13}(Fe,Mn)_4$	79.35	0.77	19.88			25.97		3.99
AA8079 H4	$Al_{13}(Fe,Mn)_4$	82.31	0.60	17.09			28.60		4.82
AA8079 H4	α-AlFeMnSi	63.92	9.14	26.95			2.95		2.37
AA8079 H4	α-AlFeMnSi	78.58	3.16	18.25			5.77		4.31
AA8079 H4	α-AlFeMnSi	75.18	3.72	21.10			5.67		3.56
AA8079 H4	$Al_6(Fe,Mn)$	91.72		8.28					11.08
AA8079 H4	$Al_6(Fe,Mn)$	92.99	0.33	6.67			20.13		13.93
AA8079 F4	β-AlFeSi	67.49	8.54	23.97			2.81		2.82
AA8079 F4	α-AlFeMnSi	75.24	3.38	21.38			6.32		3.52
AA8079 F4	$Al_{13}(Fe,Mn)_4$	74.39	0.71	24.90			35.21		2.99
AA8079 F4	$Al_{13}(Fe,Mn)_4$	90.22	0.43	9.35			21.97		9.64
AA8079 F4	β-AlFeSi	87.59	4.22	8.19			1.94		10.69
AA8079 F4	$Al_6(Fe,Mn)$	94.61		5.39					17.54
AA8079 H5	α-AlFeMnSi	66.66	4.02	29.32			7.30		2.27
AA8079 H5	$Al_{13}(Fe,Mn)_4$	67.14	0.69	32.17			46.94		2.09
AA8079 H5	α-AlFeMnSi	70.43	4.10	25.47			6.22		2.77
AA8079 H5	$Al_{13}(Fe,Mn)_4$	81.51	0.45	18.03			39.81		4.52
AA8079 H5	$Al_{13}(Fe,Mn)_4$	77.12	0.53	22.35			41.86		3.45
AA8079 F5	$Al_{13}(Fe,Mn)_4$	74.81	0.54	24.65			45.24		3.04
AA8079 F5	$Al_{13}(Fe,Mn)_4$	79.55	0.55	19.90			36.13		4.00
AA8079 F5	$Al_{13}(Fe,Mn)_4$	72.02	0.79	27.19			34.55		2.65

AA8079 F5	$Al_{13}(Fe,Mn)_4$	67.82	0.67	31.51			46.97		2.15
AA8079 H6	$Al_{13}(Fe,Mn)_4$	65.50	0.57	33.94			59.93		1.93
AA8079 H6	$Al_{13}(Fe,Mn)_4$	64.67	0.44	34.89			80.20		1.85
AA8079 H6	$Al_{13}(Fe,Mn)_4$	67.53	0.53	31.94			60.27		2.11
AA8079 H6	$Al_{13}(Fe,Mn)_4$	65.02	0.55	34.43			62.89		1.89
AA8079 H6	$Al_6(Fe,Mn)$	73.39	0.41	26.19			63.29		2.80
AA8079 F6	$Al_{13}(Fe,Mn)_4$	62.45	0.50	36.65	0.39		74.64	92.80	1.69
AA8079 F6	$Al_{13}(Fe,Mn)_4$	60.96	0.63	38.42			61.43		1.59
AA8079 F6	$Al_{13}(Fe,Mn)_4$	60.96	0.46	38.58			84.20		1.58
AA8079 F6	$Al_{13}(Fe,Mn)_4$	60.74	0.56	38.70			69.39		1.57

13.7 Scanning Electron Microscope images with a magnification of 400x

13.7.1 AA8011

- AA8011 As-cast (AA8011 AC)

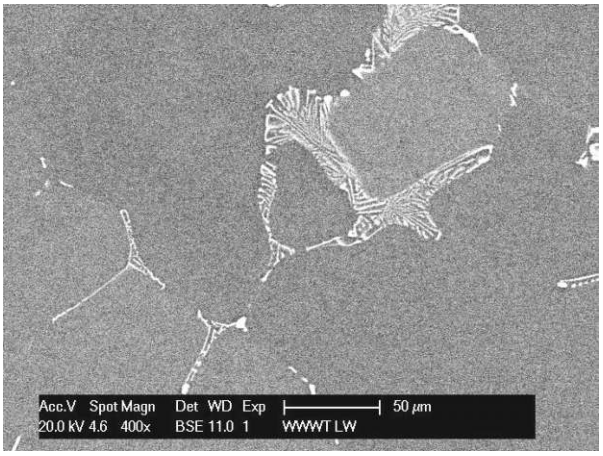

- AA8011, 400°C long term annealing, left: half-time (AA8011 H4), right: full-time (AA8011 F4)

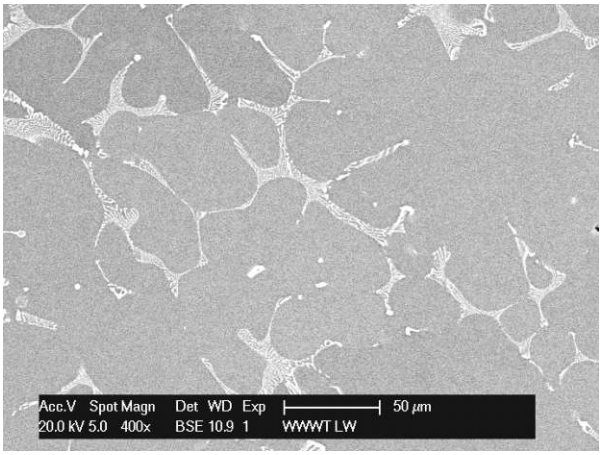

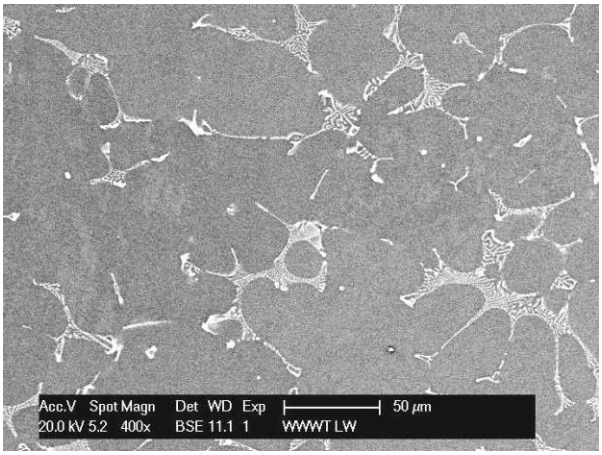

- AA8011, 500°C long term annealing, left: half-time (AA8011 H5), right: full-time (AA8011 F5)

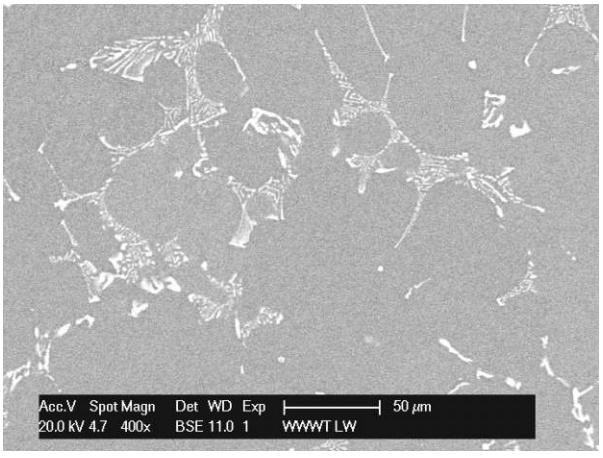

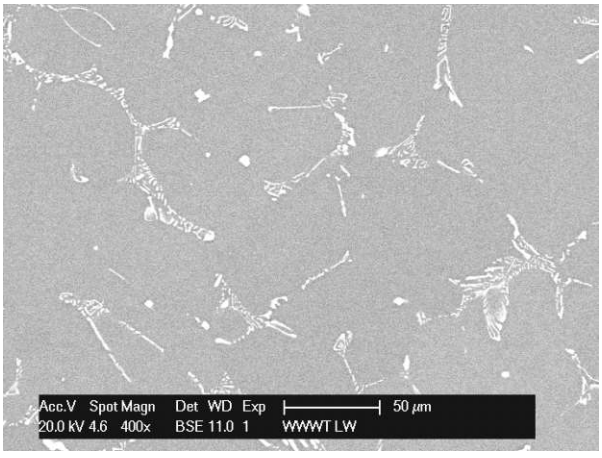

- AA8011, 600°C long term annealing, left: half-time (AA8011 H6), right: full-time (AA8011 F6)

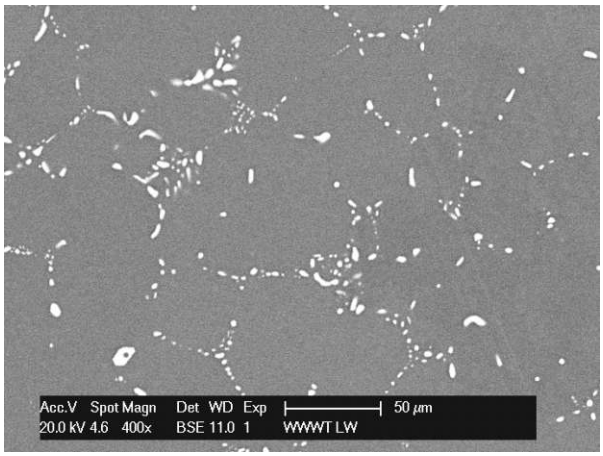

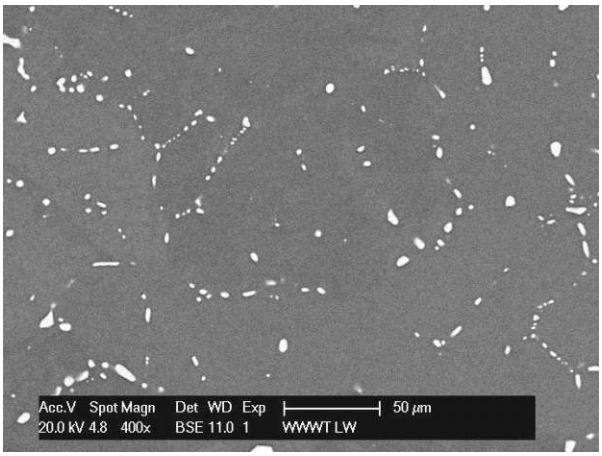

13.7.2 AA8014

- AA8014 As-cast (AA8014 AC)

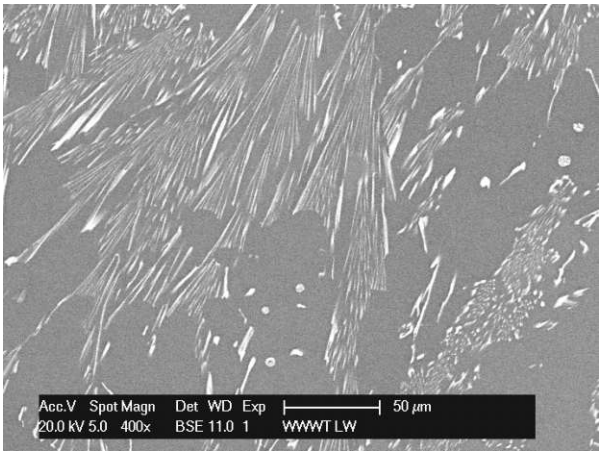

- AA8014, 400°C long term annealing, left: half-time (AA8014 H4), right: full-time (AA8014 F4)

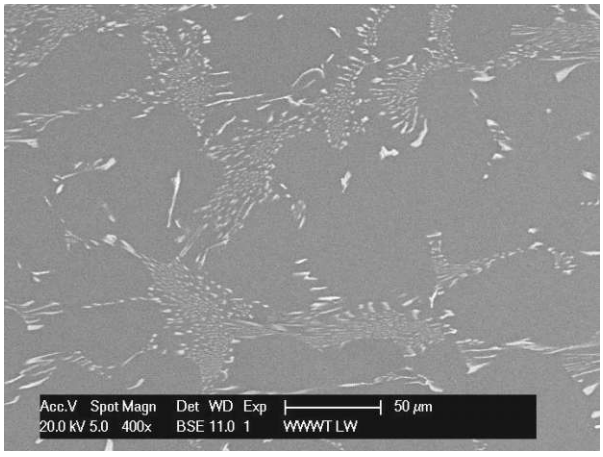

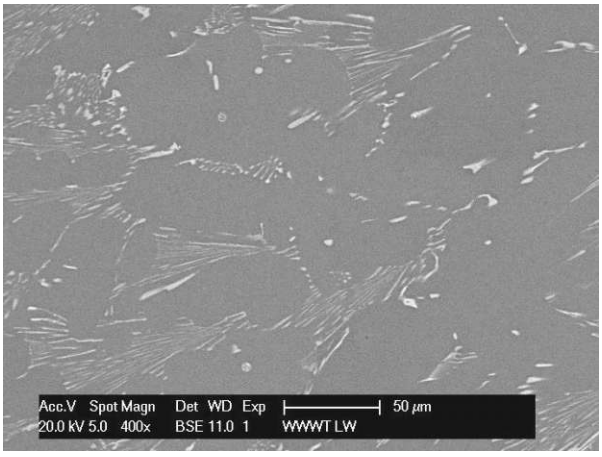

- AA8014, 500°C long term annealing, left: half-time (AA8014 H5), right: full-time (AA8014 F5)

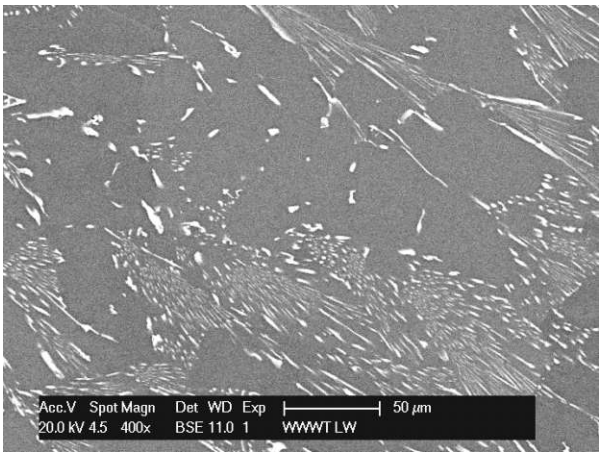

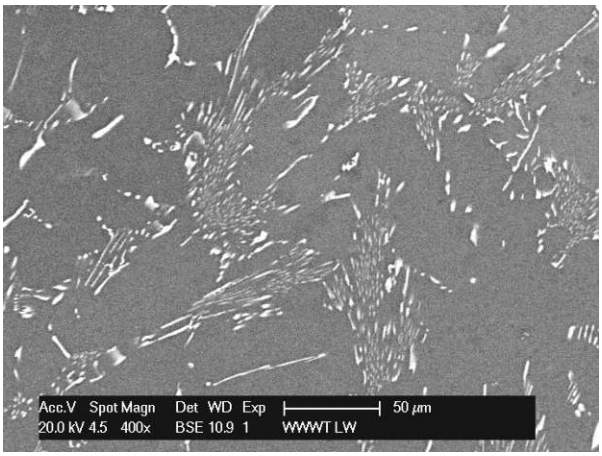

- AA8014, 600°C long term annealing, left: half-time (AA8014 H6), right: full-time (AA8014 F6)

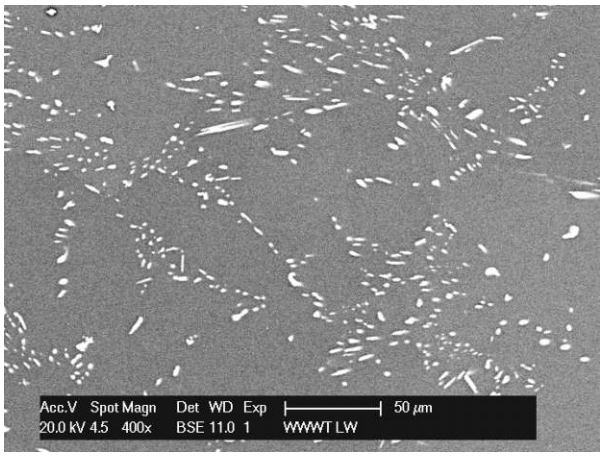

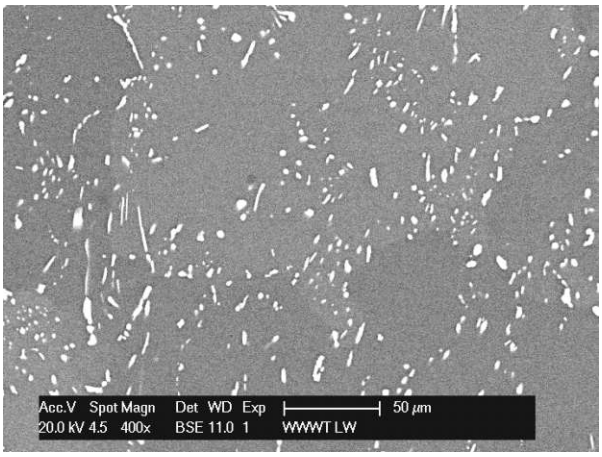

13.7.3 AA8021

- AA8021 As-cast (AA8021 AC)

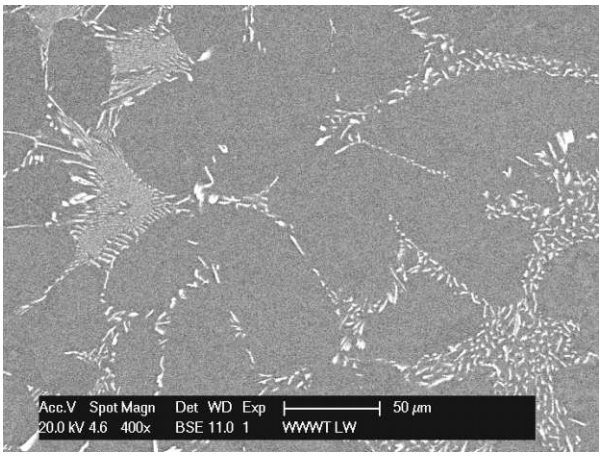

- AA8021, 400°C long term annealing, left: half-time (AA8021 H4), right: full-time (AA8021 F4)

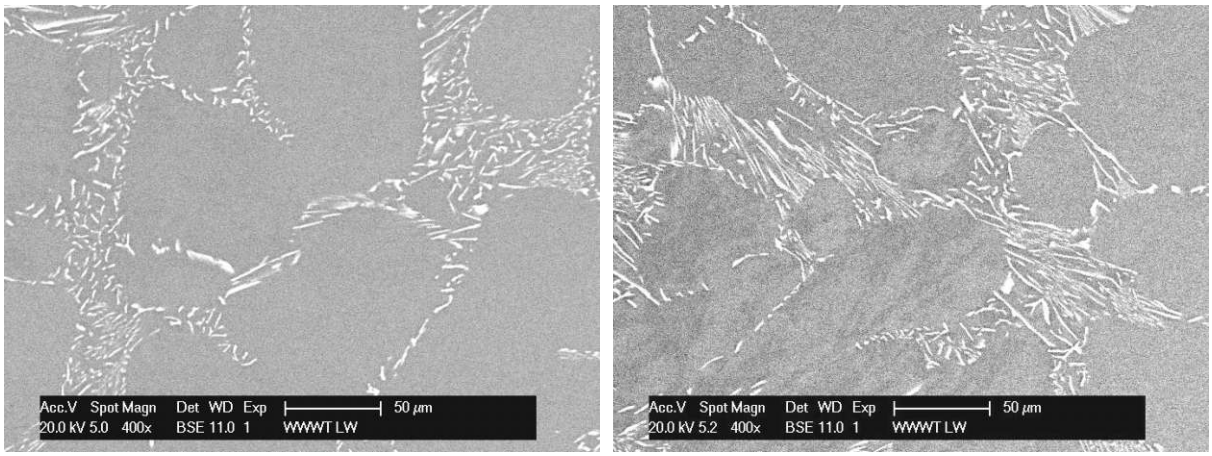

- AA8021, 500°C long term annealing, left: half-time (AA8021 H5), right: full-time (AA8021 F5)

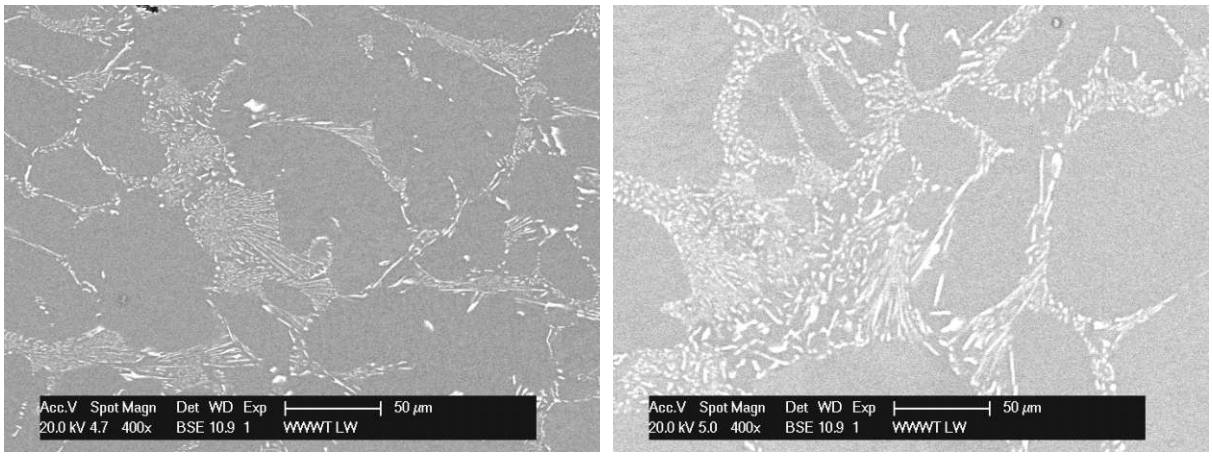

- AA8021, 600°C long term annealing, left: half-time (AA8021 H6), right: full-time (AA8021 F6)

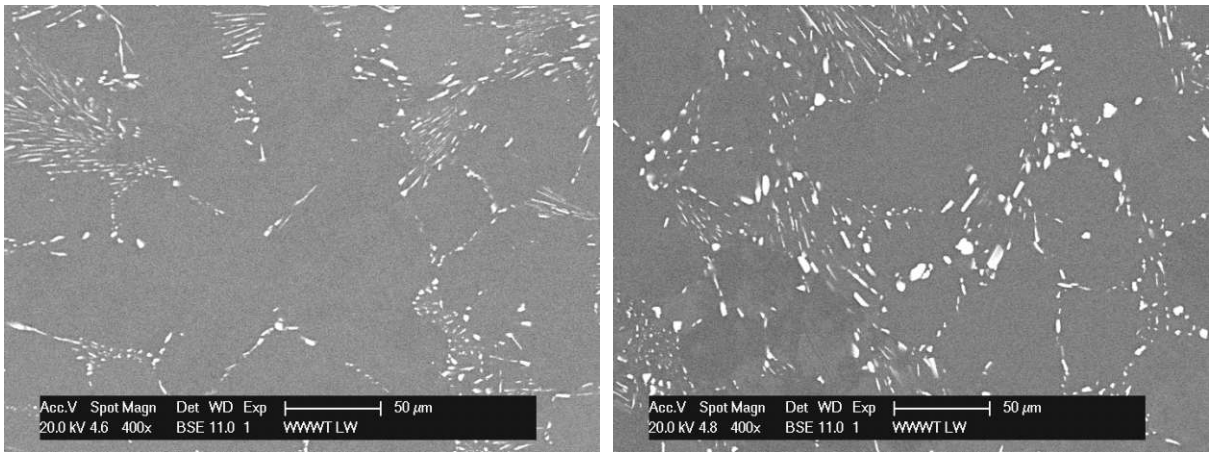

13.7.4 AA8079

- AA8079 As-cast (AA8079 AC)

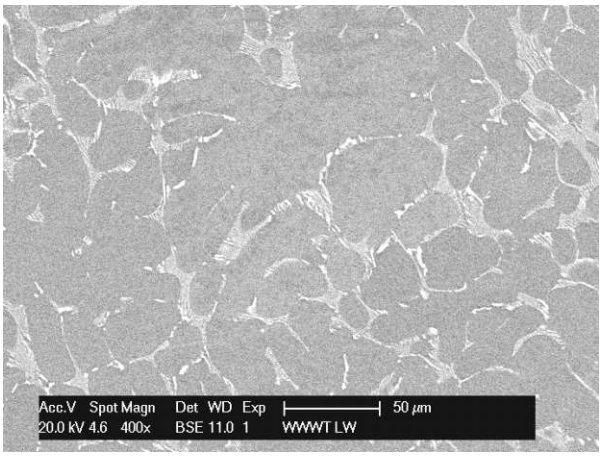

- AA8079, 400°C long term annealing, left: half-time (AA8079 H4), right: full-time (AA8079 F4)

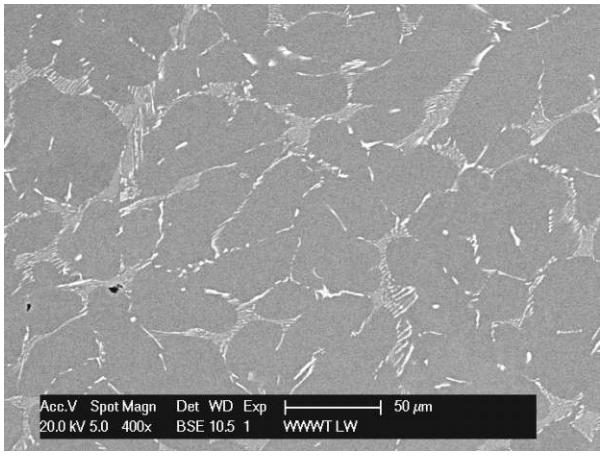

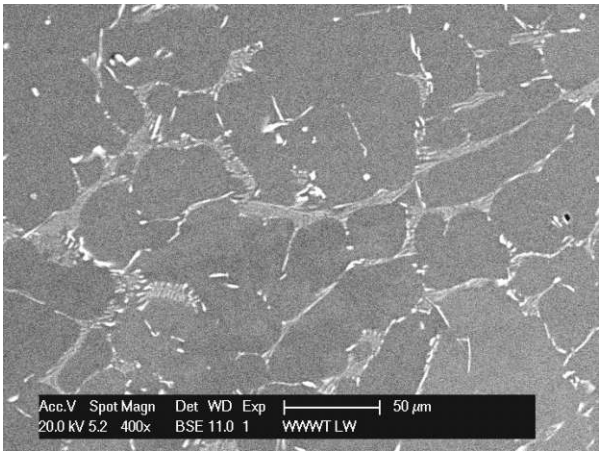

- AA8079, 500°C long term annealing, left: half-time (AA8079 H5), right: full-time (AA8079 F5)

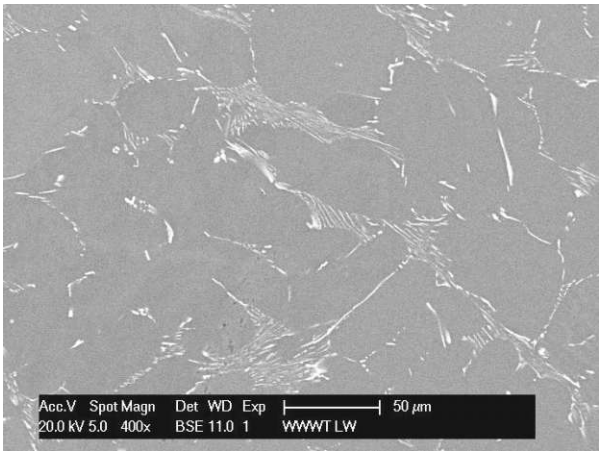

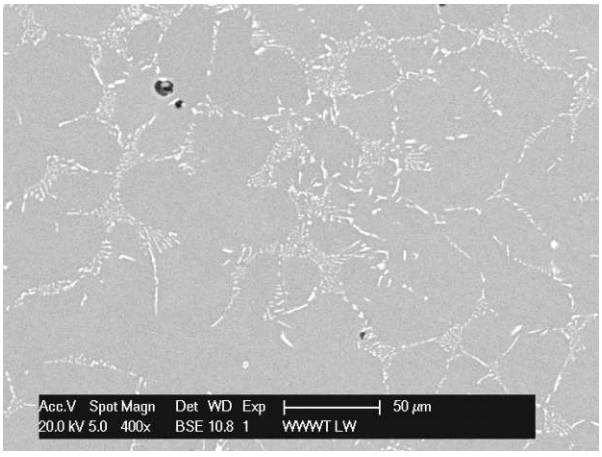

- AA8079, 600°C long term annealing, left: half-time (AA8079 H6), right: full-time (AA8079 F6)

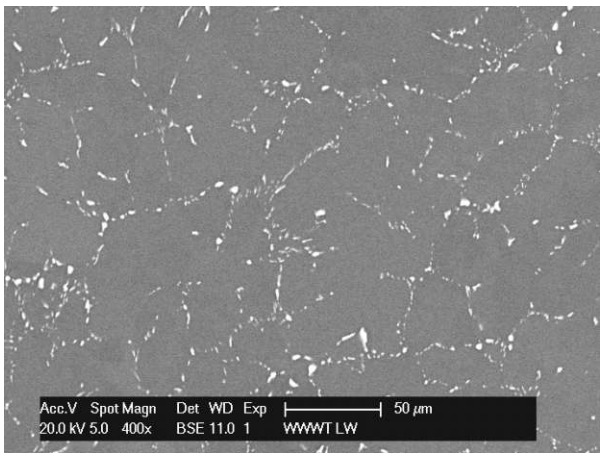

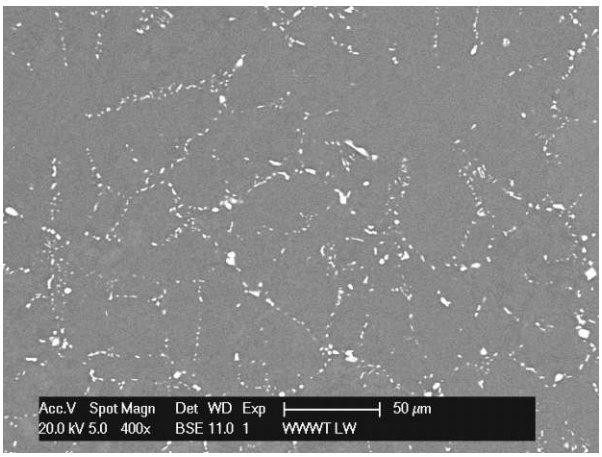

13.8 Unetched light microscopy images

13.8.1 AA8011

- AA8011 As-cast (AA8011 AC)

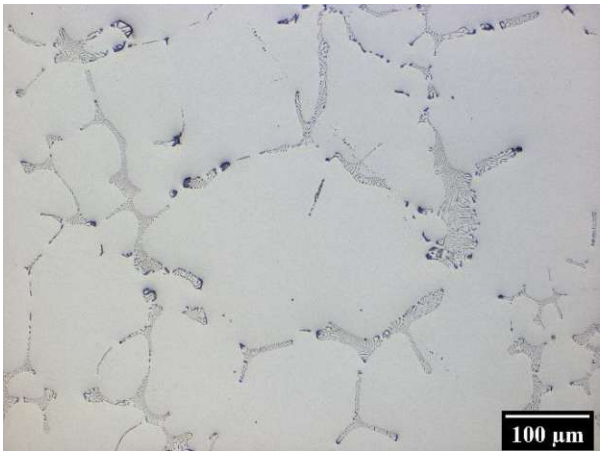

- AA8011, 400°C long term annealing, left: half-time (AA8011 H4), right: full-time (AA8011 F4)

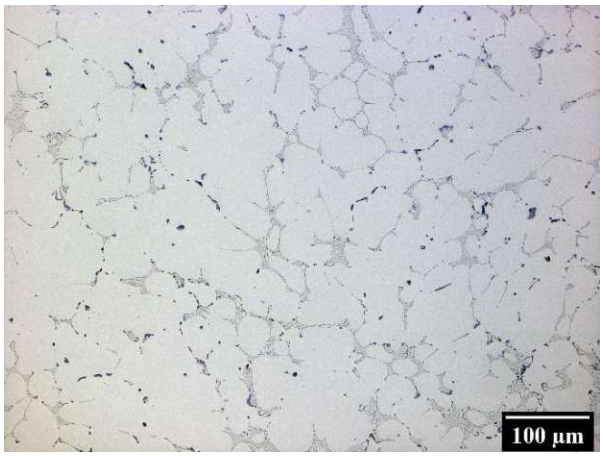

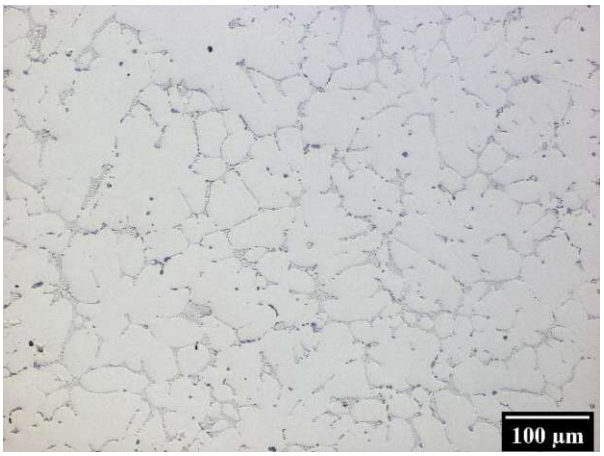

- AA8011, 500°C long term annealing, left: half-time (AA8011 H5), right: full-time (AA8011 F5)

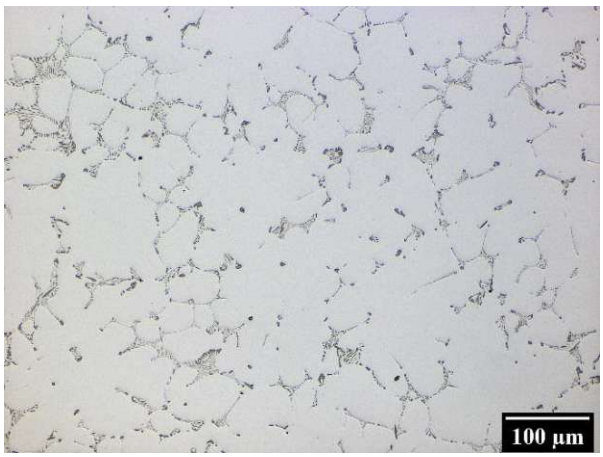

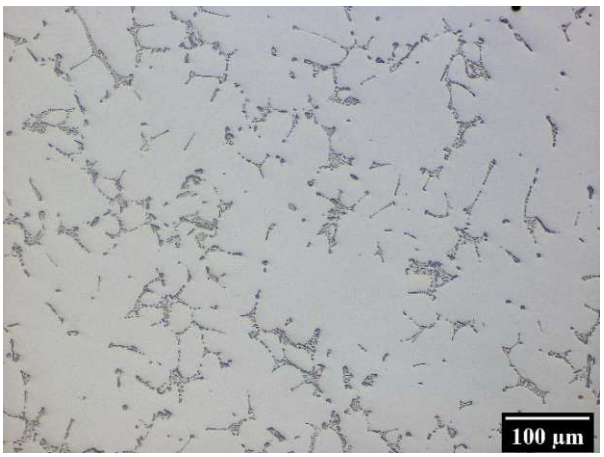

- AA8011, 600°C long term annealing, left: half-time (AA8011 H6), right: full-time (AA8011 F6)

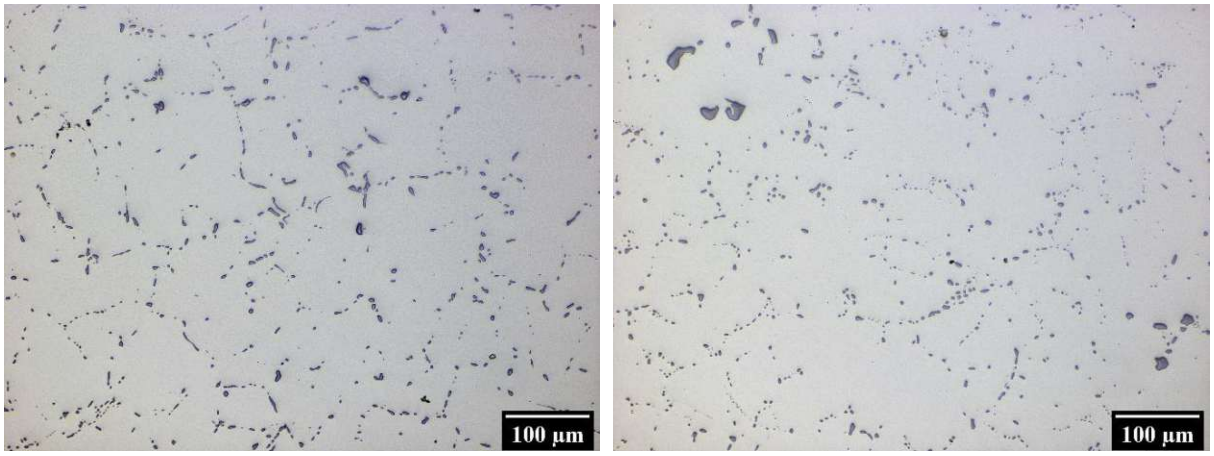

13.8.2 AA8014

- AA8014 As-cast (AA8014 AC)

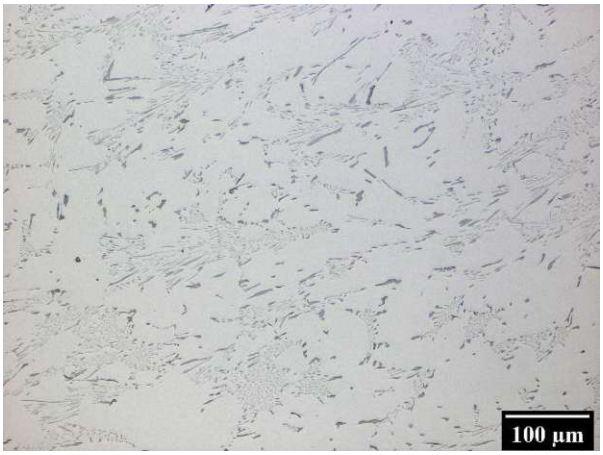

- AA8014, 400°C long term annealing, left: half-time (AA8014 H4), right: full-time (AA8014 F4)

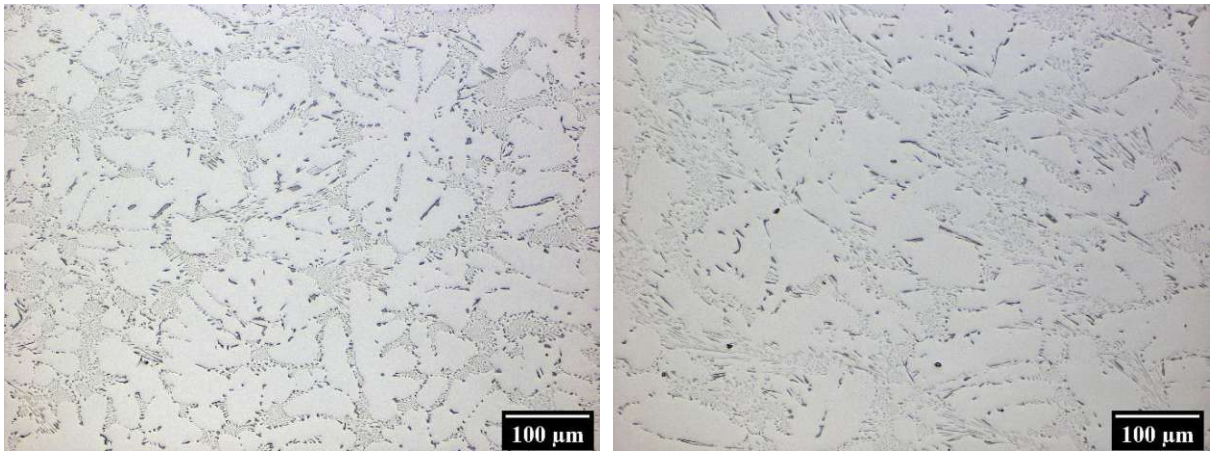

- AA8014, 500°C long term annealing, left: half-time (AA8014 H5), right: full-time (AA8014 F5)

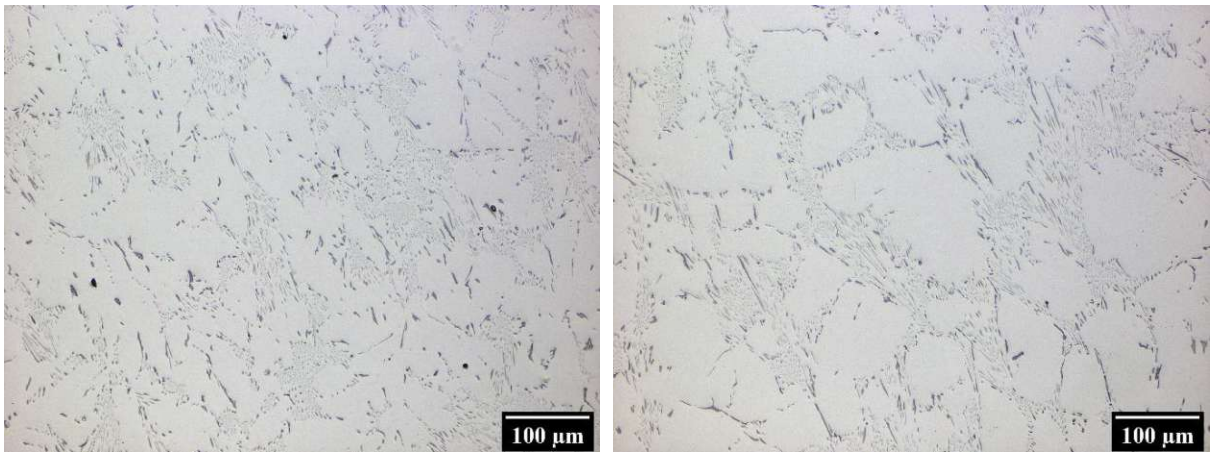

- AA8014, 600°C long term annealing, left: half-time (AA8014 H6), right: full-time (AA8014 F6)

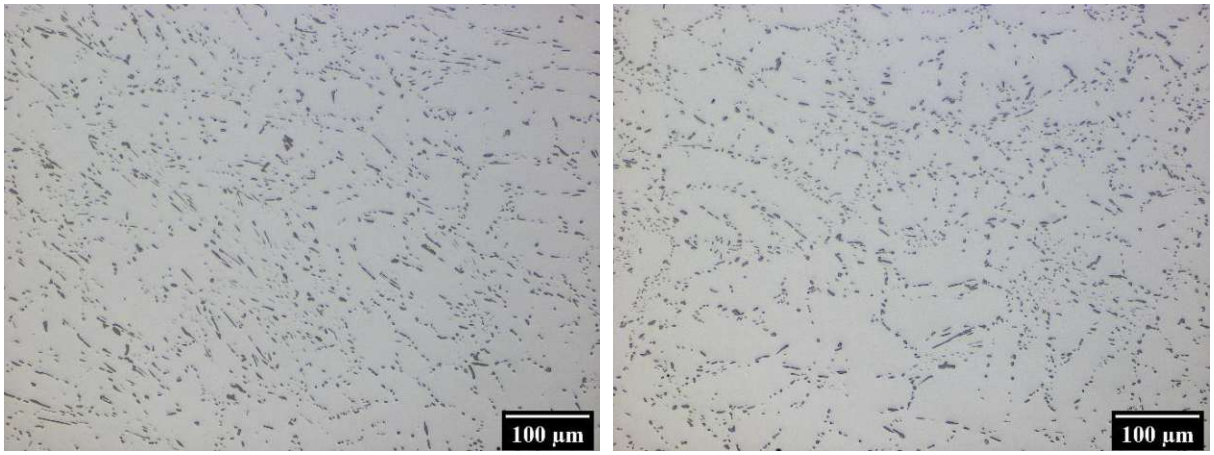

13.8.3 AA8021

- AA8021 As-cast (AA8021 AC)

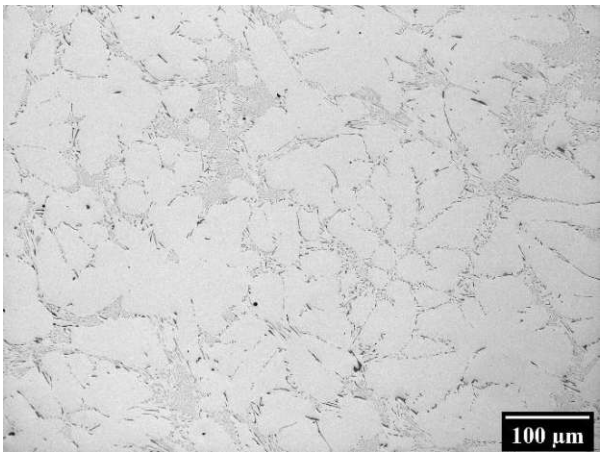

- AA8021, 400°C long term annealing, left: half-time (AA8021 H4), right: full-time (AA8021 F4)

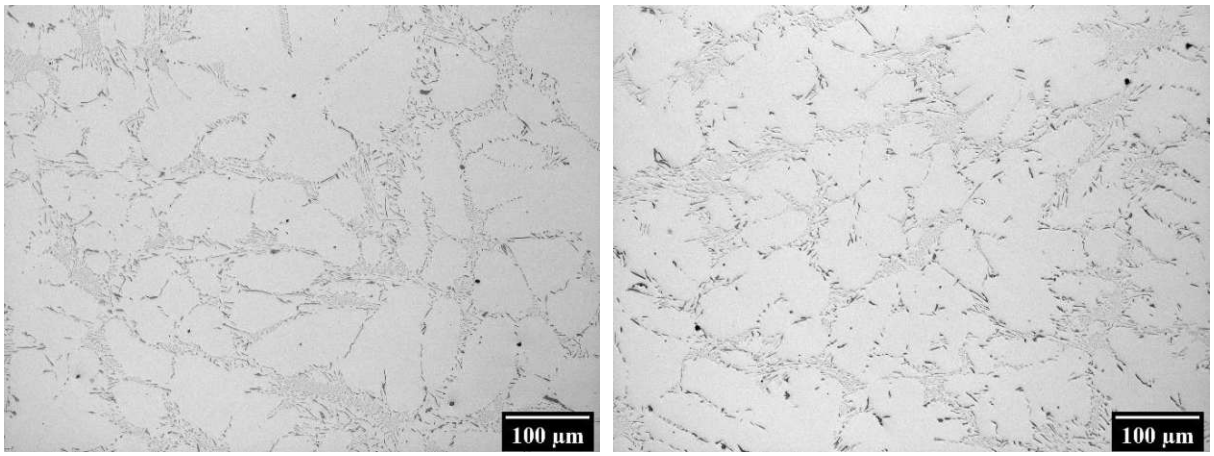

- AA8021, 500°C long term annealing, left: half-time (AA8021 H5), right: full-time (AA8021 F5)

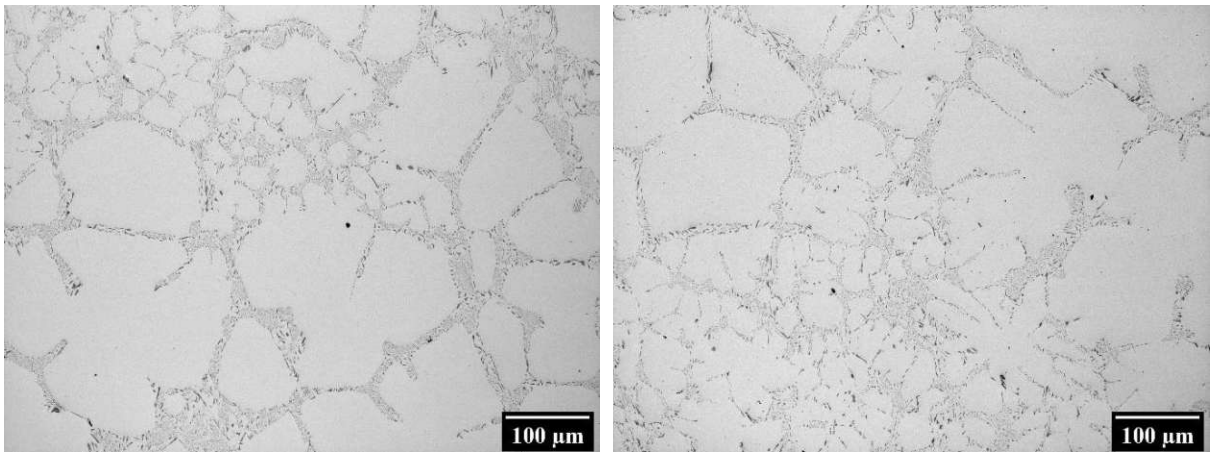

- AA8021, 600°C long term annealing, left: half-time (AA8021 H6), right: full-time (AA8021 F6)

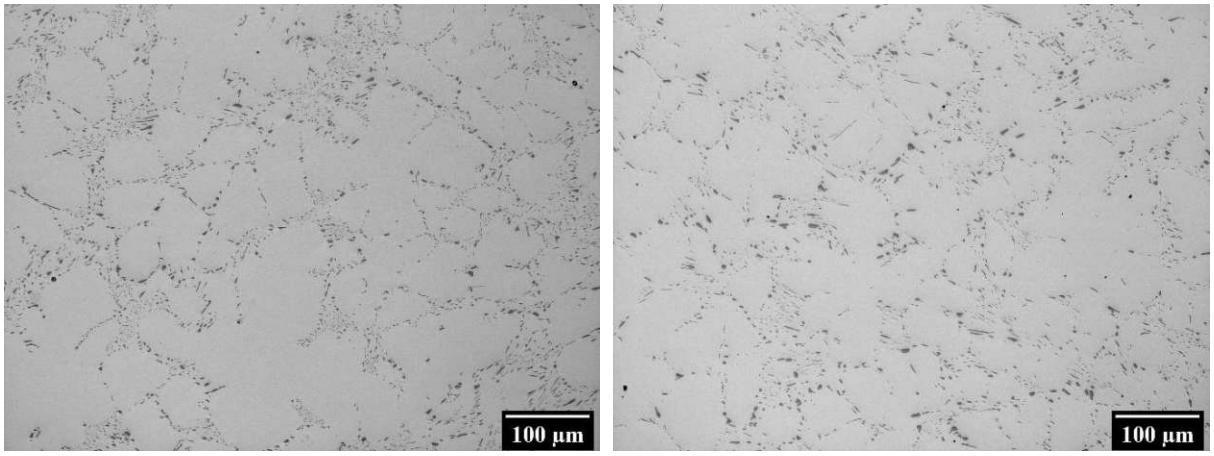

13.8.4 AA8079

- AA8079 As-cast (AA8079 AC)

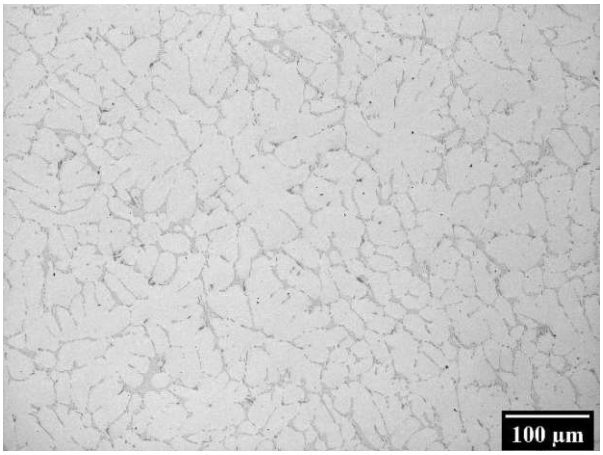

- AA8079, 400°C long term annealing, left: half-time (AA8079 H4), right: full-time (AA8079 F4)

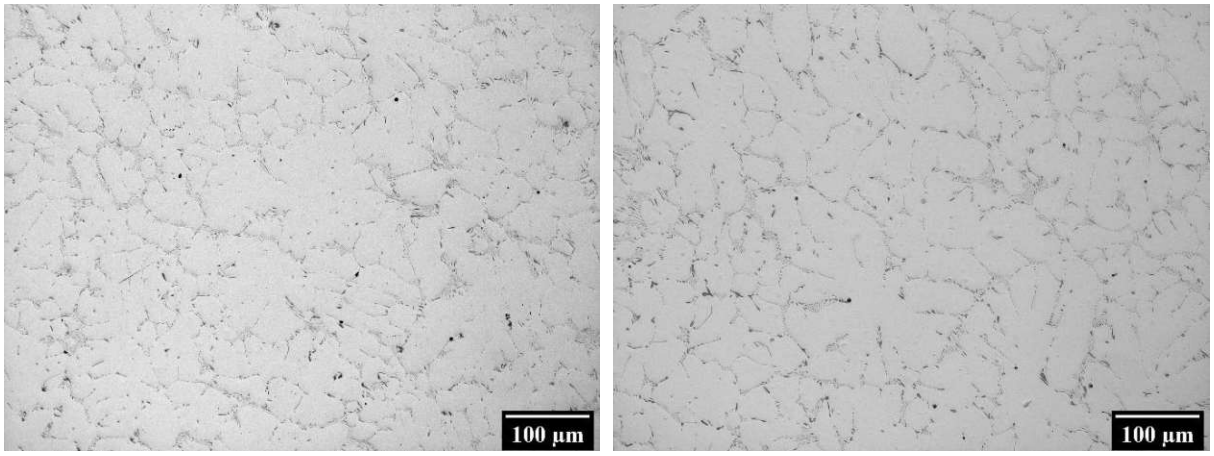

- AA8079, 500°C long term annealing, left: half-time (AA8079 H5), right: full-time (AA8079 F5)

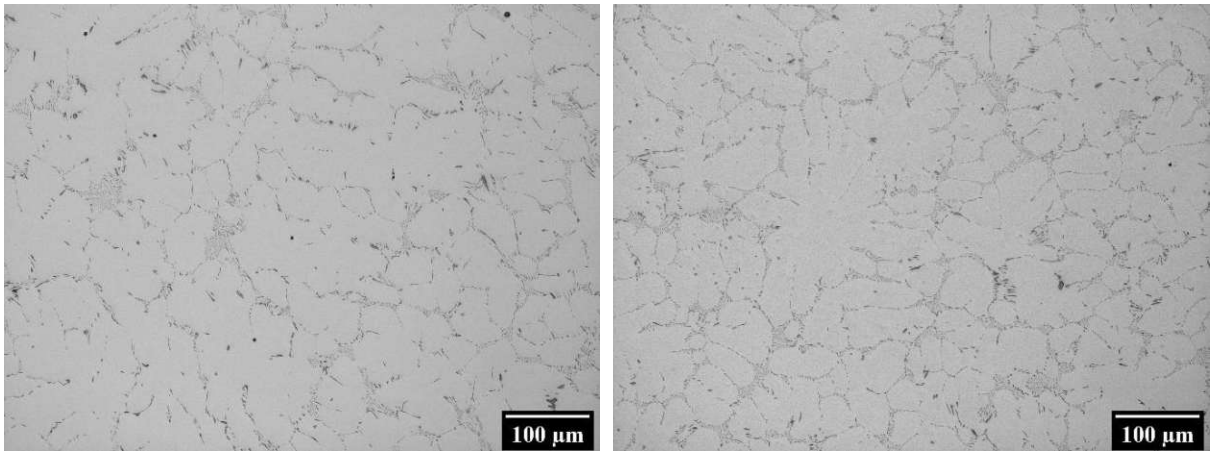

- AA8079, 600°C long term annealing, left: half-time (AA8079 H6), right: full-time (AA8079 F6)

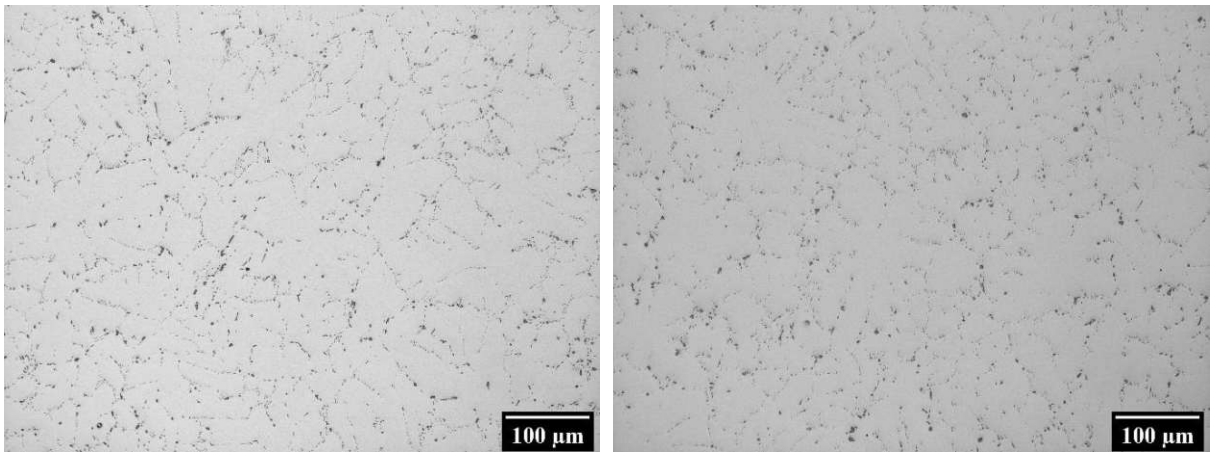

13.9 Etched light microscopy images

13.9.1 AA8011

- AA8011 F4

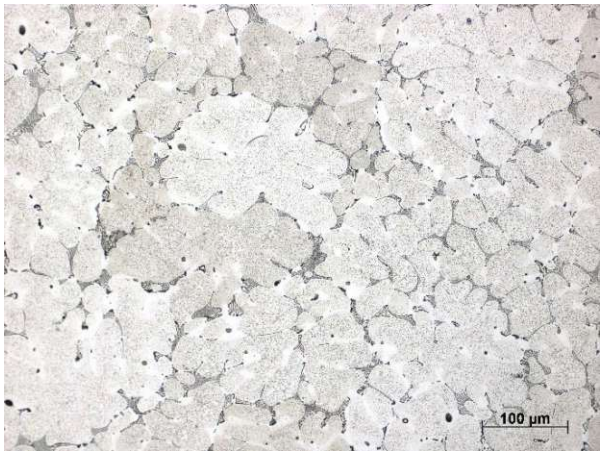

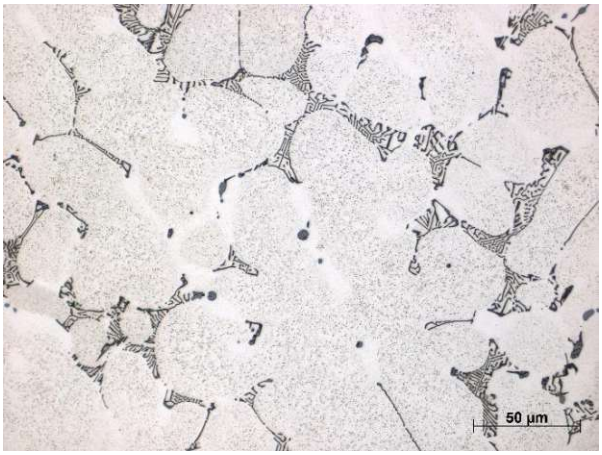

- AA8011 F5

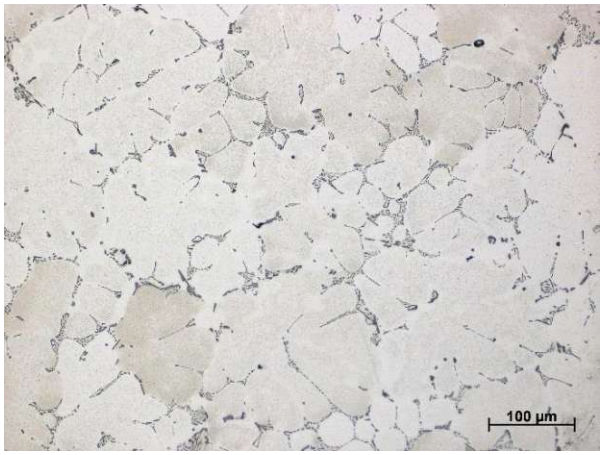

- AA8011 F6

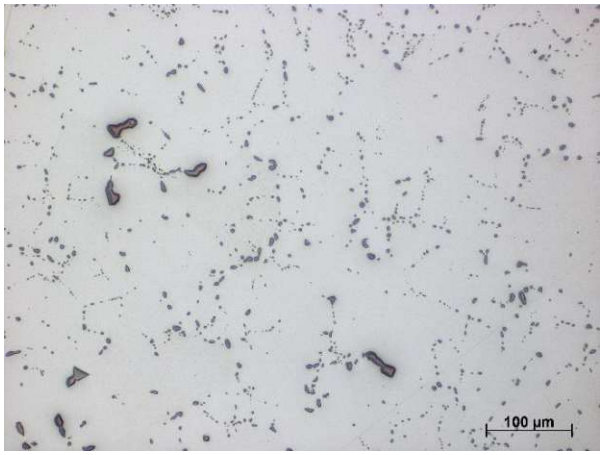

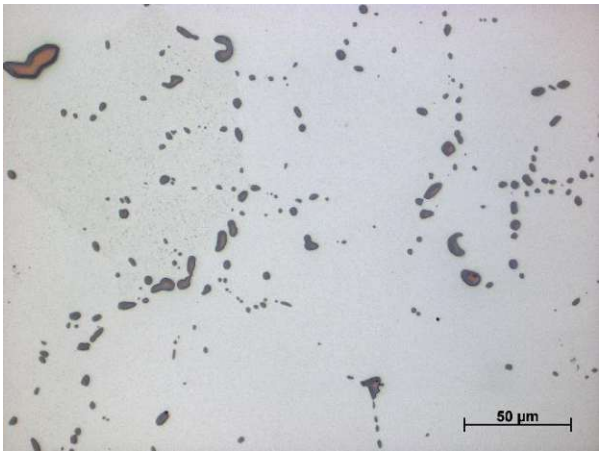

13.9.2 AA8014

- AA8014 F4

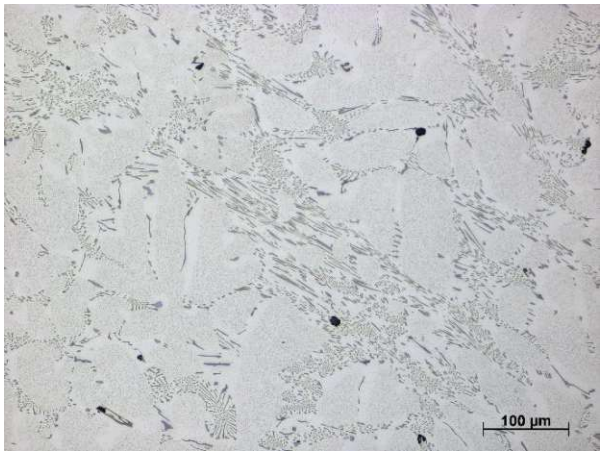

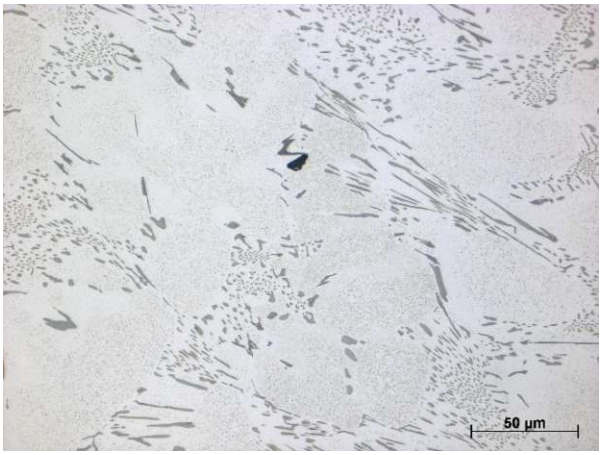

- AA8014 F5

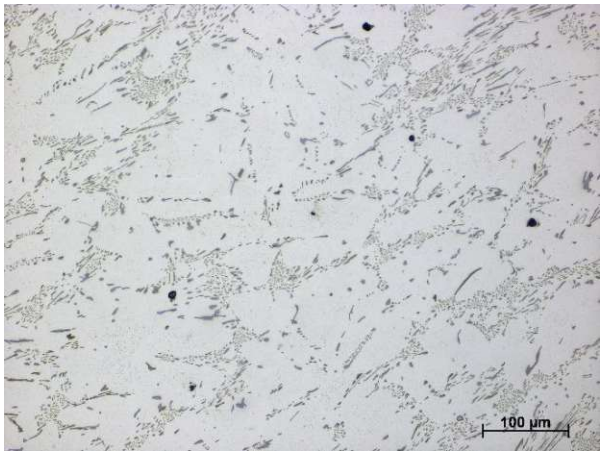

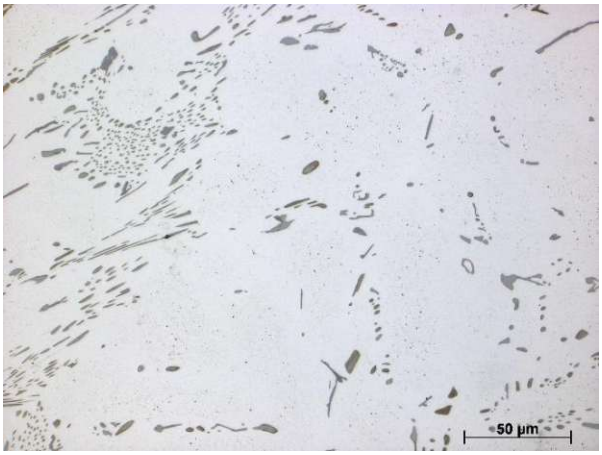

- AA8014 F6

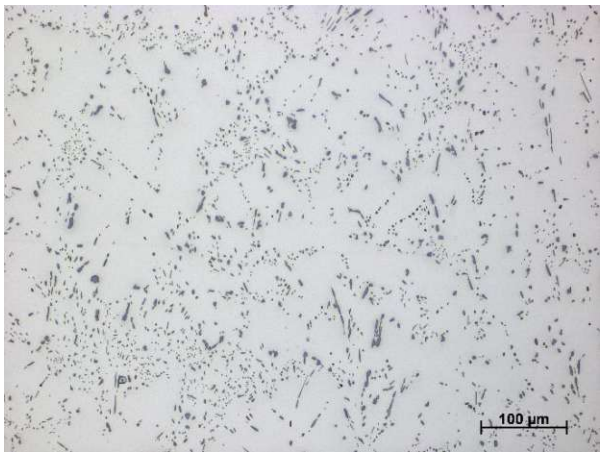

13.9.3 AA8021

- AA8021 F4

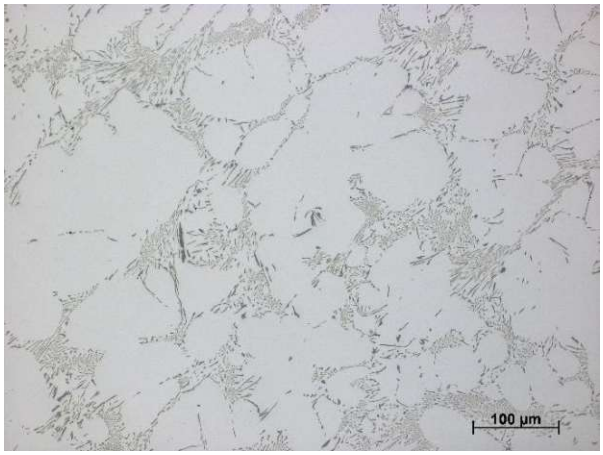

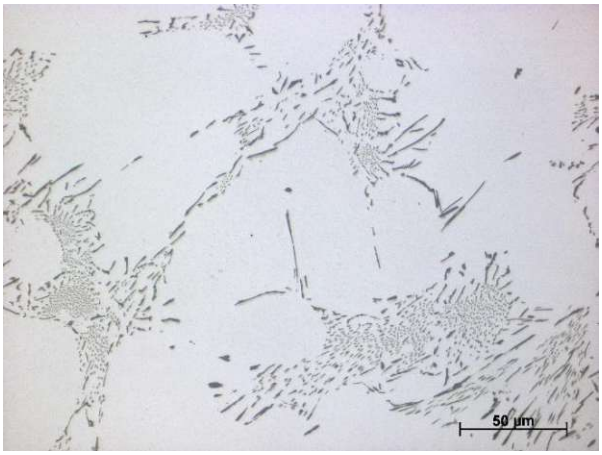

- AA8021 F5

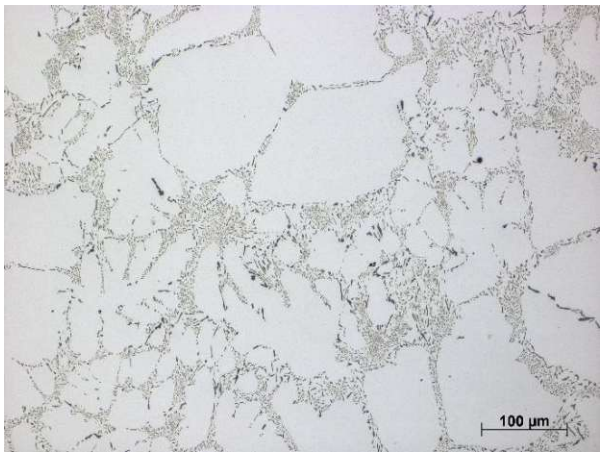

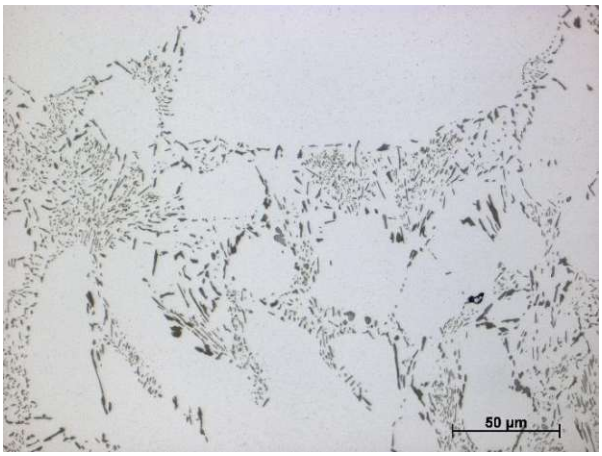

- AA8021 F6

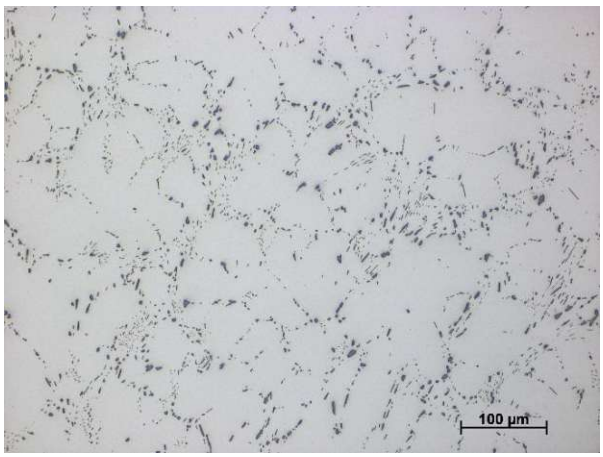

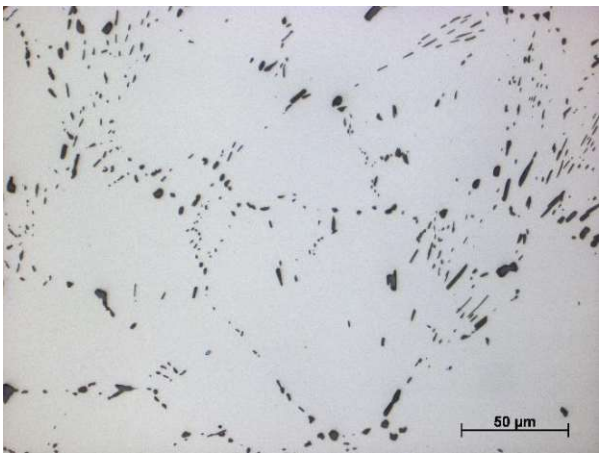

13.9.4 AA8079

- AA8079 F4

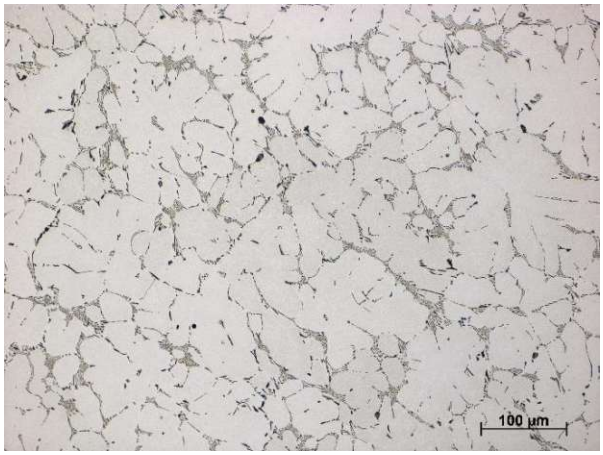

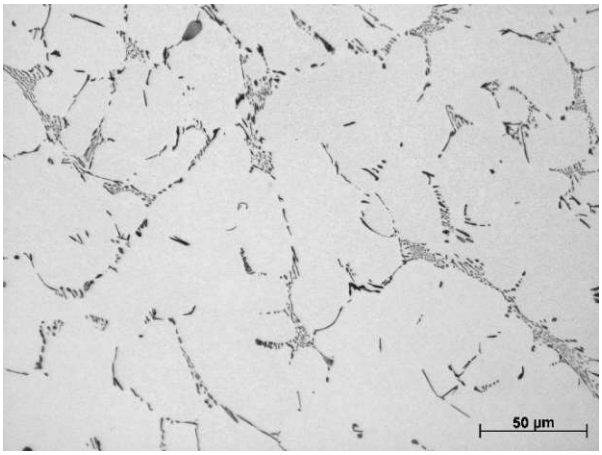

- AA8079 F5

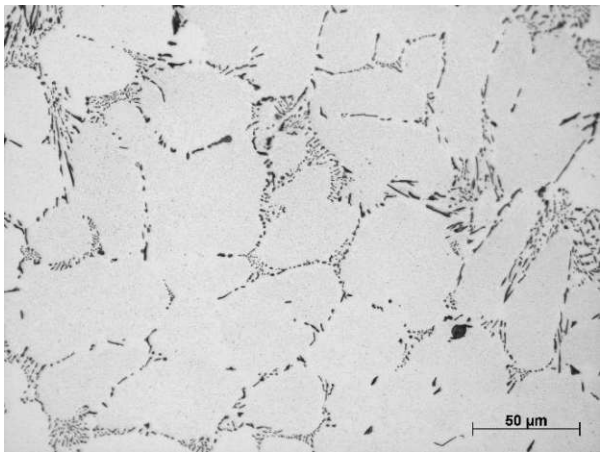

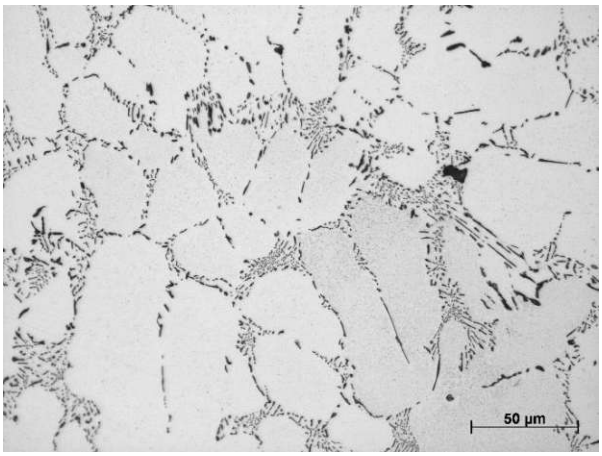

- AA8079 F6

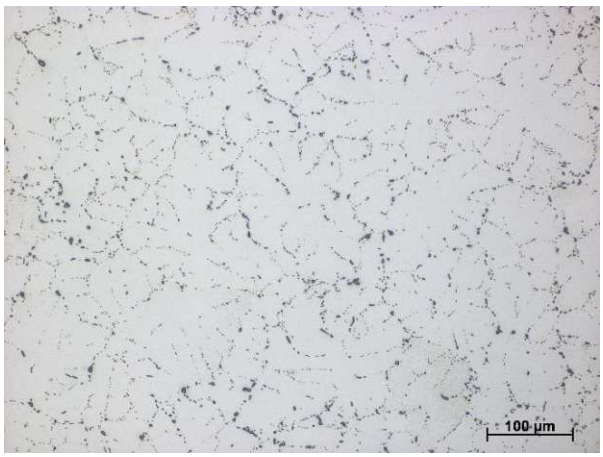

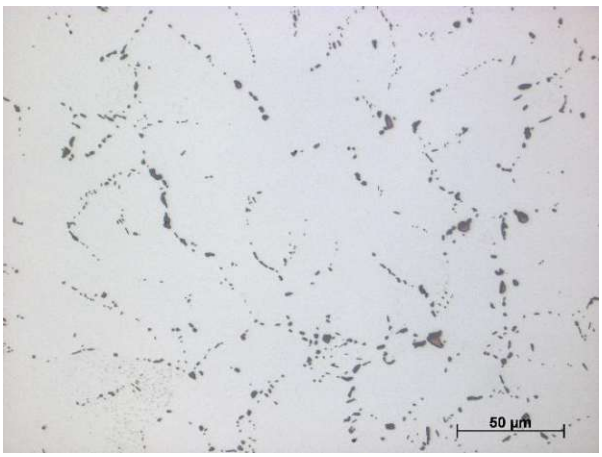

13.10 XRD Diffractograms

13.10.1 Bulk samples

13.10.1.1 AA8011

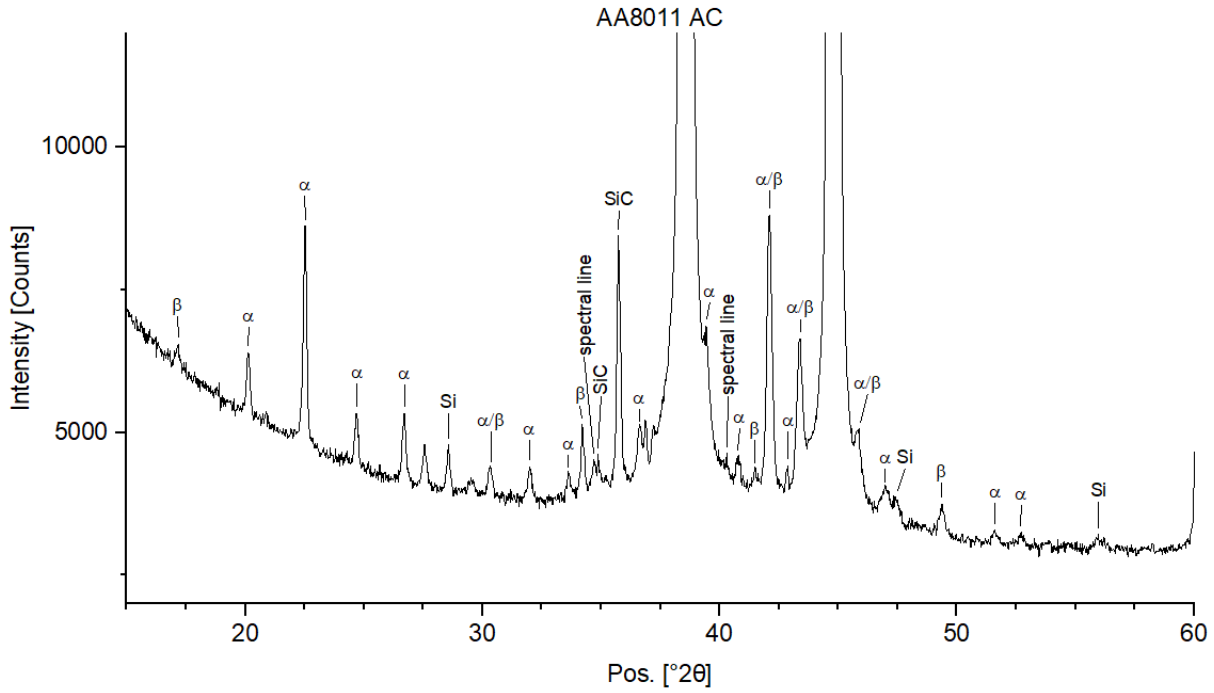

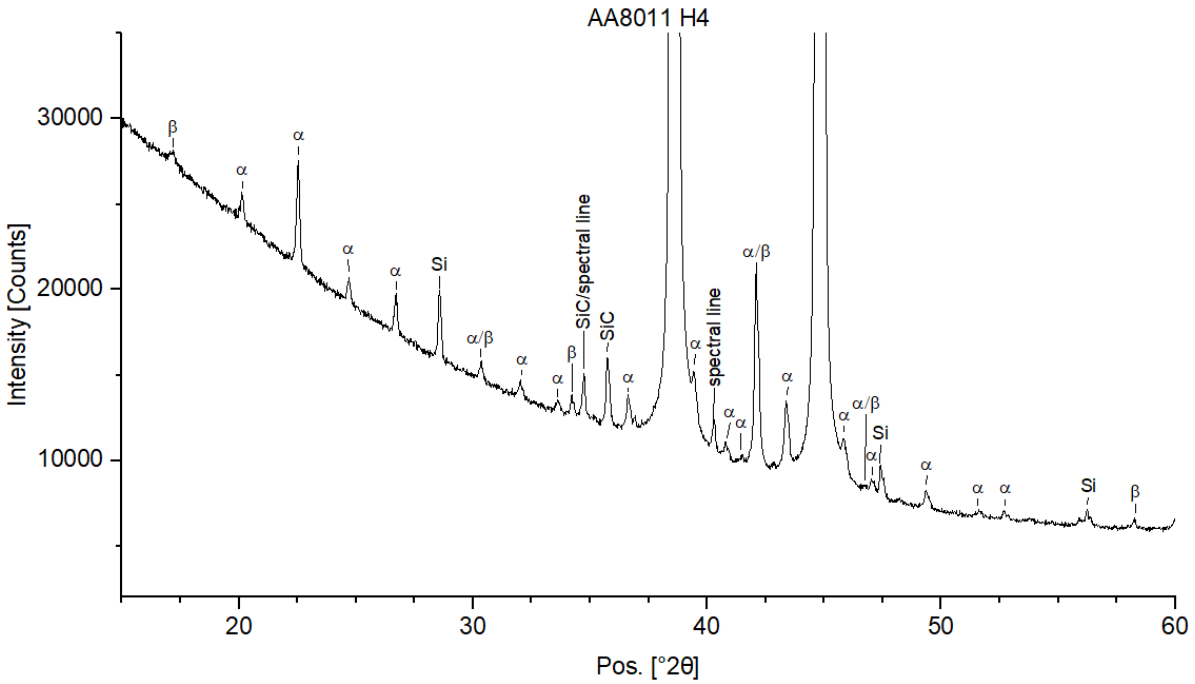

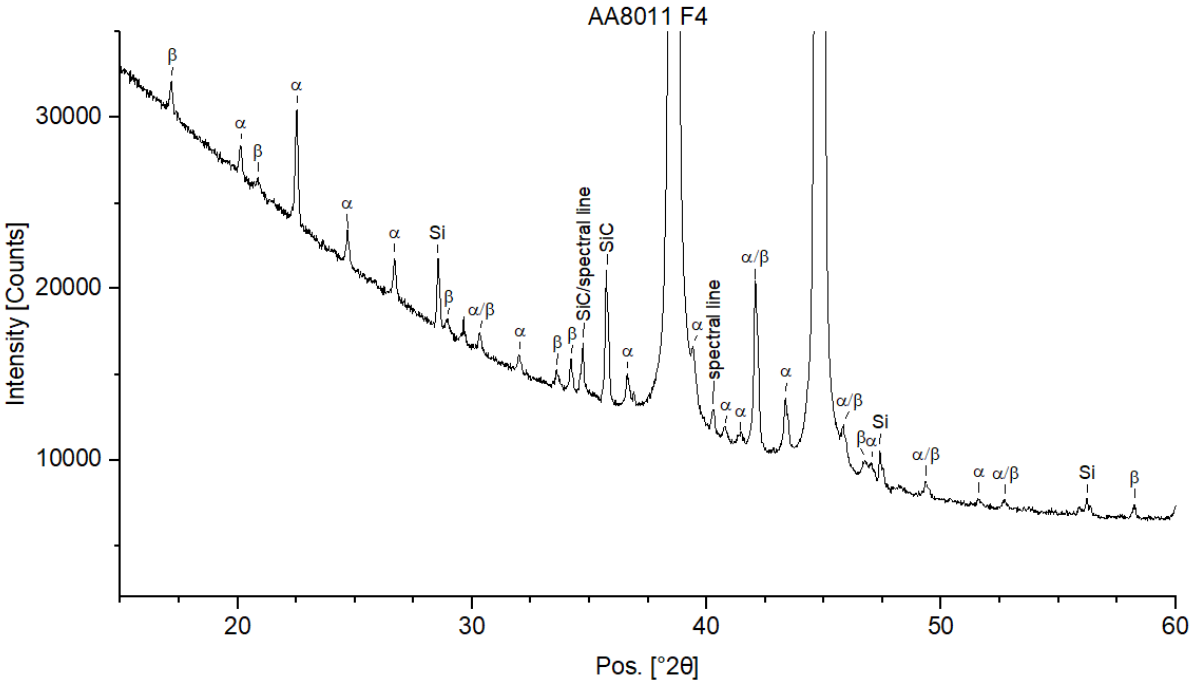

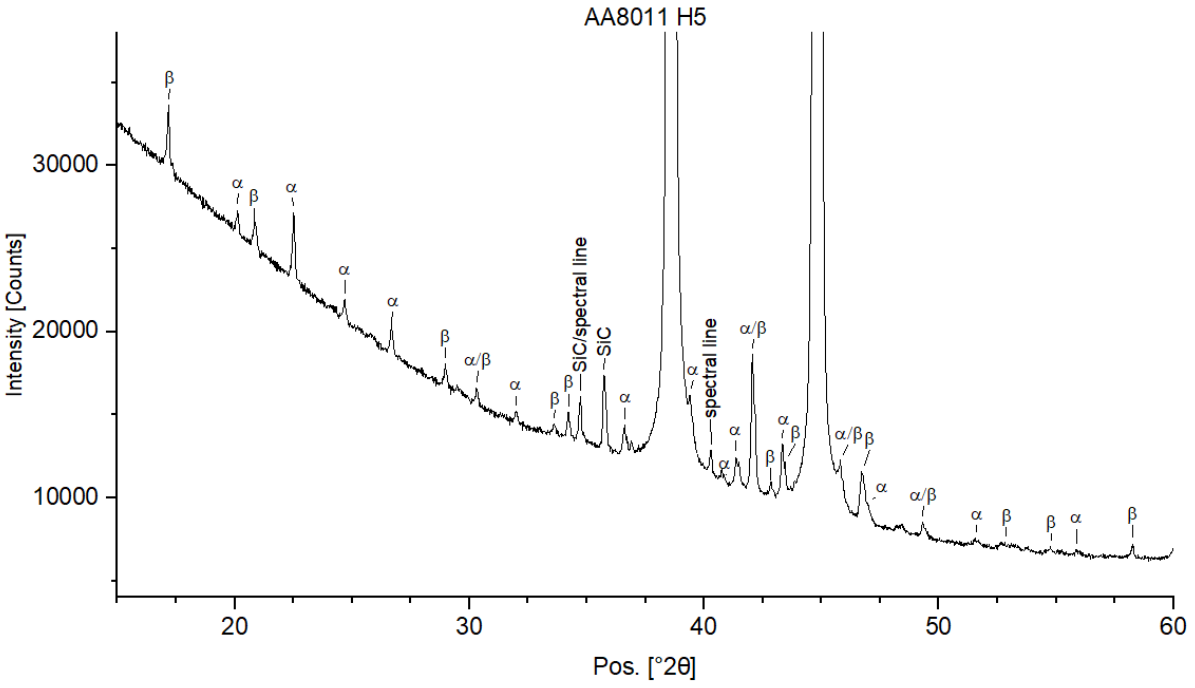

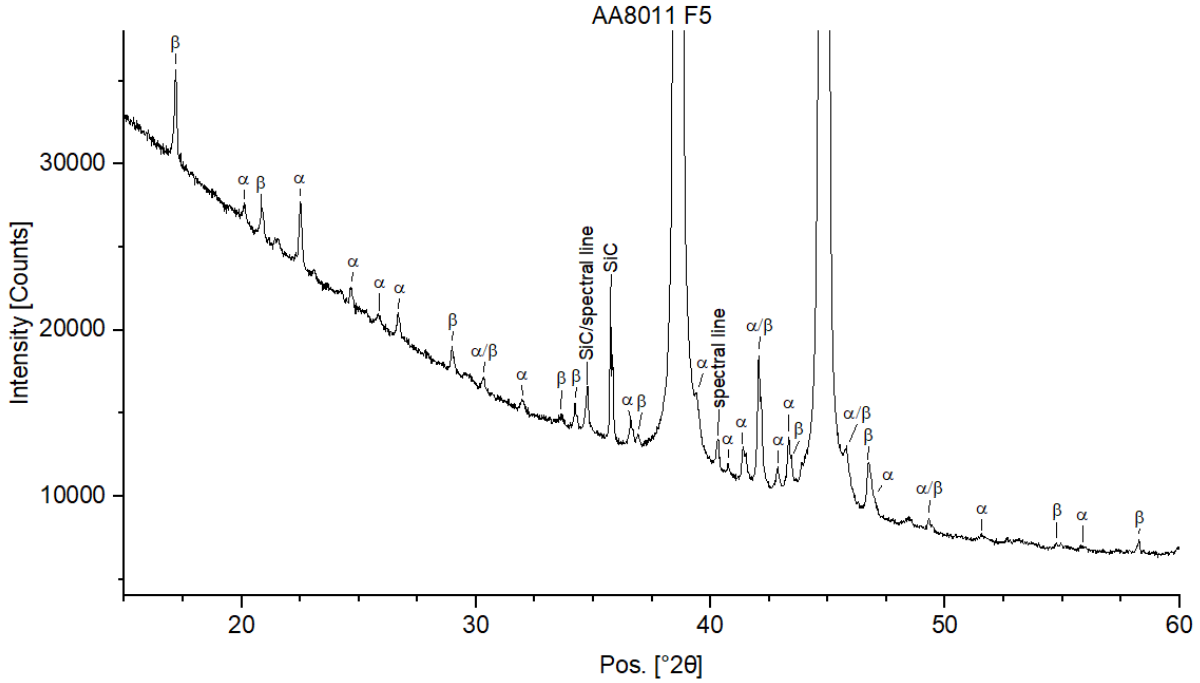

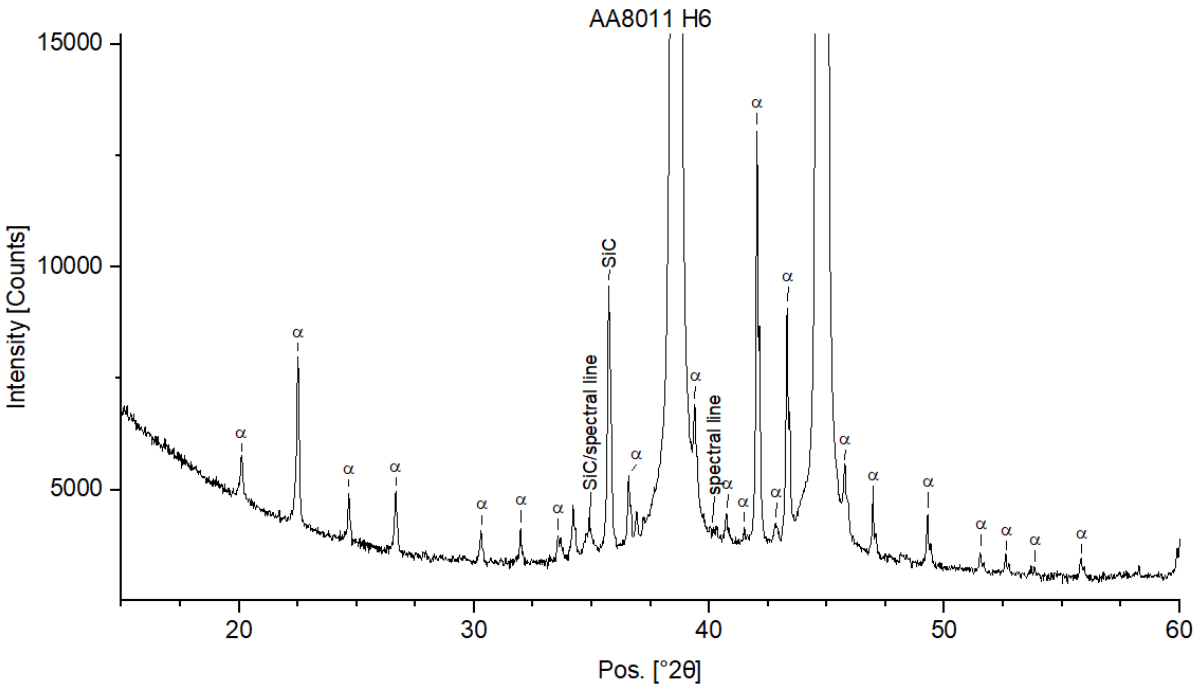

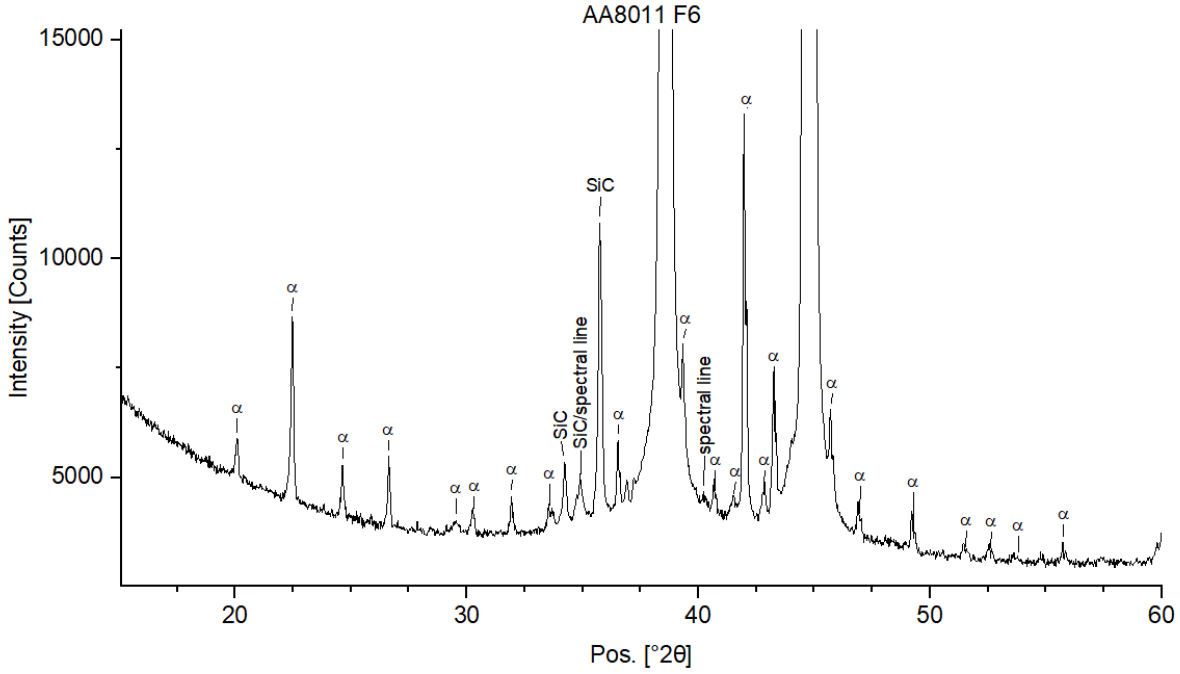

13.10.1.2 AA8014

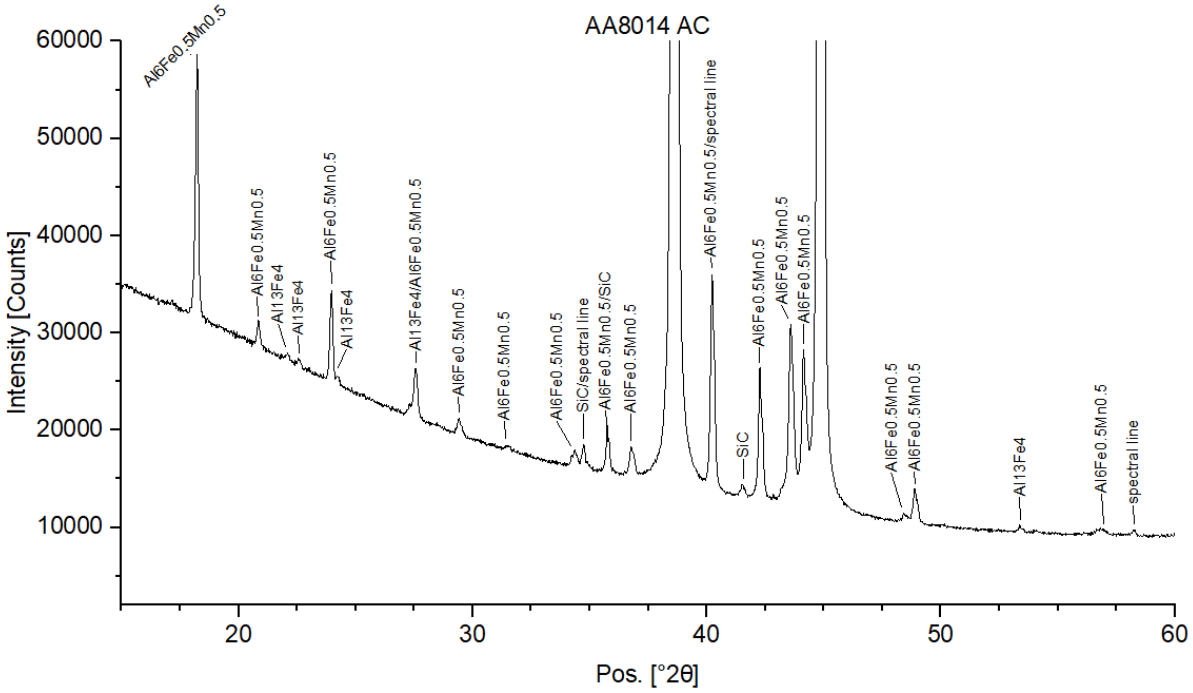

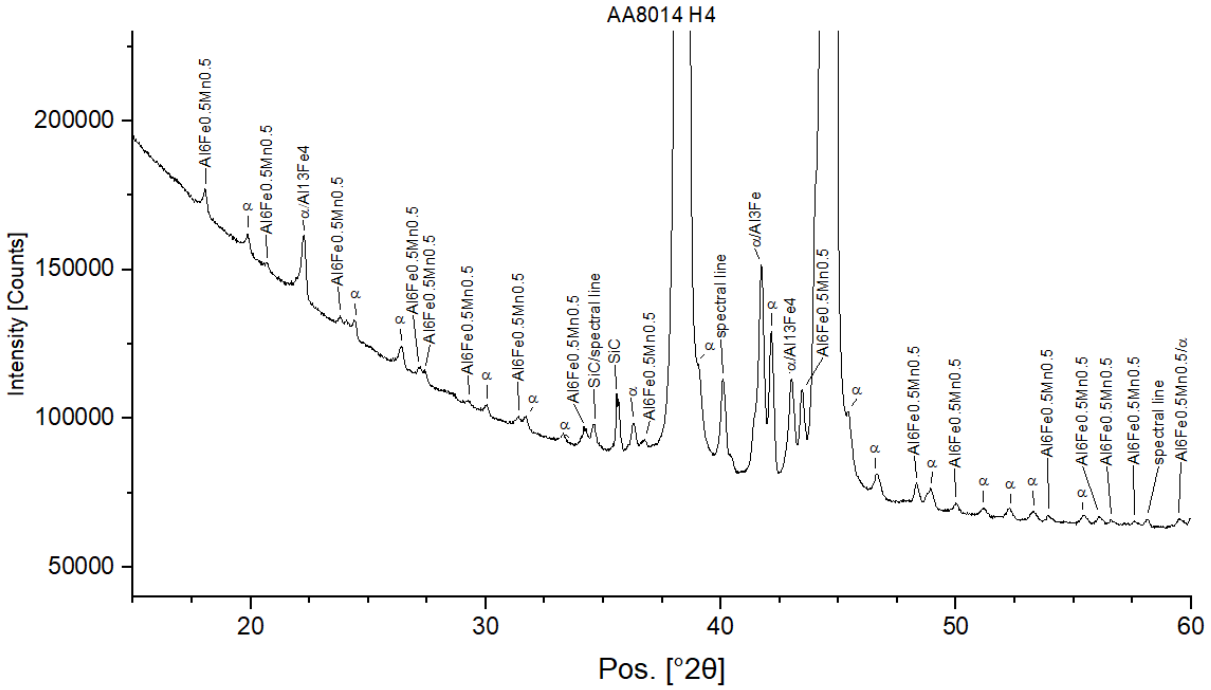

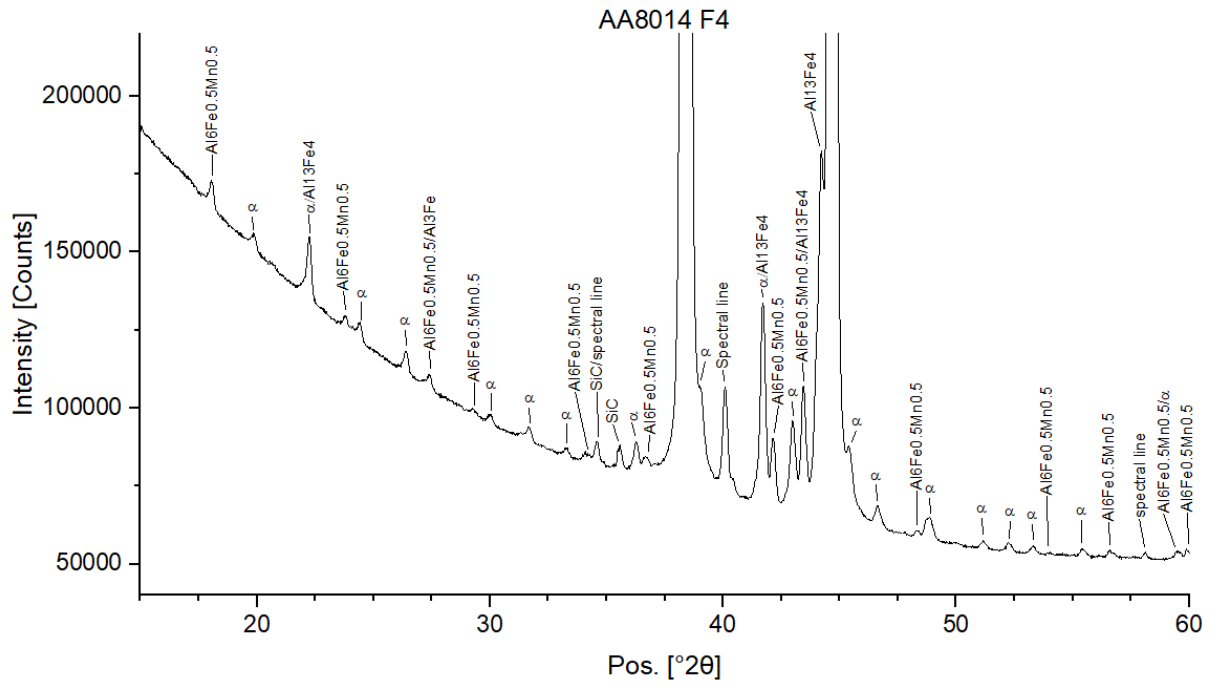

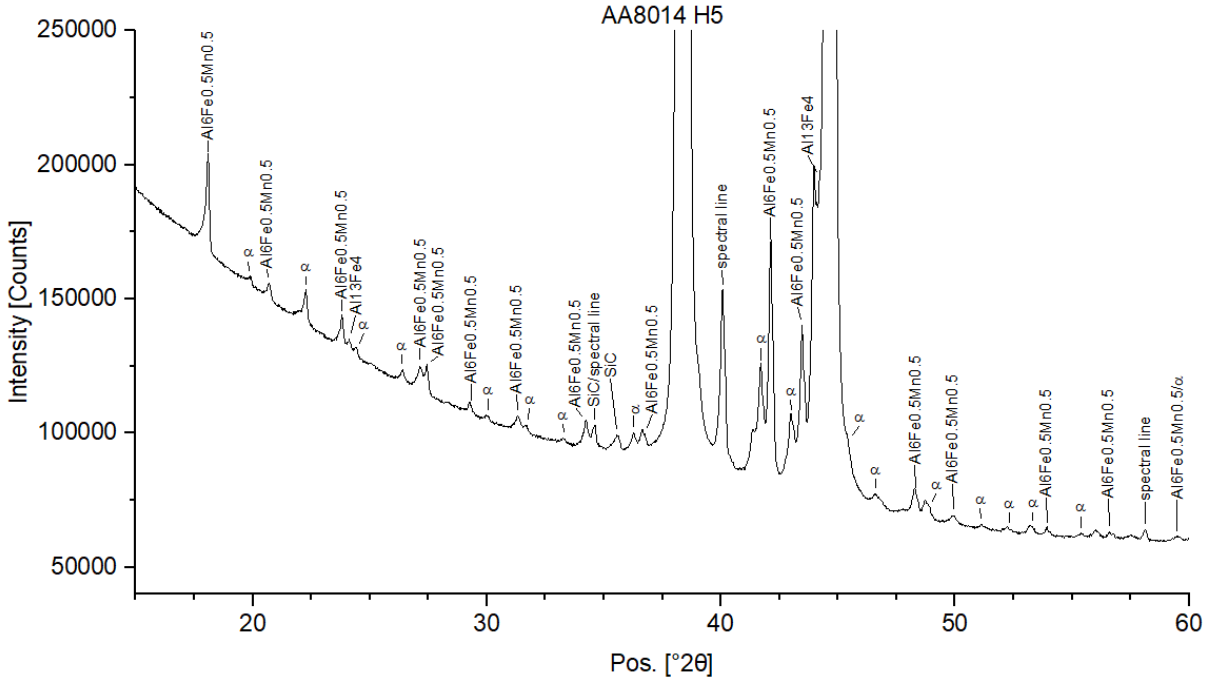

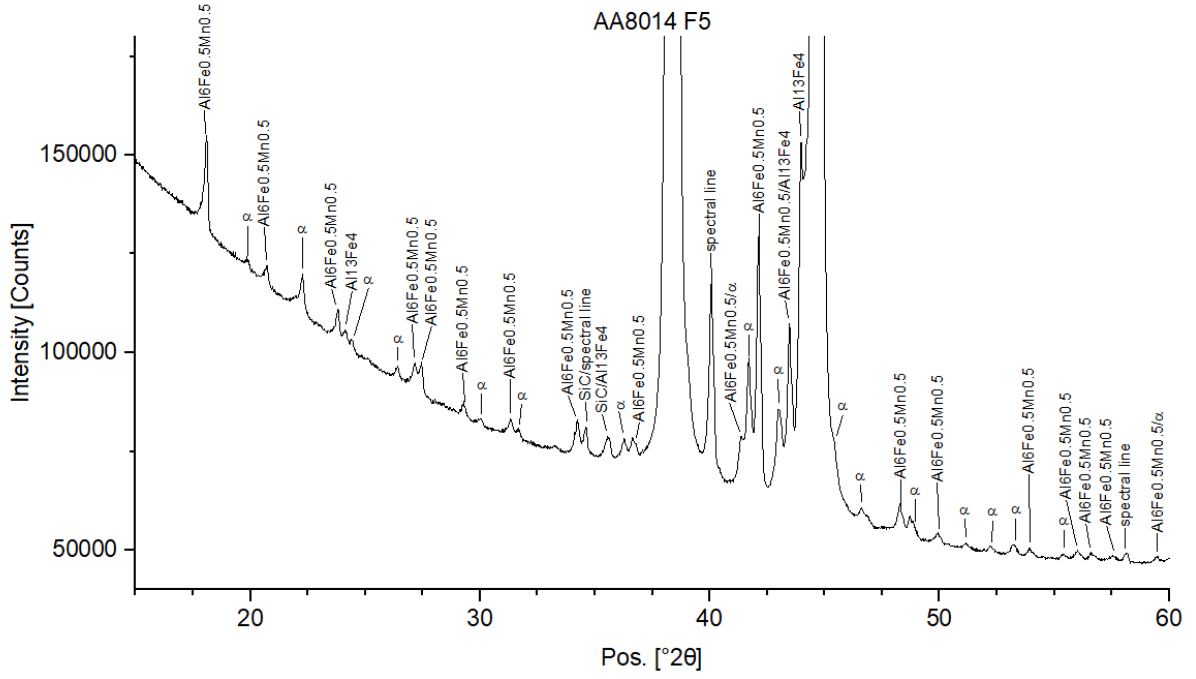

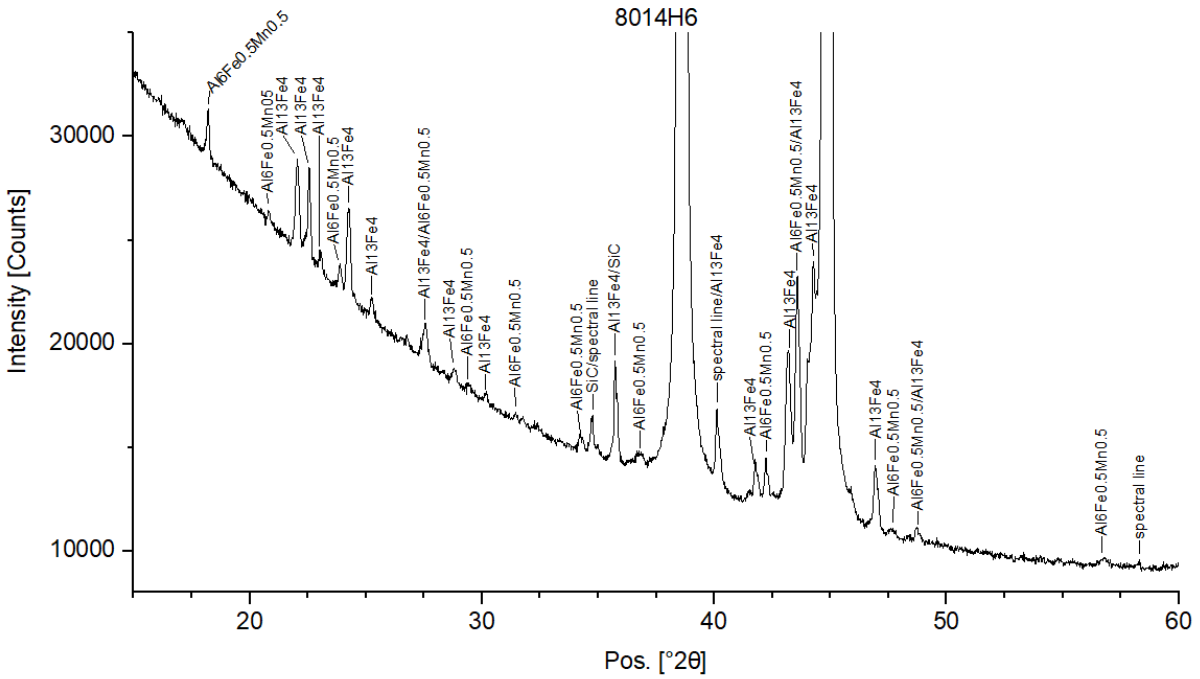

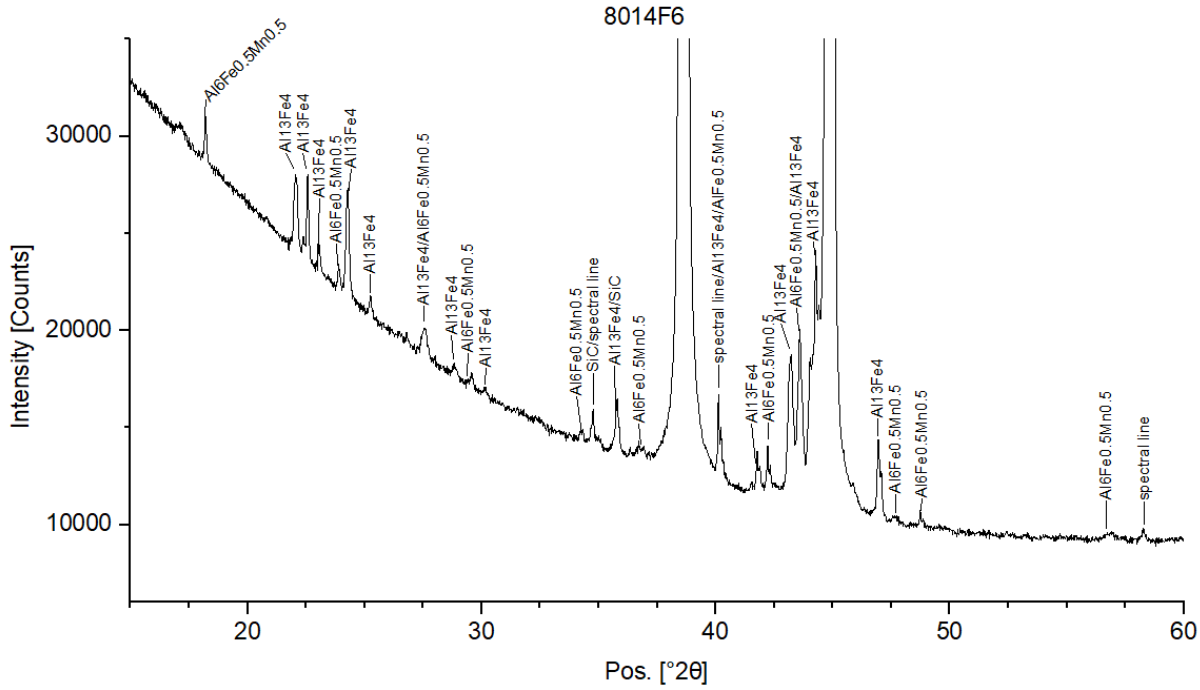

13.10.1.3 AA8021

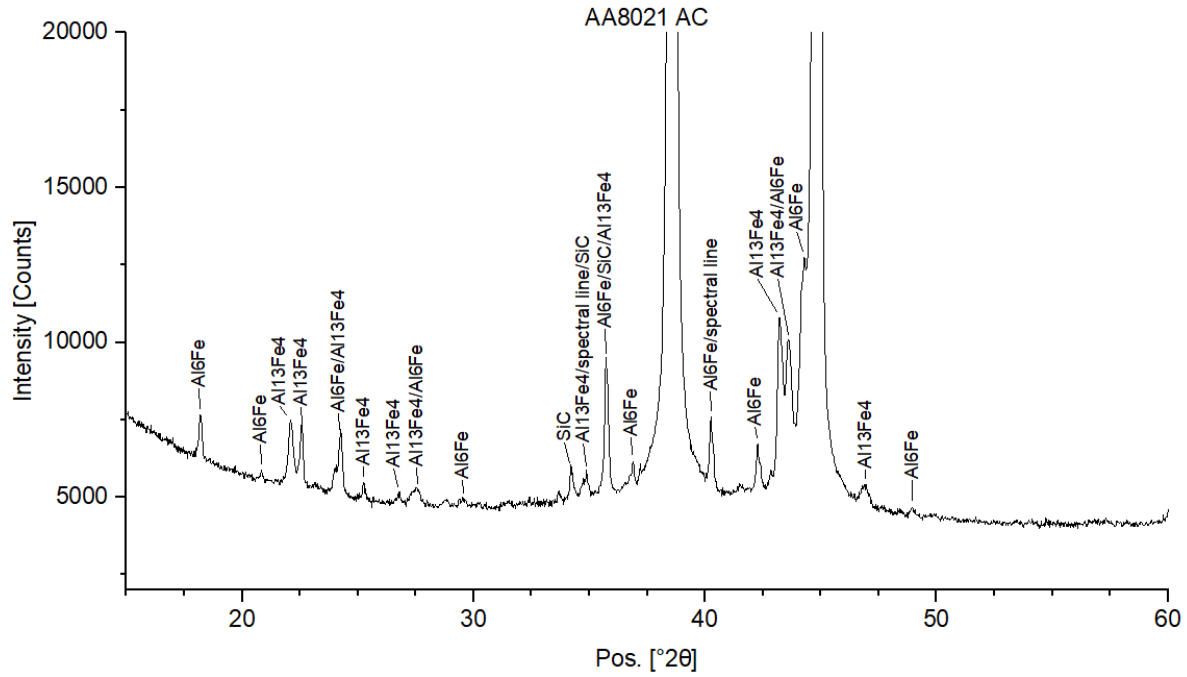

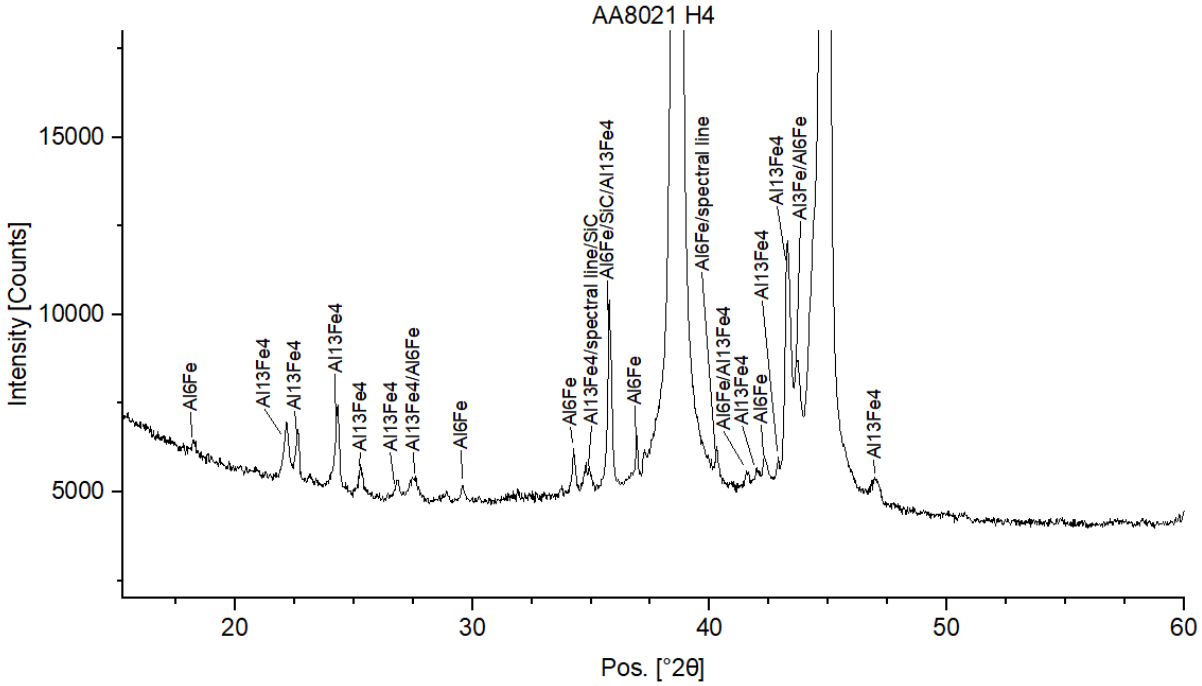

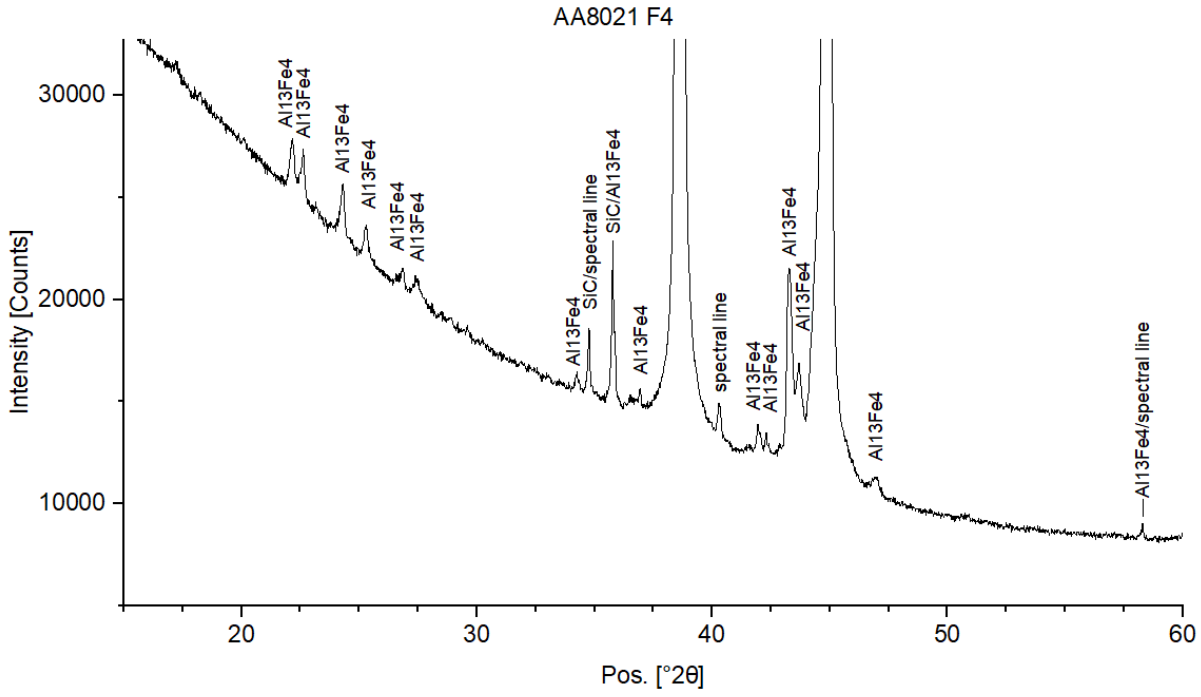

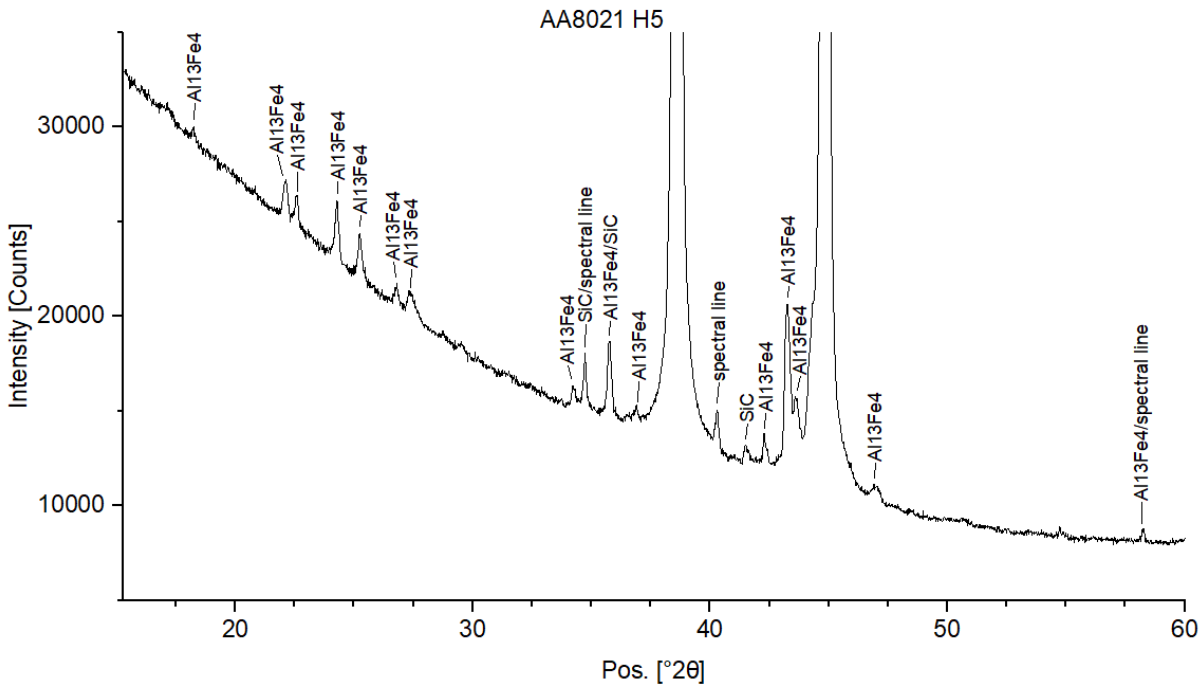

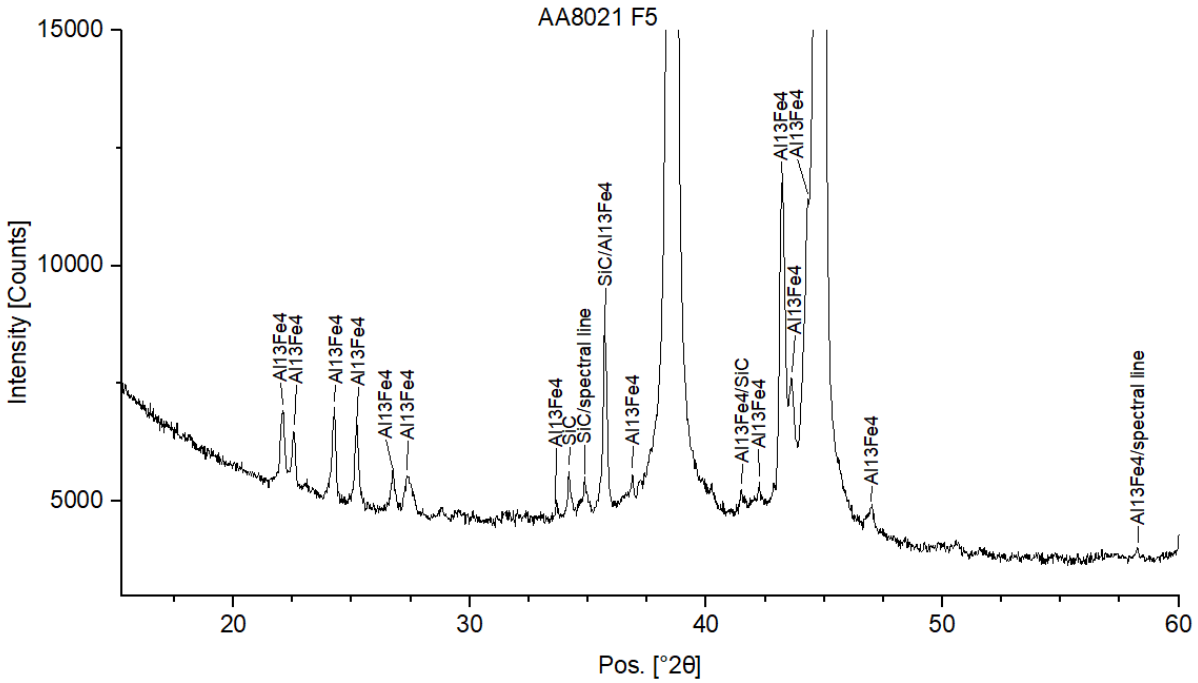

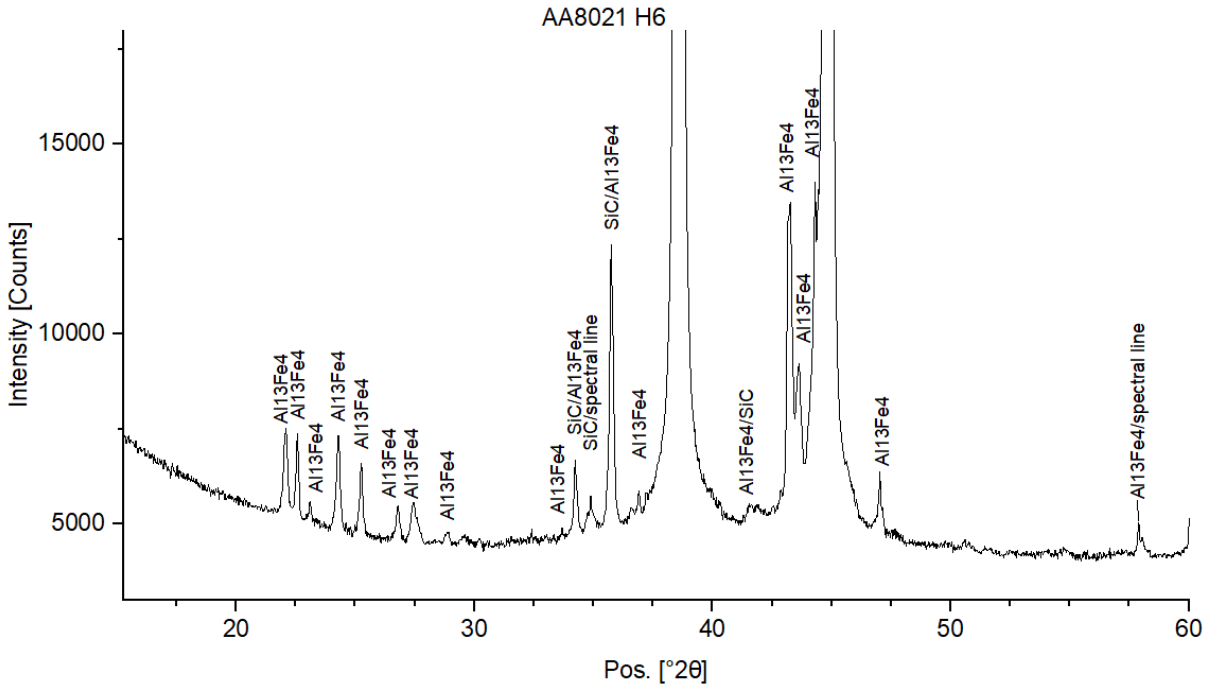

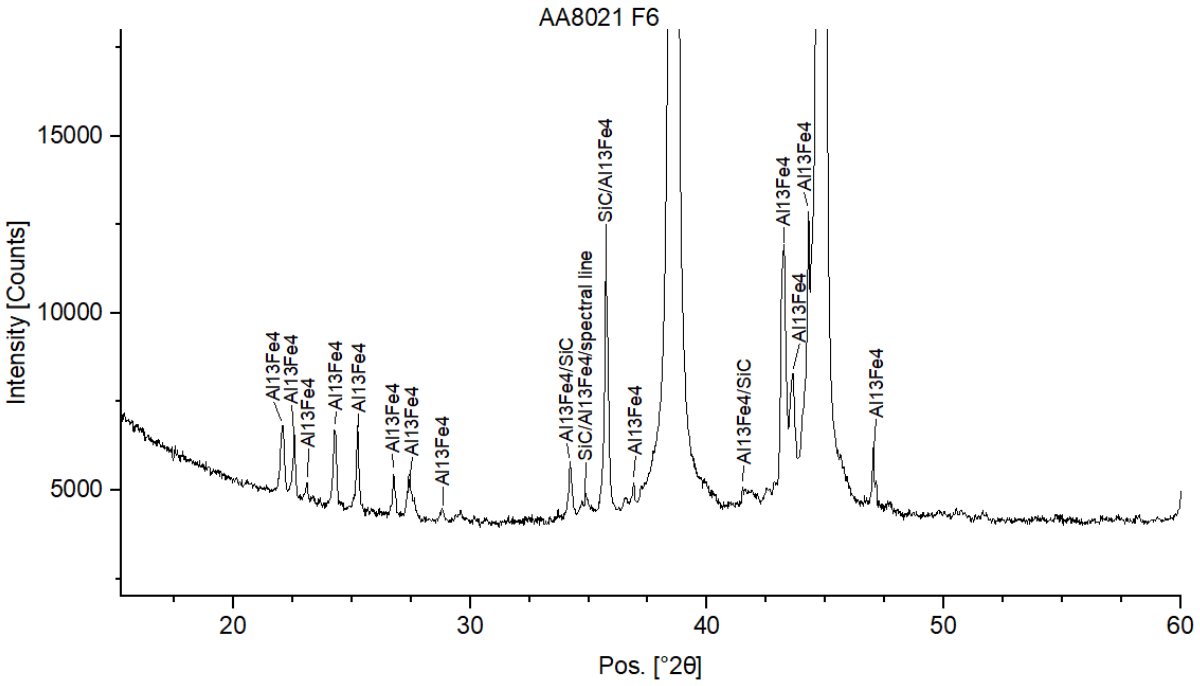

13.10.1.4 AA8079

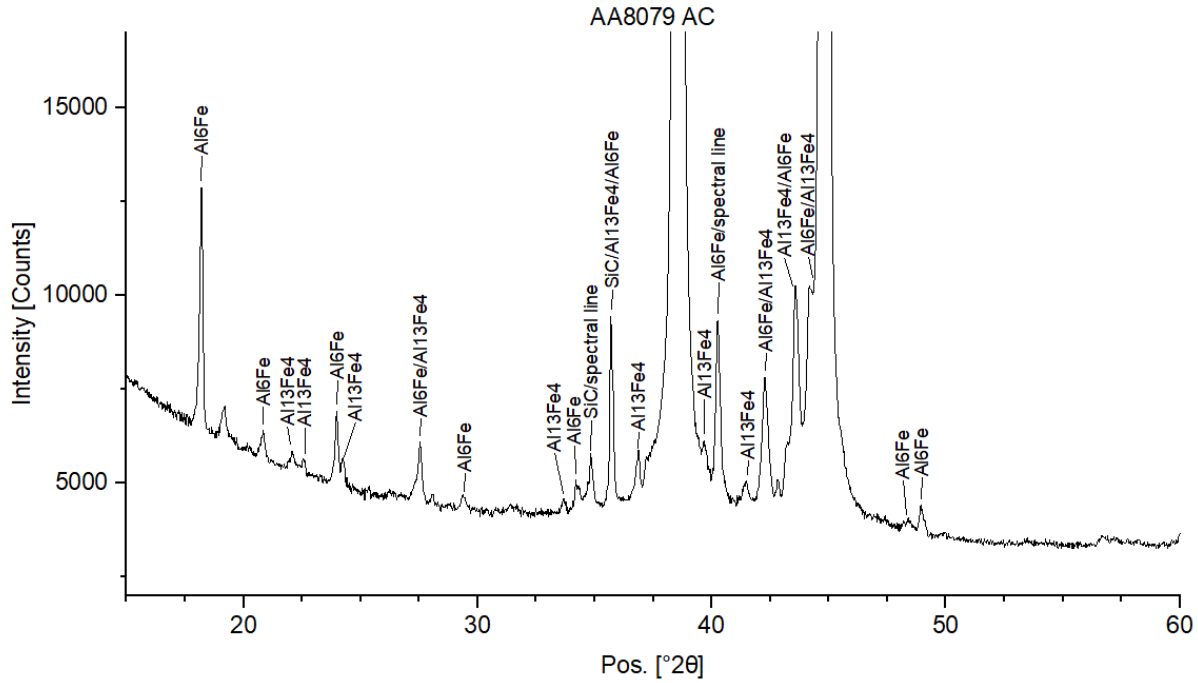

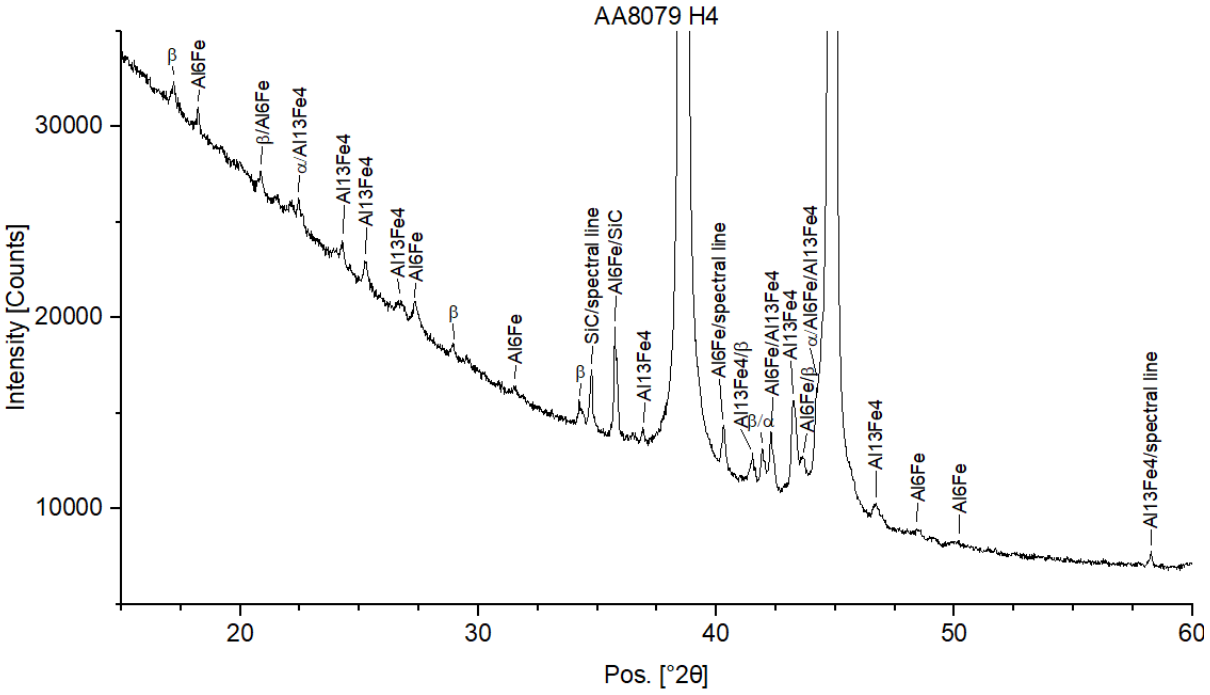

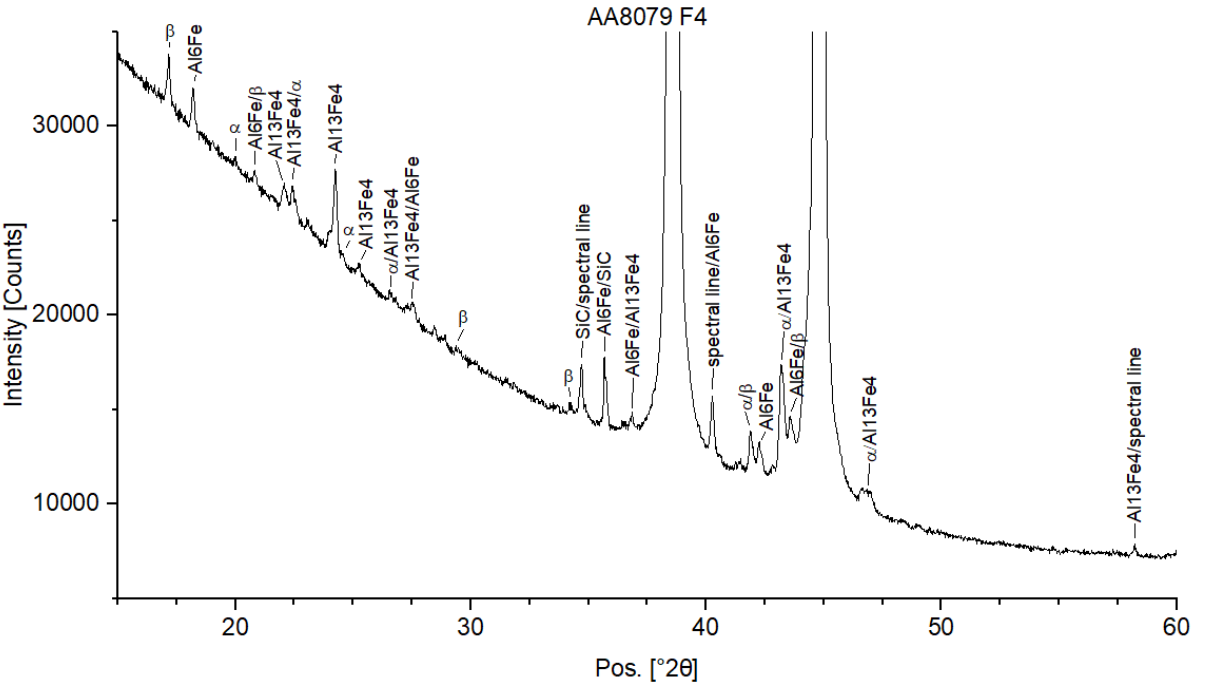

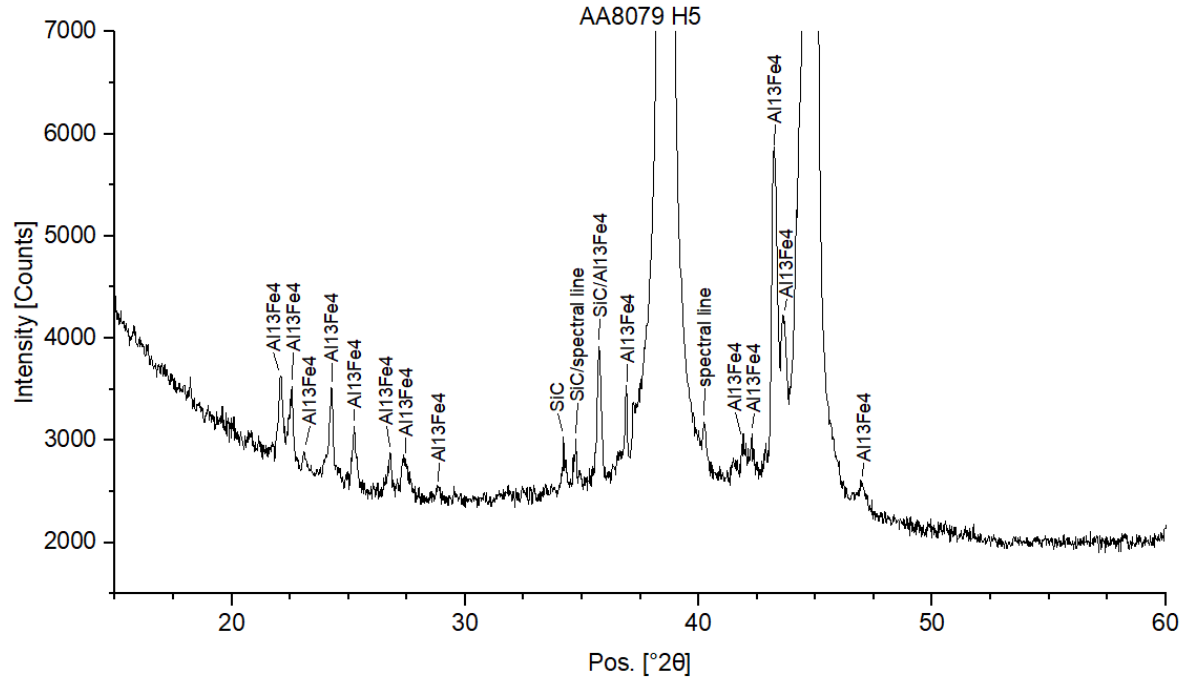

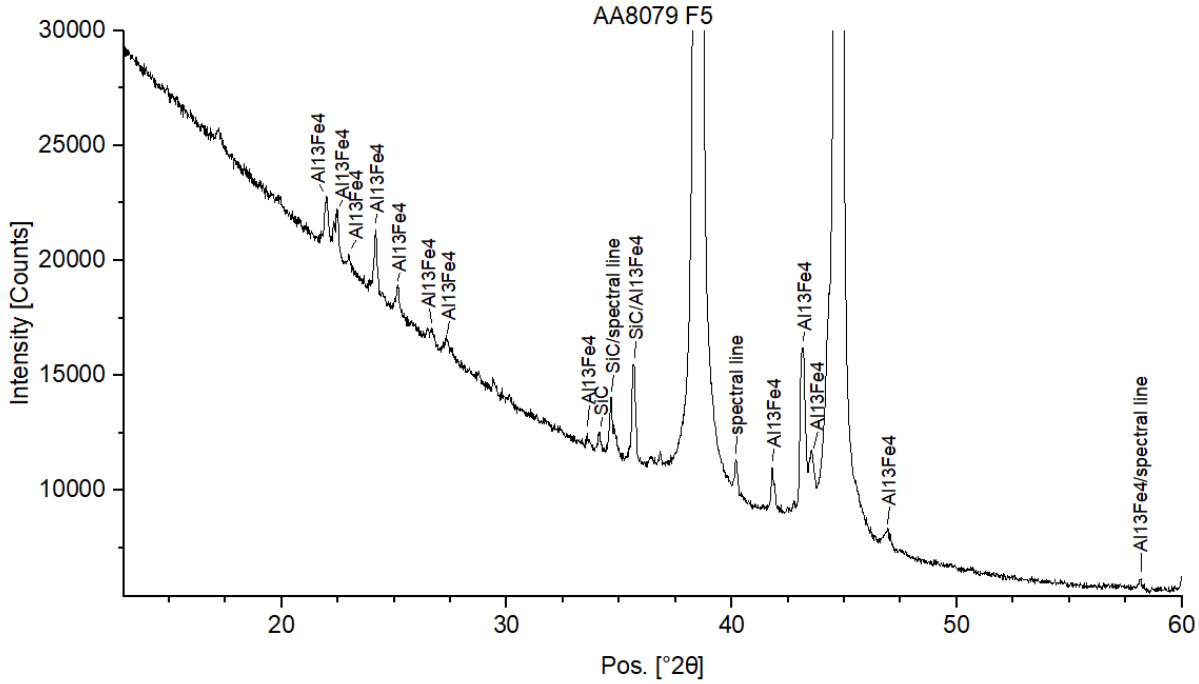

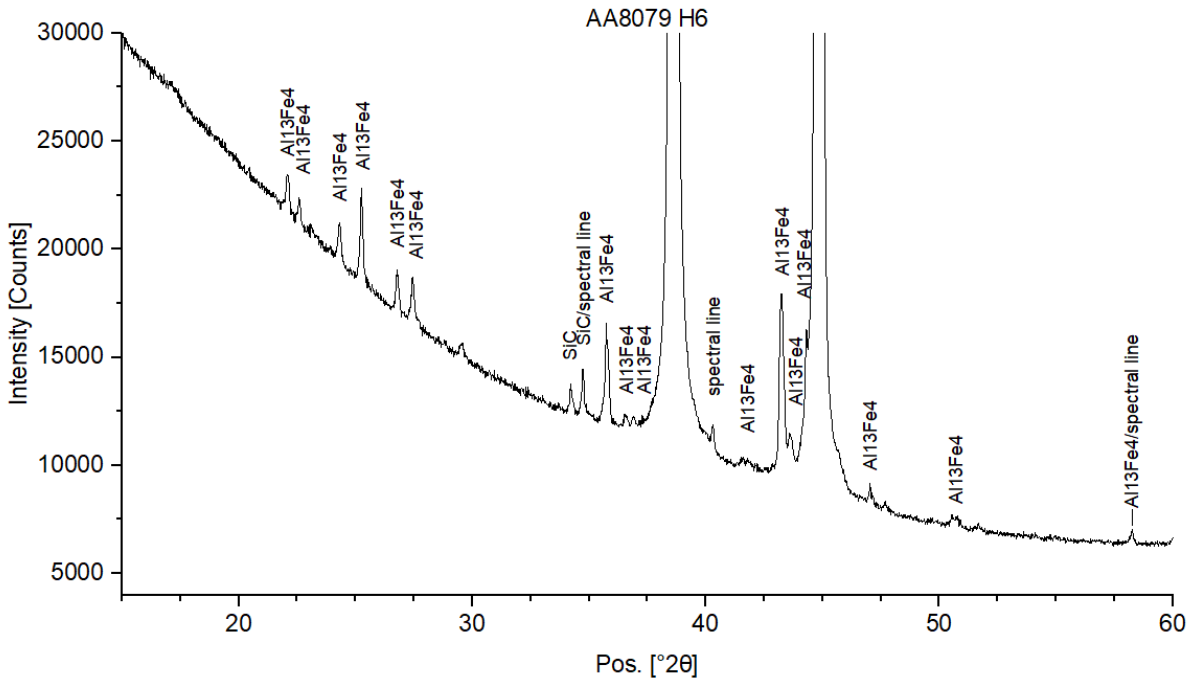

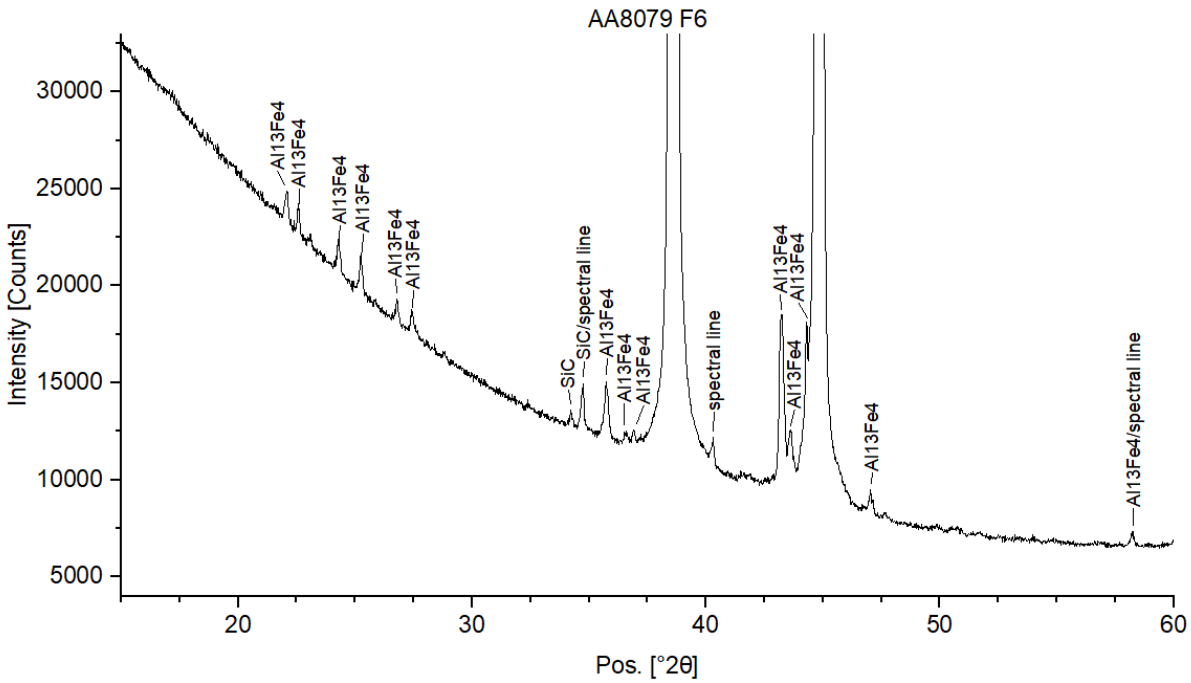

13.10.2 The powders

13.10.2.1 AA8011

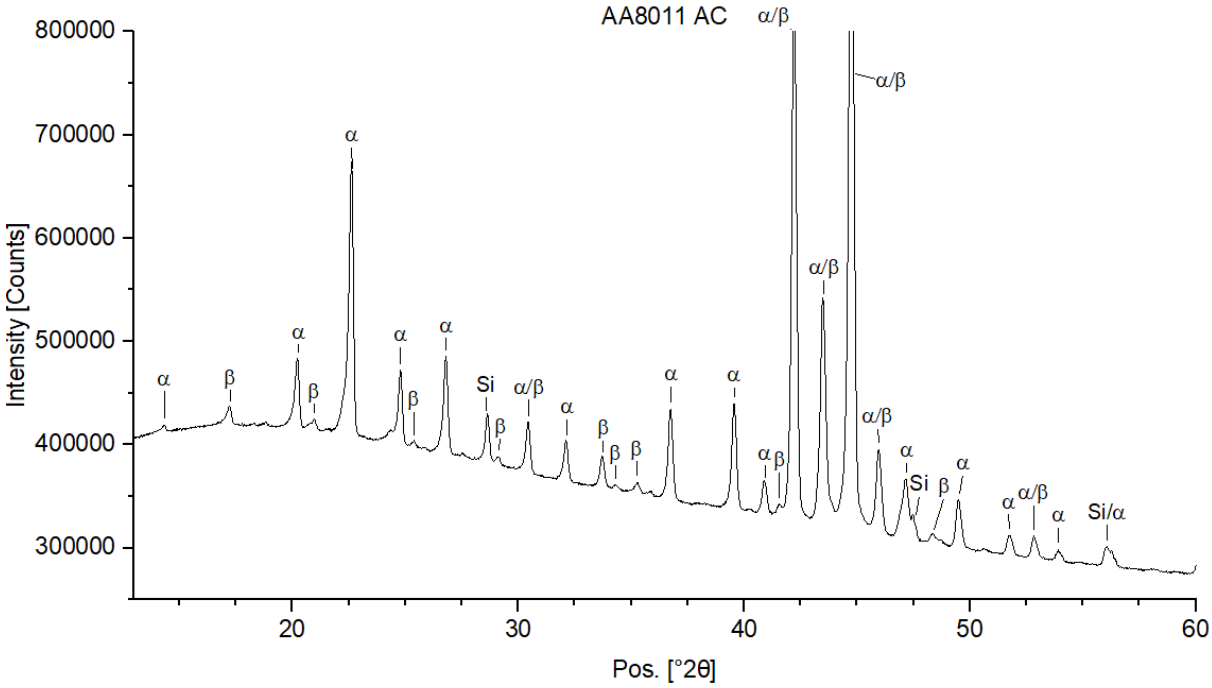

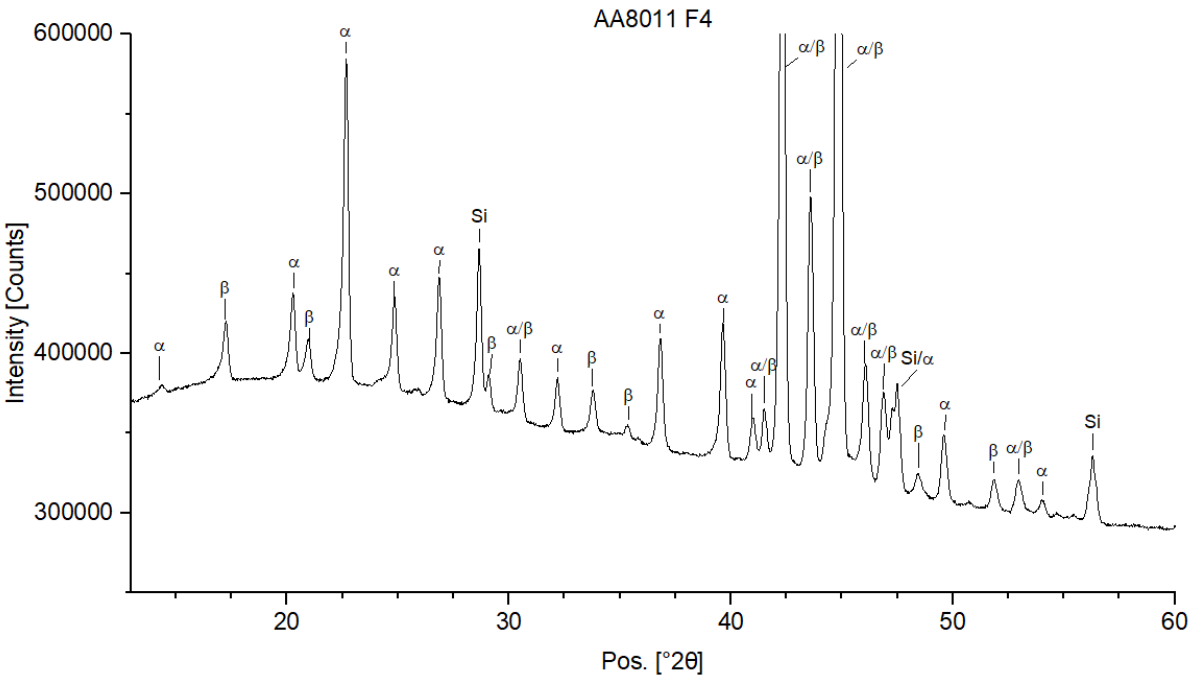

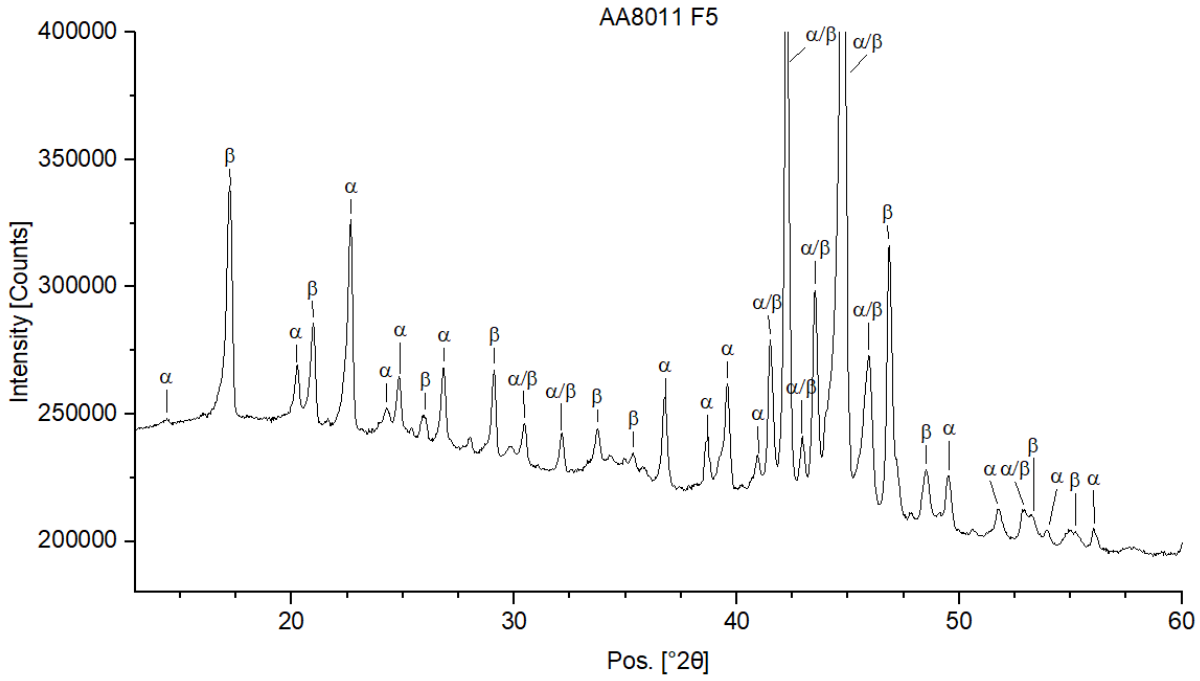

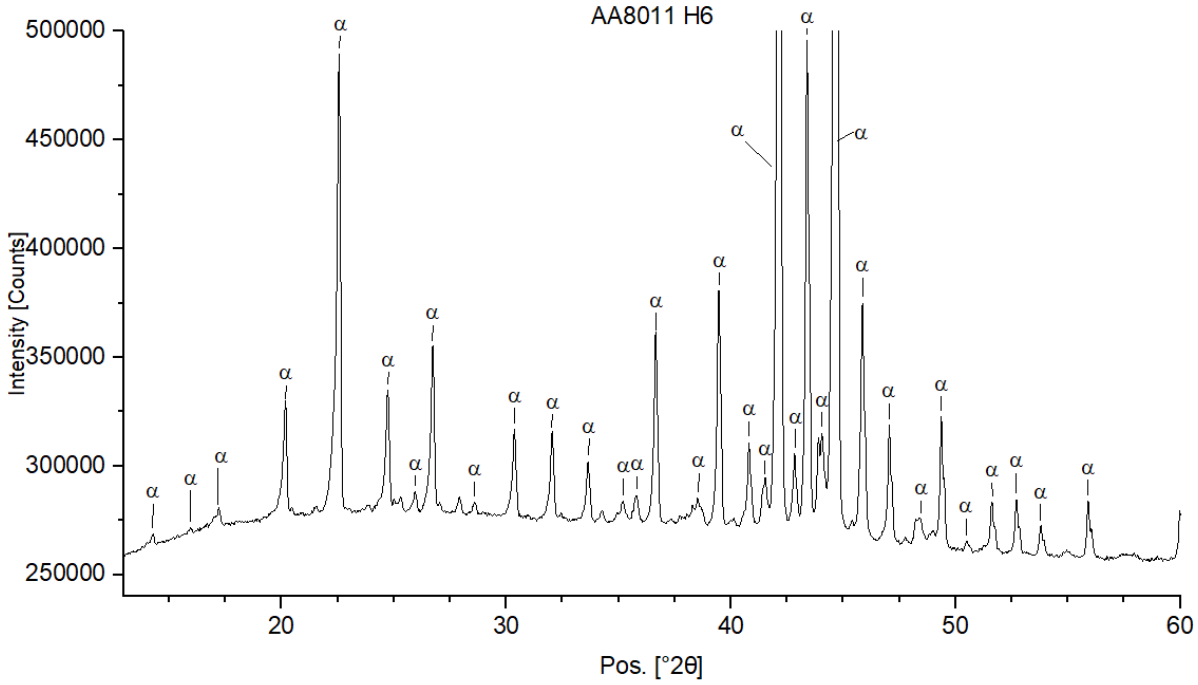

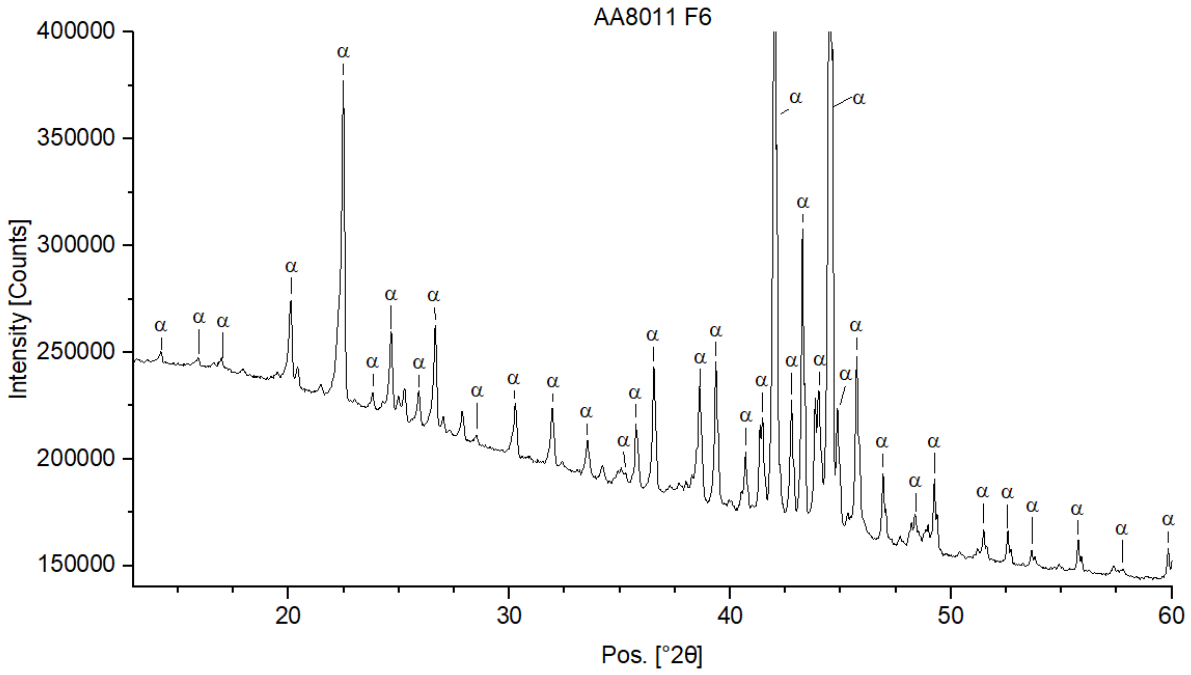

13.10.2.2 AA8014

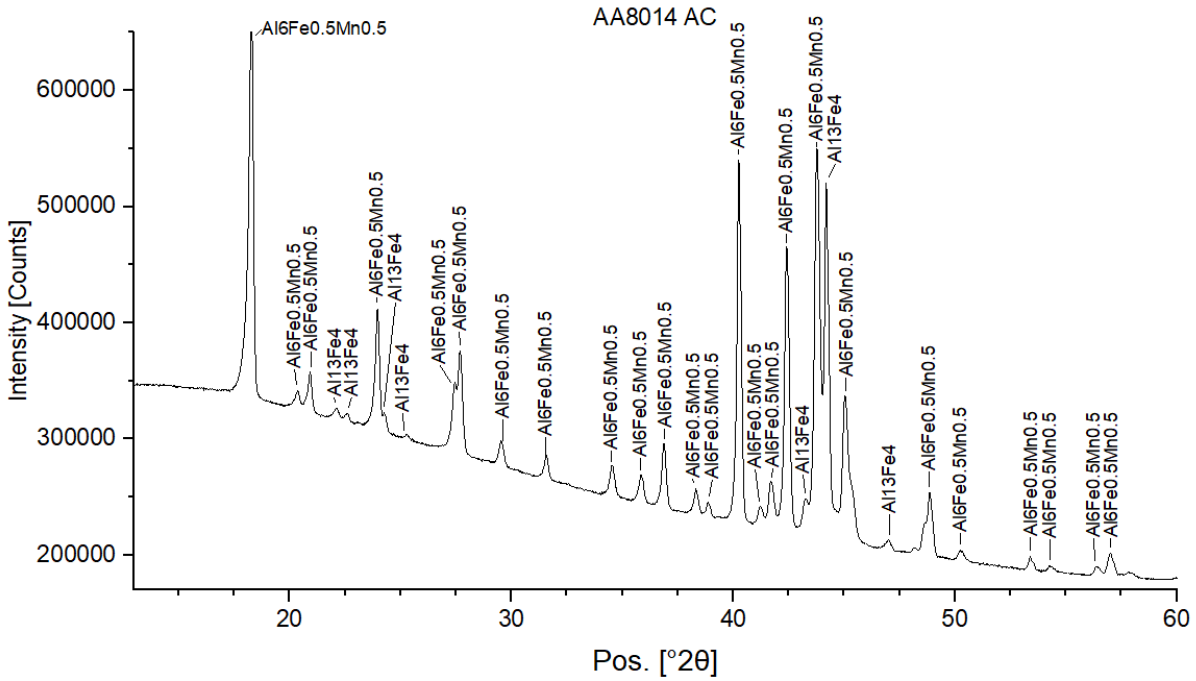

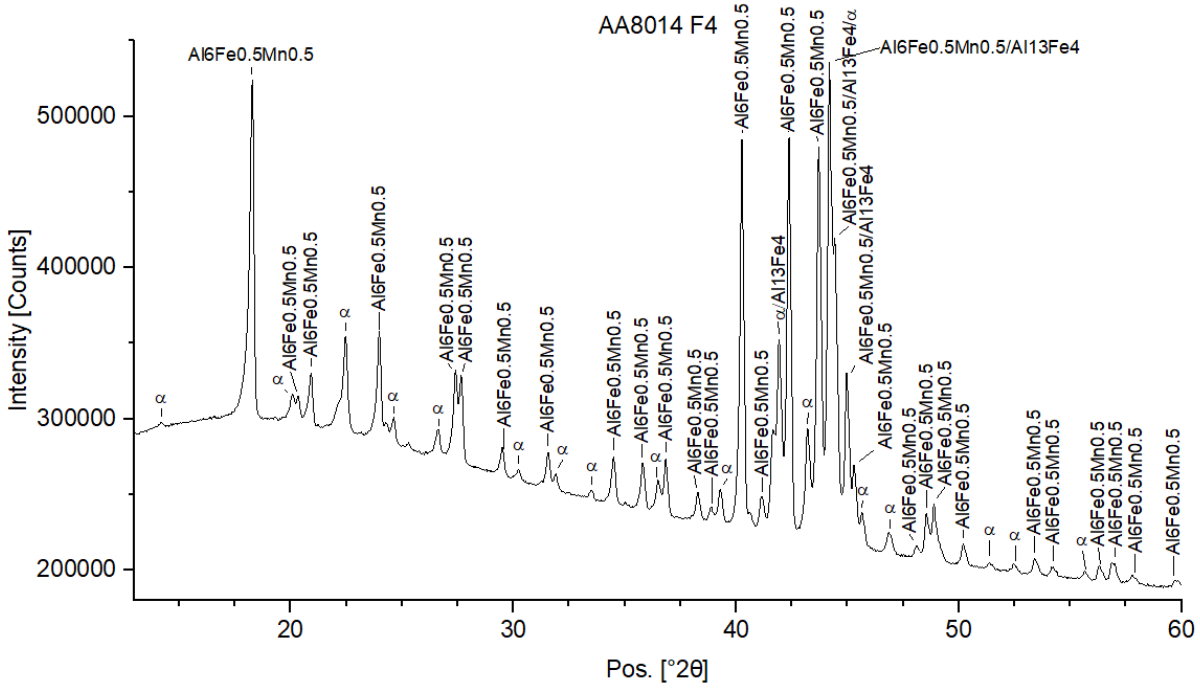

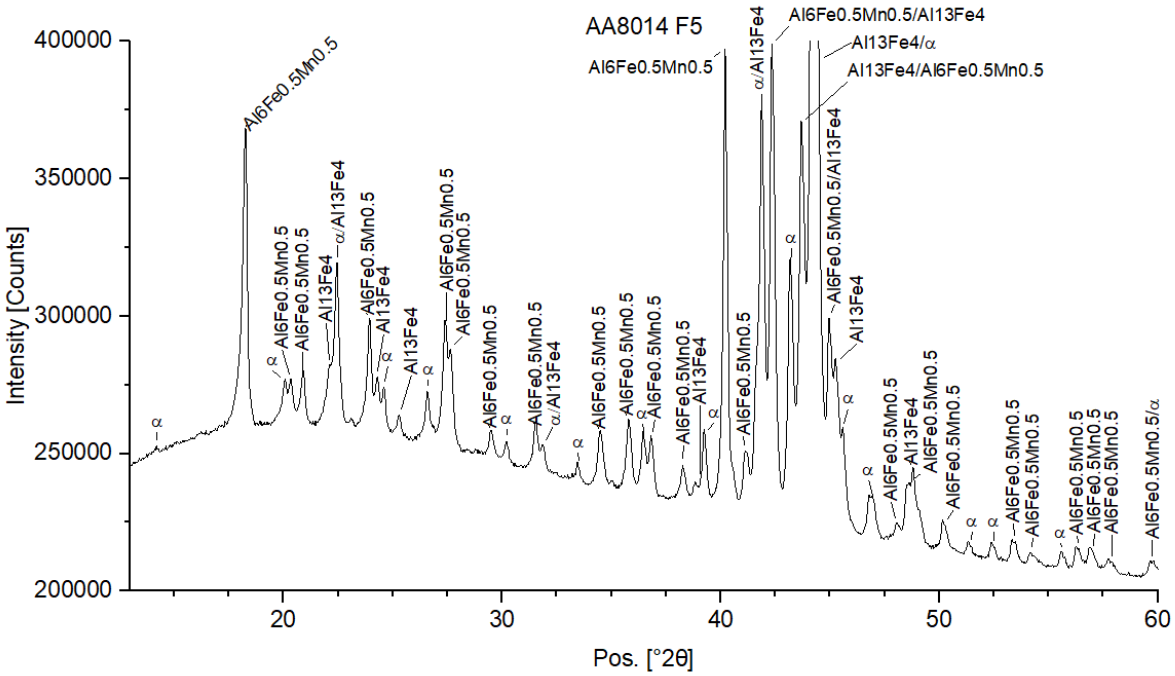

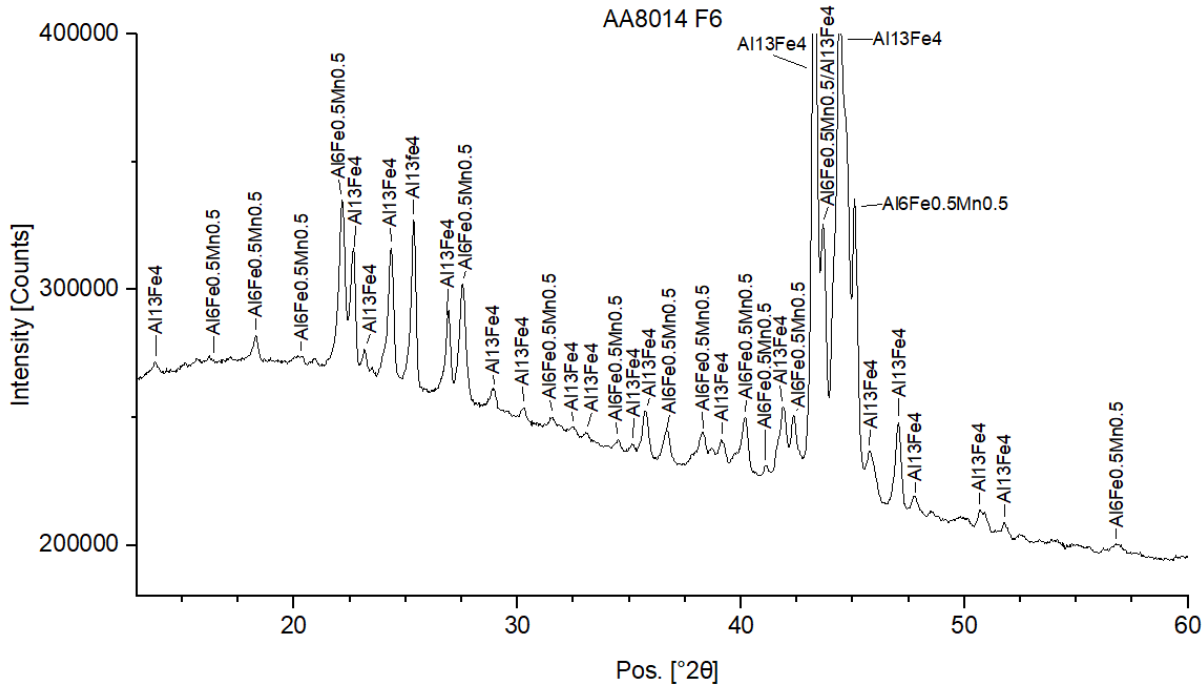

13.10.2.3 AA8021

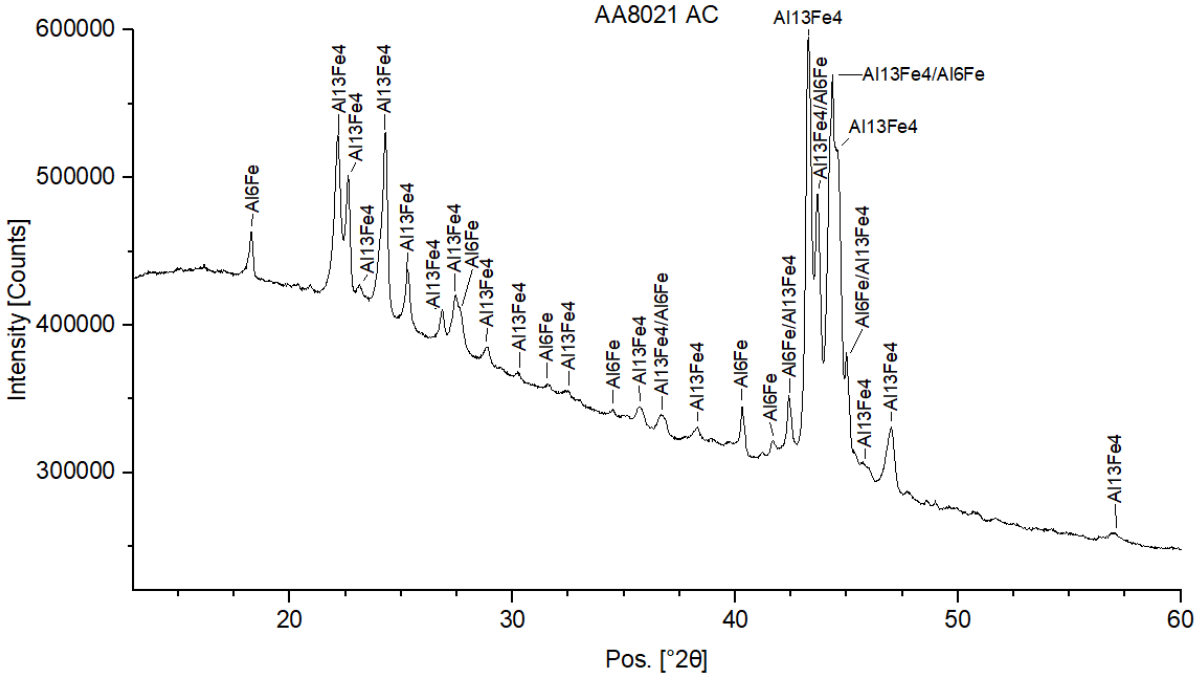

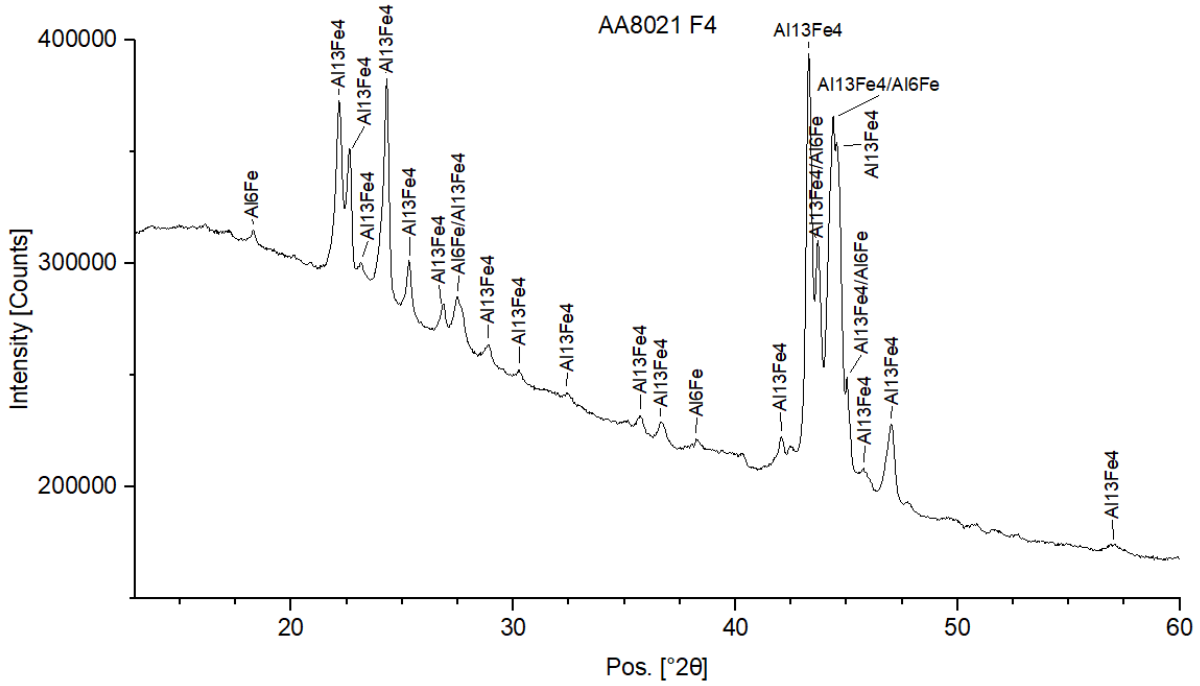

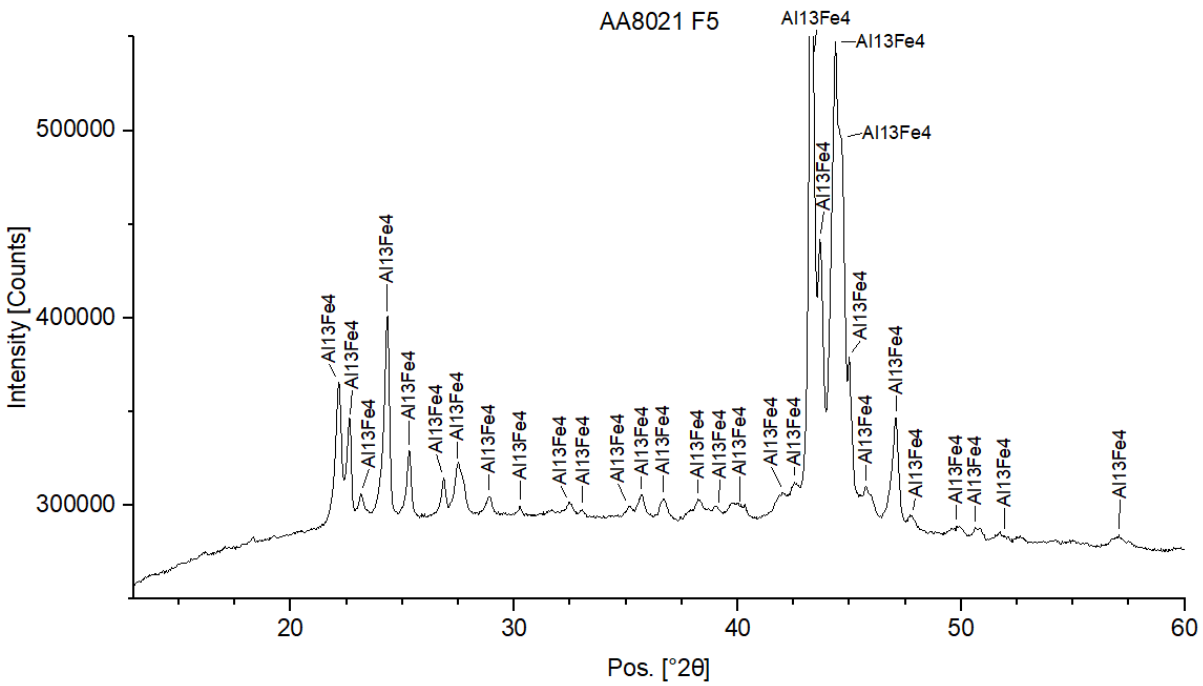

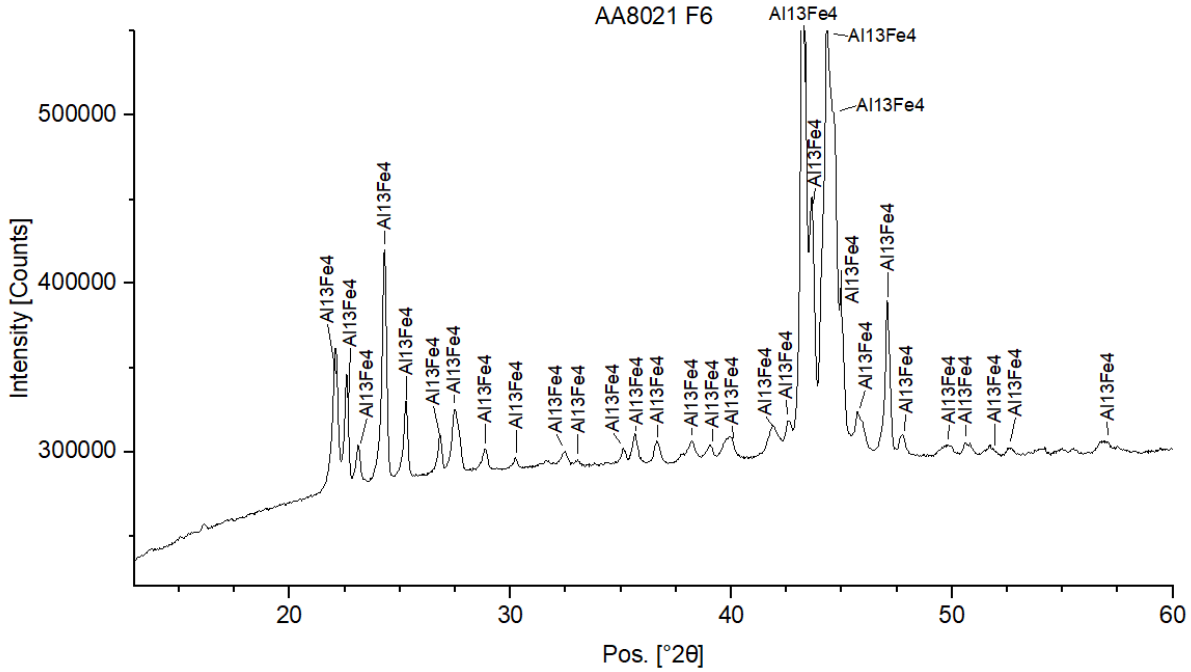

13.10.2.4 AA8079